

DISSERTATION

CHARACTERISTICS AND ORGANIZATION OF PRECIPITATING FEATURES
DURING NAME 2004 AND THEIR RELATIONSHIP TO
ENVIRONMENTAL CONDITIONS

Submitted by

Luis Gustavo P. Pereira

Department of Atmospheric Science

In partial fulfillment of the requirements

For the Degree of Doctor of Philosophy

Colorado State University

Fort Collins, Colorado

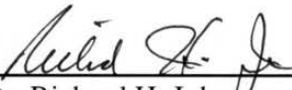
Fall 2008

COLORADO STATE UNIVERSITY

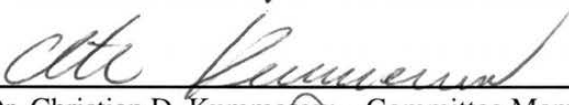
September 8, 2008

WE HEREBY RECOMMEND THAT THE DISSERTATION PREPARED UNDER OUR SUPERVISION BY LUIS GUSTAVO P. PEREIRA ENTITLED CHARACTERISTICS AND ORGANIZATION OF PRECIPITATING SYSTEMS DURING NAME 2004 AND THEIR RELATIONSHIP TO ENVIRONMENTAL CONDITIONS BE ACCEPTED AS FULFILLING IN PART REQUIREMENTS FOR THE DEGREE OF DOCTOR OF PHILOSOPHY.

Committee on Graduate Work



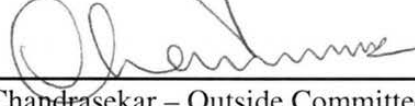
Dr. Richard H. Johnson – Committee Member



Dr. Christian D. Kummerow – Committee Member



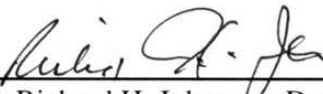
Dr. Robert C. Cifelli – Committee Member



Dr. V. Chandrasekar – Outside Committee Member



Dr. Steven A. Rutledge - Adviser



Dr. Richard H. Johnson - Department Head

ABSTRACT OF DISSERTATION

CHARACTERISTICS AND ORGANIZATION OF PRECIPITATING SYSTEMS DURING NAME 2004 AND THEIR RELATIONSHIP TO ENVIRONMENTAL CONDITIONS

The focus of this study is to examine the characteristics of convective precipitating features (PFs) during the 2004 North American Monsoon Experiment (NAME) and their precursor environmental conditions. The goal is to gain a better insight into the predictability and variability of warm season convective processes in the southern portion of the North American Monsoon core region. The organization and characteristics of PFs are evaluated using composite radar reflectivity images over the southern portion of the Gulf of California. The environmental conditions are assessed using satellite images and a plethora of atmospheric observational analysis maps, such as winds at multiple levels, upper-level divergence, vorticity, vertical air motion, moisture and vertical cross-sections.

Our study reveals that most PFs occurred during the afternoon and evening over land, especially near the foothills of the Sierra Madre Occidental. The vast majority of the precipitating features (~95%) were small, isolated, unorganized, short-lived convective cells. Mesoscale convective systems (MCSs) made up only 5% of the PF population. Nonetheless, these large, long-lived, precipitating features were responsible for 72% of the total precipitation within the radar composite region. An analysis of the number and rainfall produced by these MCSs revealed that they were not constant from day to day, but rather, varied significantly throughout NAME. We found that MCSs were more frequent when the atmosphere is thermodynamically unstable and the wind shear or large-scale dynamics favors the development of organized convection. Lastly, we examined the synoptic conditions associated with episodes of above average MCS rainfall in the southern portion of the NAME core region. Tropical waves were found to be an essential source of moisture and instability in the region. We also found that transient upper-level inverted troughs interact with the upper-level anticyclone to produce

a “North American Monsoon Jet Streak” that created favorable dynamical uplift and wind shear conditions for MCS development.

Luis Gustavo P. Pereira
Department of Atmospheric Science
Colorado State University
Fort Collins, CO 80523
Fall 2008

ACKNOWLEDGEMENTS

I would like to express my sincere gratitude to my advisor, Dr. Steven Rutledge, for his advice and guidance in the research work presented here, and also for the numerous career-enriching opportunities he enabled me to participate throughout the course of my PhD program, including the data collection efforts of the North American Monsoon Experiment. The contributions of Dr. Robert Cifelli to this research and to my career are inestimable, and are sincerely appreciated. I would also like to acknowledge the contributions made by the remaining members of my committee, Dr. Richard Johnson, Dr. Christian Kummerow, and Dr. V. Chandrasekar. Paul Hein's computer guidance was paramount to the successful development of this research. I would also like to thank Dr. Stephen Nesbitt, Dr. Timothy Lang, Paul Ciesielski, Dr. Walter Petersen, Dr. Sarah Tessendorf, Brenda Dolan, Angela Rowe, Kristen George, Russ Schumacher and Laura Ciasto for their invaluable contributions and discussions. I would further like to acknowledge Dr. Maria Assunção Silva Dias for being instrumental in my pursuit of this career. Finally, I would like to express my thanks to my family and friends, who cheerfully supported me through all these years. This research was funded by the National Oceanic and Atmospheric Administration grant NA17RJ1228 and by the National Science Foundation grant ATM-0340544.

TABLE OF CONTENTS

1	INTRODUCTION.....	1
1.1	Motivation and Objectives.....	1
1.2	Scientific Background.....	4
2	DATA AND METHODOLOGY.....	16
2.1	North American Monsoon Experiment Overview.....	16
2.2	Radar Dataset and Methodology.....	18
2.2.1	Radar Data Quality Control.....	19
2.2.2	Radar Data Compositing and Gridding.....	22
2.2.3	Rainfall Retrieval.....	23
2.2.4	Precipitating Feature Identification.....	25
2.2.5	Convective and Stratiform Partitioning.....	26
2.2.6	Precipitating Feature Horizontal Organization Modes.....	29
2.2.7	Normalization Issues.....	31
2.3	Environmental Dataset and Methodology.....	31
2.3.1	Convective Available Potential Energy Calculations.....	32
2.3.2	Vertical Wind Shear Calculations.....	34
2.3.3	Identification of Tropical Upper Tropospheric Troughs.....	36
2.3.4	Identification of Tropical Easterly Waves.....	37
3	CHARACTERISTICS AND ORGANIZATION OF PRECIPITATING FEATURES DURING NAME.....	55
3.1	Overview.....	55
3.2	Overall Characteristics of Convective Precipitating Features During NAME.....	55
3.3	Type 1: Sub-Mesoscale Non-Linear Precipitating Features.....	61
3.4	Type 2: Sub-Mesoscale Linear Precipitating Features.....	64
3.5	Type 3: Mesoscale Non-Linear Precipitating Features.....	66
3.6	Type 4: Mesoscale Linear Precipitating Features.....	69
4	THERMODYNAMIC & WIND SHEAR CONDITIONS DURING NAME AND THEIR RELATIONSHIP TO PRECIPITATING FEATURES.....	99
4.1	Overview.....	99
4.2	The CAPE Conditions During NAME.....	101
4.3	The Shear Environment During NAME.....	104
4.4	CAPE Components.....	107
4.5	Shear Components.....	108
4.6	Shear Depth Sensitivity.....	110

5	SYNOPTIC ANALYSIS OF THE CONDITIONS AFFECTING THE DEVELOPMENT OF PRECIPITATING FEATURES DURING NAME	140
5.1	Overview.....	140
5.2	Map Analyses.....	141
5.2.1	July 10-13, 2004	141
5.2.2	July 19-22, 2004.....	143
5.2.3	August 2-6, 2004.....	145
5.2.4	Other periods of interest.....	148
6	CONCLUSIONS.....	204
6.1	Overview.....	204
6.2	Summary & Conclusions.....	204
6.3	Suggestions for Future Research.....	216
	REFERENCES.....	218

LIST OF TABLES

#	Caption	Page
2.1	Operating specifications for the three radars used in the NAME radar composites.	41
2.2	List of cases used to tune the partitioning algorithm.	45
3.1	Mean characteristics of precipitating features in the NAME radar composite region.	75
3.2	Mean characteristics of Type 1 precipitating features in the NAME radar composite region.	83
3.3	Mean characteristics of Type 2 precipitating features in the NAME radar composite region.	88
3.4	Mean characteristics of Type 3 precipitating features in the NAME radar composite region.	93
3.5	Mean characteristics of Type 4 precipitating features in the NAME radar composite region.	98
4.1	Thermodynamic characteristics at 12Z within the NAME Enhanced Convection Area.	121
4.2	Mean shear conditions at 12Z within the NAME Enhanced Convection Area.	126
4.3	Linear correlation between total MCS rainfall within the NAME ECA and mean wind shear within the NAME ECA for different wind shear depths.	138
5.1	Approximate dates when tropical easterly waves were identified in synoptic maps between 100° and 110° W.	194

LIST OF FIGURES

#	Caption	Page
1.1	Map illustrating the July-August total precipitation over western Mexico as estimated from climatological rain gauge records (illustration from Gochis et al. 2006).	11
1.2	Mean 1200 and 0000 UTC meridional wind profile for July at Yuma, AZ (illustration from Douglas, 1995).	12
1.3	Mean pilot balloon winds and streamline analyses at 450 m AGL at 1200, 1800, 0000, and 0600 UTC. Isotachs with contours at 3, 5 and 7 m s ⁻¹ are also shown at 1200 UTC. Jet core is shaded. Shading of topography (light, intermediate and darkest) indicates elevations above 915 m, 1830 m, and 2745 m (3000 ft, 6000 ft, and 9000 ft), respectively (illustration from Douglas, 1995).	13
1.4	Image examples of each of the four basic modes of precipitating features organization as viewed in radar reflectivity (dBZ) images in constant altitude plan position indicator (upper panel) and range height indicator (lower panel) for a) sub-MCS non-linear, b) sub-MCS linear, c) MCS non-linear, and d) MCS linear. Solid black line in upper panels indicates position of corresponding vertical cross-sections (illustration from Rickenbach and Rutledge 1998).	14

1.5	Upper panel shows the development of a cold pool spreading out in a non-sheared environment (left) and regenerating new cells in a sheared environment (right). Bottom panel shows the evolution of a convective cell in a sheared environment in a) initial stage, when the vorticity generated by the environmental shear dominates, b) intermediate stage, when the vorticity generated by the cold pool and environmental shear are in balance, and c) final stage, when cold pool vorticity dominates (illustration from Weisman and Rotunno 2004).	15
2.1	NAME multi-tier domain (illustration from Higgins 2004).	39
2.2	Summary of NAME 2004 EOP instrument platforms (illustration from Higgins 2004).	40
2.3	Illustration of a NAME reflectivity composite image overlaid on a map with the location and approximate range rings for each radar.	42
2.4	Relationship between precipitating feature volumetric rainfall and precipitating feature size during NAME.	43
2.5	a) Cumulative Rainfall as a Function of Feature Size during NAME, b) same as 2.3a, but zoomed in at the lower end of the feature size spectrum.	44
2.6	Composite Reflectivity image and corresponding convective and stratiform areas assigned by the partitioning algorithm for each of the cases listed in Table 2.2: a) Scattered Convection case, b) Mesoscale Convective System case, c) Organized and Isolated Convection Mix case, d) Linear Convection case, e) Convection Embedded in Stratiform Precipitation case.	46
2.7	Domains of the NAME Gridded Analysis. The boundaries of the T1A dataset used in this study are depicted by the black lines (illustration from Cielsielski and Johnson 2006).	49

2.8	Map of Convective Available Potential Energy obtained using the CSU Gridded Analysis data for 28 July 2004 at 12Z. The white crosses indicate the position of the radars.	50
2.9	Map of 0-6 km Vertical Wind Shear obtained using the CSU objective gridded analysis data for 5 August 2004 at 12Z. The black crosses indicate the position of the radars.	51
2.10	Map showing synoptic features in the NAME region (illustration from the 2004 NAME Field Catalog).	52
2.11	An example of a CSU streamline analysis at 250-hPa for 23 July 2004 at 12Z.	53
2.12	An example of a CSU vorticity analysis at 250-hPa for 23 July 2004 at 12Z.	54
3.1	Map illustrating the geographical variations in frequency of occurrence of precipitating features in the NAME radar composite domain. The black thick line delineates the topography above 1000 m.	72
3.2	Distribution of Precipitating Feature sizes within the NAME radar composite region; a) feature total area, b) feature convective area.	73
3.3	Distribution of Precipitating Feature mean rain rates within the NAME radar composite region; a) feature mean rain rate, b) feature mean convective rain rate.	75
3.4	Diurnal hourly variation in a) frequency of occurrence of precipitating features; b) percentage of total (solid line) and convective (dashed line) rainfall generated by precipitating features; c) same as a), but for features over water only; and d) same as c), but for features over water only.	77
3.5	Horizontal Organization of precipitating features during NAME. a) Percentage of precipitating feature population in each organization mode; b) contribution to total rainfall by each organization mode.	78

3.6	Map illustrating the geographical variations in frequency of occurrence of Type 1 precipitating features in the NAME radar composite domain. The black thick line delineates the topography above 1000 m.	79
3.7	Distribution of Type 1 Precipitating Feature sizes within the NAME radar composite region; a) feature total area, b) feature convective area.	80
3.8	Distribution of Type 1 Precipitating Feature mean rain rates within the NAME radar composite region; a) feature mean rain rate, b) feature mean convective rain rate.	81
3.9	Diurnal hourly variation in a) frequency of occurrence of Type 1 precipitating features, and b) percentage of total (solid line) and convective (dashed line) rainfall generated by Type 1 precipitating features.	82
3.10	Map illustrating the geographical variations in frequency of occurrence of Type 2 precipitating features in the NAME radar composite domain. The black thick line delineates the topography above 1000 m.	84
3.11	Distribution of Type 2 Precipitating Feature sizes within the NAME radar composite region; a) feature total area, b) feature convective area.	85
3.12	Distribution of Type 2 Precipitating Feature mean rain rates within the NAME radar composite region; a) feature mean rain rate, b) feature mean convective rain rate.	86
3.13	Diurnal hourly variation in a) frequency of occurrence of Type 2 precipitating features, and b) percentage of total (solid line) and convective (dashed line) rainfall generated by Type 2 precipitating features.	87
3.14	Map illustrating the geographical variations in frequency of occurrence of Type 3 precipitating features in the NAME radar composite domain. The black thick line delineates the topography above 1000 m.	89
3.15	Distribution of Type 3 Precipitating Feature sizes within the NAME radar composite region; a) feature total area, b) feature convective area.	90

3.16	Distribution of Type 3 Precipitating Feature mean rain rates within the NAME radar composite region; a) feature mean rain rate, b) feature mean convective rain rate.	91
3.17	Diurnal hourly variation in a) frequency of occurrence of Type 3 precipitating features, and b) percentage of total (solid line) and convective (dashed line) rainfall generated by Type 3 precipitating features.	92
3.18	Map illustrating the geographical variations in frequency of occurrence of Type 4 precipitating features in the NAME radar composite domain. The black thick line delineates the topography above 1000 m.	94
3.19	Distribution of Type 4 Precipitating Feature sizes within the NAME radar composite region; a) feature total area, b) feature convective area.	95
3.20	Distribution of Type 4 Precipitating Feature mean rain rates within the NAME radar composite region; a) feature mean rain rate, b) feature mean convective rain rate.	96
3.21	Diurnal hourly variation in a) frequency of occurrence of Type 4 precipitating features, and b) percentage of total (solid line) and convective (dashed line) rainfall generated by precipitating features.	97
4.1	Same as Fig. 3.1, but with a red box overlaid on the map indicating the Enhanced Convection Area.	114
4.2	Three-day moving average of daily mean CAPE within the Enhanced Convection Area of NAME (solid line), and three-day moving average of the daily number of Type 1 PFs during NAME (dashed line), shown as a percentage of total number of Type 1 PFs in the entire period.	115
4.3	Three-day moving average of daily mean CAPE within the Enhanced Convection Area of NAME (solid line), and three-day moving average of the daily number of MCSs during NAME (dashed line), shown as a percentage of total number of MCSs in the entire period.	116

- 4.4 Three-day moving average of daily mean CAPE within the Enhanced Convection Area of NAME (solid line), and three-day moving average of the daily rainfall (as a percentage of rainfall in the entire period) generated by Type 1 PFs during NAME (dashed line). 117
- 4.5 Three-day moving average of daily mean CAPE within the Enhanced Convection Area of NAME (solid line), and three-day moving average of the daily rainfall (as a percentage of rainfall in the entire period) generated by MCSs during NAME (dashed line). 118
- 4.6 Three-day moving average of daily mean size of Type 1 PFs within the Enhanced Convection Area of NAME (solid line), and three-day moving average of the daily rainfall (as a percentage of rainfall in the entire period) 119
- 4.7 Three-day moving average of mean Convection Inhibition (CIN) within the Enhanced Convection Area of NAME. 120
- 4.8 Three-day moving average of daily mean 0-6 km wind shear within the Enhanced Convection Area of NAME (solid line), and three-day moving average of the daily number of Type 1 PFs during NAME (dashed line), shown as a percentage of total number of Type 1 PFs in the entire period. 122
- 4.9 Three-day moving average of daily mean 0-6 km wind shear within the Enhanced Convection Area of NAME (solid line), and three-day moving average of the daily number of MCSs during NAME (dashed line), shown as a percentage of total number of MCSs in the entire period. 123
- 4.10 Three-day moving average of daily mean 0-6 km wind shear within the Enhanced Convection Area of NAME (solid line), and three-day moving average of the daily rainfall (as a percentage of rainfall in the entire period) generated by Type 1 PFs during NAME (dashed line). 124
- 4.11 Three-day moving average of daily mean 0-6 km wind shear within the Enhanced Convection Area of NAME (solid line), and three-day moving average of the daily rainfall (as a percentage of rainfall in the entire period) generated by MCSs during NAME (dashed line). 125

- 4.12 Three-day moving average of daily mean Convective Available Potential Energy (CAPE) within the Enhanced Convection Area of NAME (solid line), and three-day moving average of 12Z surface temperature within the ECA (dashed line). 127
- 4.13 Three-day moving average of daily mean Convective Available Potential Energy (CAPE) within the Enhanced Convection Area of NAME (solid line), and three-day moving average of surface mixing ratio within the ECA (dashed line). 128
- 4.14 Three-day moving average of temperature within the Enhanced Convection Area of NAME at a) 1 km (solid line) and 2 km (dashed line) MSL; b) 3 km (solid line) and 4 km (dashed line) MSL; and c) 5 km (solid line) and 6 km (dashed line) MSL. 129
- 4.15 Three-day moving average of daily mean wind shear within the Enhanced Convection Area of NAME. The thick solid line represents the 0-6 km wind shear, while the thin solid line indicates the meridional component of the wind shear and the dashed line shows the zonal component of the wind shear. 131
- 4.16 Three-day moving average of daily mean zonal wind shear and its components within the Enhanced Convection Area of NAME. The thick solid line represents the total zonal component of wind shear. The thin solid line indicates the average zonal wind in the lowest 500 m of the atmosphere, and the dashed line shows the zonal mean wind at 6 km AGL. 132
- 4.17 Three-day moving average of daily mean meridional wind shear and its components within the Enhanced Convection Area of NAME. The thick solid line represents the total meridional component of wind shear. The thin solid line indicates the average meridional wind in the lowest 500 m of the atmosphere, and the dashed line shows the mean meridional wind at 6 km AGL. 133

4.18	Three-day moving average of wind shear within the Enhanced Convection Area of NAME over different depths above ground level: 0-6 km AGL (thick solid line), 0-5 km AGL (dashed line), 0-3 km AGL (thin solid line), 0-1 km AGL (dashed-dotted line).	134
4.19	Three-day moving average of wind shear within the Enhanced Convection Area of NAME over different depths above mean sea level: 0-6 km MSL (thick solid line), 0-5 km MSL (dashed line), 0-3 km MSL (thin solid line), 0-1 km MSL (dashed-dotted line). The blue thick line depicts the 0-6 km	135
4.20	Three-day moving average of wind shear within the Enhanced Convection Area of NAME between different pressure levels: 800-400 hPa (thick solid line), 950-700 hPa (dashed line), 1000-800 hPa (thin solid line). The blue thick line depicts the 0-6 km AGL wind shear used in this study.	136
4.21	Three-day moving average of 5-10 AGL wind shear within the Enhanced Convection Area of NAME.	137
4.22	Three-day moving average of 1000-800 mb wind shear within the Enhanced Convection Area of NAME (blue dashed line) and three-day moving average of the daily rainfall (as a percentage of rainfall in the	139
5.1	Map identifying synoptic features within the NAME Tier II region on a) 10 July 2004, b) 11 July 2004, c) 12 July 2004, and d) 13 July 2004.	153
5.2	CSU streamline analysis map at 250 mb for a) 10 July 2004, b) 11 July 2004, c) 12 July 2004, and d) 13 July 2004.	155
5.3	CSU streamline analysis map at 700 mb for a) 10 July 2004, b) 11 July 2004, c) 12 July 2004, and d) 13 July 2004.	157
5.4	CSU longitudinal Cross Section at 25 °N showing the profile of relative humidity and wind barbs on a) 10 July 2004, b) 11 July 2004, c) 12 July 2004, and d) 13 July 2004.	159
5.5	Skew-T plot of the sounding launched from Los Mochis, Mexico on 12 July 2004 at 00Z.	161

5.6	CSU vertical air motion analysis at 700 mb within the NAME Tier II region on 12 July 2004 at 12Z.	162
5.7	Infrared Satellite Image from GOES-10 on 13 July 2004 at 0154 UTC.	163
5.8	Map identifying synoptic features within the NAME Tier II region on a) 19 July 2004, b) 20 July 2004, c) 21 July 2004, and d) 22 July 2004.	164
5.9	CSU streamline analysis map at 250 mb for a) 19 July 2004, b) 20 July 2004, c) 21 July 2004, and d) 22 July 2004.	166
5.10	CSU cross section perpendicular to the southern portion of the Gulf of California from 111°N, 23 °N to 102 °W, 29 °N showing the profile of relative humidity and wind barbs on 22 July 2004 at 12 UTC.	168
5.11	CSU divergence analysis at 250 mb within NAME Tier II region on 21 July 2004 at 12Z.	169
5.12	CSU vertical air motion analysis at 500 mb within the NAME Tier II region on 21 July 2004 at 12Z.	170
5.13	Skew-T plot of the sounding launched from Los Mochis, Mexico on 21 July 2004 at 16Z.	171
5.14	Infrared Satellite Image from GOES-10 on 21 July 2004 at 2254 UTC.	172
5.15	Infrared Satellite Image from GOES-10 on 22 July 2004 at 1009 UTC.	173
5.16	950 mb wind speed and direction along the flight path of NOAA's P3 airplane on 22 July 2004 around 1300 UTC.	174
5.17	Wind and relative humidity profile time series at Empalme, Mexico. The red box highlights the moist southeasterly flow pushing moisture northward along the Gulf of California.	175
5.18	Infrared Satellite Image from GOES-12 on 20 July 2004 at 1439 UTC.	176

5.19	CSU cross section perpendicular to the southern portion of the Gulf of California from 111°N, 23 °N to 102 °W, 29 °N showing the profile of relative humidity and wind barbs on a) 5 August 2004 at 12 UTC, and b) 6	177
5.20	Map identifying synoptic features within the NAME Tier II region on a) 3 August 2004, b) 4 August 2004, c) 5 August 2004, and d) 6 August 2004.	178
5.21	CSU streamline analysis map at 300 mb for a) 2 August 2004 at 12 UTC, and b) 4 August at 00Z.	180
5.22	Rapid Update Cycle model analysis of 250 mb wind observations, with cyan streamlines for 4 August 2004 at 12 UTC. The thick red line highlights the axis of the inverted trough.	181
5.23	Infrared Satellite Image from GOES-12 on 3 August 2004 at a) 0939 UTC and b) 2238 UTC. The red dashed line indicates the position of the tropical wave.	182
5.24	CSU streamline analysis map at 700 mb for a) 3 August 2004 at 12 UTC, and b) 4 August at 00Z.	183
5.25	Climate Prediction Center/ <i>Servicio Meteorológico Nacional</i> precipitation analysis within NAME Tier 1 for 4 August 2004.	184
5.26	Water Vapor Satellite Image from GOES-12 on 4 August 2004 at 1838 UTC.	185
5.27	CSU vorticity analysis map at 400 mb for a) 5 August 2004 at 00 UTC, b) 5 August 2004 at 12 UTC, c) 6 August 2004 at 00 UTC, and d) 6 August 2004 at 12 UTC.	186
5.28	Water Vapor Satellite Image from GOES-12 on 5 August 2004 at 1838 UTC. The red L marks the position of the TUTT, and the arrow highlights the circulation bringing mid-level moisture into the NAME ECA region.	188
5.29	Infrared Satellite Image from GOES-12 on 6 August 2004 at 0139 UTC.	189

5.30	Climate Prediction Center/ <i>Servicio Meteorológico Nacional</i> precipitation analysis within NAME Tier 1 for 5 August 2004.	190
5.31	NCAR 12-km WRF model analysis of 500 mb winds on 6 July 2004 at 12 UTC.	191
5.32	<i>Servicio Meteorológico Nacional</i> synoptic features map overlaid on satellite imagery valid on a) 1 July 2004, and b) 31 August 2004.	192
5.33	<i>Servicio Meteorológico Nacional</i> synoptic features map overlaid on satellite imagery valid on a) 16 July 2003, and b) 27 August 2003.	193
5.34	<i>Servicio Meteorológico Nacional</i> synoptic features map overlaid on satellite imagery valid on a) 16 July 2004, b) 21 July 2004, c) 22 July 2004, and d) 23 July 2004. The red box highlights the same tropical wave	195
5.35	<i>Servicio Meteorológico Nacional</i> synoptic features map overlaid on satellite imagery valid on a) 23 July 2004, and b) 11 August 2004.	197
5.36	<i>Servicio Meteorológico Nacional</i> daily precipitation map over Mexico for a) 8 August 2004, b) 9 August 2004, c) 10 August 2004, d) 11 August 2004, and e) 12 August 2004.	198
5.37	NCAR 12-km WRF model analysis of 300 mb winds on a) 8 August 2004 at 00 UTC, and b) 10 August 2004 at 00 UTC.	201
5.38	CSU analysis on 10 August 2004 at 00 UTC of a) 300 mb divergence, and b) 700 mb omega field.	203

CHAPTER I

Introduction

1.1 - Motivation and Objectives

One of the most important atmospheric circulation patterns affecting summertime weather over the southwest United States and northwest Mexico is the North American Monsoon. This circulation pattern is experienced as a pronounced increase in rainfall from a very dry June to a rainy July and lasts until mid-September, when a drier regime is reestablished in the region (Adams and Comrie, 1997). Some areas in northwest Mexico receive 60-80% of their annual rainfall during monsoon season (Fuller and Stensrud, 2000). Climatological data from rain gauges (Fig. 1.1) and past studies using satellite data have indicated rainfall of up to 600 mm over some portions of the Sierra Madre Occidental (SMO) in July-August (Negri et al. 1993, Gochis et al. 2007).

One of the main scientific objectives of the North American Monsoon Experiment (NAME) field campaign was to achieve a better understanding and more realistic numerical simulations of the convective and mesoscale processes of the warm season precipitation over the complex terrain of the North American Monsoon region (Higgins et

al. 2006). Improved understanding of these precipitation processes in the NAME core domain will provide insight leading to improved parameterizations for numerical weather prediction models (Gochis et al., 2003).

An important mechanism responsible for the transport of moisture northward through the Gulf of California (GoC) and occasionally as far inland into Arizona was described by Hales (1972) and Brenner (1974). This transport mechanism was termed a gulf surge and was described as a coastally trapped disturbance that propagates northward, channeled along the Gulf of California carrying moist Tropical Pacific air. Many other investigations have subsequently supported this moisture surge hypothesis and their role in active periods of precipitation within the North American Monsoon system (Houghton 1979; Jauregui and Cruz 1981; Tang and Reiter 1984; Carleton 1985, 1986; Hasimoto and Reyes 1988; Reyes and Cadet 1988; Carleton et al. 1990; Badan-Dangon et al. 1991; Rowson and Colucci 1992; Douglas 1995; Maddox et al. 1995; McCollum et al. 1995; Stensrud et al. 1997). More recently Rogers and Johnson (2007) hypothesized that gulf surges may be initiated by evaporational cooling associated with convective rainfall over the GoC coastal plain and Sierra Madre Occidental (SMO), leading to the development of a surface mesohigh over the coastal plain. They further hypothesized that the cold pool associated with these mesohighs could impinge on nocturnal inversions and trigger a surge in the form of bore-like disturbances. Thus, in order for these disturbances to be properly simulated, it is of paramount importance that we have a good understanding of the characteristics of convective precipitating features, particularly organized convective features such as Mesoscale Convective Systems (MCSs), which typically generate substantial rainfall (Gochis et al. 2007, Nesbitt et al.

2008). Moreover, if rainfall underwent an intraseasonal variation during NAME, as it has been indicated by Gochis et al. (2007) and Lang et al. (2007), then what environmental conditions favor the development of significant rainfall events in the region?

Higgins and Gochis (2007) summarized some of the early results recently published using NAME 2004 and stated that “Additional work is needed to determine contributions of rainfall-producing systems (e.g., mesoscale convective systems, organized sea-breeze convection lines, etc.) to the mean diurnal cycle of precipitation, including documentation of the frequency of occurrence of rainfall-producing systems. Results from these studies can be used to improve the ability of models to simulate the diurnal cycle toward achieving more accurate precipitation forecasts”. Furthermore, they also stated that “It has become clear that there are complex interactions between tropical easterly waves, upper-level inverted troughs, cold fronts, cutoff lows, open troughs, and Gulf of California moisture surges that are not well understood despite the fact that they are likely to be important in the prediction of monsoon precipitation”. The overarching goal of this study is to gain better insight into the predictability and variability of warm season convective processes in the southern portion of the North American Monsoon core region. This research should also provide a climatological context in which to place future case studies of specific events in the region. The specific objectives of this study are the following:

- 1) Identify the horizontal organization modes of convective precipitation near the southern portion of the GoC and their characteristics, such as frequency of occurrence, rainfall contribution, rain rate, geographical distribution and diurnal cycle.

- 2) Unveil the environmental conditions that favored the development of this organized convection.
- 3) Examine the synoptic disturbances and patterns responsible for favorable environmental conditions when episodes of enhanced rainfall occurred in the region.

1.2 - Scientific Background

As mentioned in the previous section, a substantial portion of the annual precipitation over northwest Mexico and the US desert southwest occurs during the wet phase of the North American Monsoon. This circulation pattern is experienced as a pronounced increase in rainfall from a very dry June to a rainy July and last until mid-September, when a drier regime is reestablished in the region (Adams and Comrie, 1997). The abundant storms that form during the North American Monsoon season (Campbell 1906; Beals 1922; Blake 1923) are capable of creating flash floods, copious cloud-to-ground lightning and dust storms responsible for a significant amount damage, injuries and deaths in the region and, therefore, are an important operational forecasting concern (Stensrud et al., 1997).

In the last several decades, there has been a debate on the source of moisture for the North American Monsoon. The rainy season in the region is usually associated with the northward migration of an upper-level anticyclone and an associated zonal wind shift at upper-levels from west to east (Bryson and Lowry 1955, Saleeby and Cotton 2004, Xu et al. 2004, Johnson et al. 2007). This shift led some scientists to believe that the Gulf of

Mexico was the source of moisture for the North American Monsoon (Bryson and Lowry 1955; Green 1963; Green and Sellers 1964; Hastings and Turner 1965). However, Reitan (1957) showed that the greatest amount of precipitable water during the Arizona monsoon is found below 800 mb. Considering that the topography between Arizona and the Gulf of Mexico rises far above this level, it appeared unlikely that the Gulf of Mexico was the source of this low-level moisture. Rasmusson (1967) found a northward flux of moisture into Arizona from the Gulf of California. Since then, the more recent literature has tended to focus on the GoC as the dominant source of moisture for the North American Monsoon. Nevertheless, most investigators subscribe to the idea that low and middle level moisture comes from the tropical Pacific and the GoC, while moisture in the middle and upper troposphere comes from the Gulf of Mexico (Hales 1974; Brenner 1974; Mitchell 1976; Carleton 1985, 1986; Carleton et al. 1990; Harrington et al. 1992; Watson et al. 1994; Stensrud et al. 1995; Schmitz and Mullen 1996; Adams and Comrie 1997).

Several pilot balloon and aircraft measurements took place in the U.S. and in Mexico during the South-West Area Monsoon Project (SWAMP) in the summer of 1990. These observations were aimed at examining the importance of the GoC as a source of low-level moisture. Douglas (1995) documented the presence of a semi-permanent low-level northward flow over Yuma, Arizona. Fig. 1.2 shows that this low-level southerly jet is strongest at 500 m AGL and during the nighttime (1200 UTC or 0500 LST). Douglas (1995) also obtained the mean winds and streamlines at 450 m AGL over and in the

vicinity of the GoC as a function of the diurnal cycle (Fig. 1.3). The observed streamlines indicate the presence of the low-level up-gulf flow along the entire GoC, strongest at 250-400 m MSL. Fig. 1.3 shows the nocturnal nature of the low-level flow and the interaction of the jet with other mesoscale circulation, such as mountain-valley and land-sea breezes. Fig. 1.3 shows that during the afternoon (0000 UTC) the low-level jet is weakened by the sea breeze and upslope circulation. This circulation suggests the origin of the diurnal convection over the foothills of the SMO. At night and during the morning, as the convection moves from the mountains towards the coastal areas, the land breeze converges with the low-level jet along the Gulf, strengthening it.

Several studies have suggested that moisture is frequently the most important ingredient necessary for thunderstorm development (Bryson and Lowry 1955; Green and Sellers 1964; Adang and Gall 1989; McCollum et al. 1995). Despite the presence of this summertime semi-permanent low-level jet over the GoC, the occurrence of strong thunderstorms in the United States desert southwest is not continuous throughout the monsoon season. There can be periods during the monsoon season in which little or no precipitation occurs in Arizona, termed monsoon breaks, followed by an extensive period of thunderstorm development and heavy rainfall, termed monsoon bursts (Stensrud et al. 1997). To explain the monsoon burst, Hales (1972) and Brenner (1974) offered the Gulf Surge mechanism described in the previous section. Hales (1972) divided surges into two categories: major surges (or Type I) and minor surges (or Type II). The former type was observed to be associated with a deeper layer of moisture (i.e. up to 8000 ft) and with a

longer-lasting "monsoon burst", while the latter is associated with shorter monsoon "bursts" and the moisture layer is shallower (i.e. up to 5000 ft).

Hales (1972) noticed that occurrence of gulf surges coincided with the arrival of large cloud masses (i.e. at least 220 km x 220 km) over the central or the south part of the GoC. Recent examination of a gulf surge event on 13-14 July 2004 pointed to the role of convective precipitation in triggering these gulf surges through the development of bore (Simpson 1997) and Kelvin-like (Reason and Steyn 1992) disturbances as convective cold pools impinge on a nocturnal inversion over the coastal plains west of the SMO (Rogers and Johnson 2007). The presence of deep convection and intense rainfall, as seen in MCSs and tropical cyclones, has also been shown to be a necessary ingredient, albeit not necessarily sufficient, to the development of gulf surges in several other studies (Hales 1972, Adams and Comrie 1997, Stensrud et al. 1997, Fuller and Stensrud 2000, Douglas and Leal 2003).

Horizontal convective organization has been classified according to different schemes designed to test specific hypotheses in past studies, with particular attention given to the size and morphology of precipitating features. The size of convective features has been shown to be important to the magnitude of energy transported vertically in the atmosphere, with MCSs as a fundamental unit to large-scale circulations in the Tropics (Houze 1982). Morphologically, precipitating features have been divided according to their organization into convective lines, since linear systems have been shown to increase momentum at upper (lower) levels against (with) the line propagation

direction (LeMone et al. 1984). Rickenbach and Rutledge (1998) classified convective organization of radar echoes during TOGA-COARE (Tropical Ocean Global Atmosphere Coupled Ocean-Atmosphere Response Experiment) using four basic modes of horizontal structure during TOGA-COARE (Fig. 1.4): Sub-MCS non-linear, Sub-MCS linear, MCS non-linear and MCS linear. They found that the most common snapshot of organization were fields solely composed of sub-MCS non-linear precipitating features, which accounted for 12% of total rainfall during TOGA-COARE. However, they found that MCS scale feature generated 80% of the precipitation in the region and most of these precipitating features attained linear characteristics, which had a mean convective rainfall fraction of 66%. Using the TRMM satellite data Nesbitt et al. (2006) showed that MCSs (linear and non-linear) contributed to nearly 70% of the total rainfall in the west coast of Central America and nearby East Pacific.

Lang et al. (2007) indicated that there was a great degree of intraseasonal variability in the rainfall within the NAME radar composite region. Gochis et al. (2007) identified such periods as observed in the NAME Rain Gauge Event Network and related at least one such period (21-24 July) as being associated with the occurrence of MCS scale precipitating features. Variability in MCS rainfall is, arguably, controlled primarily by environmental conditions such as thermodynamic instability and wind shear (Jirak and Cotton, 2007). There are a variety of parameters that can be used to estimate the atmospheric instability, such as CAPE, Total Totals, SWEAT, and K index, all of which have been used in previous MCS studies to indicate the likelihood of their development

(Maddox 1983, Laing and Fritsch 2000, Jirak et al. 2003, Jirak and Cotton 2007). Higgins et al (2004) suggested that CAPE should be an important element driving precipitation since persistent orographic forcing for vertical motions is always present in the core monsoon region. Low-level wind shear has also been shown to play a role in MCS development through the deep lifting which is generated when the ambient shear interacts with convectively-generated cold air pools (Rotunno et al. 1988, Weisman 1992, Weisman and Rotunno 2004). This mechanism, illustrated in Fig. 1.5, explains how initially isolated convective cells regenerate new cells and become longer-lived. Weisman and Rotunno (2004) also found that the best skill in MCS prediction in their modeling simulations occurred when wind shear was computed over 0-5 km AGL. A correlation between stronger wind shear and MCS occurrence was also observed during TOGA-COARE (Rickenbach and Rutledge 1998), whereas in NAME shear has also been suggested to play a role in the development of intense rainfall periods by Lang et al. (2007) and by Gochis et al. (2007).

Favorable environmental conditions may be brought about by certain synoptic disturbances or circulation patterns leading to development of stronger instability, stronger wind shear and/or stronger upper-level divergence. Farfán and Zehnder (1994) suggested that propagating MCSs occurred when stronger midlevel easterly-northeasterly flow were present in the NAME core region. Carleton (1986) and Higgins et al. (2004) noticed that an important synoptic feature modulating rainfall in the North American Monsoon system is the position of the upper-level subtropical ridge. Rainfall appeared to

be favored with the northward progression of the upper-level anticyclone from Mexico towards the four corners area. Another synoptic disturbances which has been documented to affect the North American Monsoon system are easterly wave troughs passing south of the GoC (Stensrud et al. 1997; Fuller and Stensrud 2000). In addition to that, Stensrud et al. (1997) observed that surges strengthened when a mid-latitude trough precede, by 1 or 2 days, the passage of the easterly wave trough along the same longitudinal belt. Later, Fuller and Stensrud (2000) noticed that this phase relationship between the westerly and easterly waves occurs only once a year on average. Finally, Douglas and Englehart (2007) showed that tropical inverted troughs are among the most important transient synoptic features to affect the North American Monsoon system, affecting the region an average of 55 days per season and contributing 20% to 25% of the total summer rainfall. The number of inverted troughs between mid July and mid August in 2004, when most NAME data were collected, appeared to be close to the climatological average, although the shorter 2004 monsoon season resulted in an overall fewer number of days with inverted troughs present (Douglas and Englehart, 2007). These inverted troughs have been suggested by Douglas and Englehart (2007) and by Pytlak et al. (2005) to favor the development of MCSs and intense rainfall episodes during NAME through the emergence of a favorable wind flow from the northeast and the interaction with the upper level anticyclone and consequential formation of areas of upper-level divergence.

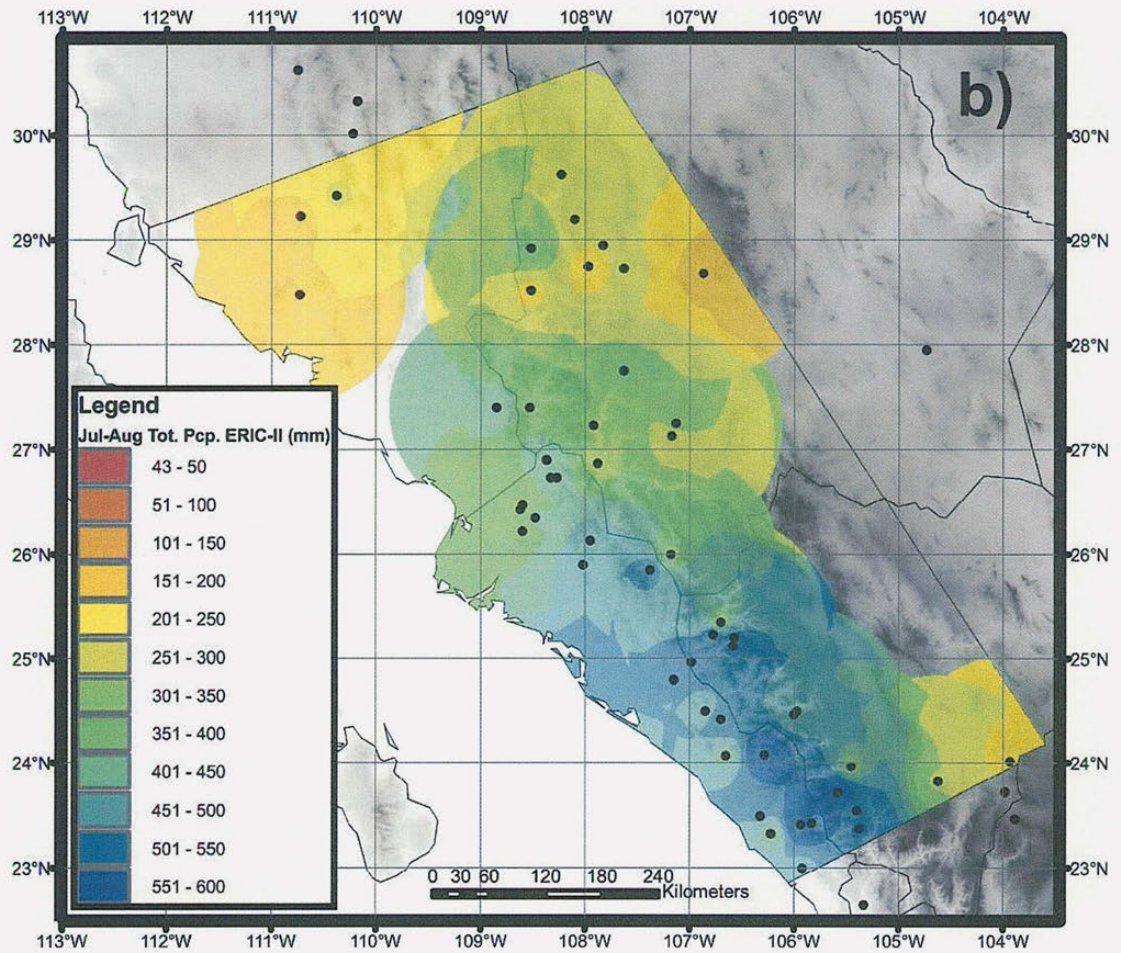


Fig. 1.1 - Map illustrating the July-August total precipitation over western Mexico as estimated from climatological rain gauge records (illustration from Gochis et al. 2006).

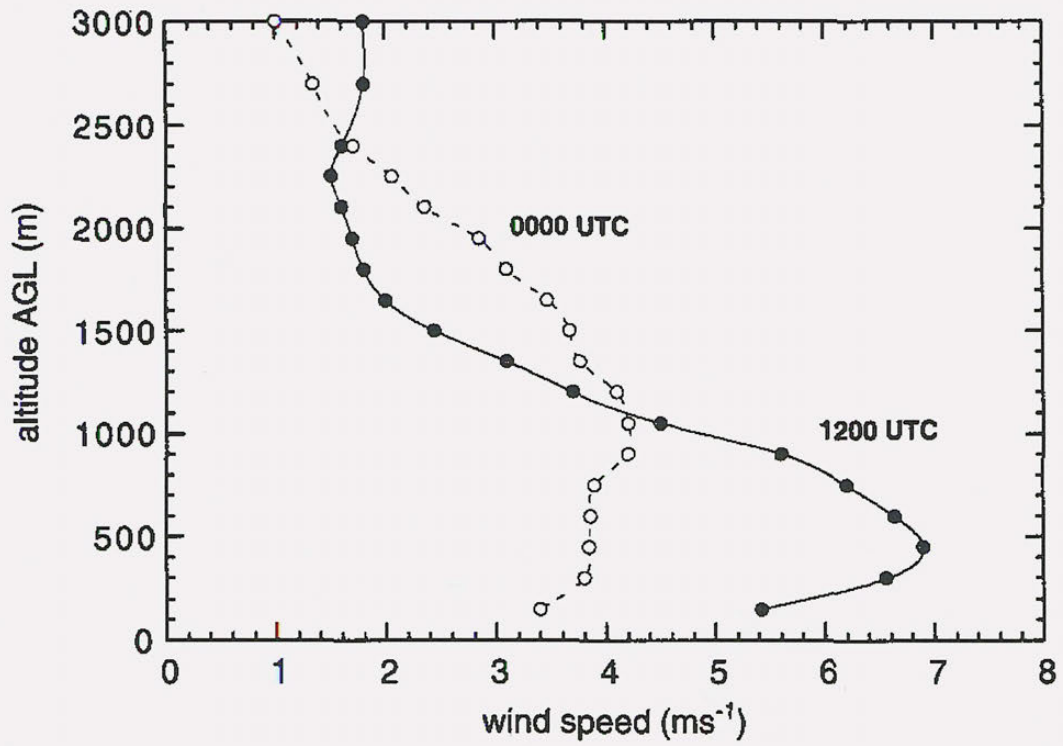


Fig. 1.2 – Mean 1200 and 0000 UTC meridional wind profile for July at Yuma, AZ (illustration from Douglas, 1995).

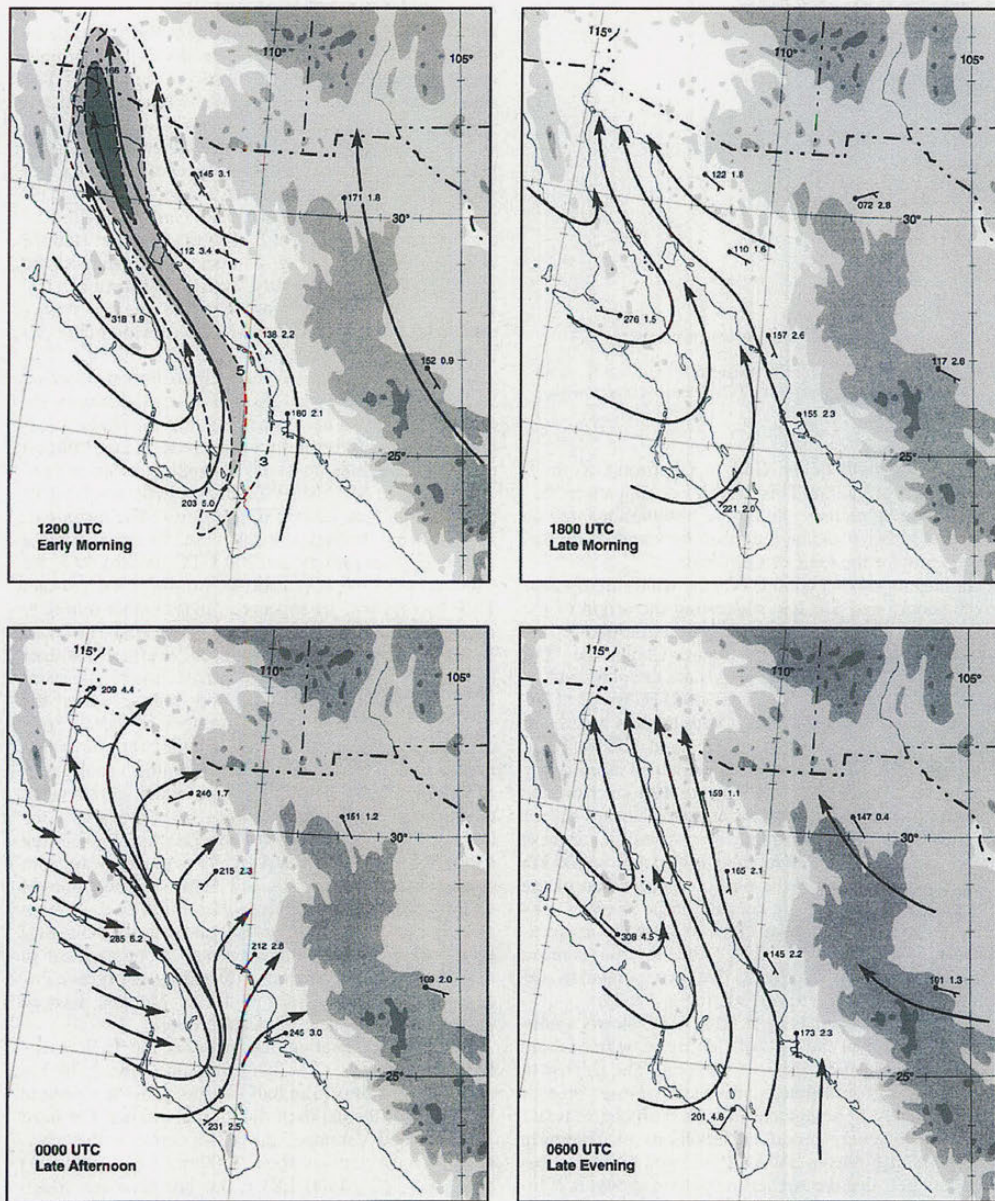


Fig. 1.3 – Mean pilot balloon winds and streamline analyses at 450 m AGL at 1200, 1800, 0000, and 0600 UTC. Isotachs with contours at 3, 5 and 7 m s⁻¹ are also shown at 1200 UTC. Jet core is shaded. Shading of topography (light, intermediate and darkest) indicates elevations above 915 m, 1830 m, and 2745 m (3000 ft, 6000 ft, and 9000 ft), respectively (illustration from Douglas, 1995).

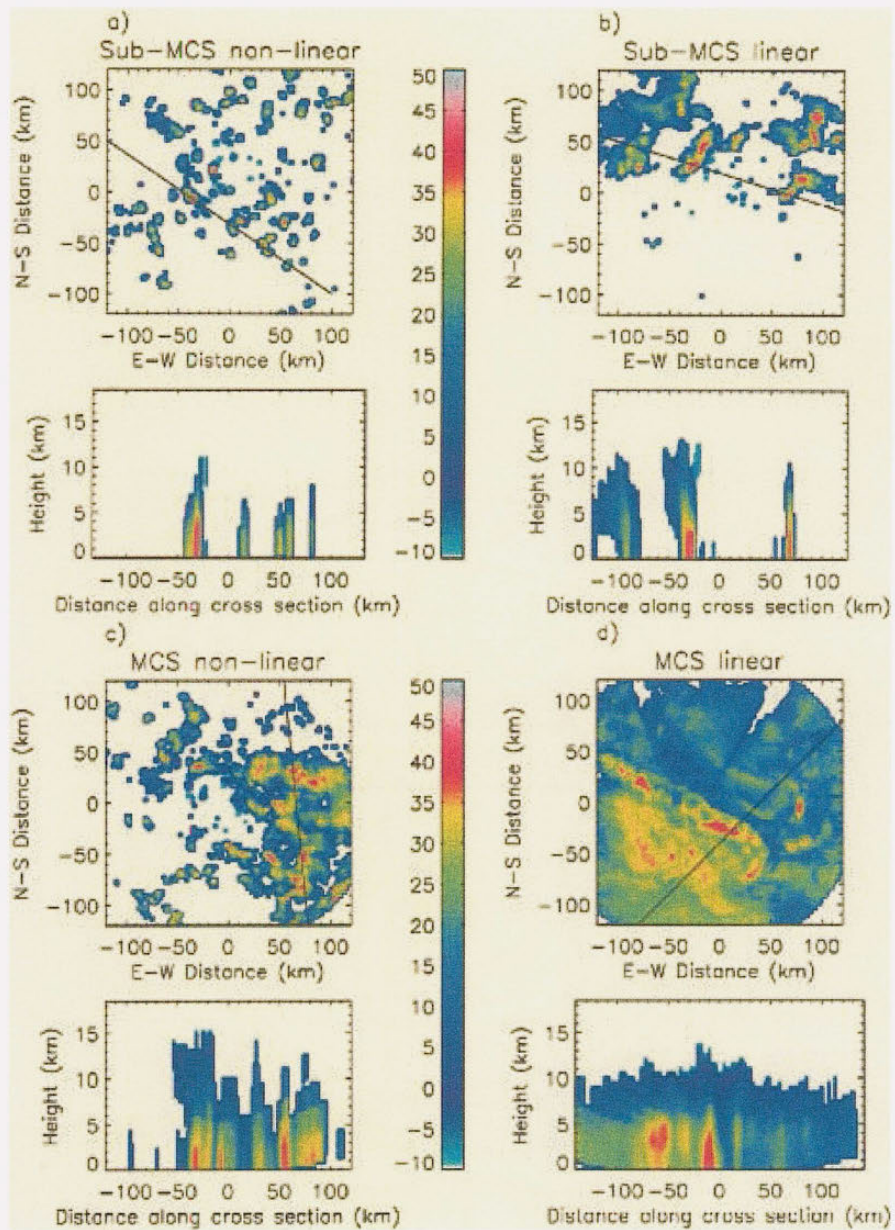


Fig. 1.4 – Image examples of each of the four basic modes of precipitating features organization as viewed in radar reflectivity (dBZ) images in constant altitude plan position indicator (upper panel) and range height indicator (lower panel) for a) sub-MCS non-linear, b) sub-MCS linear, c) MCS non-linear, and d) MCS linear. Solid black line in upper panels indicates position of corresponding vertical cross-sections (illustration from Rickenbach and Rutledge 1998).

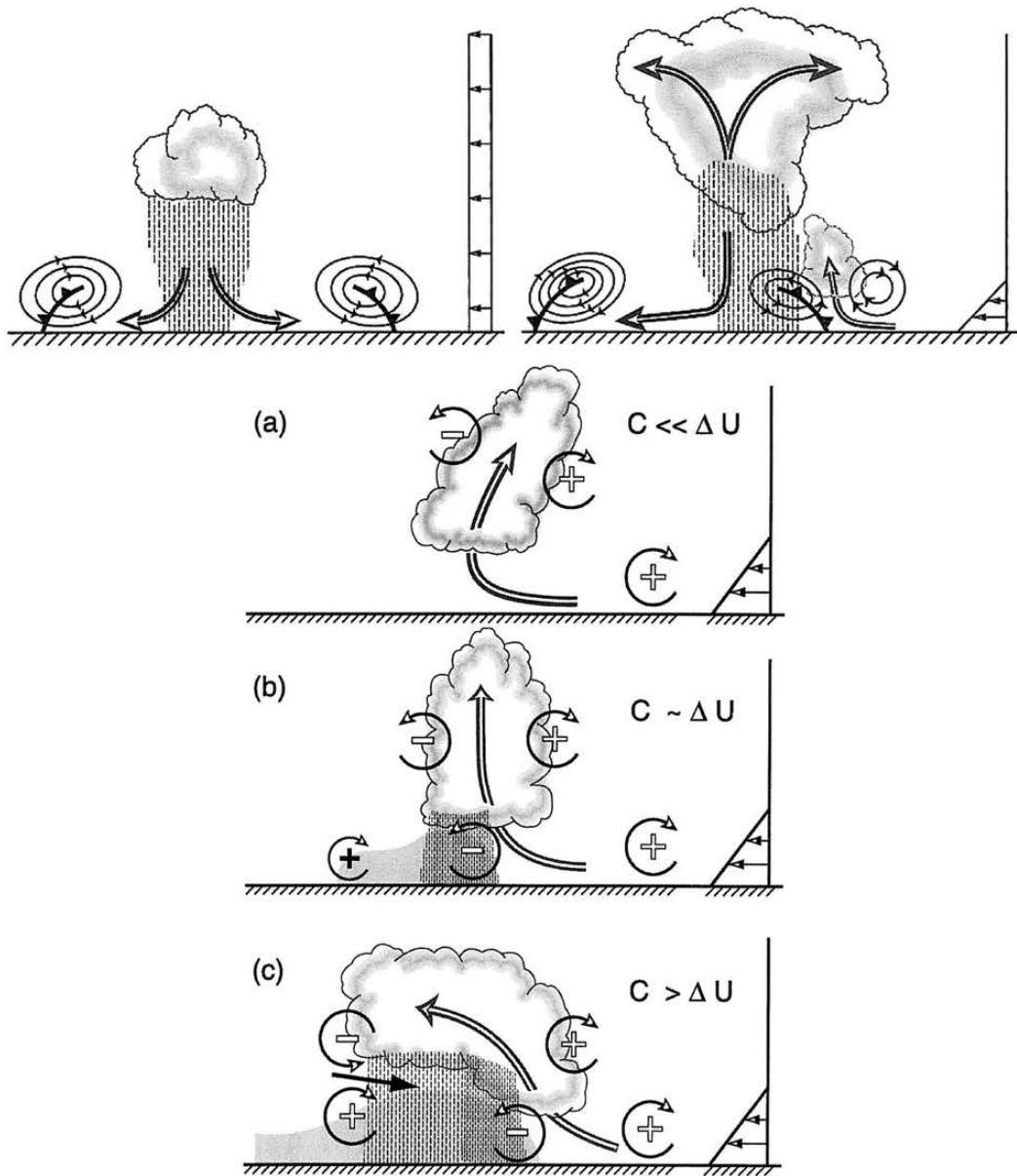


Fig. 1.5 – Upper panel shows the development of a cold pool spreading out in a non-sheared environment (left) and regenerating new cells in a sheared environment (right). Bottom panel shows the evolution of a convective cell in a sheared environment in a) initial stage, when the vorticity generated by the environmental shear dominates, b) intermediate stage, when the vorticity generated by the cold pool and environmental shear are in balance, and c) final stage, when cold pool vorticity dominates (illustration from Weisman and Rotunno 2004).

CHAPTER II

Data and Methodology

2.1 - North American Monsoon Experiment Overview

The North American Monsoon Experiment (NAME) is an international study that seeks to determine the sources and limits of predictability of warm season precipitation over North America (Carbone et al. 2003). During the NAME field campaign, the observational domain was divided into three scales (Fig. 2.1) in order to achieve its objectives: monsoon core (Tier 1), regional scale (Tier 2) and continental scale (Tier 3). The focus of this research is on precipitation processes within Tier 1, where the main scientific objective is to improve the characterization of warm season convective processes in complex terrain.

Some of the key questions to be addressed at the Tier I level include:

- 1) What are the main processes controlling the convective diurnal cycle over ocean and land?
- 2) What are the microphysical and dynamical characteristics of precipitation

systems within the monsoon region?

- 3) How well do models simulate convective precipitation in a region of complex terrain?
- 4) What are the characteristics of gulf surges (structure, evolution and frequency)?
- 5) What is the connection between gulf surges and synoptic variability?

To achieve the aforementioned goals, a comprehensive NAME Enhanced Observing Period (EOP) took place from June to September 2004, with the primary field observations phase occurring in July and August 2004. The array of instruments available during the EOP included (Fig. 2.2):

- 100 tipping bucket rain gauges across the SMO for better topographic and temporal sampling (Gochis et al. 2003).
- 1000 simple (daily) accumulation rain gauges in northwest and north-central Mexico.
- Enhanced ALERT network (T, RH, P, WS, WD and Precipitation) near the Arizona-Mexico border.
- 16 recording temperature and humidity sensors deployed along SMO transects.
- Land-atmosphere flux tower, sounding and tethered sonde measurements over a deciduous forest site.

- NCAR S-pol radar deployed near La Cruz, Sinaloa.
- 2 upgraded Doppler C-band radars from the Mexican National Meteorological Service (SMN).
- NOAA P-3 aircraft, T, P, q, WS and WD.
- 3 NCAR Integrated Sounding Systems (ISS) and one additional NCAR GLASS system (2-6 soundings/day).
- Enhanced Operational Soundings at 9 U.S. and 8 Mexican sites.
- PIBAL soundings deployed at 20 stations.
- Vertical wind profiler, disdrometer, soil moisture and ceilometer at coastal site near S-pol.
- Mexican R/V Altair (two 17-day cruises) deployed at the mouth of the Gulf of California measuring ocean-atmosphere fluxes, CTD ocean profiles, cloud ceiling, vertical wind profile and rawinsondes.
- CICESE vessel with tethersondes, pilot balloons, radiosondes, surface meteorology, water temperature, salinity and current mapping (drifter deployment).

2.2 - Radar Dataset and Methodology

The radar dataset consists of information collected by three radars in the vicinity

of the south-central part of the Gulf of California. These three radars were the National Center for Atmospheric Research S-pol radar near the town of La Cruz (approximately 100 km north of Mazatlán), the *Servicio Meteorológico Nacional* (SMN; National Weather Service) radar in Guasave and the SMN radar in Cabo San Lucas. Table 2.1 and Figure 2.3 show, respectively, the general operating specifications and a map indicating the location and approximate range of each radar used in the aforementioned dataset. Radar data was gathered by all three radars during the NAME Enhanced Observation Period (EOP) and are available between 8 July 2004 0000 UTC and 21 August 2004 2345 UTC. Low-angle, 360° surveillance scans were scheduled and generally available every 15 minutes, though a few periods exist when one or two radars were down due to maintenance, technical problems or Ka-band testing at S-pol. The range of each radar also varied somewhat during NAME due to changes in radar pulse repetition frequency, but the coverage extended to no less than 150 km from each radar.

2.2.1 - Radar Data Quality Control

This section briefly describes some of the highlights of the rigorous quality control process through which the radar dataset was subjected prior to compositing and gridding. A complete description of this quality control effort is found in Lang et al. (2007).

Due to the availability of polarimetric data from S-pol, the corrections applied to that dataset were more extensive. The S-pol data was corrected for both gaseous and

liquid attenuation, clutter, noise, anomalous propagation, second-trip echoes, insect contamination and beam blockage. Echoes with two or less contiguous gates were removed using the despeckle feature of NCAR's SOLOII software. Noise and clutter were eliminated using a range-based correlation coefficient (ρ_{hv}) filter. All gates where ρ_{hv} was less than 0.8 were flagged bad, except for ranges greater than 90 km and horizontal reflectivity (Z_h) greater than 20 dBZ, where only gates with ρ_{hv} less than 0.5° were eliminated. Additionally, noise and clutter were also filtered using standard deviation of differential propagation phase ($SD(\Phi_{DP})$) over an interval of eleven gates (1.65 km). Data were removed when the $SD(\Phi_{DP})$ at a given gate was greater than 10° if $Z_h < 35$ dBZ, and when $SD(\Phi_{DP})$ was greater than 18° if $Z_h \geq 35$ dBZ. Furthermore, noise and insects were cleaned up from the dataset by discarding data where $Z_h < 0$ dBZ, where $0 \text{ dBZ} \leq Z_h < 10 \text{ dBZ}$ if the differential reflectivity (Z_{DR}) was greater than 1 dB, and also where $10 \text{ dBZ} \leq Z_h < 35 \text{ dBZ}$ if Z_{DR} was greater than $1+0.075Z_h$. Issues with second-trip echoes were addressed by removing echoes where the linear depolarization ratio (L_{DR}) was greater than -5 dB and Φ_{DP} was greater than 30°. Liquid attenuation was corrected following a methodology described by Carey et al. (2000b) whereby the variability of Z_h and Z_{DR} is evaluated as a function of Φ_{DP} for a given range of specific differential phase (K_{DP}). In areas of strong liquid attenuation, such as large Mesoscale Convective Systems (i.e. $\Phi_{DP} > 100^\circ$), Z_h was corrected for liquid attenuation by +1.71 dBZ while Z_{DR} was corrected by +0.42 dB. The gaseous attenuation of Z_h was corrected by adding 0.007 dBZ per km traveled by the electromagnetic pulse, following the value

established by Battan (1973). Considering the pulse traveling to a point 200 km from the radar and then back, Z_h was corrected for gaseous attenuation by +2.8 dBZ. Finally, beam blockage which occurred to the Northeast sector of S-pol was corrected following Carey et al. (2000a) and the location of these beam blocks were determined by visual inspection of clear air sweeps. Rainfall in the blocked areas was identified using the CSU Hydrometeor Algorithm (Tessendorf et al. 2005) and then Z_h was examined as a function of azimuth for a given range of K_{DP} values. In area where rainfall was occurring, Z_h should only vary by a small amount for a given small range of K_{DP} values due to the self consistency between polarimetric variables (Scarchilli et al. 1996). Therefore, the difference between the Z_h in blocked and unblocked regions corresponds to the positive dBZ correction that had to be applied to Z_h in the blocked area. Blocked Z_{DR} was also corrected using a similar methodology with drizzle areas following Giangrande and Ryzhkov (2005).

The quality control effort implemented for the SMN radars in Cabo and Guasave was much simpler due to the unavailability of polarimetric information. Reflectivity data were despeckled in the same fashion as for the S-pol radar (described above). Automated filters were applied on Z_h , noise-corrected power (NCP), and on total power (DM). Areas of clutter were also determined and removed using clear radar sweeps as comparison. Strong insect echoes were almost always present overnight in the vicinity of the Guasave radar and they were manually removed using the SOLOII software. Gaseous attenuation correction for C-band radars was also applied using Battan (1973) methodology, while

liquid attenuation by rain was corrected following Patterson et al. (1979). The latter correction was generally 2-3 dBZ downrange from strong convection. Sea clutter was also a persistent problem to the west and south of the radar. Intercomparisons between the radar data and the Geostationary Orbiting Environmental Satellite (GOES) infrared data indicated that the sea clutter was associated with brightness temperatures greater than 290 K. These echoes were not removed from the original dataset; however, they were removed later in the analyses presented in this study.

Finally, intercomparisons between the corrected reflectivity data for the three radars and Tropical Rainfall Measuring Mission (TRMM) Precipitation Radar (PR) indicated good agreement between the two measurements and accuracy to 1-2 dBZ (Lang et al. 2007).

2.2.2 - Radar Data Compositing and Gridding

The radar data compositing effort, led by David Ahijevych at NCAR, aimed to generate network images of reflectivity and rain rate every 15 minutes. The methodology employed consisted of merging the sweeps collected by each radar every 15 minutes and then choosing the lowest gate in areas where coverage by two or all three radars overlapped. An overlap was deemed to occur wherever data from a gate of one radar was within one-half of a gate width and one-half of a beam width of data from a different radar.

Subsequently, the radar data was interpolated to a regular latitude/longitude grid

and to a horizontal spacing of 0.02° (~ 2 km) using Delauney triangulation and a combination of softwares such as IDL, QHULL and GRIDDATA (Barber et al., 1996). Additionally, an inverse-distance weighting technique was used to generate interpolated values found within 0.03 degrees of each grid point and a circular filter with 0.001 degrees was employed to smooth the data.

2.2.3 - Rainfall Retrieval

Two methodologies were employed for rainfall calculation in the composite images. A simple Z-R relationship, shown in Eq. 2.1, was used for grid points within the composite images which used reflectivity data from the SMN radars. A cap of 57 dBZ, corresponding to 250 mm h^{-1} , was used to reduce ice contamination. This Z-R relationship was determined using the polarimetric tuning methodology of Bringi et al. (2004) and by comparing the S-pol reflectivity over the NOAA profiler site, located 45 km northwest of S-pol, with the data obtained by the gauge rain rates in that same location (Lang et al. 2006).

$$Z = 133R^{1.5} \quad \text{Eq. 2.1}$$

For areas of the composite created with S-pol data, rain rates were calculated using the Colorado State University blended rainfall algorithm described by Cifelli et al.

(2002). This algorithm selects and utilizes the best rain estimators between $R(Z_H)$, $R(Z_H, Z_{DR})$, $R(K_{DP})$ or $R(K_{DP}, Z_{DR})$ depending on the values of the polarimetric variables and the presence of mixed-phase precipitation. Although extreme rain rates were unexpected in the region, all rain rates were truncated at the same 250 mm h^{-1} maximum threshold used for the SMN radars regardless of the relationship employed for the retrieval in the S-pol region. The presence of mixed-phase precipitation was assessed using a difference reflectivity (Z_{DP}) method described by Golestani et al. (1989).

The use of different approaches to calculate rain rates in different areas of the radar composite certainly affects the quality of the rainfall retrieval. However, we would like to emphasize that in this study we neither aim to intercompare rainfall in different areas within the radar composites nor use rain rate as a threshold for feature identification and classification. Rather, we intend to examine rainfall differences between feature organization types, their temporal variability, and how trends in precipitation relate to changes in thermodynamic and synoptic conditions in the NAME region. Hence, it is our assessment that we must use the best rainfall retrieval methodology available in each area of the composite. Cifelli et al. (2002) showed that the CSU blended algorithm provides superior rainfall estimation than Z-R relationships or any other polarimetric relationship alone. A quick sensitivity test indicated that if we were to apply Eq. 2.1 as the sole rainfall estimator in the entire composite (rather than just for the SMN radars), one would observe an increase of 9% in the convective rainfall fraction. This is an expected result, since the CSU blended algorithm does not generally apply the Z-R relationship in the

convective areas and this Z-R relationship tends to overestimate rain rates in areas of strong reflectivity in the NAME region.

2.2.4 – Precipitating Feature Identification

Precipitating features (PFs) are identified as contiguous areas of reflectivity in the radar composite images following a similar methodology first employed in the Tropical Rainfall Measuring Mission Precipitation Radar and Microwave Imager (Simpson et al. 1998, Nesbitt et al. 2000). A contiguous area of 5 pixels (20 km²), including diagonally adjacent pixels, possessing reflectivity greater or equal to 15 dBZ was required for a PF to be identified by the algorithms employed in this study. The choice for the 15 dBZ minimum reflectivity threshold is due to the sensitivity of the SMN radars (Lang et al. 2007), and the inaccuracy of convective/stratiform partitioning methods and very low contribution to total rainfall statistics of these low reflectivities. Moreover, this value allows for future intercomparisons with results obtained by TRMM's precipitation radar. The reasons for the five pixel minimum size are twofold: 1) it reduces the number of potential anomalous echoes, not properly eliminated by the extensive quality control efforts, which could be misidentified as PFs, and 2) reduces the sample of features identified during NAME to keep only those features that significantly contribute to the total rainfall. Figure 2.4 shows that there is a strong correlation between precipitating feature size and total rainfall contribution, while Fig. 2.5 shows the cumulative rainfall as a function of feature size. Figure 2.5b indicates that 1% of the total rainfall that occurred

within the radar composite images of NAME was generated by features less than 18 km^2 . Therefore, by choosing a minimum size of 5 pixels we eliminated a large number of echoes that contributed very little to the rainfall in NAME radar composite area and enabled us to focus on the characteristics and dominant forcings that modulate the most important precipitating features in terms of rainfall.

2.2.5 - Convective and Stratiform Partitioning

In order to study the structure and characteristics of the different modes of horizontal organization in the NAME region, a partitioning algorithm was employed to identify convective and stratiform precipitation, following a methodology first described by Steiner and House (1993), and later improved by Steiner et al. (1995) and by Yuter and Houze (1997, 1998). This procedure consists of running the composite reflectivity data through two tests. The first test, known as the absolute (or intensity) test, simply assigns as a convective center any grid point where the reflectivity exceeds a user defined threshold. This absolute threshold was set to 40 dBZ following numerous previous studies, including Steiner et al. (1995), DeMott (1998a,b), Rickenbach and Rutledge (1998), Biggerstaff and Listemaa (2000), Cifelli et al. (2002), Petersen et al. (2003), and Pereira and Rutledge (2007). Grid points that are not tagged as a convective center by the absolute test are run through a second test, known as the gradient (or peakedness) test, whereby the reflectivity at each grid point is compared to the background reflectivity surrounding that grid point. The background reflectivity (Z_{bg}) is defined as the mean

reflectivity within an 11-km radius of the grid point being tested. Only reflectivities values greater than 0 dBZ are used in the computation of this mean background reflectivity. A convective center is identified by the gradient test whenever Eq. 2.2 is satisfied.

$$Z > Z_{bg} + \Delta Z \quad \text{Eq. 2.2}$$

Therefore, in order for a convective center to be identified by the gradient test, the reflectivity at that grid point must exceed the sum of two values that are variable: Z_{bg} , and ΔZ , which is defined in Eq. 2.3.

$$\Delta Z = a \cos\left(\frac{\pi}{b} Z_{bg}\right) \quad \text{Eq. 2.3}$$

The adjustable parameters a and b , used in Eq. 2.3 above, were tuned for the radar dataset used in this study by evaluating the performance of the algorithm using a number of representative cases shown in Table 2.2. Extensive tuning tests, completed in collaboration with Angela Rowe, indicated that the best partitioning results were obtained when a was set to 8.0 and b was set to 150.

After executing these two tests where all convective centers are identified, the

partitioning algorithm proceeds to also tag as convective all grid points (with a reflectivity greater or equal to 15 dBZ) within a given radius of the convective center. The size of this convective radius (C_{radius}) depends on the value of Z_{bg} surrounding that convective center, as shown in Eqs. 2.4.

$$\begin{aligned}
 \text{If } Z_{\text{bg}} \leq 20 \text{ dBZ} &\rightarrow C_{\text{radius}} = 1 \text{ km} \\
 \text{If } 20 \text{ dBZ} < Z_{\text{bg}} \leq 25 \text{ dBZ} &\rightarrow C_{\text{radius}} = 2 \text{ km} \\
 \text{If } 25 \text{ dBZ} < Z_{\text{bg}} \leq 30 \text{ dBZ} &\rightarrow C_{\text{radius}} = 3 \text{ km} \\
 \text{If } 30 \text{ dBZ} < Z_{\text{bg}} \leq 35 \text{ dBZ} &\rightarrow C_{\text{radius}} = 4 \text{ km} \\
 \text{If } Z_{\text{bg}} > 35 \text{ dBZ} &\rightarrow C_{\text{radius}} = 5 \text{ km}
 \end{aligned}
 \tag{Eqs. 2.4}$$

The choice of a higher value for parameter b , when compared to previous studies (Petersen et al., 2003; Lang et al., 2007, Pereira and Rutledge, 2007) was necessary due to the algorithm's misclassification of stratiform areas with moderate reflectivities. By increasing the setting of b to 155 the algorithm properly classified these areas as stratiform, but as a side effect there was a small loss in size of legitimate convective areas. Consequently, the convective radii thresholds shown in Eqs. 2.4 were tuned for our dataset and relaxed, comparatively to the aforementioned studies, to compensate for some of this convective area loss. Fig. 2.6 shows the reflectivity composite image and the corresponding partitioning classification using the above settings for each of the cases listed in Table 2.2. The maps presented in Figs. 2.6a-e indicate that the algorithm performs well in a variety of echo conditions using the tuned parameters described above.

2.2.6 - Precipitating Feature Horizontal Organization Modes

Since one of the objectives of this study is to document and characterize the horizontal structure of convective precipitation in the south-central portion of the GoC, the PFs identified by the methodology described in this chapter were grouped according to their size and morphology. We distinguish the size of convective features between those PFs which organized to attain MCS scale from those that did not, while we distinguish the morphology of the PFs between those that organized into a linear convective pattern from those that did not. This simple methodology, described by Rickenbach and Rutledge (1998), yields four main categories where the identified PFs can be placed: sub-MCS non-linear, sub-MCS linear, MCS non-linear, and MCS linear. Radar reflectivity illustrations by Rickenbach and Rutledge (1998) of each of these organization types were shown in Fig 1.4.

Classification based on size was done taking into account the entire area of the feature (regardless of whether it was stratiform or convective). An ellipse fitting technique developed by Nesbitt et al. (2006) was employed to determine the largest horizontal dimension of the PF. A PF was classified as MCS when the major axis of the ellipse fitted to that feature was greater than 100 km. The remaining PFs that did not fulfill this criterion were classified as sub-MCS features.

For the morphology classification, the convective portion of the PF was used to determine the linearity of the feature. The required conditions for a feature to be deemed linear are based on a previous definition described by Bluestein and Jain (1985), which

includes: a minimum convective length scale (i.e. major axis) of 50 km, and an aspect ratio of 5 to 1 between the major and minor axes of ellipse fitted to the convective portion of the PF. Features that satisfied these conditions were classified as linear, while the remaining features were classified as non-linear. Features that possessed multiple convective clusters (multicell features) were given the linear classification if any of the convective clusters within the multicell PF satisfied the above conditions. The remaining multicell PFs, numbering 4052 (i.e. 5% of the PF population), were manually assigned a linear classification based on the visual inspection of the reflectivity and corresponding convective/stratiform areas of the PF. This manual assignment process was repeated a second time and any PF which received a different classification than in the first inspection was evaluated a third time for a final morphology classification.

Lastly, there were a few identified PFs which were excluded from the analyses presented in this study. Any PF which had all of its precipitating area classified as stratiform were removed from analysis. This is due to fact that the linearity test requires some convective area for a feature to be evaluated. Moreover, Houze (1993) also utilizes a minimum convective area in the definition of an MCS. Therefore, the inclusion of such non-convective features in our study would force their placement in the sub-MCS non-linear category and introduce an undesired bias in our statistics. Additionally, a second group of excluded PFs is made up of those features that touched the edge of the radar composite image and were classified as sub-MCS features. The rationale for this exclusion is that those PFs that did not attain MCS size, but are also touching the edge,

cannot be properly examined and could potentially be misclassified as sub-MCS simply because their entire structure is not fully within the domain of the radar composite image.

2.2.7 - Normalization Issues

Some of the statistics presented in this study had to be normalized due to temporal variations in sampling size. This is the case for all rainfall time series calculated using the radar dataset because the spatial coverage of the composite images is not constant throughout the dataset. Variations in this spatial coverage occurred due to changes in pulse repetition frequency (PRF) by any one of the three radars and also due to occasional periods where data from one or two radars were unavailable. Since most of the precipitation over the Tier 1 section of NAME occurs over the western slopes of the SMO (Higgins et al. 2005, Johnson et al. 2007) a similar time series was calculated whereby only grid points over land were counted. The intent with the normalization factors applied to our statistics is to remove any potential biases caused by an increase in scanned areas. Since rain was mostly absent over the area covered by the Cabo radar domain, we chose to normalize our rainfall statistics by the scanned land area. Therefore, any mention hereafter to normalized rainfall statistics refer to the division of the rainfall amounts by the total scanned land area in any given day.

2.3 - Environmental Dataset and Methodology

For the analyses of the thermodynamic and synoptic conditions during the field

experiment we make use of the NAME Objective Gridded Analysis (version 3.0) created by the Mesoscale Dynamics Group at Colorado State University. This analysis consists of gridded fields of temperature, water vapor mixing ratio, geopotential height, and of zonal and meridional winds. This dataset is available at a horizontal spatial resolution of 1 degree, and a vertical resolution of 25 hPa. The gridded analyses were generated for two domains, T1A and T2A, which are shown in Fig. 2.7. Data from the smaller T1A domain were used in the calculations presented in this study and are available every 6 hours from 00Z on 7 July 2004 through 18Z on 15 August 2004. Each of the upper-air gridded fields was computed using data from quality-controlled rawinsondes, the NAME ISS wind profilers, and from PIBAL sounding sites. Surface analysis fields were generated using oceanic QuikSCAT winds, METAR reports and several other surface observational platforms. No simulated or reanalysis data were used in the T1A dataset. The data were interpolated using a multiquadric scheme developed by Nuss and Titley (1994). Additional information about the procedures used in the calculation of these fields is found in Ciesielski et al. (2003).

2.3.1 - Convective Available Potential Energy Calculations

The Convective Available Potential Energy (CAPE) represents the vertically integrated positive buoyancy of a parcel of air undergoing adiabatic ascent (Moncrief and Green, 1972). CAPE is proportional to potential energy available for a rising parcel and provides an estimate of the maximum updraft strength in convective cloud, assuming

no entrainment. Therefore, CAPE is a fundamental indicator of the potential intensity for deep, moist convection to develop.

In this study CAPE was calculated using data from the objective gridded analysis discussed previously. The computations were made using the surface-based CAPE formula shown in Eq. 2.5:

$$CAPE = g \int_{ZLFC}^{ZEL} \left(\frac{T'_v - T_v}{T_v} \right) dz \quad \text{Eq. 2.5}$$

where g is the gravity acceleration, $ZLFC$ is the height of the level of free convection, ZEL is the height of the equilibrium level, T'_v is the virtual temperature of the air parcel being lifted from the surface, T_v is the virtual temperature of the atmosphere, and z is the height. More information on CAPE and on other thermodynamic parameters used in its calculations can be found in Hess (1959) and in Doswell and Rasmussen (1994).

CAPE was calculated for all grid points within the domain of the objective analysis. Fig. 2.8 shows an example of one of the CAPE maps generated with these calculations. CAPE maps were generated four times a day between 8 July and 15 August 2004. They were used to visually inspect the quality of the CAPE calculations as well as to observe the horizontal and temporal variations of this parameter within the region.

Mean CAPE time series were calculated using data from each 12Z CAPE map.

Our decision to use only 12Z (i.e. 0600 local time) CAPE maps was made to look at the temporal variation of CAPE from day to day prior to the diurnal onset of convection (Rowe et al. 2008). Additionally, Convective Inhibition (CIN) was calculated in the same fashion as CAPE, except that the integration takes place from the surface to the level of free convection. CIN represents the work done to lift a parcel at the surface through the area of negative buoyancy typically found in the lowermost portion of the troposphere.

2.3.2 - Vertical Wind Shear Calculations

There has been a myriad of observational and modeling studies which point to the controlling importance of wind shear to the organization, longevity and precipitation efficiency of convective clouds (Newton and Newton 1959; Moncrieff and Green 1972; Hane 1973; Marwitz 1972a,b; Browning 1977; Takeda 1977, Thorpe et al. 1982; Weisman and Klemp 1982; and Fovell and Ogura 1989; Weisman and Rotunno 2004). Shear can be calculated in a number of different ways and the depth over which horizontal shear is calculated varies from study to study. Nonetheless, recent studies (Weisman and Rotunno 2004) suggest that 0-5 km AGL has the best skill in predicting the likelihood of MCS development. They further showed that the skill starts to decrease if the depth of the layer is extended to 7.5 km or greater or if it is less than 2.5 km deep. The location of convective development in the area of our study is heavily influenced by topography (Gochis et al. 2007, Rowe et al. 2008) and the SMO extends up to 3 km in some points of our domain. As a result, air flow is effectively limited in the lowest 3 km of the

atmosphere over the coastal plains, and certain atmospheric disturbances may go completely undetected. Moreover, sensitivity tests (discussed in Chapter Four) also indicated that the implementation of shallower depths severely limits the magnitude of shear, which is already typically weaker in the Tropics than in middle latitudes. Fluctuations were nearly inexistent when shear was calculated for shallow (e.g. 0-1 km) depths and progressively increased as the depth increased to 6 km. In order to maximize the amplitude of wind shear in our time series plots, we decided to adopt a shear depth of 0-6 km AGL in our calculations. Moreover, correlations to our PF results were best for that shear depth. This choice also allows for the detection of transient upper-level atmospheric disturbances (e.g. inverted troughs) and to measure winds above the mountain peaks of the SMO.

The depth of the layer used to calculate the shear may vary slightly due to the topographical variations in surface elevation (which inherently changes the altitude at the top of the 6 km shear calculation layer) and due to fact that the vertical coordinate system used in the environmental dataset is based on pressure levels. Hence, radiosonde data were visually inspected to determine the approximate average height of each pressure level. Therefore, for each grid point where the shear was being calculated, the algorithm used the surface elevation to determine the closest pressure level to the top of the 6 km shear calculation layer. For surface wind conditions we used the mean zonal and meridional wind speeds at the lowest 3 grid points (i.e. surface, 25 hPa AGL and 50 hPa AGL). There are four values that are ultimately used in the computation of wind shear:

the zonal wind speed at 6 km AGL (U_6), the meridional wind speed at 6 km AGL (V_6), the mean zonal surface wind (U_{sfc}), and the mean meridional surface wind (V_{sfc}). These parameters were combined to produce a final 0-6 km AGL wind shear value using Eq. 2.6.

$$Shear = \sqrt{(U_6 - U_{sfc})^2 + (V_6 - V_{sfc})^2} \quad \text{Eq. 2.6}$$

Maps of 0-6 km AGL wind shear (Fig. 2.9) were constructed in the same fashion as the CAPE maps using, instead, the zonal and meridional wind fields. These maps were used to inspect for possible unrealistic shear values and to assess the temporal and horizontal variations in that field. Similarly to CAPE, our choice to use only 12Z (i.e. 0600 local time) data in the calculation of wind shear time series was to assess the impact of large scale shear variations prior to the diurnal onset of convection.

2.3.3 - Identification of Tropical Waves

Tropical waves, also called African or easterly waves, are westward propagating disturbances over the Tropics, which are usually traced back to Africa and can lead to the development of tropical cyclones in the Atlantic and eastern Pacific basins (Dunn 1940; Riehl 1945, 1954; Simpson et al. 1968; Landsea 1993). Several studies have relied on 700-hPa meridional wind speeds between 10° N and 22° N to identify tropical wave

phases (Reed and Recker 1971; Burpee 1974, 1975; Reed et al. 1977; Thompson et al. 1979; Petersen et al. 2003; and Pereira and Rutledge 2007). However, the domain of our study is primarily concentrated north of 22° N so meridional wind shifts at 700 hPa are not going to be always modulated by the passage of tropical waves to the south our domain. Moreover, Pasch et al. (1998) found that wind shifts associated with many waves between 1991 and 1994 were not detectable. As a result, we decided to rely on the detection of tropical waves by qualified tropical meteorologists at the National Hurricane Center in Miami. Synoptic maps depicting the position of tropical waves and other synoptic features are normally generated twice daily. Tropical waves are tracked using the typical 700 hPa winds plus a number of other variables such as maximum low-level cyclonic vorticity, minimum surface pressure, and the presence of cloud clusters in the satellite imagery. The position of these tropical waves was transcribed to synoptic feature maps (Fig. 2.10) created daily by the NAME Forecast Office and by the *Servicio Meteorológico Nacional* in Mexico during the field experiment. For the purposes of this study we focused on tropical waves found between 100° W and 110° W.

2.3.4 - Identification of Inverted Troughs

The other important synoptic disturbance to potentially influence precipitation in the North American Monsoon system is the development of tropical upper tropospheric troughs (TUTTs) or inverted troughs (Higgins et al. 2004, Pytlak et al. 2005, Douglas and Englehart 2007, Johnson et al. 2007). These upper level disturbances commonly appear

during the summer months over the Gulf of Mexico and cross over the core region of NAME after the onset of the monsoon season, when upper-level winds shift from westerly to easterly in the region (Saddler 1967, Whitfield and Lyons 1992).

The same synoptic feature maps (Fig. 2.9) used in the identification of tropical waves were used as a first guess for identification of potential inverted troughs. Additionally, we complemented this identification process based on work by Pytlak et al. (2005) who reconfirmed the occurrence of eleven inverted troughs present in North America between 17 June and 12 August 2004. Observational studies have indicated that upper level inverted troughs are typically westward propagating disturbances, confined between 100 and 700 mb, and possess stronger cyclonic circulation and cold temperature anomalies at the mid to upper levels (Kelley and Mock 1982, Whitfield and Lyons 1992, Price and Vaughan 1992, Nieto Ferreira and Schubert 1999). Therefore, we used a combination of streamline (Fig. 2.11) and vorticity (Fig. 2.12) maps, from 700 to 200 mb, to identify and estimate the rough position of the inverted trough. It is important to stress, however, that the aim of our study was not to catalogue the exact latitude/longitude of the trough axis, but rather examine how the presence of an inverted trough in the region impacted the circulation, shear and other environmental conditions that could affect the development of MCSs and rainfall in the southern portion of the North American Monsoon core region.

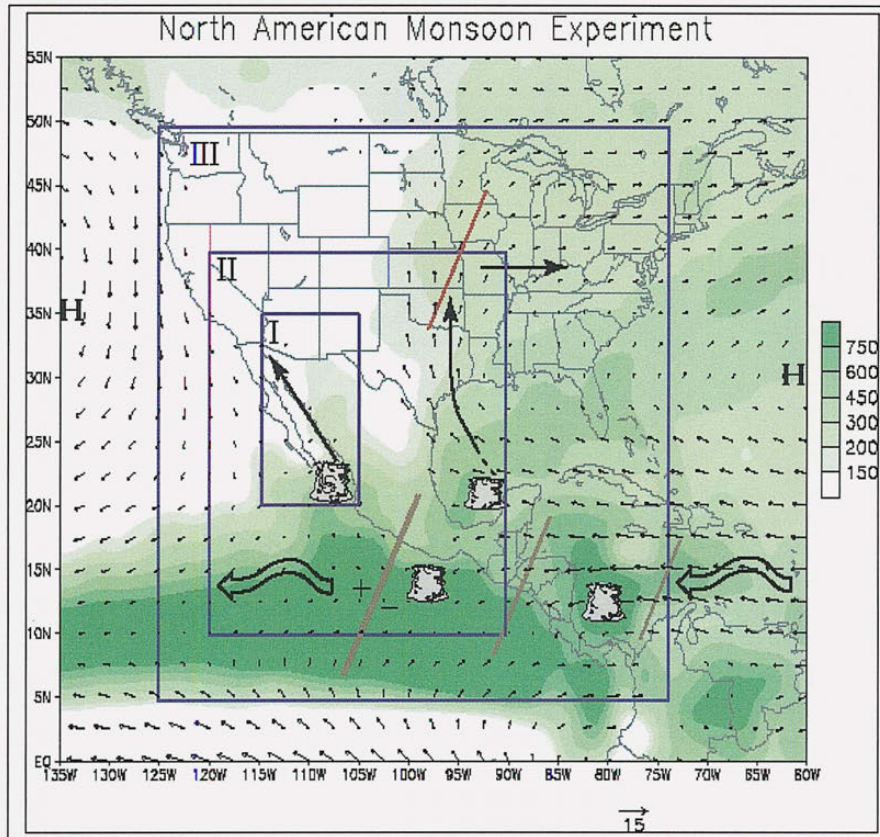


Fig. 2.1 - NAME multi-tier domain (illustration from Higgins 2004).

2004 NAME EOP Instrument Network

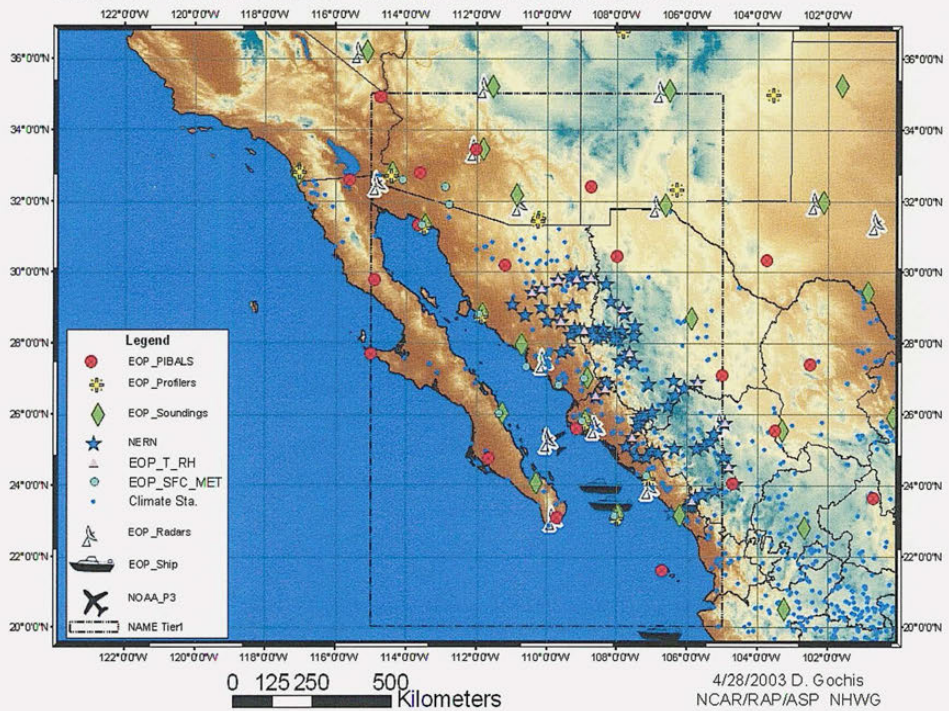


Fig. 2.2 - Summary of NAME 2004 EOP instrument platforms (illustration from Higgins 2004).

Table 2.1 - Operating specifications for the three radars used in the NAME radar composites.

Radar	S-pol	Guasave	Cabo San Lucas
Latitude	23.9290° N	25.5676° N	22.8971° N
Longitude	106.952° W	108.4633° W	109.9272° W
Altitude	20 m MSL	85 m MSL	281 m MSL
Wavelength	11 cm	5.4 cm	5.4 cm
Pulse Width	1.5 μ s	2.4 μ s	2.4 - 3.3 μ s
Pulse Repetition Frequency	720 - 1000 Hz	415-625 Hz	350-625 Hz
Peak Power	525 kW	174 kW	250 kW
Antenna Gain	45.63 dB	38.40 dB	41.00 dB
Receiver Gain	40.65 dB	45.00 dB	52.71 dB
Radar Constant	69.046	74.494	68.756
Beam Width	1.0°	1.4°	1.4°
SUR Scan Angles	0.8°, 1.3°, 1.8°	0.5°, 1.0°, 1.5°	0.6°
Receivers	H and V, simultaneously	H only	H only

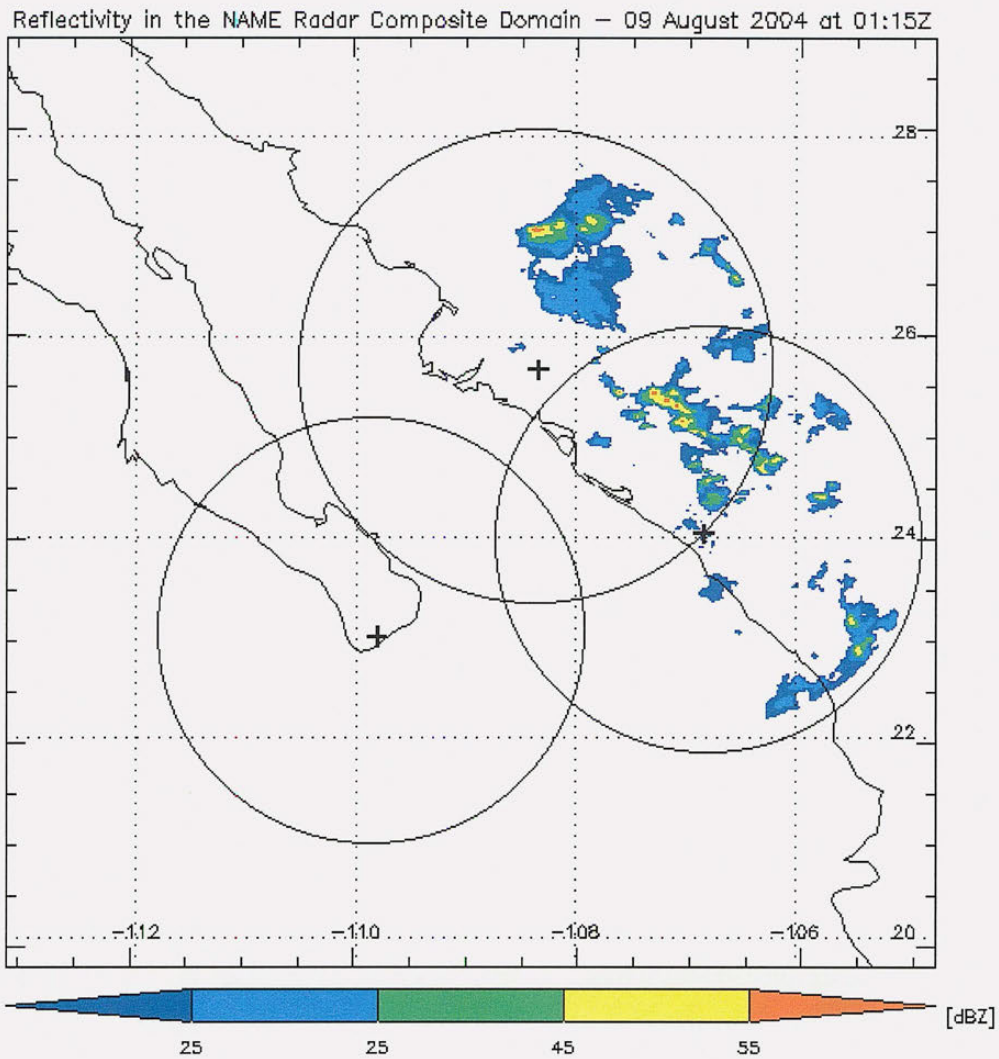


Fig. 2.3 - Illustration of a NAME reflectivity composite image overlaid on a map with the location and approximate range rings for each radar.

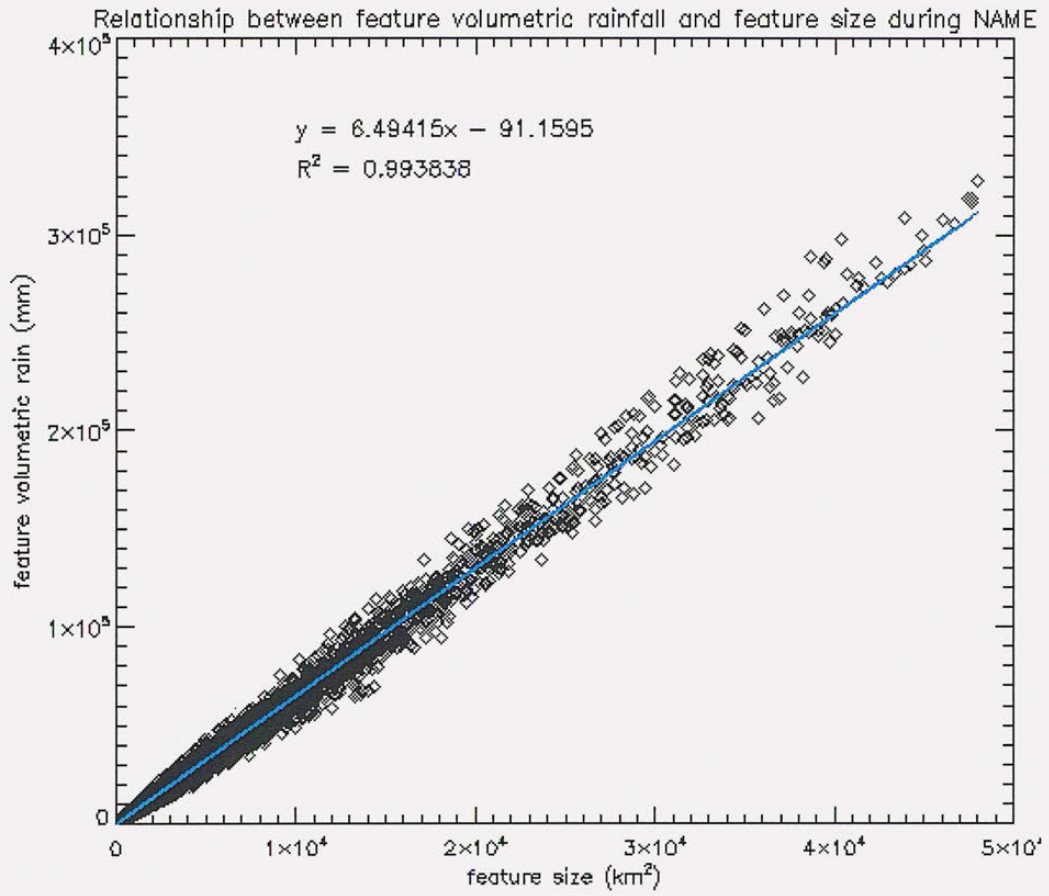
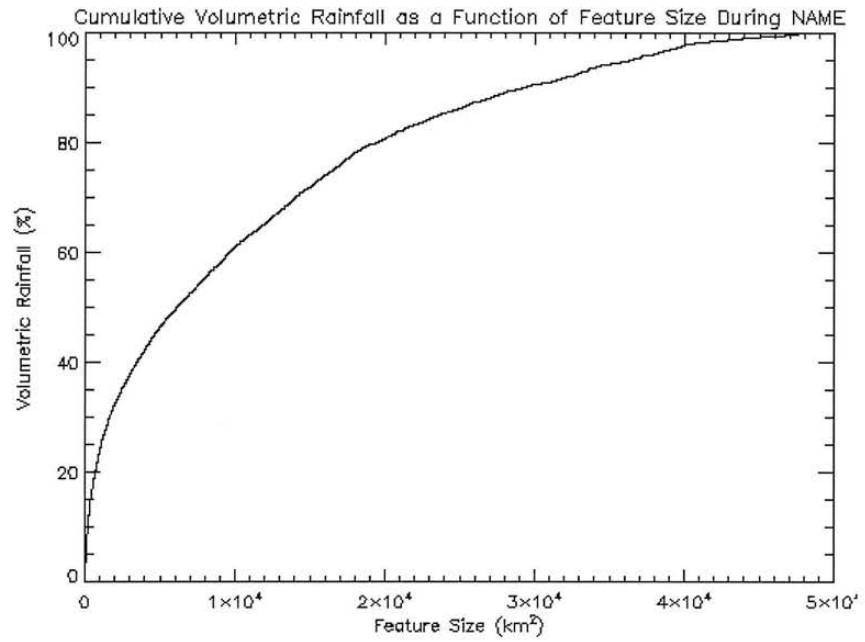


Fig. 2.4 - Relationship between precipitating feature volumetric rainfall and precipitating feature size during NAME.

a)



b)

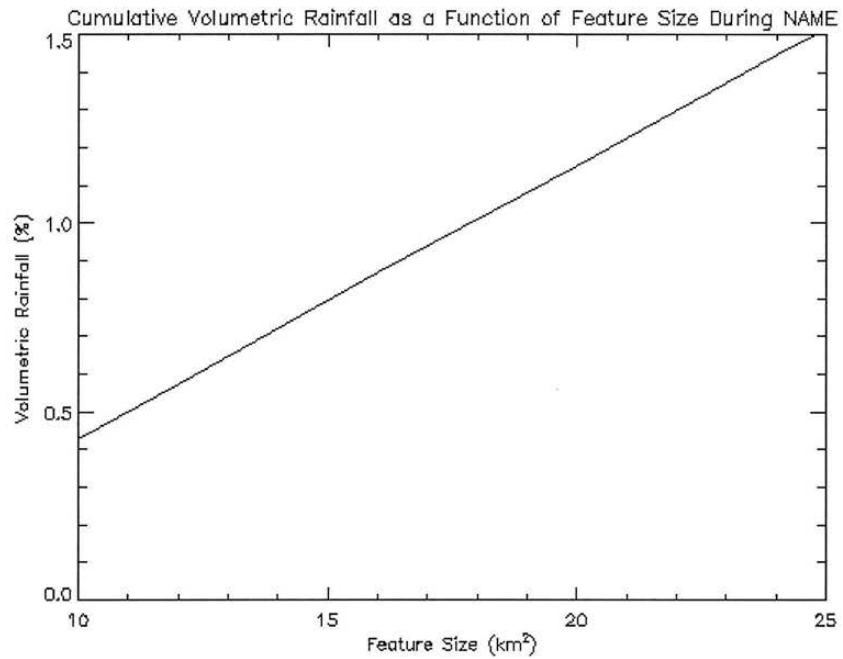
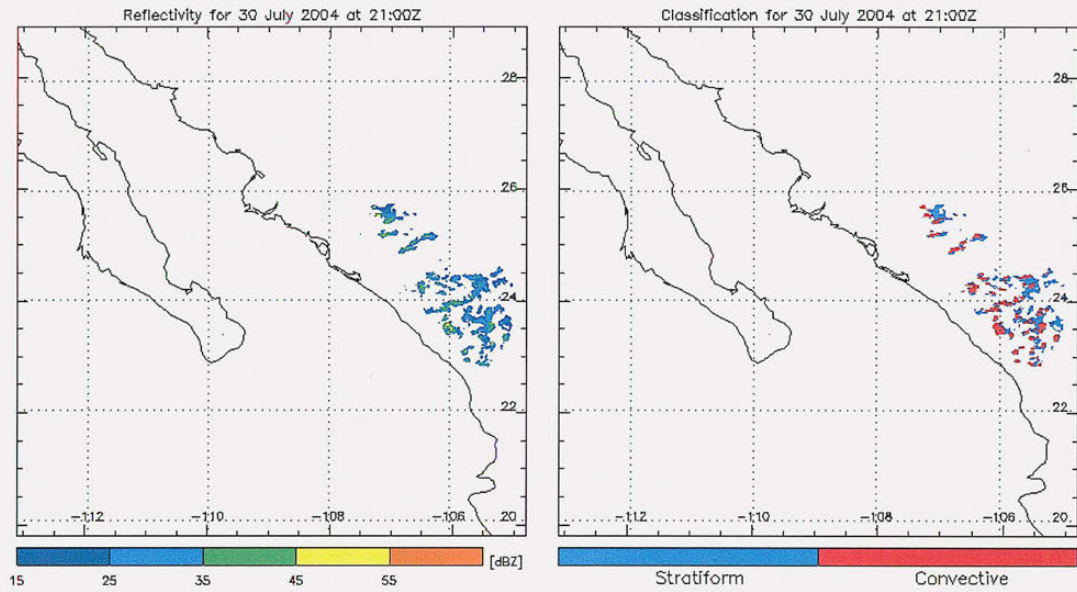


Fig. 2.5 - a) Cumulative Rainfall as a Function of Feature Size during NAME, b) same as 2.3a, but zoomed in at the lower end of the feature size spectrum.

Table 2.2 - List of cases used to tune the partitioning algorithm.

Case #	Date	Time	Description
1	30 July 2004	21:00 Z	Scattered Convection
2	31 July 2004	00:00 Z	Mesoscale Convective System
3	8 July 2004	00:00 Z	Organized & Isolated Convective Cells
4	8 July 2004	03:00 Z	Linear Convection
5	8 July 2004	06:00 Z	Convection Embedded in Stratiform Area

a)



b)

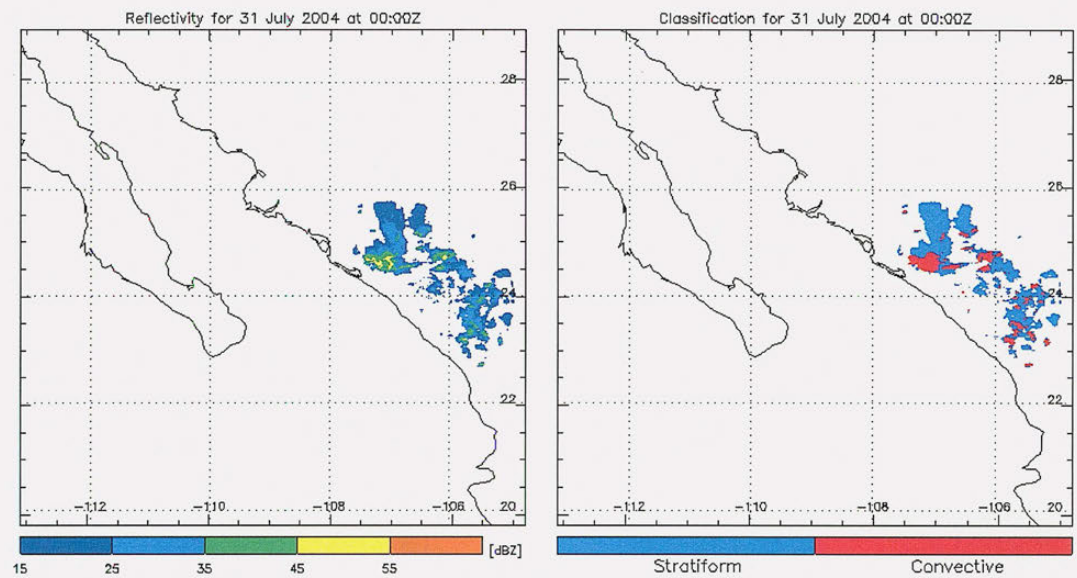
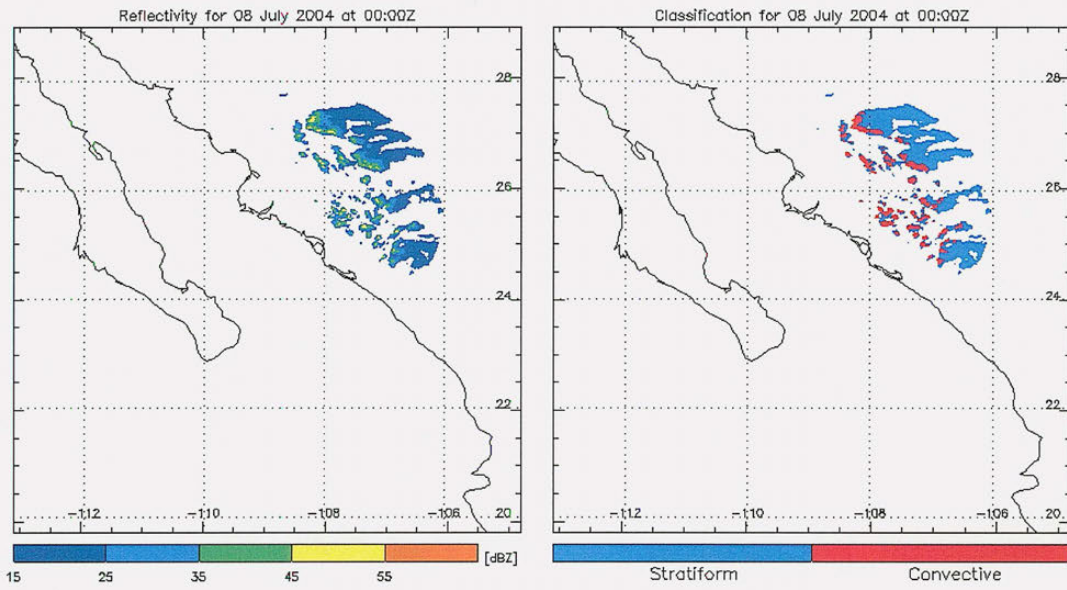


Fig. 2.6 - Composite Reflectivity image and corresponding convective and stratiform areas assigned by the partitioning algorithm for each of the cases listed in Table 2.2: a) Scattered Convection case, b) Mesoscale Convective System case, c) Organized and Isolated Convection Mix case, d) Linear Convection case, e) Convection Embedded in Stratiform Precipitation case.

c)



d)

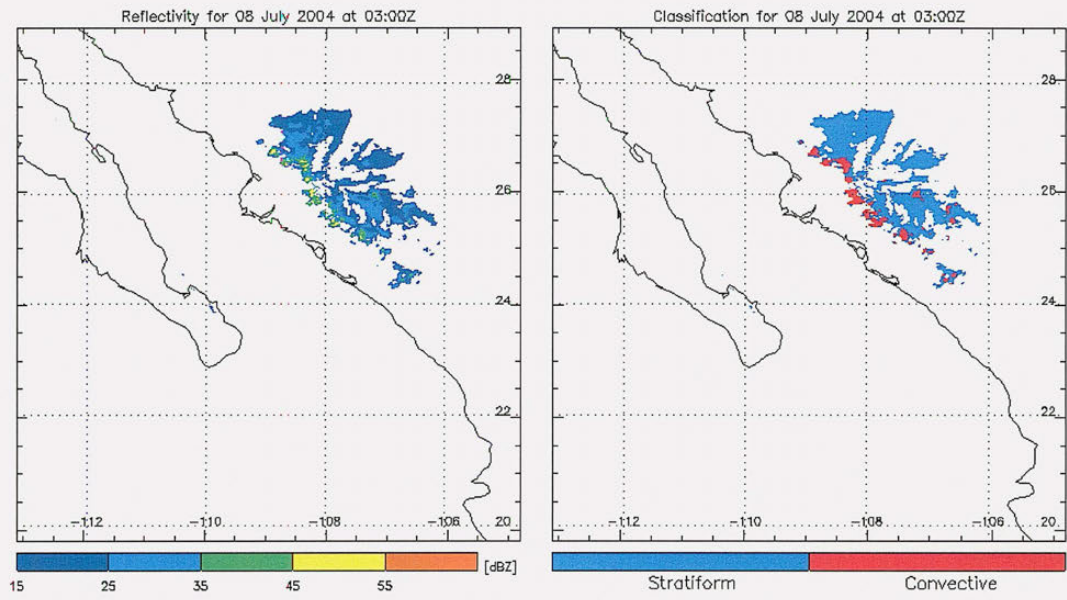


Fig. 2.6. - (continued)

e)

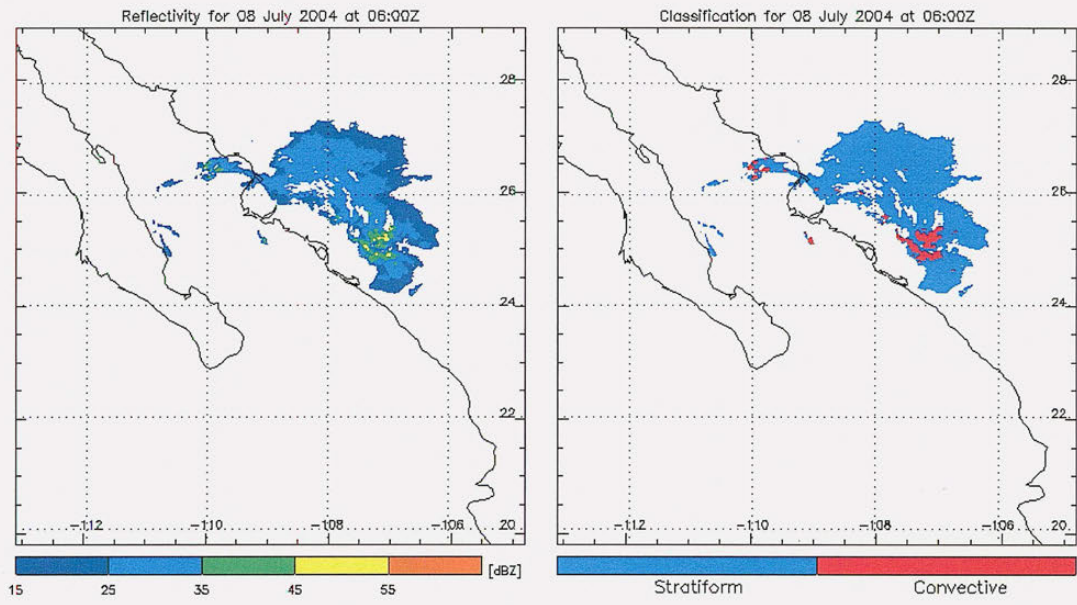


Fig. 2.6 - (continued)

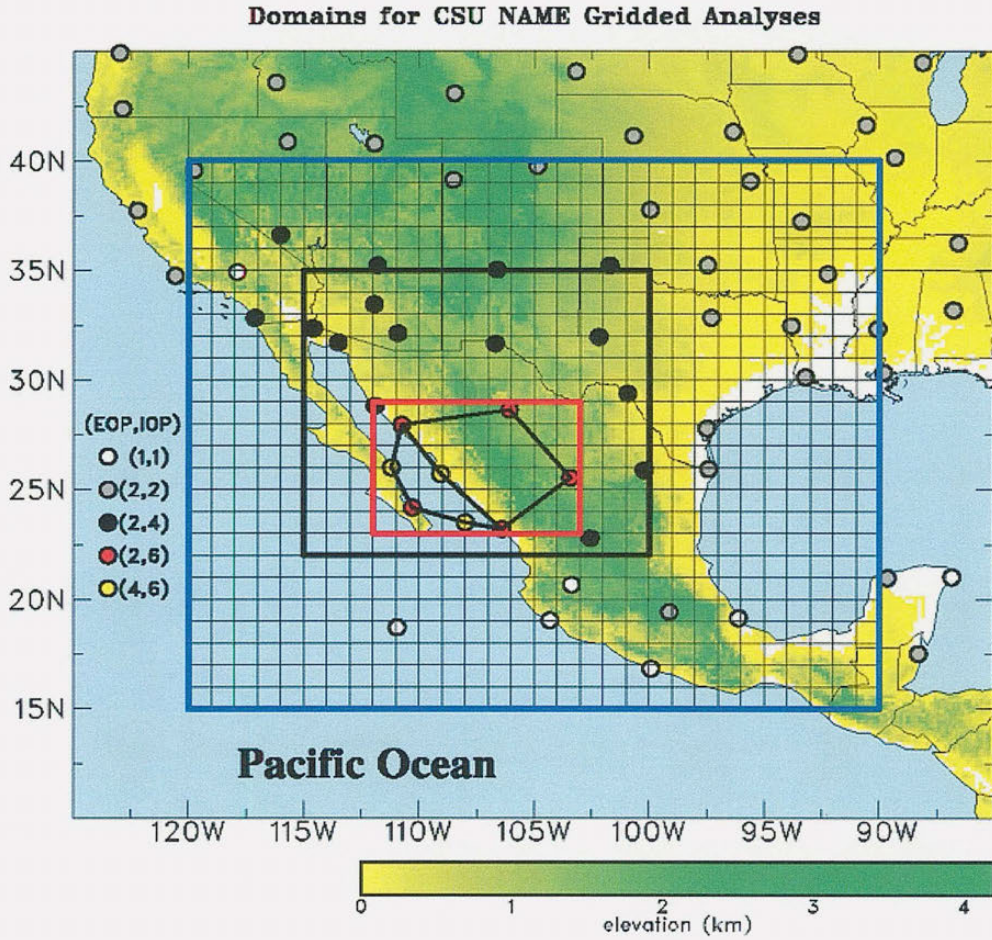


Fig. 2.7 - Domains of the NAME Gridded Analysis. The boundaries of the T1A dataset used in this study are depicted by the black lines (illustration from Cielsielski and Johnson 2006).

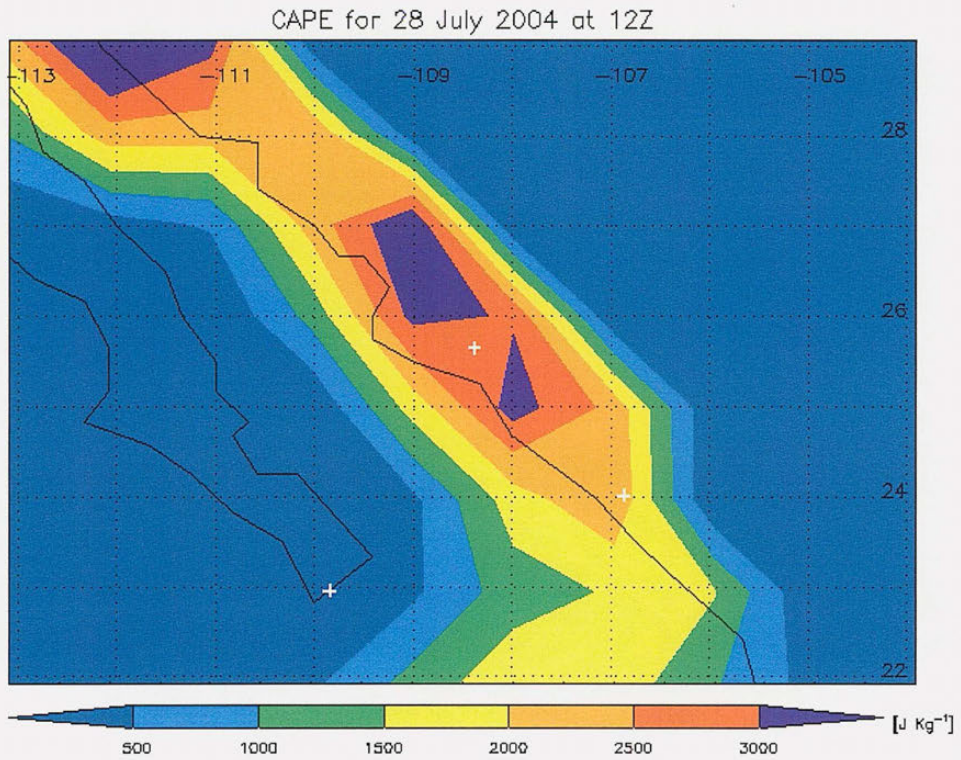


Fig. 2.8 - Map of Convective Available Potential Energy obtained using the CSU Gridded Analysis data for 28 July 2004 at 12Z. The white crosses indicate the position of the radars.

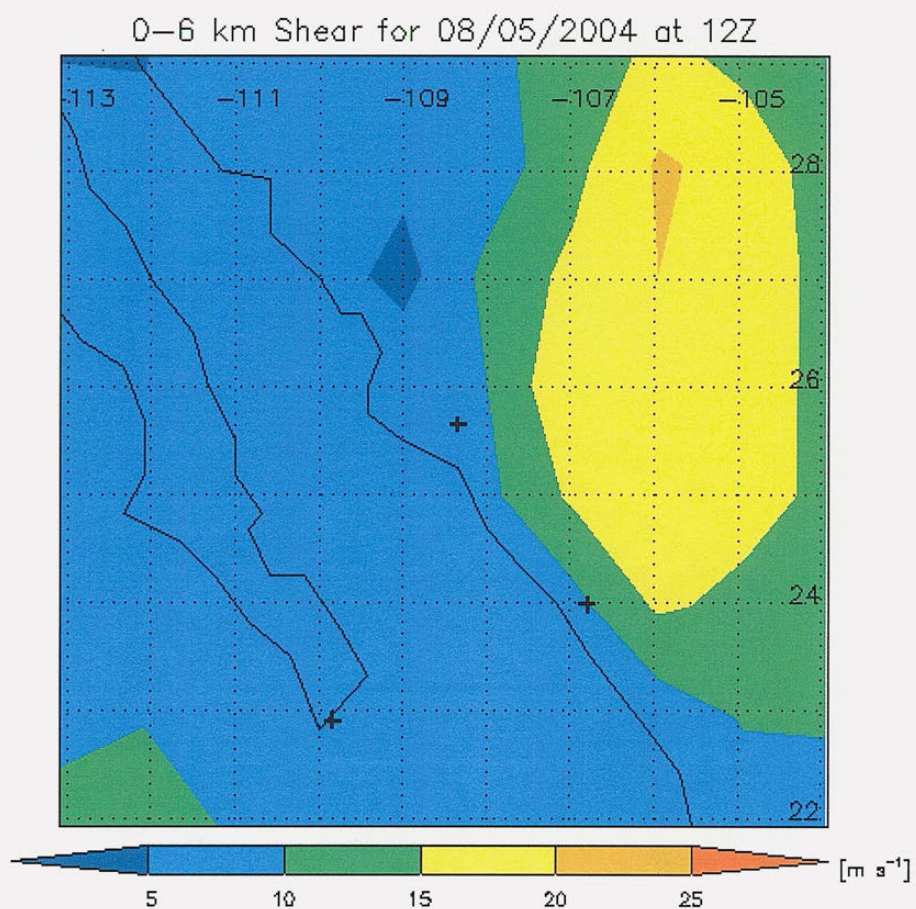


Fig. 2.9 - Map of 0-6 km Vertical Wind Shear obtained using the CSU objective gridded analysis data for 5 August 2004 at 12Z. The black crosses indicate the position of the radars.

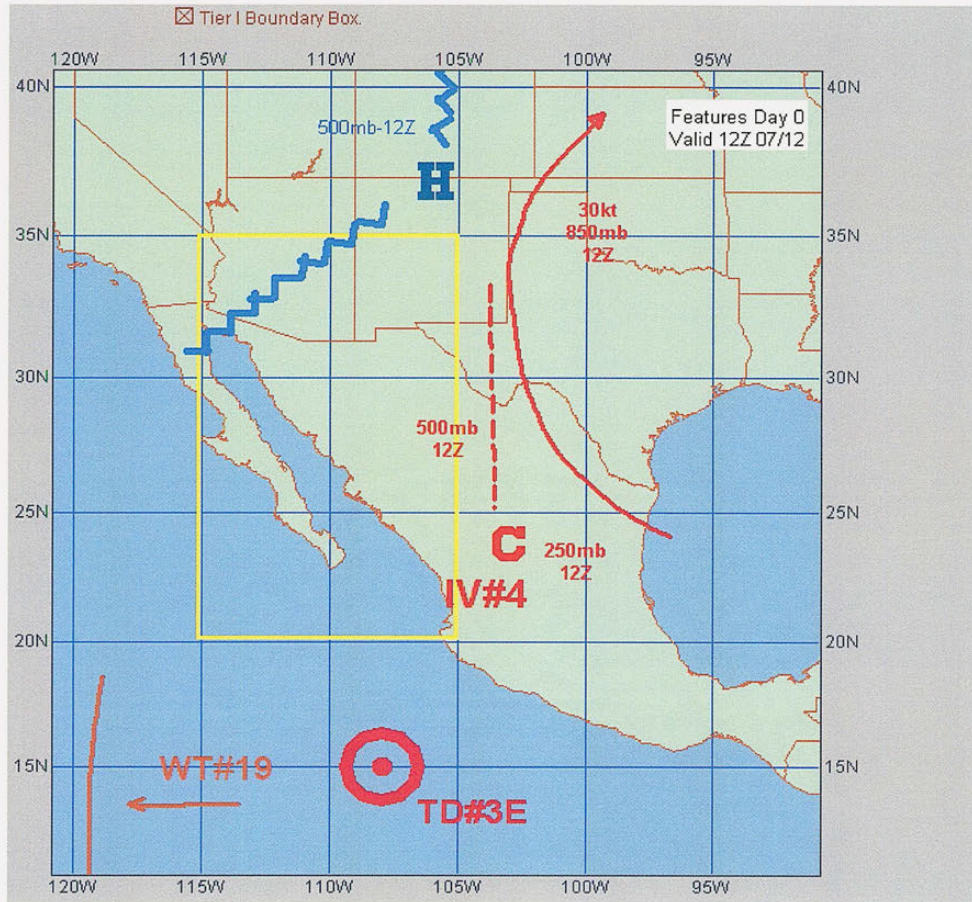


Fig 2.10 - Map showing synoptic features in the NAME region (illustration from the 2004 NAME Field Catalog).

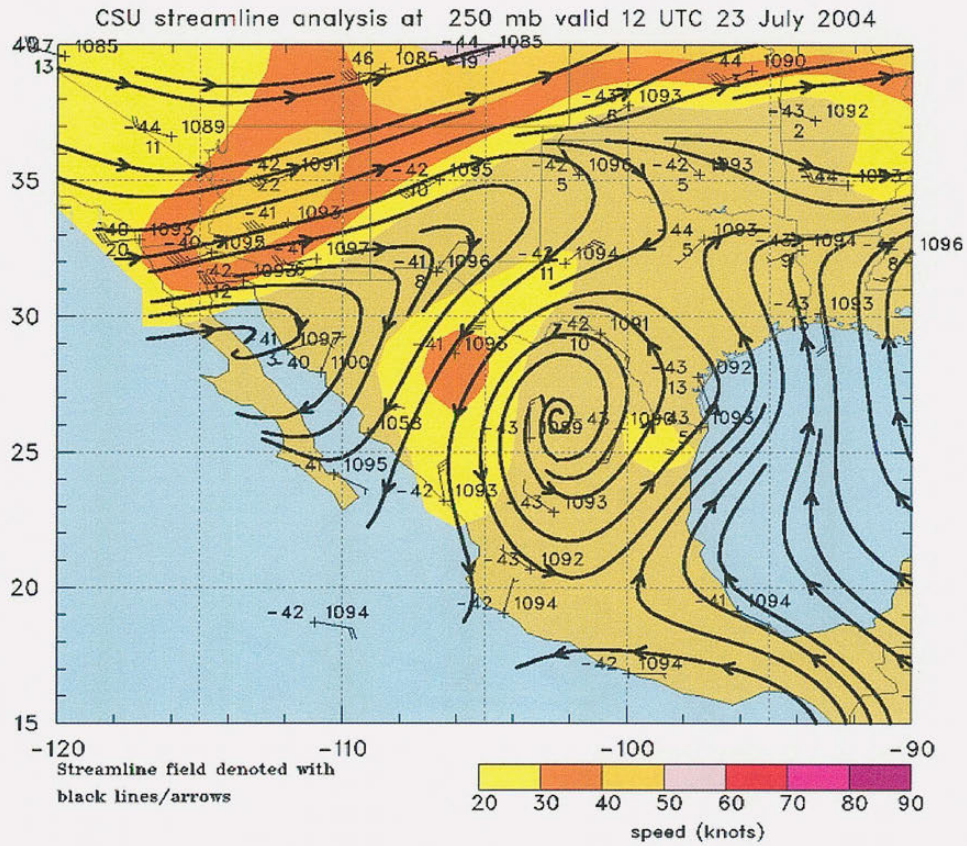


Fig. 2.11 - An example of a CSU streamline analysis at 250-hPa for 23 July 2004 at 12Z.

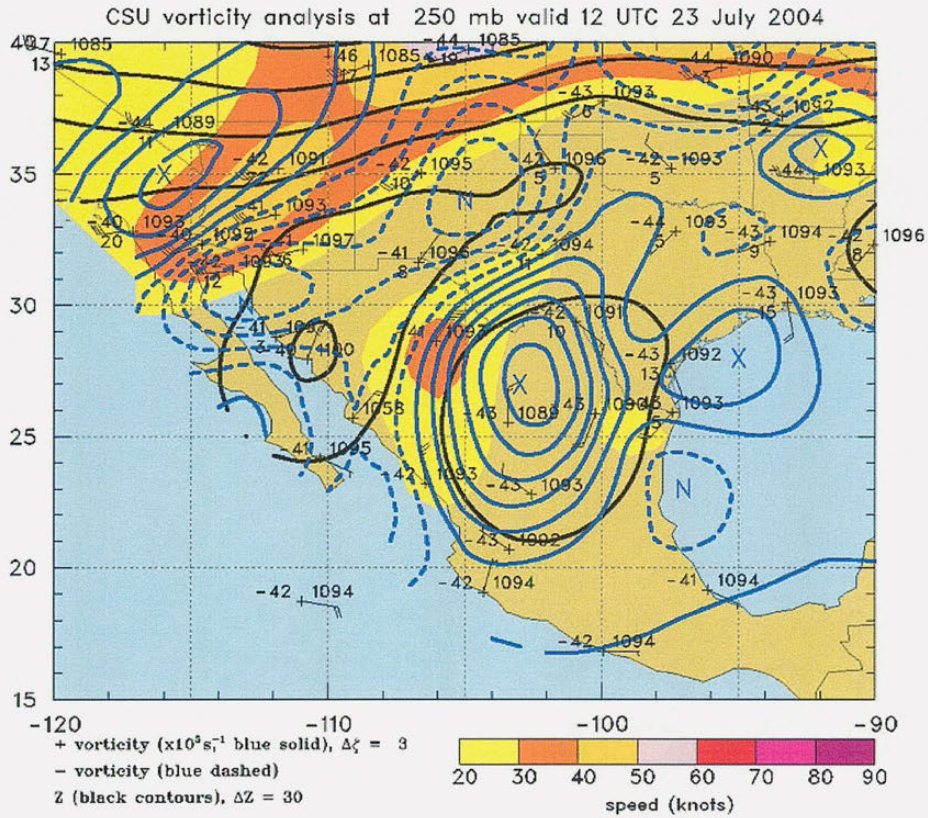


Fig. 2.12 - An example of a CSU vorticity analysis at 250-hPa for 23 July 2004 at 12Z.

CHAPTER III

Characteristics and Organization of Precipitating Features during NAME

3.1 Overview

Radar determined characteristics of convective precipitating features (PFs) during NAME are described in this chapter. As discussed in the previous chapter, these PFs were grouped according to their horizontal organization structure as observed by radar. Here we examine the frequency of occurrence, preferred times and locations, and the precipitation characteristics of these PFs. The analyses presented in this chapter are divided into five other sub-sections, starting first by a discourse on the overall characteristics of the PFs observed during NAME, followed by discussions of the PF characteristics for each organization group.

3.2 Overall Characteristics of Convective Precipitating Features During NAME

In this section we discuss the dominant characteristics of the PFs that occurred during NAME, regardless of their horizontal organization. The statistics described in this

section were created using the 79,225 PFs that comprise the entire population of features selected for examination (i.e. those PFs that possessed the required, size, reflectivity, convective characteristics, and all other requirements described in Chapter 2; recall that small, isolated convective PFs dominated the feature population).

First, we examine the geographical variability of feature occurrence over the NAME composite region. Fig. 3.1 shows the fraction of time that each grid point was occupied by a PF. In this figure we notice the low frequency of occurrence of PFs over water, in fact, almost entirely represented by values below the lowest end of fractions plotted in the map (6%). In any case, the highest fractions over water were approximately 8%, just south of Mazatlán, while the overall mean frequency of PF occurrence over water was only 0.6%. Precipitation was nearly absent in areas south and east of the Baja California Peninsula, where previous QuikSCAT analyses have indicated lower sea surface temperatures and divergent low-level winds (Bordoni et al. 2004, Johnson et al. 2007) and also where the atmosphere is consistently less unstable compared to the nearby land areas, as indicated by the CAPE distributions described in Fig. 2.9. Over land, PF occurrence fractions were much higher, particularly over the SMO, where they exceeded 16% in some locations. These fractions progressively decrease to 5% towards the coast. There is also a remarkable resemblance between the local maxima in PF occurrence and some of the topographical features located east of Mazatlán, where a few SW-NE oriented mountains emerge off of the SMO. The reduced frequency of PFs over water and their relative abundance over the SMO is consistent with observational records on

board R/V Altair, where only trace amounts of precipitation were recorded in the first cruise, and also consistent with TRMM mean precipitation rate retrievals over the region (Johnson et al. 2007). This result points to the importance of the local topography as a lifting mechanism in the development of PFs in the region, a pattern also identified in the rain gauge records (Gochis et al. 2007).

The distribution of sizes of these PFs is shown in Fig 3.2, where the upper panel (Fig 3.2a) shows the distribution of the PFs overall size, while the lower panel (Fig. 3.2b) shows the distribution of sizes of the PFs convective portion. It is evident from these figures that the population of PFs analyzed in this study is overwhelmingly comprised of relatively small PFs, which possess a total precipitating area that generally did not exceed 300 km^2 , and averaged 588 km^2 . Convective areas for these PFs were usually smaller than 100 km^2 , but averaged 95 km^2 . This 1-3 ratio between convective and total precipitating areas is also seen in Table 3.1 when the mean convective precipitating area fraction was calculated. PFs with an overall precipitating area exceeding $1,000 \text{ km}^2$ represent approximately only 8% of all the PFs analyzed in this study. Nevertheless, large PFs (and large convective areas), while much less numerous, occurred frequently during NAME. This is evident when we look at the large standard deviations for the PF total and convective areas shown in Table 3.1.

Fig. 3.3 presents a similar distribution as shown in the previous figure, except that now rain rates, rather than areas, are plotted. The majority of PFs are characterized by low rain rates, generally not exceeding 6 mm h^{-1} . Table 3.1 indicates that the mean rain

rate for PFs in the NAME radar composite region was 2.4 mm h^{-1} , and the mean convective and stratiform rain rate were, respectively 4.9 mm h^{-1} , and 1.0 mm h^{-1} . If these rain rates had been computed using only the Z-R relationship shown in Eq 2.1, the aforementioned mean rain rate values would correspond, respectively, to approximately 27 dBZ, 32 dBZ, and 21 dBZ. It was not surprising to find that most of the PFs mean rain rates were low since Fig. 3.2 showed that the majority of the PFs were relatively small and Fig. 2.4 showed a strong, positive linear correlation between feature size and volumetric rainfall. The mean ratio of convective to total rainfall for the PFs examined here was 57.5%. Schumacher and Houze (2003) found an average convective precipitation ratio of approximately 60% near the mouth of the GoC using data from TRMM's Precipitation Radar between 1998-2000, while fractions ranging between 41% and 58% were found by Pereira and Rutledge (2007) in the Eastern Pacific region located 1,800 km south of the NAME domain. Over the Atlantic Tropical Experiment (GATE) area, Cheng and Houze (1979) estimated a convective rainfall fraction of 60%, whereas Steiner et al. (1995) found that this same fraction varied between 59% and 66% in the vicinity of Darwin, Australia.

The diurnal cycle of PFs in the NAME radar composite domain is revealed in Fig 3.4, where the top (bottom) panel shows the hourly variation in the number of PFs (in total and convective rainfall) as a percentage of the overall number of features (total and convective rainfall) for each hour of day (local time). Fig. 3.4a exhibits a clear diurnal cycle with the number of features quickly increasing from 1100 LT until peaking at 1500

LT, then rapidly decreasing until 2200 LT and then rapidly decreasing again between 0500 and 1000 LT when the minimum number of PFs occur. An analysis of the rainfall diurnal cycle, shown in Fig. 3.4b, indicates a similar pattern to that described for the precipitating feature diurnal cycle, except that the diurnal increase in rainfall is noticed an hour later than the increase in PFs (i.e. 1100 LT) and rainfall peaks around 1800. The dashed line in Fig 3.4b depicts the convective rainfall cycle and, as expected, it shows a slightly more pronounced cycle than the total (convective plus stratiform) rainfall cycle depicted by the solid line. Fig. 3.1 showed that the majority of the PFs occurred over land, and the diurnal cycle observed in Fig. 3.4 is typical of those observed over land areas, with a minimum in the morning hours and a maximum in the mid to late afternoon hours due to boundary layer destabilization caused by daytime insolation (Wallace 1975; Oki and Musiaki 1994; Dai et al. 2001; Dai 2001). The lagged peak in precipitation is explained by the fact that most of the PFs that develop earlier in the diurnal cycle occur over the higher terrain of the SMO, where Rowe et al. (2008) showed that shallower warm cloud depths limits the mass collection (i.e. collision and coalescence) processes and rain rates over the SMO. The diurnal cycle of precipitating features and rainfall over water is shown in Figs. 3.4c-d. We observe a typical oceanic diurnal cycle, with a maximum number of precipitating features and rainfall overnight, as it was also noted by Rowe et al. (2008). The convective precipitation (dashed line in Fig. 3.4d) appears to be somewhat bimodal, with one maximum around midnight and another one around sunrise. The first peak is likely a result of convection that formed over land drifting over the

adjacent waters of the GoC, whereas the second peak is perhaps associated with convection forming along the coast by the land breeze (to be discussed later in section 3.4).

The contribution of each horizontal organization mode described in the previous Chapter is shown in Fig. 3.5. Hereafter, we will utilize the following simple nomenclature to refer to each of the four modes: sub-MCS non-linear features will be dubbed Type 1, sub-MCS linear features will be called Type 2, MCS non-linear features will be referred as Type 3, and Type 4 will refer to MCS linear features. The overwhelming majority of the 79,225 PFs examined in this study, nearly 95% of all PFs, are Type 1, as it can be seen in Fig. 3.5a. This is not surprising given the results presented in Fig 3.2 and 3.3 indicating that the majority of the PFs were small and had low rain rates. Moreover, unless advected into the NAME radar composite domain in a more organized state, all PFs begin their life cycle in this most basic organization state and a large majority of them end their life cycle without ever achieving a more organized mode (i.e. in size, as an MCS, or in morphology, as a linear feature). The second most frequent organization mode was Type 3, represented by approximately 4% of all features. Linear features, particularly those classified as Type 2, were not very common and comprised only 1% of the PF population analyzed here. However, a very different picture emerges when we evaluate Fig. 3.5b, which depicts the contribution of each organization mode to the total precipitation produced by all PFs. While Type 3 features made up only 4% of the total PF population, this group of PFs was responsible for more than one half of the

total precipitation. Type 4 features, which comprised roughly 1% of all PFs, generated nearly 15% of the total precipitation, whereas the frequently observed Type 1 PFs were responsible for 27% of the total precipitation. In the following sub-sections, the characteristics for each organization mode will be discussed. It will become evident that the large contribution of Type 3 and 4 features (i.e. MCSs) to the total precipitation is a result of their larger size and their higher rain rates.

3.3 Characteristics of Type 1 Precipitating Features During NAME

Given the sheer number of Type 1 (Sub-Mesoscale Non-Linear) precipitating features, the statistics presented thus far were strongly skewed by this PF type. Hence, many of the results discussed in this section are similar to those just presented in section 3.2.

The spatial distribution of Type 1 PFs in the NAME radar composite area, shown in Fig. 3.6, differs substantially from Fig. 3.1. First we notice that the highest incidence of Type 1 features occurs over the SMO and towards the southeastern end of the domain. Larger fraction contours which followed topographical contours evident in Fig. 3.1 are also obvious in Fig. 3.6, indicating that the location of occurrence of Type 1 PFs is strongly influenced by the complex terrain of the region. While observed in the entire domain of our analysis, the short life span of Type 1 PFs limits the bulk of their presence to the immediate surroundings of where they develop in the SMO. Fig. 3.6 shows that areas in the coastal plains were covered by Type 1 PFs less than 3% of the time, whereas

some portions of the SMO were affected by this mode of horizontal organization up to 9% of the time.

The distribution of sizes of Type 1 PFs shown in Fig 3.7 is nearly identical to those shown in Fig. 3.2 (as expected, since 95% of PFs were classified as Type 1). Approximately 85% of all Type 1 PFs had a total precipitating area of less than 300 km², and averaged 195 km². This is a relatively small area, considering this type of organization could be comprised of PFs up to 9800 km² in size. Given their small size, convective areas in these PFs were also quite small, 90% of which were less than 100 km², and averaged 48 km². Table 3.2 shows that the convective precipitating area was 33%, which is very similar to the value presented in the previous table.

The distribution of rain rates for Type 1 features is shown in Fig. 3.8. Fig 3.8a has an identical distribution to that discussed for Fig. 3.2a, with Type 1 PFs characterized by mean rain rates generally less than 10 mm h⁻¹. However, Fig. 3.8b displays a distribution skewed towards higher mean convective rain rates compared to Fig. 3.2b. While most Type 1 features possessed mean convective rain rates below 3 mm h⁻¹, approximately 35% of these PFs had mean convective rain rates ranging from 3 to 15 mm h⁻¹. The mean values presented in Table 3.2 indicate that the mean rain rate for PFs in the NAME radar composite region was 2.3 mm h⁻¹ and the mean convective rain rate was 4.4 mm h⁻¹. The mean convective rainfall fraction for Type 1 PFs was 57.9%. These rain rates are somewhat lower than the 8-10 mm h⁻¹ found in other tropical locations (Simpson et al. 1993, Rickenbach and Rutledge 1998). However, shallow convection in the Eastern Pacific region was found to have mean rain rates ranging from 4.7 mm h⁻¹ to 5.6 mm h⁻¹

depending on the synoptic wind regime (Pereira and Rutledge, 2007). Furthermore, the partitioning algorithm was tuned for better results for this dataset. Recall that among the modifications made in the partitioning algorithm was to relax the reflectivity thresholds necessary to increase the convective radius. The practical effect of this change was that a larger portion of the precipitating area in a Type 1 feature was placed within the convective radius and, consequently, classified as convective. As a result, some lighter rain rates surrounding the convective core of the PF were averaged into the mean rain rate figures presented here. Stratiform convection in this region typically forms from decaying convection as opposed to developing through other processes and co-existing with convection. The convective rainfall fraction reported here is also lower than in other tropical areas. This is primarily caused by the presence of relatively large Type 1 PFs which had a much larger stratiform region, but did not satisfy the requirements to be classified as an MCS (i.e. Type 3 or 4). However, more than half of Type 1 PFs indicated convective rainfall fractions greater than 80%.

Fig. 3.9a shows the hourly frequency of occurrence of Type 1 PFs in the NAME radar composite area. Practically identical to Fig. 3.4a, Fig. 3.9a displays a clear diurnal cycle with the number of features peaking at 1500 LT and with a minimum around 1000 LT. However, the rainfall diurnal cycle, shown in Fig. 3.9b, differs from the one shown in Fig 3.4b by possessing a much more pronounced diurnal cycle, which closely follows the diurnal cycle of number of features (Fig. 3.9a). The peak in rainfall generated by Type 1 features occurs between 1600 LT and 1700 LT, with 54% of all precipitation generated by this group occurring in a period of 6 hours between 1400 LT and 2000 LT. These results, coupled with those found from Fig. 3.6, suggest that the numerous Type 1

PFs found in this region are a result of the complex terrain of the area coupled with the diurnal boundary layer destabilization of the land by daytime insolation.

3.4 Characteristics of Type 2 Precipitating Features During NAME

Type 2 (Sub-Mesoscale Linear Features) were the least frequent of all the horizontal organizational modes examined here, making up only 0.16%, or 127, of all PFs analyzed here. Hence, results are much noisier than those obtained for the other organizational modes. Due to the rarity of this type of organizational mode, further analysis with a larger dataset would be required for a statistically significant result. We include the results for the NAME radar dataset for completeness, but we will not attempt to further examine and correlate this type of PF to the thermodynamic and synoptic environment of NAME in following chapters.

Fig 3.10 indicates that Type 2 features were not as homogeneously distributed as their non-linear counterparts (Type 1). A few features occurred over the elevated terrain, while others occurred in the coastal plains and over water. In any case, their presence never exceeded more than 0.2% of the time at any particular location.

The distribution of sizes of Type 2 PFs is shown in Fig 3.11. The distribution is rather uneven, but this is largely caused by the rather small sample of PFs in this group in our dataset. Nearly 84% of all Type 2 PFs had precipitating areas ranging from 300 km² to 1500 km², averaging 1136 km². Convective precipitating areas in Type 2 PFs were found to usually have 200 km² to 600 km² areas, with a mean value of 468 km². Type 2

sizes are obviously larger than Type 1 PFs since the former type requires a PF to have minimum dimension of 50 km in any given direction. Table 3.3 shows that the ratio of convective to total precipitating area within Type 2 PFs was 43.7%.

The distribution of rain rates for Type 2 features is shown in Fig. 3.12. Fig 3.12a shows that the overall mean rain rates for most Type 2 ranged from 4 mm h⁻¹ to 16 mm h⁻¹. The convective portion of Type 2 PFs has much more intense rain rates than Type 2 features. Approximately three-quarters of Type 2 PFs had mean convective rain rates greater than 12 mm h⁻¹. The mean values presented in Table 3.3 indicate that the mean rain rate for PFs in the NAME radar composite region was 10.0 mm h⁻¹ and the mean convective rain rate was 20.2 mm h⁻¹. These substantially higher mean rain rates, compared to Type 2 features, are perhaps a result of the more intense downdrafts one would expect to find in the convective portions of a linear feature. Consequently, higher mean convective rainfall fractions would be expected for these PFs, and Table 3.3 indicates that this mode of organization has a mean convective rainfall fraction of 87.4% and a relatively low standard deviation (5.9%).

The plots shown in Fig. 3.13 were noisy, so a moving average of 3 hours was applied to the hourly fractions prior to plotting. In both panels we observe a similar trend, with primary maximum in the afternoon hours, and a small secondary peak just before dawn. While the major peak is associated with convection over land, the secondary morning peak is associated with the Type 2 features over water, but immediately adjacent to coast (near 24.5° N, 108° W). Although relatively rare, a few coastal features of this nature were observed during the field project during the early morning hours, during

commutes between Mazatlán and the S-pol radar site. The timing of their formation, their orientation and proximity to the coast suggest that they could possibly be the result of the land breeze pushing the moist coastal plan air over a more thermodynamically stable maritime air, although more data and analyses are required to verify this hypothesis.

3.5 Characteristics of Type 3 Precipitating Features During NAME

In this section we discuss the statistics for the second most common type of horizontal organization, Type 3 (Mesoscale Non-Linear) PFs. While comprising only 5% of the PF population examined here, this features were responsible for 58% of the rainfall produced by all PFs.

Fig. 3.14 illustrates the fraction of time each grid point in the NAME radar composite was covered by a Type 3 PFs. The areas covered by higher fractions are more widespread than those observed for Type 3 PFs (Fig. 3.6). Fractions of up to 5% are observed in some portions of the coastal plains, whereas fractions up to 9% are observed in the foothills north of Mazatlán. Moreover, while the highest frequencies of occurrence of Type 1 PF occurred at higher elevations (Fig. 3.6), Type 3 PFs occurred a little closer to the foothills (Fig. 3.14), at a mean elevation of 795 m MSL. One of the reasons why Type 3 PFs are more frequent at lower elevations is that most of these PFs initiate as Type 1 PFs at the higher terrain, and then evolve into large mesoscale-size PFs as they slowly move from the SMO towards the coastal plains, where sea breeze convergence is more pronounced. Nonetheless, many of these were confined to the foothills and never moved all the way into the coastal plains. Gochis et al. (2007) noted that most high

precipitation events, typically associated with MCSs, occurred at the foothills. Additionally, Farfán and Zehnder (1994) found that some MCSs in this region remain nearly stationary, which would explain the higher frequency observed near the foothills where they first develop. Lastly, it is important to stress that the entire area of the MCS is taken into account in the preparation of these geographical distribution maps shown in Figs. 3.1, 3.6, 3.10, 3.14, and 3.18. Consequently, trailing stratiform regions from these MCSs were frequently located over the higher terrain and were counted as the system moved away from the SMO. Also noteworthy is that Type 3 PFs are more frequently observed in areas north of Mazatlán, as opposed to the south as it is in the case of Type 1 PFs. It is possible that the prevalence of these Type 3 PFs to the north of Mazatlán is caused by a favorable topographical orientation with respect to the mean surface winds in the region, which were shown by Johnson et al. (2007) to blow from S-SW. Otherwise, other environmental conditions may have been more favorable for the development of larger MCS systems towards the northern end of our domain.

Notice that Fig. 3.15a, which shows the distribution of MNL feature sizes, has a multiplying factor of 10^3 (rather than 10^2 as in the previous corresponding plots). This figure shows that, unlike Type 1 features, Type 3 features vary widely in size, with the mode in the $2,000 \text{ km}^2$ to $4,000 \text{ km}^2$. However, due to the wide distribution of Type 3 PF areas, the largest of which had $47,600 \text{ km}^2$, the mean precipitating area was much larger than the mode: $8,161 \text{ km}^2$; and a rather large standard deviation of $7,763 \text{ km}^2$ (Table 3.4). Convective areas are also distributed through a large range of values, but are generally less than $1,200 \text{ km}^2$ and average 910 km^2 . The convective precipitation area fraction is only 13.4%, which is a result of their very large stratiform areas.

The distribution of rain rates for Type 3 features is shown in Fig. 3.16. Fig 3.16a shows that mean rain rates for the entire area of a Type 3 are relatively low, generally less than 10 mm h^{-1} , a result of the large, low rain rate, stratiform areas that these PFs usually possess. However, Fig. 3.8b displays a mean convective rain rate with a much wider distribution, with most values ranging up to 25 mm h^{-1} , but with some cases where the mean rain rate exceeds 40 mm h^{-1} . Table 3.4 shows that the mean rain rate for Type 3 PFs was 3.6 mm h^{-1} and the mean convective rain rate 13.1 mm h^{-1} . These rain rates are also greater than the ones found for Type 1. This is likely caused by the better dynamics and reduced entrainment found with mesoscale-sized systems. The mean convective rainfall fraction for Type 3 PFs was 45.2%, the lowest of all four types of horizontal organization.

The diurnal cycle of Type 3 PFs is revealed in Fig 3.16. Fig. 3.16a exhibits a delayed diurnal cycle in number of Type 3 PFs, with most of these PFs occurring in the evening hours. The minimum in Type 3 features occurs between 0900 LT and 1300 LT and a well-defined peak occurs at 1900 LT, 4 hours after isolated convective cells (i.e. Type 1 PFs) reach their peak in frequency of occurrence. The delayed cycle, when compared to Type 1 features, is likely a result of Type 1 growing in size and achieving mesoscale-size to become Type 3 PFs. An analysis of the rainfall diurnal cycle, shown in Fig. 3.17b, indicates a similar pattern to that described for the diurnal cycle of features, except that the percentage of rainfall from Type 3 PFs does not quickly decrease immediately after its peak (around 1900 LT), but rather continue to contribute to precipitation up until roughly local midnight. Convective rainfall contributions peak an hour earlier (at 1800 LT) and then quickly decrease after that. Rainfall contributions by

Type 3 PFs in the morning and early afternoon hours are very small, demonstrating that this type of PF is just an evolved state that a few Type 1 PFs, which initiate earlier over the SMO, are able to achieve.

3.6 Characteristics of Type 4 Precipitating Features During NAME

Type 4 (Mesoscale Linear) PFs encompass only 1% of the all PFs examined in this study, but generated 15% of all the precipitation within the NAME radar composite region (Fig. 3.5).

Fig 3.18 indicates that Type 4 PFs were generally confined to the northern parts of SMO foothills within the domain of the NAME radar composite. The mean elevation where most Type 4 PFs were found was 1,229 m MSL, much lower than the elevation observed for Type 1 PFs. The distribution of sizes of Type 4 PFs, shown in Fig 3.19, is the most widespread of all organization modes. Most Type 4 PFs had precipitating areas less than 16,000 km², but a few were twice that size. Convective precipitating areas for Type 4 PFs was also widely variable, but most frequently ranged from 900 to 1,800 km². Table 3.5 shows that the mean precipitating area for Type 4 PFs was 10,494 km², while the mean convective precipitating area was 1,740 km². Nesbitt et al. (2006) completed a survey of tropical MCSs over the Tropics using TRMM satellite data. Their results identified a mean MCS size over Africa, South America, the East Pacific Ocean, and the West Pacific Ocean of, respectively, 10,946 km², 10,539 km², 19,914 km², and 15,846 km². In the middle-latitudes some MCSs can grow to sizes greater than 200,000 km² (Maddox et al. 1982). The mean fraction of convective to total precipitating area for Type

4 PFs was slightly higher than their non-linear counterparts: 21.7%.

The distribution of rain rates for Type 4 features is shown in Fig. 3.20. Fig 3.20a shows that the overall mean rain rates for most Type 4 were generally less than 10 mm h⁻¹. The convective portion of Type 4 PFs had rather intense rain rates, just like the Type 2 PFs. Most of the mean convective rain rates were found in the range of 15 mm h⁻¹ to 21 mm h⁻¹. The mean values presented in Table 3.5 indicate that the mean rain rate for Type 4 PFs was 6.3 mm h⁻¹ and the mean convective rain rate was 20.9 mm h⁻¹, an amount almost identical to that obtained by Type 1 PFs. As a result, it is not surprising to see in Table 3.5 a higher mean convective rainfall fraction for Type 4 features compared to their non-linear counterparts. We found such fraction to be 65.8%, while several previous studies have found that these fractions vary between 45% and 70% in tropical squall lines (Houze 1977; Zipser et al. 1981; Gamache and Houze 1983; Houze and Rappaport 1984; Leary 1984), within which our current estimate lies.

Fig. 3.21 shows the diurnal cycle of Type 4 PFs. In Fig. 3.21a we observe that there is a rapid increase in frequency of occurrence of Type 4 PFs after 1400 LT, with a peak in observation occurring between 1700 LT and 2000 LT. Despite the quick decrease in observation after 2100 LT, a secondary peak is observed in the morning hours. Fig 3.21b shows a curve that also rapidly increases after 1400 LT, but peaks only at 2100 LT and is followed by a rapid decrease. While the primary peak is associated with the development of unorganized convection from the SMO (i.e. Type 1 PFs) into large linear systems closer to the SMO foothills, the secondary peak in rainfall observed at 0500 LT, is associated with PFs over water. Likewise in the case of Type 2 PFs discussed

previously, a few PFs were found to appear in the pre-dawn hours in areas adjacent to the coast and to grow into mesoscale size while acquiring a linear structure and orientation parallel to the coast. Events like this were observed in the early morning hours of 23 July 2004 and 12 August 2004. Once again, it is possible that these early morning Type 4 PFs are a result of the land breeze impinging over a more stable layer of air over the GoC. The earlier peak at 0200 LT in Fig. 3.21a was also found to be associated with PFs over the water.

As it was described briefly in this chapter, each of these PFs has specific characteristics and affects the local hydrological cycle of this monsoon region in different ways. Is the occurrence of these PFs modulated by variations in the thermodynamic and kinematic conditions in the region? Is there a particular type of environment and synoptic pattern that favors the development of organized convection? These are some of the questions we attempt to address in the next two chapters.

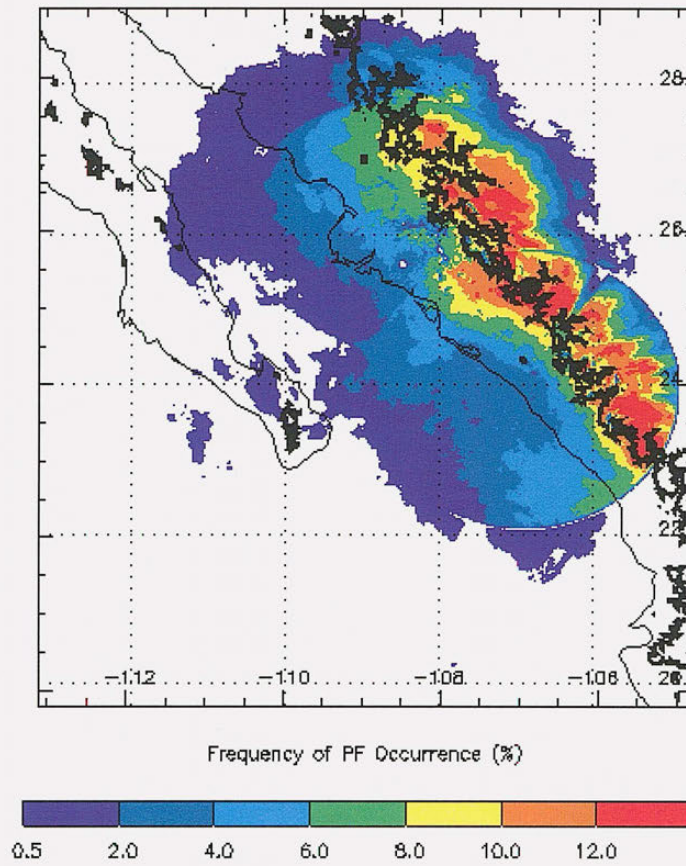
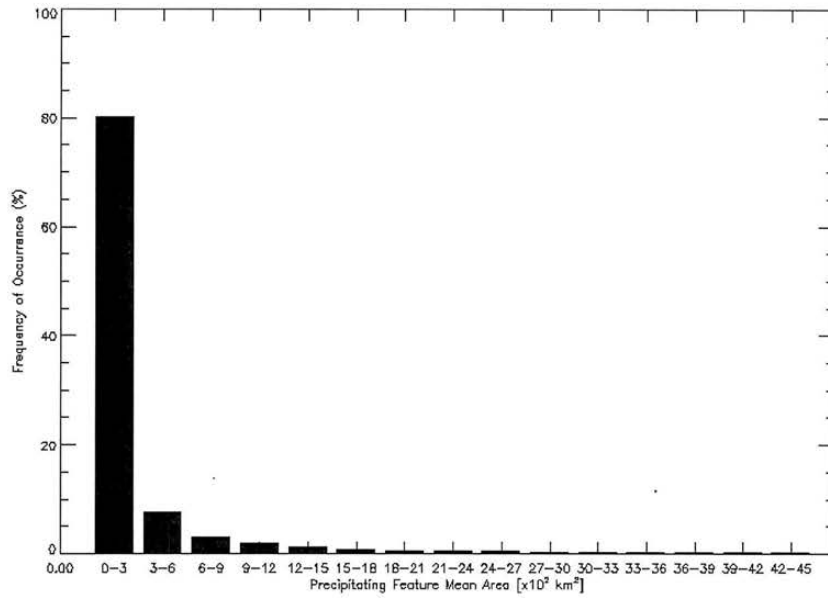


Fig. 3.1 - Map illustrating the geographical variations in frequency of occurrence of precipitating features in the NAME radar composite domain. The black thick line delineates the topography above 1000 m.

a)



b)

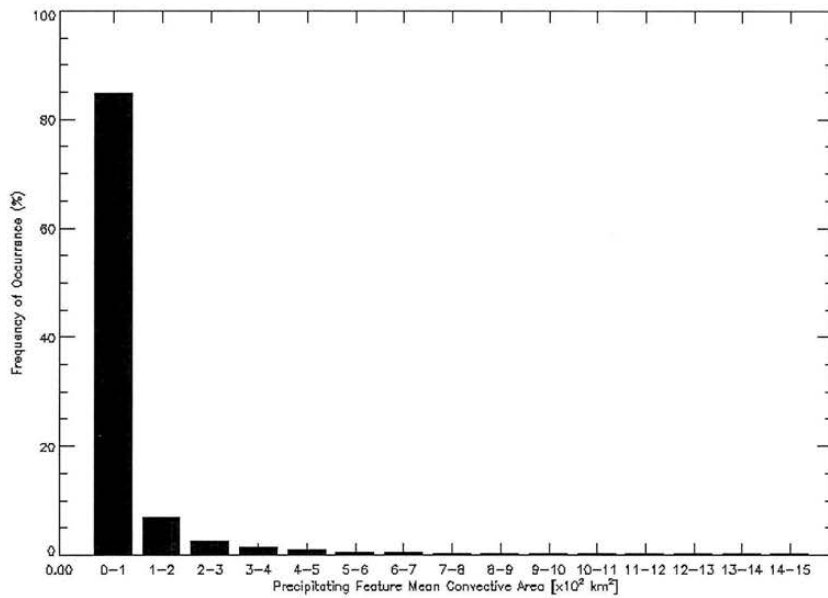
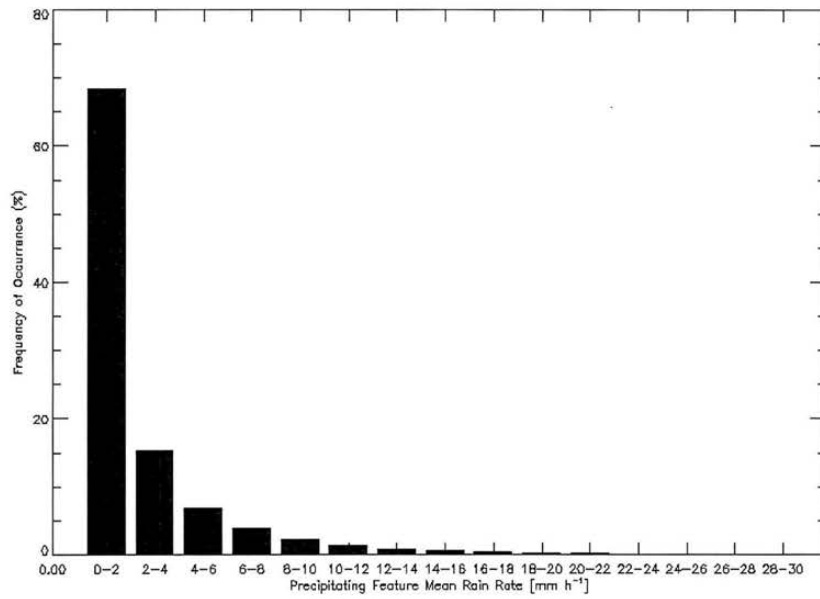


Fig. 3.2 - Distribution of Precipitating Feature sizes within the NAME radar composite region; a) feature total area, b) feature convective area.

a)



b)

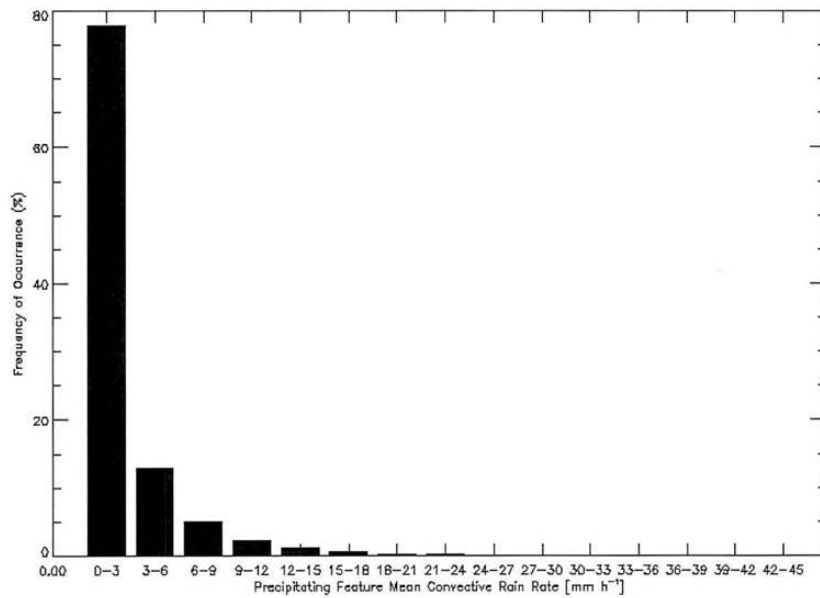
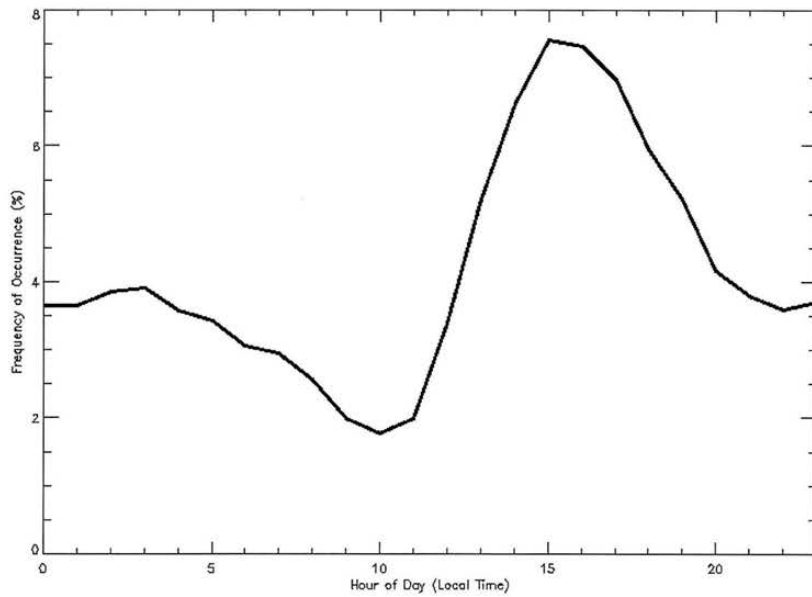


Fig 3.3 - Distribution of Precipitating Feature mean rain rates within the NAME radar composite region; a) feature mean rain rate, b) feature mean convective rain rate.

Table 3.1 - Mean characteristics of precipitating features in the NAME radar composite region.

Characteristic	Mean	Std. Deviation
PF Total area	588 km ²	2,508 km ²
PF Convective area	95 km ²	312 km ²
PF Convective Area Fraction	32.1%	19.3%
PF Rain rate	2.4 mm h ⁻¹	3.1 mm h ⁻¹
PF Convective Rain Rate	4.9 mm h ⁻¹	6.7 mm h ⁻¹
PF Stratiform Rain Rate	1.0 mm h ⁻¹	0.7 mm h ⁻¹
PF Convective Rain Fraction	57.5%	27.6%

a)



b)

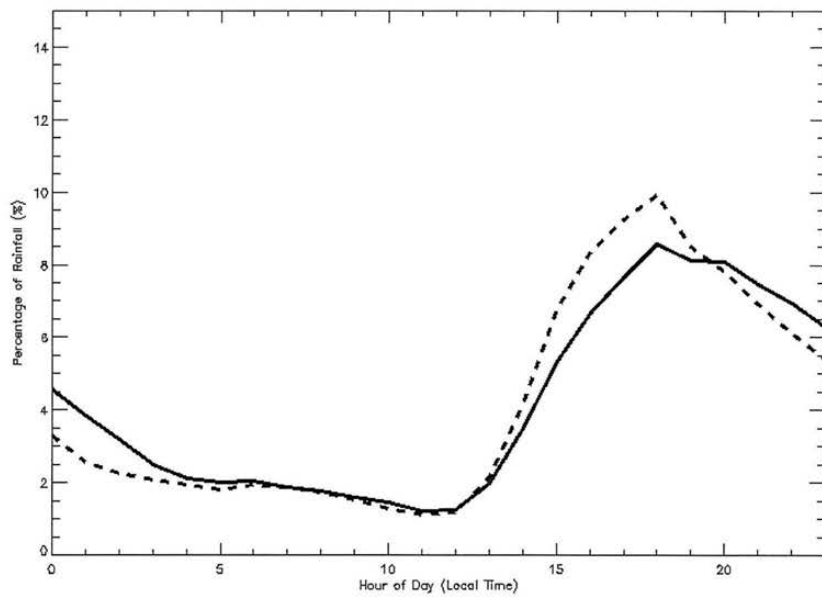
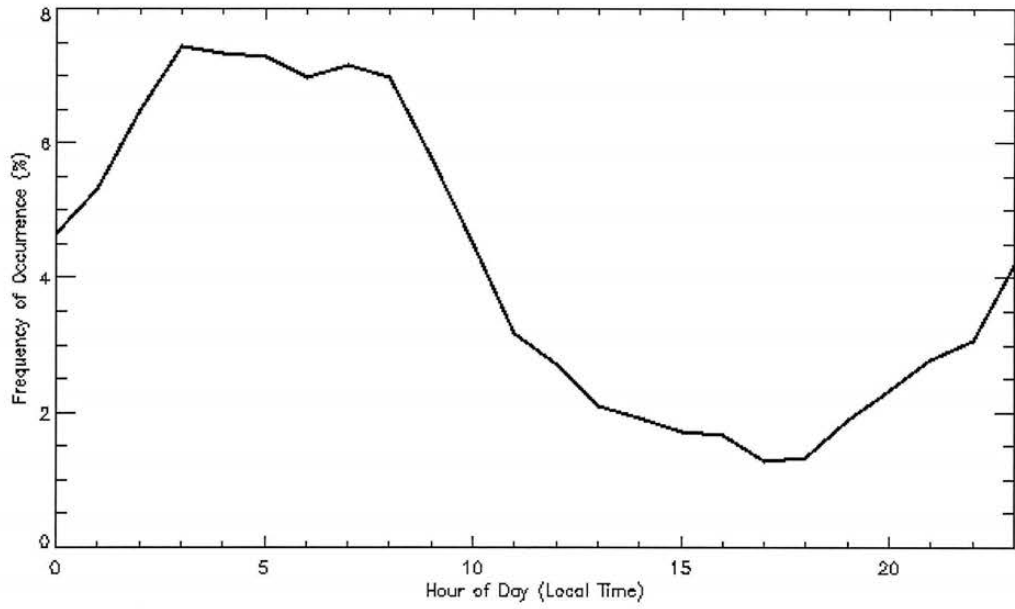


Fig 3.4 - Diurnal hourly variation in a) frequency of occurrence of precipitating features; b) percentage of total (solid line) and convective (dashed line) rainfall generated by precipitating features; c) same as a), but for features over water only; and d) same as c), but for features over water only.

c)



d)

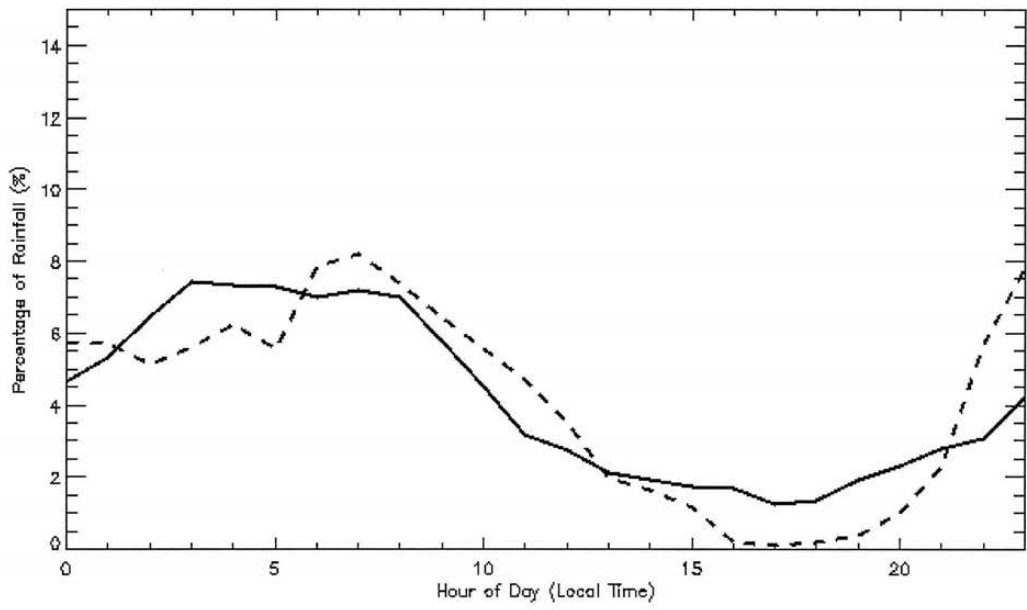
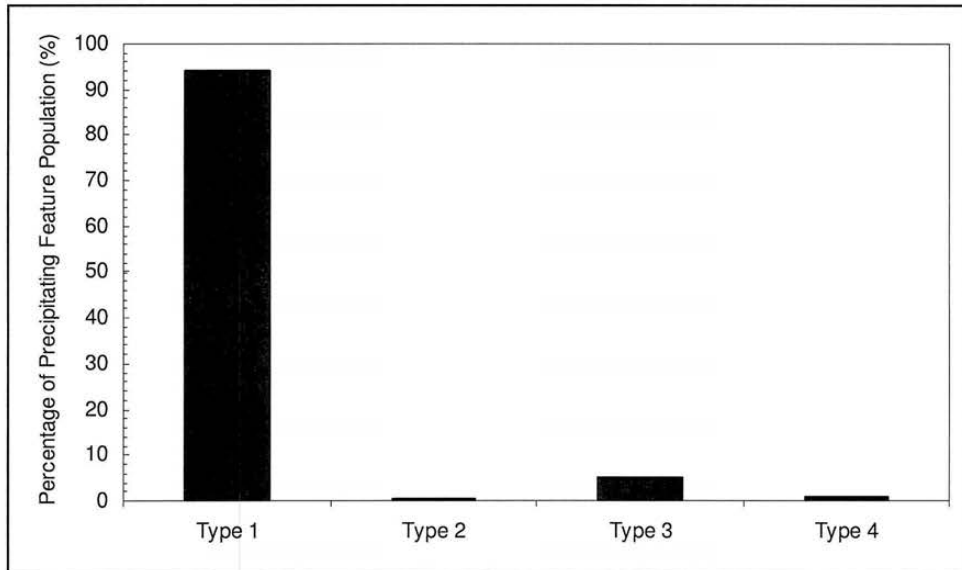


Fig. 3.4 – (cont.)

a)



b)

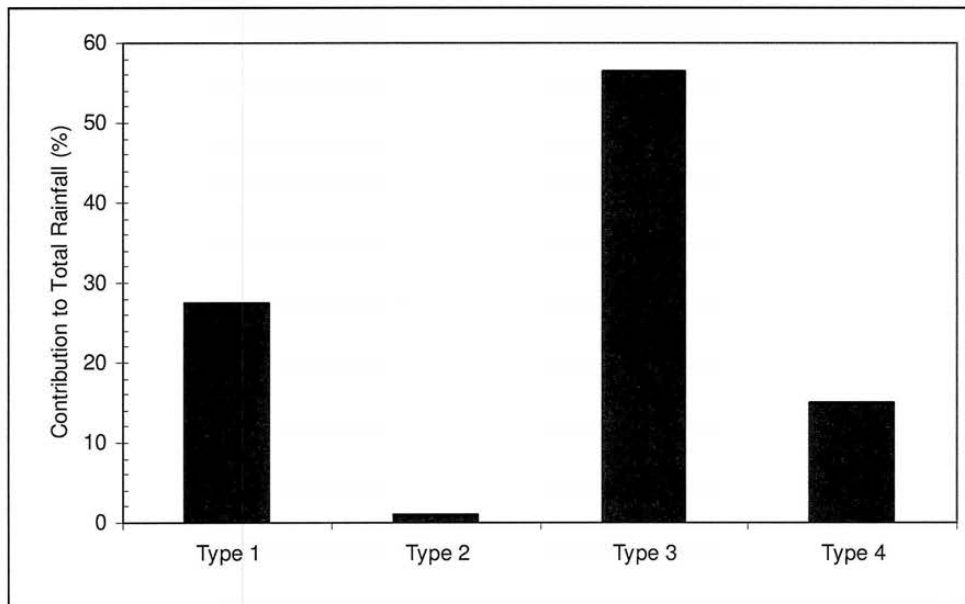


Fig 3.5 - Horizontal Organization of precipitating features during NAME. a) Percentage of precipitating feature population in each organization mode; b) contribution to total rainfall by each organization mode.

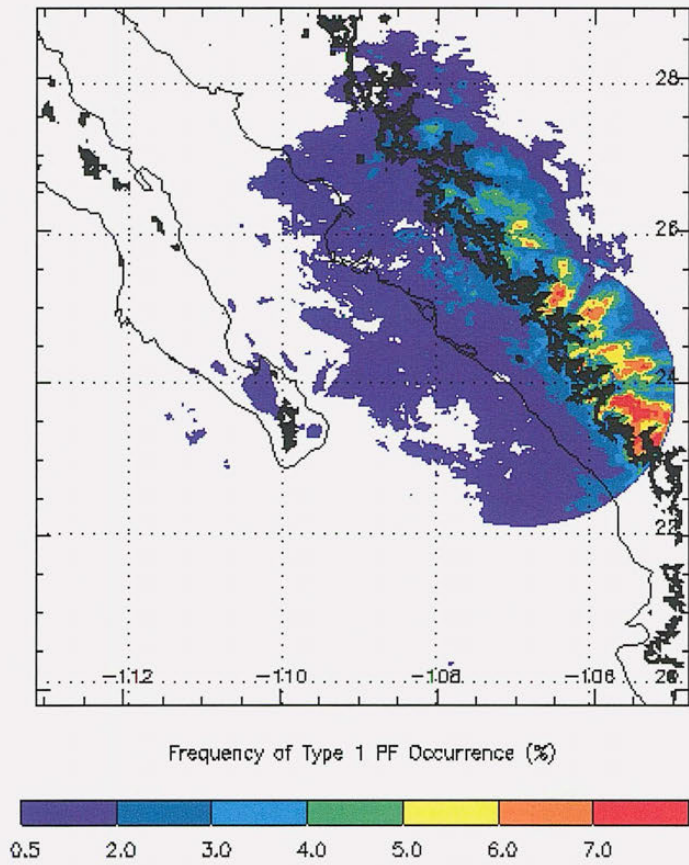
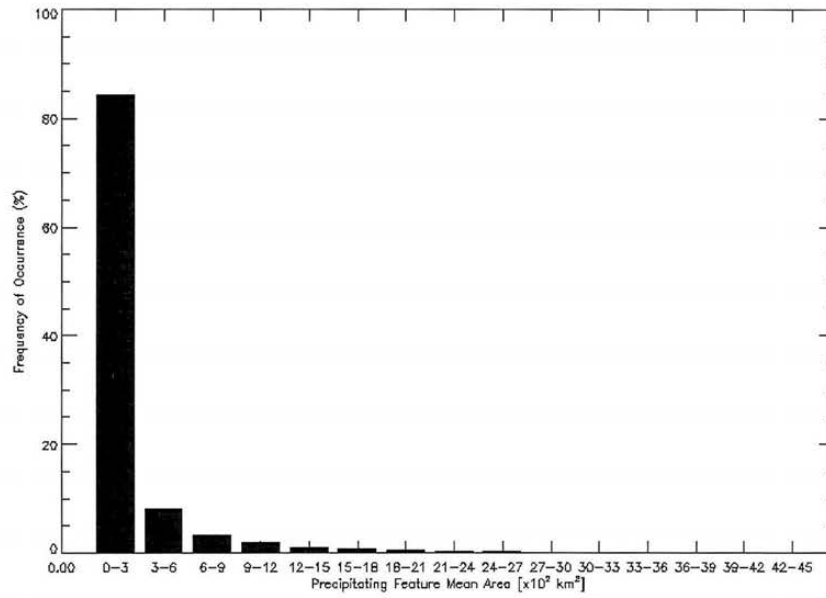


Fig. 3.6 - Map illustrating the geographical variations in frequency of occurrence of Type 1 precipitating features in the NAME radar composite domain. The black thick line delineates the topography above 1000 m.

a)



b)

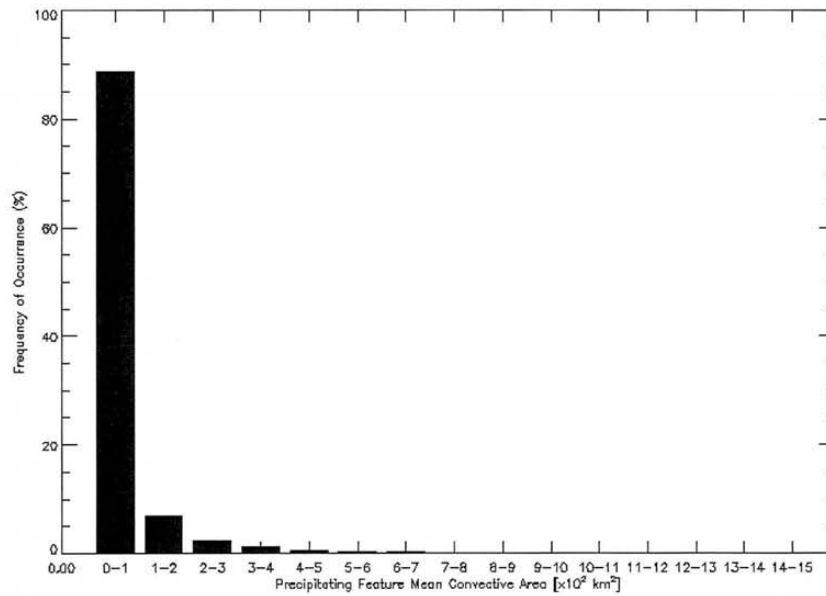
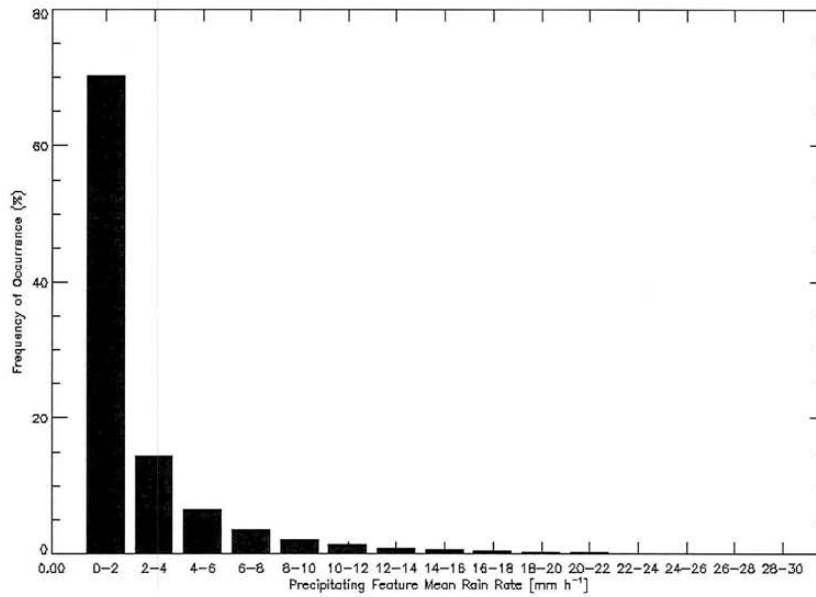


Fig. 3.7 - Distribution of Type 1 Precipitating Feature sizes within the NAME radar composite region; a) feature total area, b) feature convective area.

a)



b)

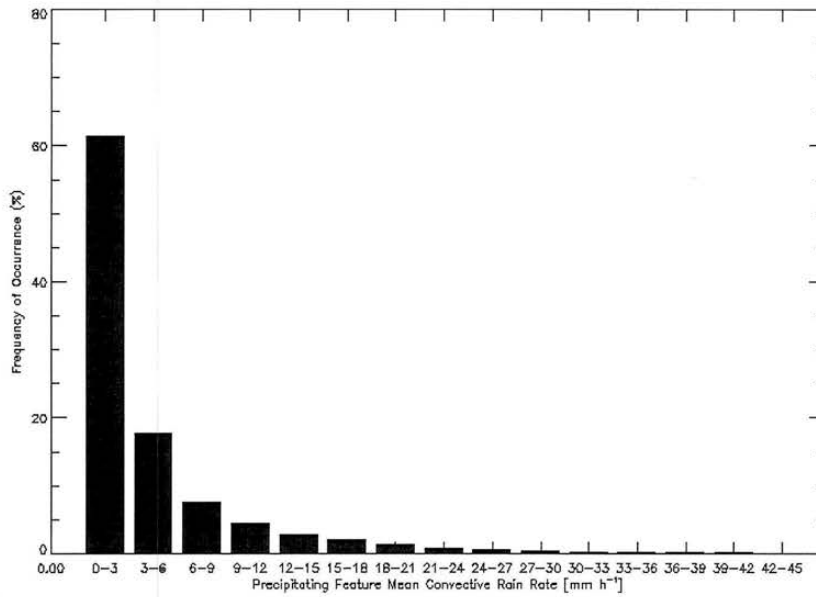
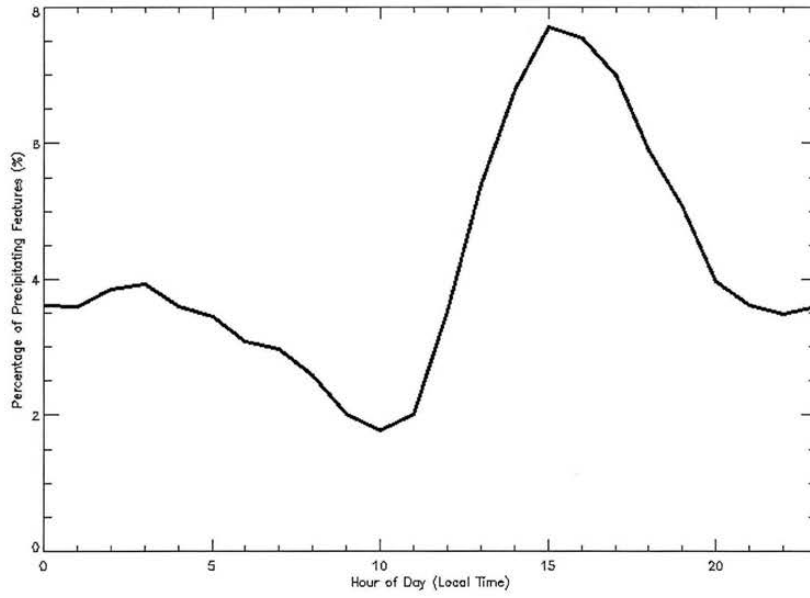


Fig. 3.8 - Distribution of Type 1 Precipitating Feature mean rain rates within the NAME radar composite region; a) feature mean rain rate, b) feature mean convective rain rate.

a)



b)

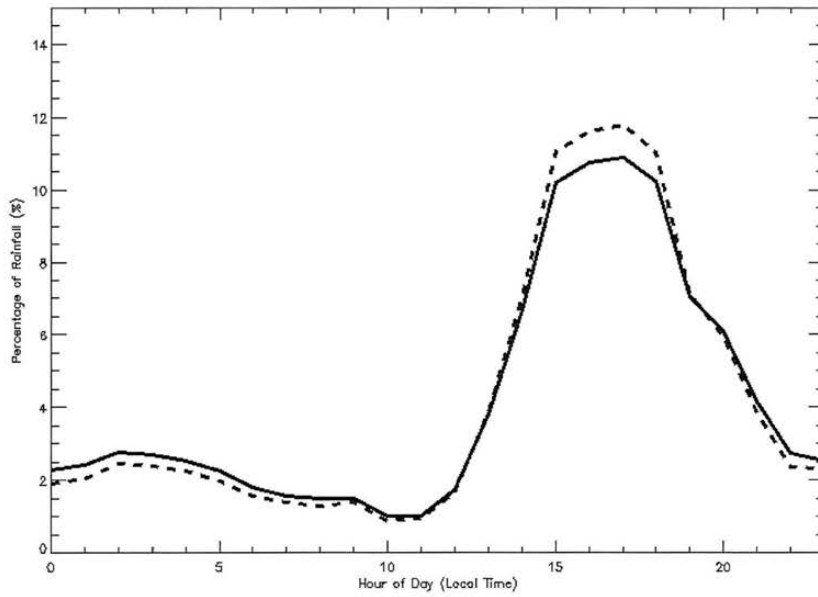
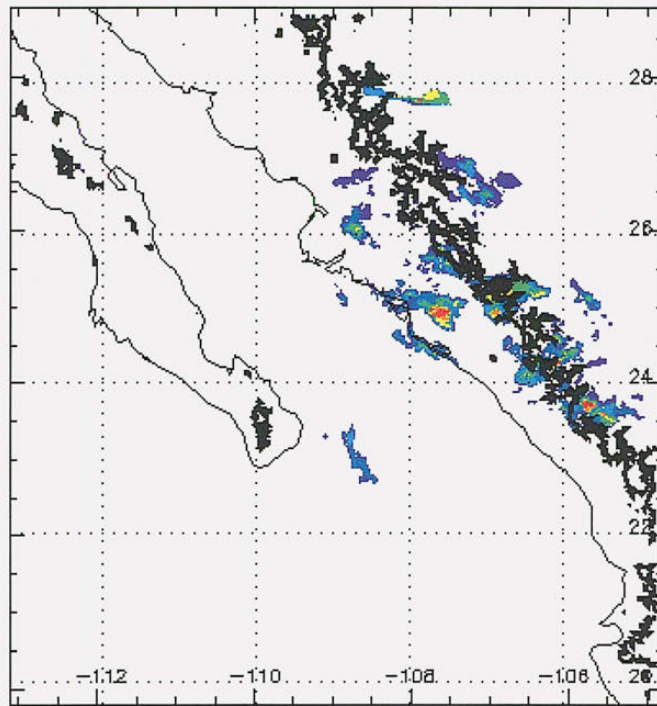


Fig 3.9 - Diurnal hourly variation in a) frequency of occurrence of Type 1 precipitating features, and b) percentage of total (solid line) and convective (dashed line) rainfall generated by Type 1 precipitating features.

Table 3.2 - Mean characteristics of Type 1 precipitating features in the NAME radar composite region.

Characteristic	Mean	Std. Deviation
PF Total area	195 km ²	352 km ²
PF Convective area	48 km ²	82 km ²
PF Convective Area Fraction	33.0%	19.2%
PF Rain rate	2.3 mm h ⁻¹	3.1 mm h ⁻¹
PF Convective Rain Rate	4.4 mm h ⁻¹	6.0 mm h ⁻¹
PF Stratiform Rain Rate	0.9 mm h ⁻¹	0.7 mm h ⁻¹
PF Convective Rain Fraction	57.9%	27.5%

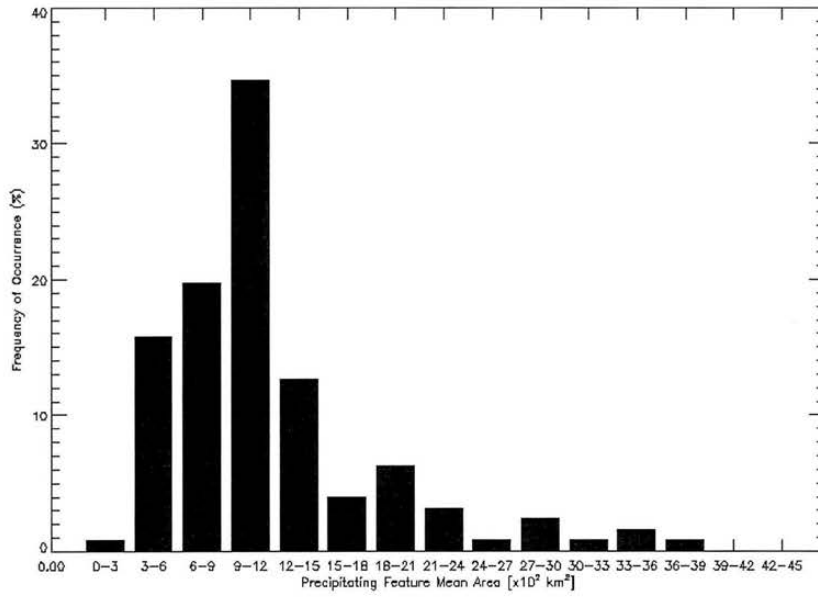


Frequency of Type 2 PF Occurrence (%)



Fig. 3.10 - Map illustrating the geographical variations in frequency of occurrence of Type 2 precipitating features in the NAME radar composite domain. The black thick line delineates the topography above 1000 m.

a)



b)

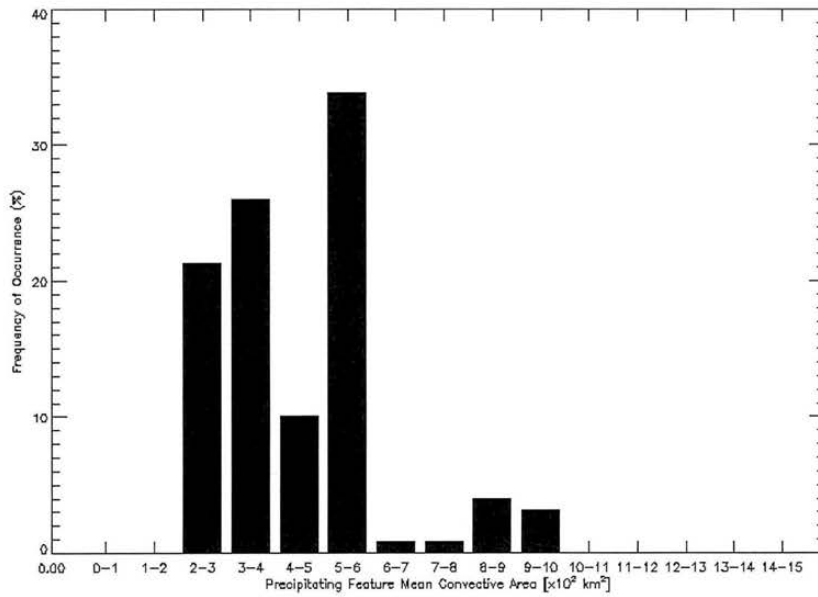
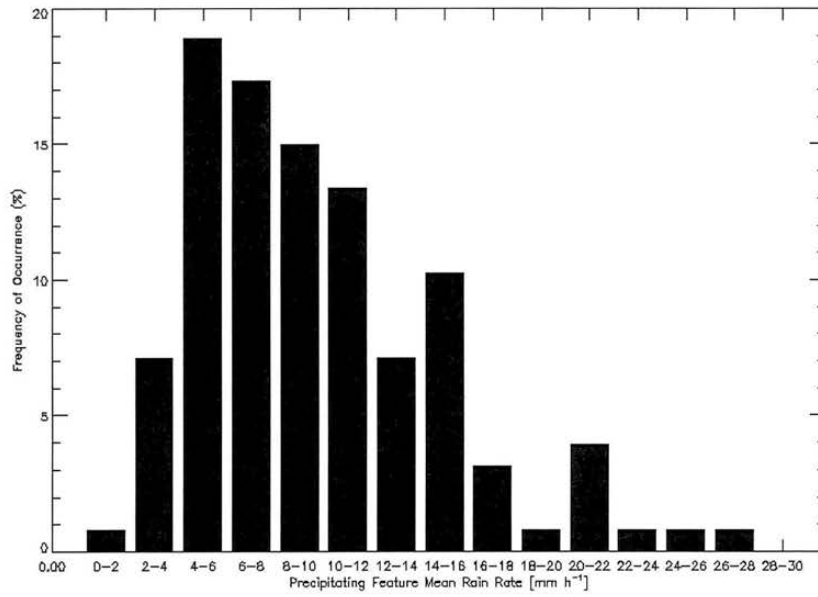


Fig. 3.11. - Distribution of Type 2 Precipitating Feature sizes within the NAME radar composite region; a) feature total area, b) feature convective area.

a)



b)

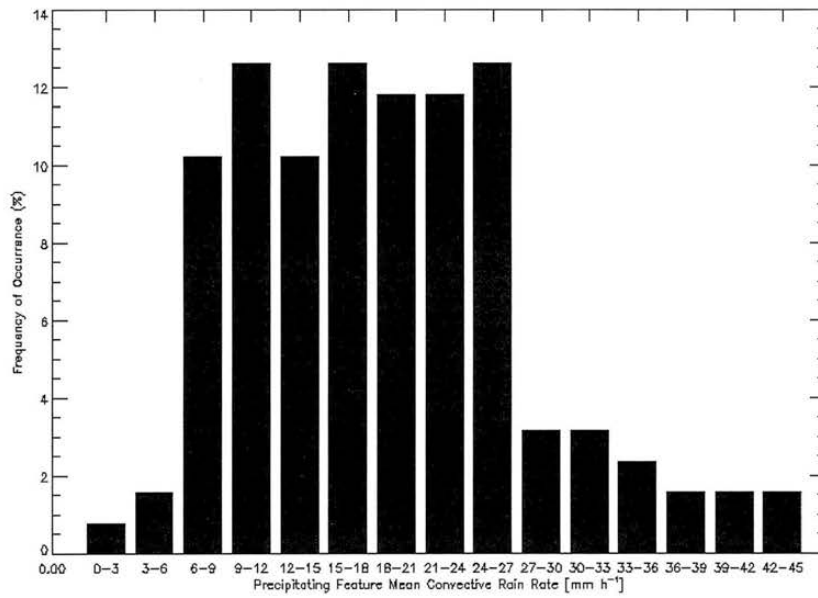
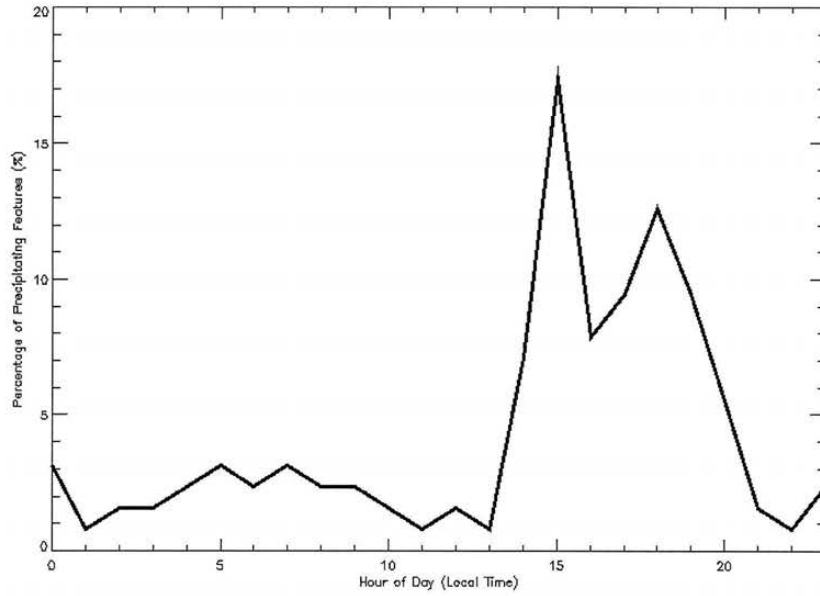


Fig. 3.12 - Distribution of Type 2 Precipitating Feature mean rain rates within the NAME radar composite region; a) feature mean rain rate, b) feature mean convective rain rate.

a)



b)

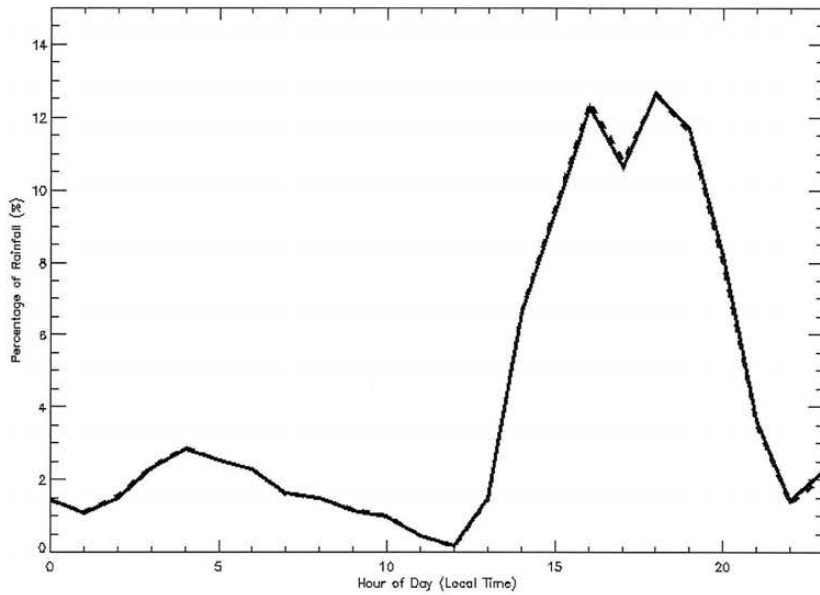


Fig 3.13 - Diurnal hourly variation in a) frequency of occurrence of Type 2 precipitating features, and b) percentage of total (solid line) and convective (dashed line) rainfall generated by Type 2 precipitating features.

Table 3.3 - Mean characteristics of Type 2 precipitating features in the NAME radar composite region.

Characteristic	Mean	Std. Deviation
PF Total area	1,136 km ²	586 km ²
PF Convective area	468 km ²	194 km ²
PF Convective Area Fraction	43.7%	9.3%
PF Rain rate	10.0 mm h ⁻¹	5.3 mm h ⁻¹
PF Convective Rain Rate	20.2 mm h ⁻¹	10.6 mm h ⁻¹
PF Stratiform Rain Rate	2.3 mm h ⁻¹	0.9 mm h ⁻¹
PF Convective Rain Fraction	87.4%	5.9%

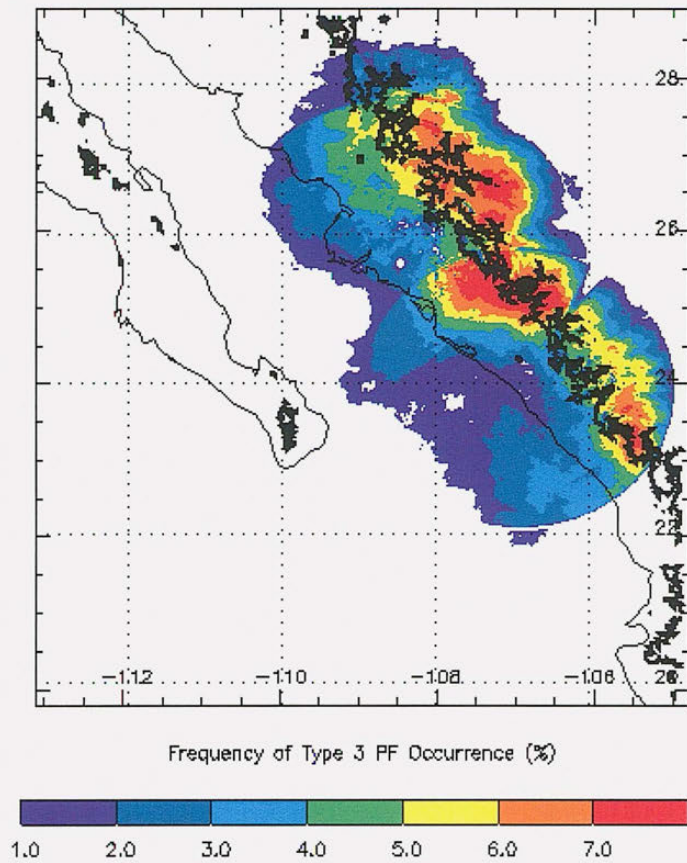
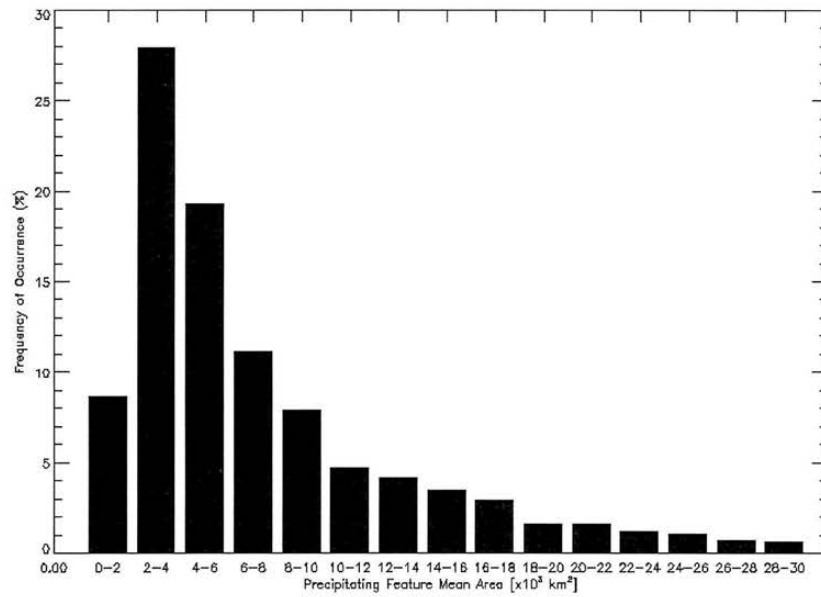


Fig 3.14 - Map illustrating the geographical variations in frequency of occurrence of Type 3 precipitating features in the NAME radar composite domain. The black thick line delineates the topography above 1000 m.

a)



b)

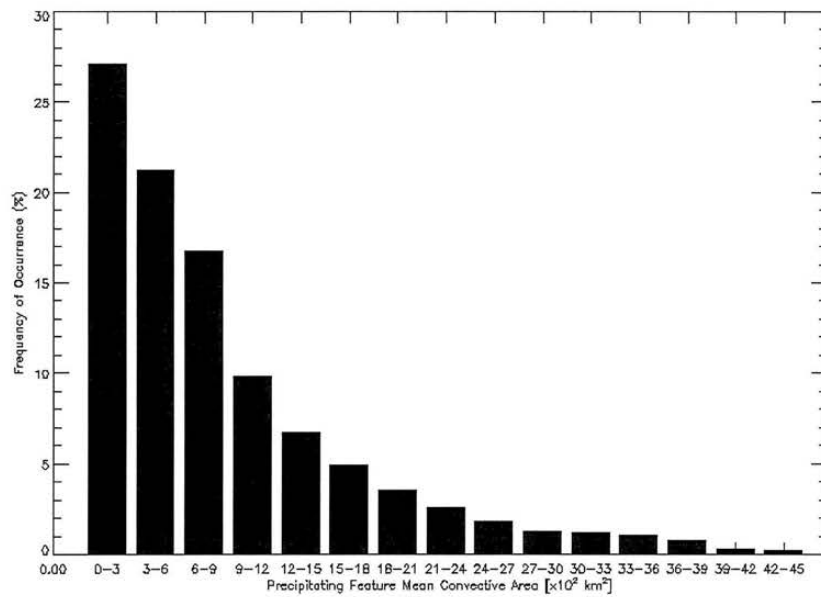
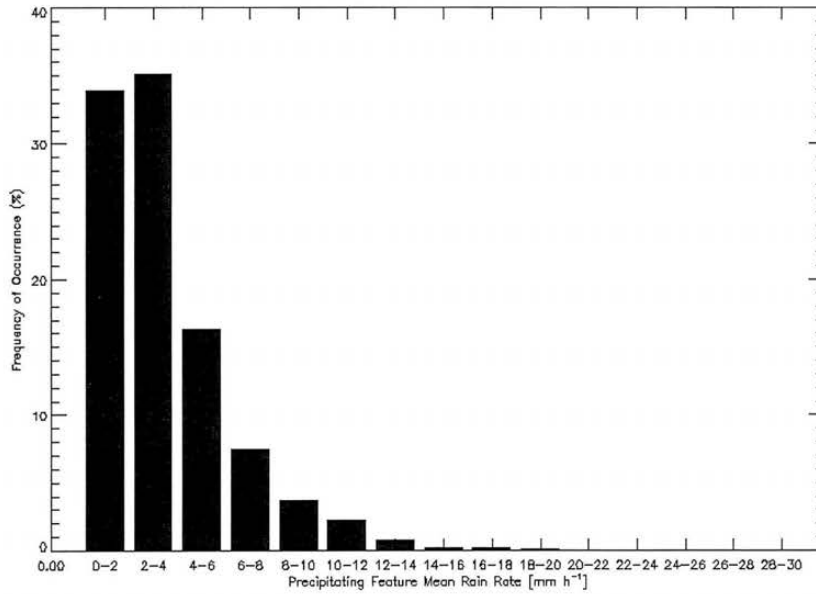


Fig. 3.15 - Distribution of Type 3 Precipitating Feature sizes within the NAME radar composite region; a) feature total area, b) feature convective area.

a)



b)

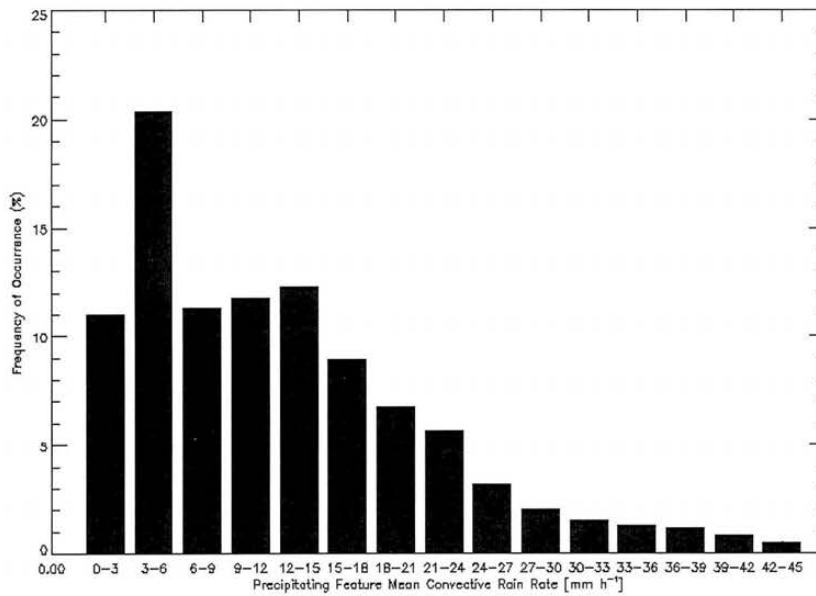
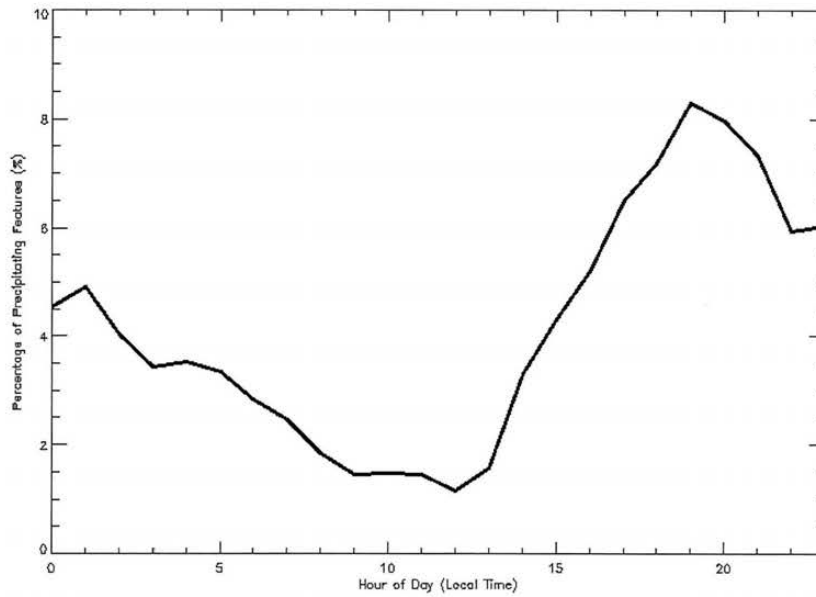


Fig. 3.16 - Distribution of Type 3 Precipitating Feature mean rain rates within the NAME radar composite region; a) feature mean rain rate, b) feature mean convective rain rate.

a)



b)

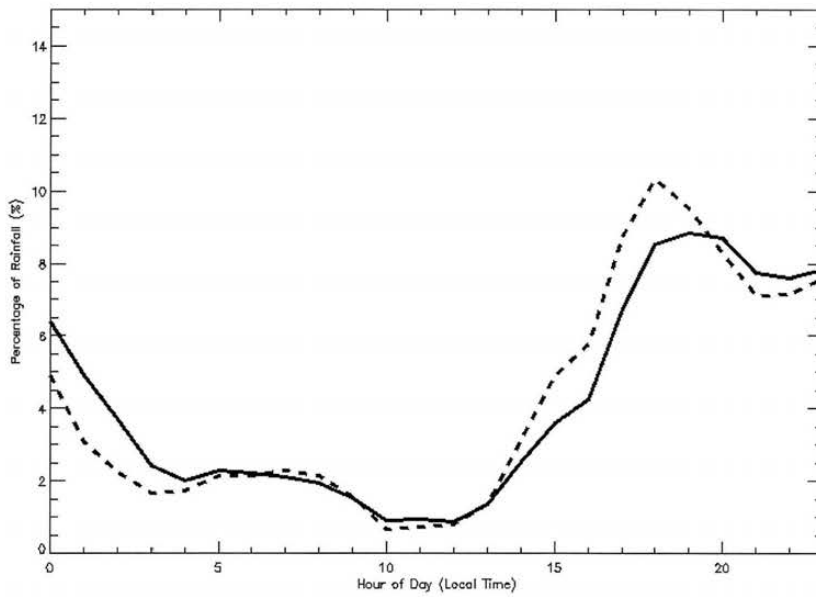


Fig. 3.17 - Diurnal hourly variation in a) frequency of occurrence of Type 3 precipitating features, and b) percentage of total (solid line) and convective (dashed line) rainfall generated by Type 3 precipitating features.

Table 3.4 - Mean characteristics of Type 3 precipitating features in the NAME radar composite region.

Characteristic	Mean	Std. Deviation
PF Total area	8,161 km ²	7,763 km ²
PF Convective area	910 km ²	936 km ²
PF Convective Area Fraction	13.4%	10.1%
PF Rain rate	3.6 mm h ⁻¹	2.7 mm h ⁻¹
PF Convective Rain Rate	13.1 mm h ⁻¹	10.7 mm h ⁻¹
PF Stratiform Rain Rate	1.7 mm h ⁻¹	0.8 mm h ⁻¹
PF Convective Rain Fraction	45.2%	27.3%

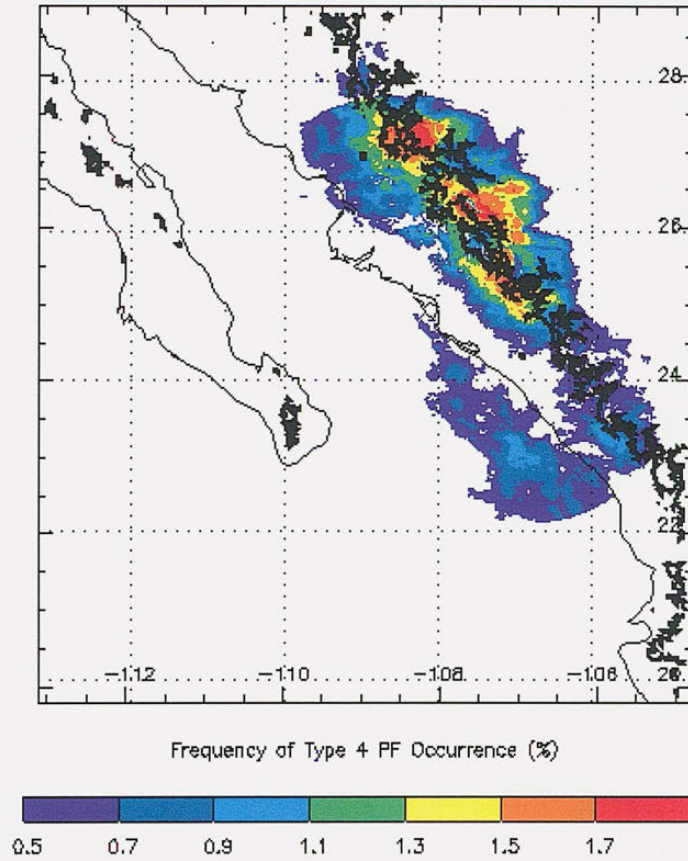
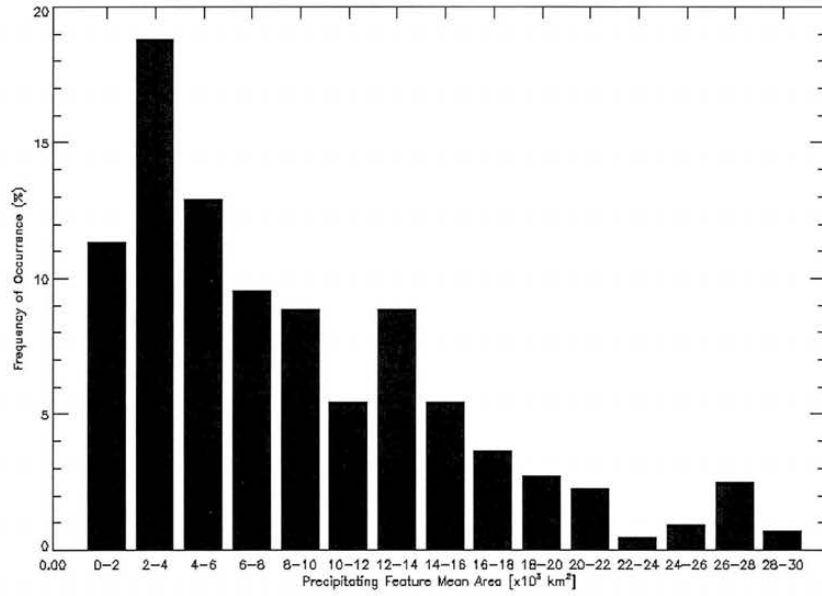


Fig. 3.18 - Map illustrating the geographical variations in frequency of occurrence of Type 4 precipitating features in the NAME radar composite domain. The black thick line delineates the topography above 1000 m.

a)



b)

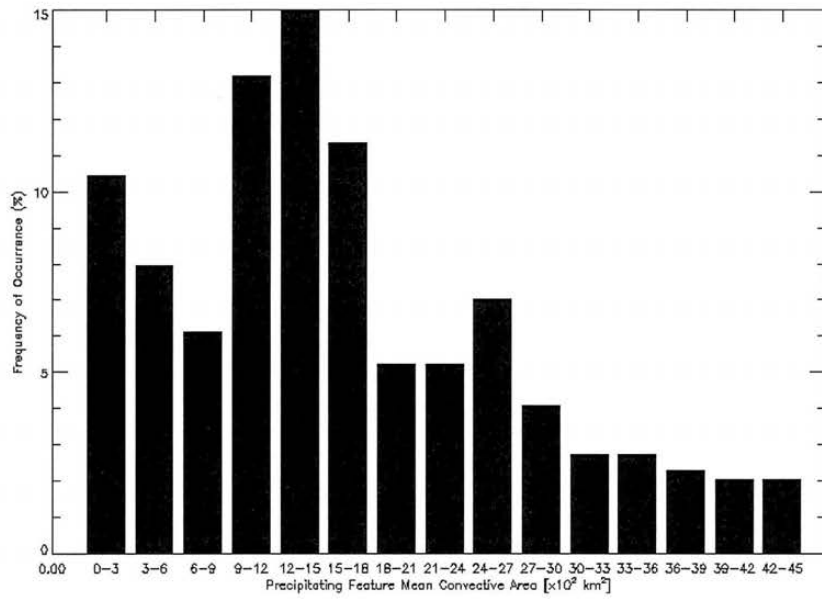
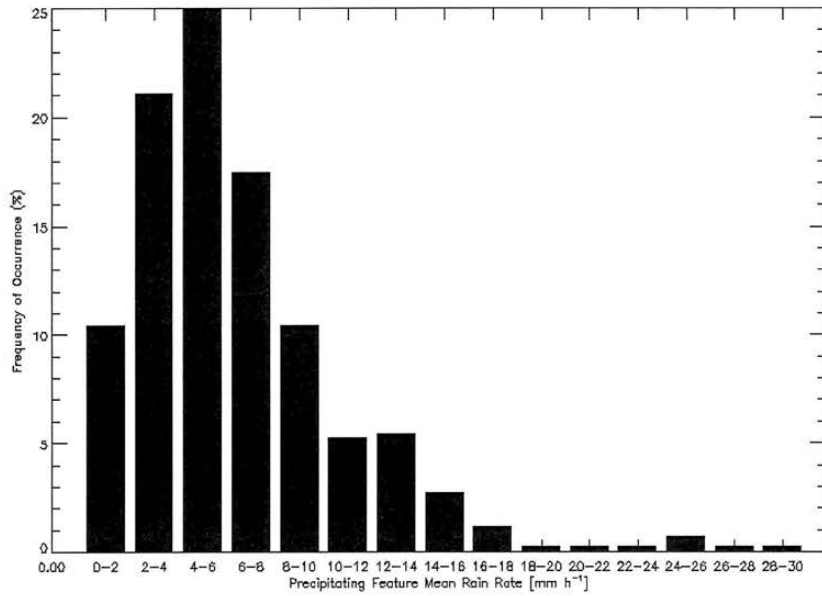


Fig. 3.19 - Distribution of Type 4 Precipitating Feature sizes within the NAME radar composite region; a) feature total area, b) feature convective area.

a)



b)

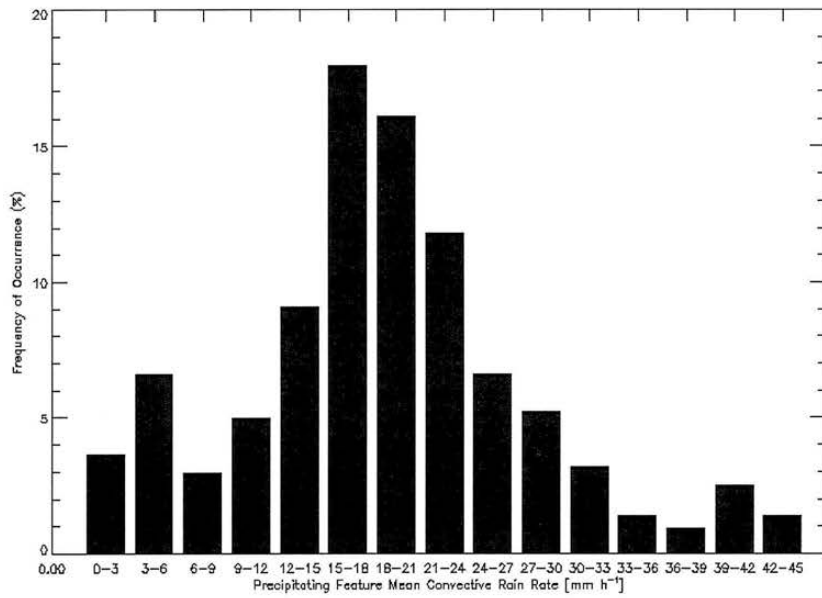
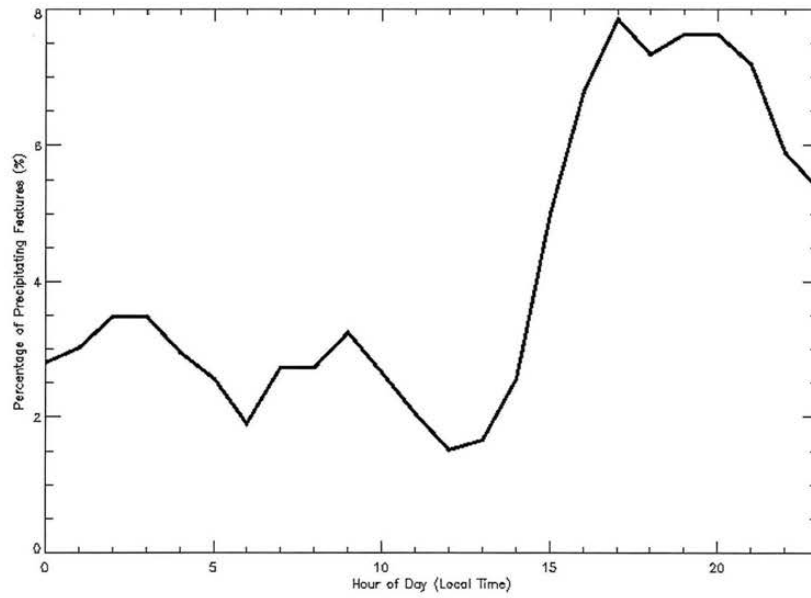


Fig. 3.20 - Distribution of Type 4 Precipitating Feature mean rain rates within the NAME radar composite region; a) feature mean rain rate, b) feature mean convective rain rate.

a)



b)

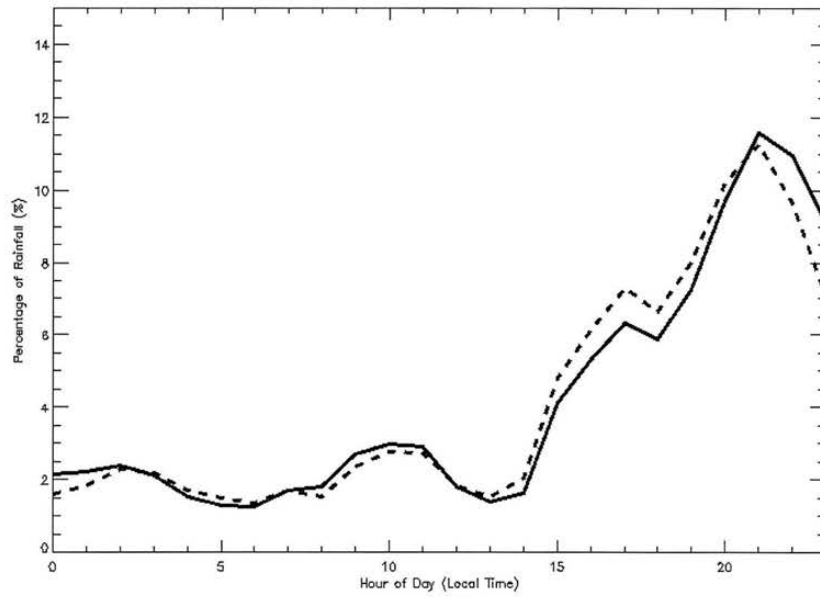


Fig. 3.21 - Diurnal hourly variation in a) frequency of occurrence of Type 4 precipitating features, and b) percentage of total (solid line) and convective (dashed line) rainfall generated by precipitating features.

Table 3.5 - Mean characteristics of Type 4 precipitating features in the NAME radar composite region.

Characteristic	Mean	Std. Deviation
PF Total area	10,494 km ²	9,853 km ²
PF Convective area	1,740 km ²	1,285 km ²
PF Convective Area Fraction	21.7%	13.1%
PF Rain rate	6.3 mm h ⁻¹	4.0 mm h ⁻¹
PF Convective Rain Rate	20.9 mm h ⁻¹	12.5 mm h ⁻¹
PF Stratiform Rain Rate	2.1 mm h ⁻¹	0.8 mm h ⁻¹
PF Convective Rain Fraction	65.8%	23.0%

CHAPTER IV

Thermodynamic & Kinematic Conditions During NAME and Their Relationship to Precipitating Features

4.1 Overview

In this chapter we analyze the variations in number of PFs and rainfall generated by sub-MCS (i.e. Type 1), and MCS (i.e. Types 3 and 4). Then, we compare such variations to the temporal changes in thermodynamic and kinematic conditions in the NAME region. Namely, we are interested in identifying any potential correlations between CAPE, vertical wind shear and PF type and organization. In the first section we examine thermodynamic fields during NAME, and in the following section we examine kinematics. Mean CAPE and vertical wind shear were calculated using the CSU NAME Gridded Analysis. The details of these calculations were explained in Chapter 2, but recall that we made use of 12Z values to assess conditions prior to the regular diurnal onset of convection. The individual components used to calculate CAPE and shear are also examined in order to narrow the potential drivers behind their temporal variation. Sensitivity tests using different times indicated changes only in the magnitude of CAPE,

but no substantial change in the CAPE trend lines shown later in this chapter. Sensitivity of our results to shear depths is discussed at the end of this chapter.

Maps displayed in Chapter 3 indicated that 99% of PFs were concentrated within a narrow region of the domain, hereafter named the Enhanced Convection Area (ECA). As discussed in the previous chapter, this concentration is attributed to the high number of Type 1 PFs in our sample (95%) and their favorable development by orographic lifting and diurnal heating of the land. Most MCSs (i.e. Types 3 and 4) developed as these Type 1 PFs grew into larger systems, so they were also frequently found near the foothills of the SMO as was also noted by Gochis et al. (2007). CAPE and shear were calculated using data points within the ECA only, which is illustrated in Fig. 4.1. The number of PFs and rainfall were added at 24-hour periods starting at 0600 local time each day, and were normalized for temporal variations in the scanned area. Recall from Chapter 2 that due to changes in radar coverage some of our results had to be divided by the total scanned area, including the daily totals in number of PFs and rainfall [see section 2.2.7 for more information]. Our analysis is limited to times when both radar and gridded analysis data were available: 8 July 2004 through 14 August 2004 (Julian Day 190 through 227). In order to provide a more robust statistical significance to our correlations, we have decided to 1) not evaluate Type 2 PFs (i.e. sub-mesoscale linear) due to their very small population; and 2) group all MCS-scale features together (Types 3 and 4) because linear PFs were also rather uncommon (less than 1% of PFs). We did not simply exclude Type 4 PFs (as it was done to Type 2) because they still provided a significant portion of the

rainfall in the region. Therefore, any reference in the text to MCS rainfall or number of features is to be understood as the sum of the rainfall produced by (or the total number of) Type 3 and Type 4 PFs.

4.2 The CAPE Conditions During NAME

In this section we discuss the variations in CAPE, number of PFs and rainfall by organization mode. The CAPE and PF trends shown in the plots discussed in this section were smoothed using a three-day moving average.

First, we examine the temporal variability in the number of Type 1 PFs in the NAME composite region, as shown by the dashed line in Fig. 4.2. It shows that there are two maxima periods in the number of Type 1 PFs, the first on Julian Day 195, and the second on Julian Day 217. The minima in number of Type 1 PFs occurred at the beginning and end of the period examined here, as well as around JD 207. The solid line in Fig. 4.2 depicts the temporal variations in CAPE within the ECA. It is evident that the environment within the ECA undergoes alternating periods of increasing CAPE and decreasing CAPE. While localized areas of CAPE exceeding 3000 J kg^{-1} were observed in a few occasions, CAPE values averaged within the entire ECA produced peaks of approximately 1200 J kg^{-1} . The more prominent peaks occurred on Julian Days 192, 201-203, 209 and 217. Low CAPE values of approximately 500 J kg^{-1} took place on Julian Days 195, 206 and 214. The solid and dashed lines of Fig. 4.2 are not very well correlated. Fig. 4.3 is analogous to Fig. 4.2, except that the dashed line indicates the

relative number of MCSs. The lines in Fig. 4.3 show a better correlation, although JD 208 shows a maximum in CAPE, while the number of MCSs was at a minimum. As it will be discussed in the next section, there are other factors controlling the frequency of occurrence of MCSs, such as wind shear (and wind shear was at a minimum on JD 208).

The dashed line in Fig. 4.4 depicts the rainfall generated by Type 1 PFs. It indicates that the temporal variation in Type 1 rainfall is less pronounced than the number of PFs (shown in Fig. 4.2). Another noticeable feature in this figure is that the peaks in rainfall occurred in closer proximity to peaks in CAPE compared to the number of PFs. Fig. 4.5 is analogous to the previous one, but the dashed line illustrates the rainfall produced by MCSs. In this figure, as in Fig. 4.4, we observe that trends in CAPE are closely matched by trends in MCS rainfall, but there are a few noteworthy differences. First we observe sharper decreases in mesoscale PF rainfall following the peaks in CAPE. There is also a rather sizable peak in mesoscale PF rainfall around Julian Day 202-203. No apparent trends in rainfall are observed in association with the third CAPE peak (Julian Day 209), which is the period when the number of MCSs (and wind shear) was very low. Rainfall produced by mesoscale PFs substantially increased starting on Julian Day 207 and also peaked on Julian Day 217, when CAPE was higher than average. It is interesting to note that while all peaks in CAPE were not matched by peaks in MCS rainfall, the peaks in MCS rainfall that did take place in this period occurred when CAPE was higher than average (i.e. 750 J kg^{-1}). However, the absolute magnitude of CAPE cannot be directly correlated to specific values of rainfall.

It is interesting to compare Figs. 4.2 through Fig. 4.5 to identify the relationships between number of PFs and corresponding rainfall. First, it is evident that the Type 1 rainfall peaks do not exactly match the number of Type 1 PFs, but rather occur approximately a day before the peaks in number of Type 1 PFs. The reason for this lag is that total rainfall is controlled by the number of PFs and how much rain each one is producing. The latter factor is controlled either by more intense rain rates or larger precipitating areas. Fig. 4.6 shows that in most instances, the relatively smaller number of Type 1 PFs was compensated by the presence of a few larger Type 1 PFs that generated more substantial precipitation and contributed to a daily peak in rainfall by that organizational group. Another interesting feature is that the daily number of Type 1 PFs appeared to undergo more pronounced changes than the actual rainfall generated by this group (Figs. 4.2 and 4.4), whereas the opposite may be said about MCSs (Figs. 4.3 and 4.5). Fig. 4.7 shows the convective inhibition (CIN) time series within NAME's ECA and it indicates that stronger convection inhibition was present around JD 215-220. It is important to stress that CIN was calculated at 12Z, when the strongest capping is typically present. CIN values typically decrease as surface temperatures progressively increased through the morning hours until the convective temperature is achieved. Lifting in the region is also enhanced by the local topography, which aids surface air parcels in breaking through any remaining capping present in the early afternoon hours. Table 4.1 summarizes the mean CAPE and CIN conditions found within the ECA during the period of our analysis.

4.3 The Shear Environment During NAME

In this section we discuss the variations in vertical wind shear, number of PFs and rainfall by organization mode. The wind shear trends shown in the plots discussed in this section, as well as the trends in number of PFs and rainfall, were also smoothed using a three-day moving average.

We first examine the temporal fluctuations in the solid line of Fig. 4.8, which depicts the vertical wind shear within the ECA. Recall from Chapter 2, that shear was calculated over a depth of 6 km AGL. Sensitivity tests using variable shear depths are discussed later in this chapter. It indicates that the period of our analysis was characterized by two main cycles of shear increase and decrease and one minor peak. The two major peaks in vertical wind shear, both of approximately 8.5 m s^{-1} , occurred around JD 202 and JD 219. The minor peak in vertical wind shear had a magnitude of approximately 5 m s^{-1} and occurred on JD 211 and JD 212.

The dashed lines in Figs. 4.8-4.11 are identical, respectively, to those shown in Figs. 4.2-4.5 and both display the temporal variability in the number of PFs or rainfall by Type 1 PFs or MCSs. At first, a simple comparison of the dashed and solid lines in Fig. 4.8 reveals little resemblance between the two lines, particularly the absence of a major increase in PFs around JD 202 and the decrease in number of PFs after JD 195 while the vertical shear steadily increased. As expected, shear is not a controlling factor in the development of Type 1 PFs. Fig. 4.9 presents a better match between the dashed and

solid lines. The number of MCS PFs seems to follow the general trend line of shear, although it obviously not the only factor modulating the number of MCSs, since their numbers decreased around JD 195 when shear was increasing. It is possible that the synoptic scale atmospheric dynamics were unfavorable (e.g. subsidence) around that period.

Fig. 4.10 depicts the rainfall generated by Type 1 PFs. It indicates that the temporal variation in Type 1 rainfall is less pronounced than the number of PFs (shown in Fig. 4.8). Type 1 rainfall quickly increases at the beginning of our data period and maintains a steady value until just after the first major peak in wind shear (i.e. JD 202), when it decreases substantially. This reduction is likely caused by the lower CAPE values shown in Fig. 4.4, which (as it will be discussed in section 4.4) was largely caused by the lower surface temperatures observed around JD 205 in the region. Soon after this reduction, Type 1 rainfall steadily increased again until reaching a peak again on JD 221.

Fig. 4.11 is analogous to the previous one, but now we compare the wind shear to the rainfall generated by MCSs (dashed line). In this figure, while we observe that trends in shear do not exactly match trends in mesoscale PF rainfall, there is a striking pattern between the two variables. The rainfall produced by MCSs undergoes more frequent cycles than the wind shear, but the two peaks in wind shear are closely matched by the two strongest peaks in rainfall generated by mesoscale PFs. The pronounced reduction in wind shear after JD 202 is also followed by a sharp decrease in MCS rainfall. The linear correlation between these two variables provides is 0.63. Additionally, a partial linear

correlation is calculated by excluding the period between JD 197 and 200, our result increases to 0.75. Despite the favorable wind shear in that period, it is likely that MCS rainfall was suppressed on those dates due to other controlling factors, such as large-scale subsidence and the modest CAPE values observed around that time. The mean 0-6 km shear within the NAME ECA during the period of our analysis is presented in Table 4.2

After examining all the figures shown so far in this chapter, it is clear that some correlations between environmental conditions and PF number or rainfall do not show as well as others. Nonetheless, one would not expect 100% of the variability of PF numbers and rainfall to be explained by a single variable. By combining information from CAPE, wind shear, and the synoptic forcing present at the time over the NAME ECA, it is possible to understand the factors modulating the variability of rainfall in the region. The best correlation found here was between MCS rainfall and wind shear. However, periods of enhanced MCS rainfall only took place when both, CAPE and shear were higher. This result is consistent with studies of heavy rain events generated by MCSs during TOGA-COARE (Lucas and Zipser, 2000). They found that these events took place during periods of favorable thermodynamic conditions, namely a moist atmosphere at mid-levels and modest amounts of CAPE. They also stated that “it is not enough to simply look at thermodynamic properties of the environment to accurately predict the amount of rainfall. The kinematic properties also play an important role in determining MCS properties”. They found that the most favorable environments for heavy rainfall from MCSs occur

when there was a modest amount of deep tropospheric shear. Hence, in the next chapter we will examine the synoptic conditions that led to the two main peaks in wind shear discussed here.

4.4 CAPE components

The thermodynamic conditions discussed earlier in this chapter are a function of changes in the temperature and humidity profiles of the atmosphere within the ECA. Therefore, in order to better understand the sources of this variability we now examine the relationship between CAPE and changes in the atmospheric conditions near the surface.

Fig. 4.12 shows the same CAPE plot presented in the previous chapter, but with temperature overplotted in the same figure. In Fig. 4.12 we observe that there is a somewhat coherent pattern in variability of temperature and CAPE. The highest surface temperature occurred around JD 201, which was concurrent with one of the CAPE peaks. While the absolute magnitude of the 12Z temperature was not directly proportional to CAPE, increases (decreases) in 12Z temperature are associated with increases (decreases) in CAPE. The only notable exception to this trend was the CAPE peak that occurred on JD 209, when marked temperature swings were absent.

Surface mixing ratio is examined in Fig. 4.13, which shows that several of the up and down cycles in the CAPE are also a reflection of the increase and decrease cycles in surface mixing ratio within the ECA. The only noteworthy exception to this pattern is the CAPE peak on JD 209. Furthermore, the two main peaks in mixing ratio, of

approximately 15 g kg^{-1} (JD 201 and 219), not only match peaks in CAPE, but also the two main peaks in wind shear.

The temporal variability of temperature above the surface is examined in Fig. 4.14. It is clear that the lower levels, shown in Fig. 4.14a, undergo a higher number of cycles, likely due to its proximity to surface forcing mechanisms (e.g. clouds, precipitation, and radiation). In Fig. 4.14b, we observe that there is only one clear cycle in temperature at 4 km (solid line) with a minimum temperature on JD 196 and a maximum on JD 202. In Fig. 4.14c, there are few and not much pronounced changes in temperature at 5 and 6 km. The only obvious trend, clearly seen in the solid line (6 km), is the steady increase in temperature through most of the analyzed period, which is probably associated with the seasonal net gain in radiation over the summer and the continent heating associated with monsoonal rain.

4.5 Shear components

As indicated in Eq. 2.6, the wind shear results presented in the previous chapter result from the summation of the zonal and meridional components of the shear. Each component is calculated based on the difference between the mean zonal (or meridional) wind in the lowest 500 meters and the mean zonal (or meridional) wind at 6 km AGL.

Fig. 4.15 shows the breakdown between zonal and meridional components of the wind shear. The total wind shear, illustrated by the thick solid line, is the same presented in plots 4.7-4.10. Again, two episodes of stronger shear are observed during the NAME

EOP, the first around JD 202 and the second near JD 219. In Fig. 4.15 we learn that the main driver behind these wind shear peaks comes from the zonal component (dashed line), which has a temporal variability that resembles that of the total wind shear. The meridional component is somewhat more erratic in the first half of the analyzed period, which coincides with the first peak of total shear, while the second half shows less temporal variability than the zonal counterpart.

We can further examine the source of this shear by looking into the two sub-components that make up the zonal wind shear: the mean surface wind (lowest 500 m) and the mean wind at 6 km AGL. This breakdown analysis is displayed in Figs. 4.16 and 4.16. The wind shear is greatest when the thin solid line (surface wind) and the dashed line (6-km wind) are farther apart from each other because the wind shear is calculated from the difference between these two components. Fig. 4.16 indicates that the ECA generally had light easterly winds from at surface and mid-levels throughout the analyzed period. This result is in agreement with Johnson et al. (2007) and the observed position of the anticyclone over Mexico during the NAME EOP. It is also evident from Fig. 4.16 that the mean low-level zonal wind (thin solid line) within the ECA is far less variable than the mean 6-km zonal wind (dashed line). The peaks in zonal wind shear occurred when the 6-km average wind had stronger easterly magnitudes. Therefore, it appears that the high wind shear peaks are associated with episodes of stronger upper-level easterly winds. Fig. 4.17 is similar to 4.16, but looks into the breakdown of meridional wind shear. The magnitudes of low-level and 6-km average meridional winds are less than those observed for zonal winds. Additionally, the meridional wind direction alternates between northerly and southerly. Moreover, there is no consistent pattern between the

meridional wind shear and its components.

4.6 Shear Depth Sensitivity

In this section, we address the sensitivity of our results to the depth over which wind shear is calculated. In Chapter Two, we discussed how wind shear is calculated. Here we present and discuss the results of wind shear calculated over twelve different depths. The depths chosen to be analyzed here were primarily based on previous studies regarding MCS formation and development. Recall that the shear results presented previously in this chapter were based on wind shear over a 0-6 km layer above ground level. We examine how shear varies for different depths above ground level, above mean sea level, and between standard pressure levels.

Fig. 4.18 shows the results for wind shear calculated over four different depths above ground level (AGL): 0-6 km, 0-5 km, 0-3 km, and 0-1 km. It is evident that results from 0-6 km and 0-5 km are practically identical. Both of these curves peak between 8 and 9 m s^{-1} on JD 202 and 219, and possess a minimum of 3 m s^{-1} on JD 208. The 0-6 km and 0-5 km wind shear provided the best correlations (to be discussed later) to MCS rainfall during NAME. Jirak and Cotton (2007) found the skill of 0-3 km and 0-6 km AGL wind shear to be very similar in predicting MCSs in the United States. For 0-6 km AGL shear they found a Probability of Detection, False Alarm Ratio, and Heidke Skill Score (Wilks 1995) of, respectively, 0.70, 0.29 and 0.35. Weisman and Rotunno (2004) also found a similar skill in MCS prediction using 0-5 km and 0-2.5 km shear. Lucas and Zipser (2000) also found that MCSs were more likely during TOGA COARE when the difference between zonal winds at low and upper levels was at least moderate (~ 10 m

s⁻¹). Our results showed a lower correlation between MCS rainfall and shallower depths. The overall shape of our results for 0-3 km AGL shear is somewhat similar to 0-6 km AGL shear, although the magnitude is generally smaller. Lastly, 0-1 km AGL did not undergo very pronounced changes in value during the period examined here.

Fig. 4.19 is similar to the previous one, except that the 0-6 km, 0-5 km, 0-3 km, and 0-1 km depths are calculated to a maximum height above mean sea level (MSL). Once again we find a remarkable resemblance between the 0-6 km AGL wind shear depth used in this study (blue line) and the results obtained for a depth of 0-6 MSL and 0-5 km MSL. As it was discussed previously, the bulk of wind shear variations during NAME occurred due to changes in zonal wind speeds aloft. Significant differences between AGL and MSL at these larger depths are small likely due to the fact that at 6 and 5 km MSL all points within the ECA are above the top peaks of the SMO. In contrast, shear calculated over the shallower depths of 0-3 km MSL and 0-1 km MSL do not undergo pronounced changes in wind shear value. Since the SMO extends to up to 3 km MSL, the upper-air flow is obstructed and lighter wind speeds are more likely controlled by mesoscale circulations (e.g. land and sea breezes, mountain and valley breezes) and local convection rather than the synoptic-scale environmental variability which is the focus of this study.

In Fig. 4.20 we examine a few shear depths calculated between pressure levels: 800-400 mb, 950-700 mb, and 1000-800 mb. Shear between these pressure levels were used by LeMone et al. (1998) and by Alexander and Young (1992) to evaluate linear MCSs and their orientation. Wind shear between 800-400 mb matches fairly well to the shear used in this study. Since wind shear between 0-6 km AGL and 0-6 km MSL did not

show significant differences, a match to 800-400 mb wind shear is expected because 400 mb is typically found at 7.6 MSL. However, shear over 1000-800 mb and 950-700 mb did not match as well, especially in the latter half of the period examined here. Again, this is likely a result of this layer been mostly confined below the tops of the SMO.

Furthermore, we also assessed the 5-10 km AGL wind shear. Coniglio et al. (2004) found that when moderate values of 0-5 km AGL shear were present, the presence of moderate (i.e. 5-15 m s⁻¹) values of wind shear between 5-10 km AGL were the most conducive for producing large vertical air displacements, which led to larger, longer-lived, more prolific rain-producing MCSs. Jirak and Cotton (2007) did not compute the likelihood of MCS development when 5-10 km wind shear exceeded 20 m s⁻¹, arguing that stronger shear limited parcel overturning and made the atmosphere less conducive for MCSs. Fig. 4.21 shows the mean 5-10 km AGL wind shear within the NAME ECA. It is clear that shear between these layers always varied between 5-15 m s⁻¹. Thus, strong upper-level shear does not appear to have suppressed MCS activity, although it is interesting to point that the peaks in MCS rainfall occurred when wind shear between 5-10 km AGL was less than 10 m s⁻¹. Lastly, Table 4.3 lists the linear correlation between daily MCS rainfall within the NAME ECA and the mean wind shear within the NAME ECA. It is clear that a better correlation is obtained using larger shear depths, especially 0-5 km and 0-6 km. AGL. These correlations corroborate our preference for using wind shear over 0-6 km AGL in this study to understand the variability of MCS rainfall. These results are in agreement with the findings of Weisman and Rotunno (2004) and Jirak and Cotton (2007) who found, respectively, that wind shear over 0-5 km AGL and 0-6 km AGL had a good skill in predicting MCSs.

Finally, we briefly examined the relationship between low-level shear and address the occurrence of Type 4 PFs (linear MCSs). Alexander and Young (1992) found that shear between 1000-800 mb was well correlated with this type of organizational mode and a higher incidence of linear MCSs when this wind shear exceeded 4 m s^{-1} . Correlations between all wind shear depths discussed in this section and Type 4 rainfall were calculated and the best results were also obtained for wind shear between 1000-800 mb. Figure 4.22 shows the mean daily rainfall produced by Type 4 PFs and 1000-800 mb wind shear. Nonetheless, our results yielded only a modest statistical linear correlation of 0.39. It is likely that a better correlation between synoptic-scale low-level shear and linear organization is limited by the presence of complex terrain in the NAME domain. Previous studies were made over regions where the surface was generally flat, such as the ocean during TOGA-COARE. Fig. 3.18 showed that Type 4 PFs frequently formed near the foothills of the SMO. Hence, linear organization may be favored not only by the pre-storm synoptic-scale, low-level shear environment, but also by the direction a storm and its downdraft are moving relative to the orientation of the local terrain after the convection has formed. Lastly, it is important to stress that our results present Type 4 PFs in a climatological perspective rather than specific events. Therefore, the shear values presented here are mean values calculated over the entire ECA at 12Z, so these individual local interactions there may be other low-level wind interactions that are not resolved at the temporal and horizontal scale analyzed in our study.

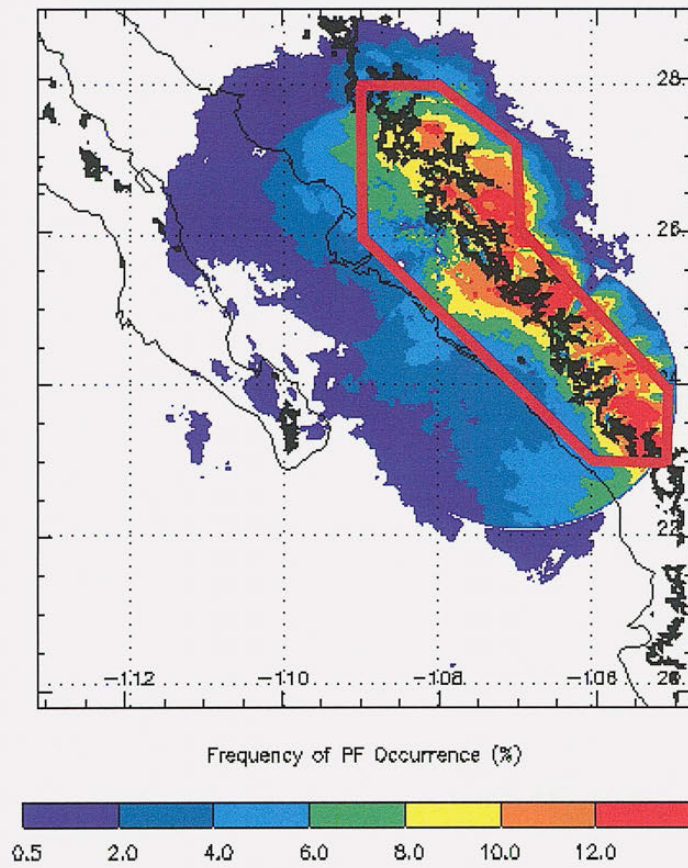


Fig. 4.1 - Same as Fig. 3.1, but with a red box overlaid on the map indicating the Enhanced Convection Area.

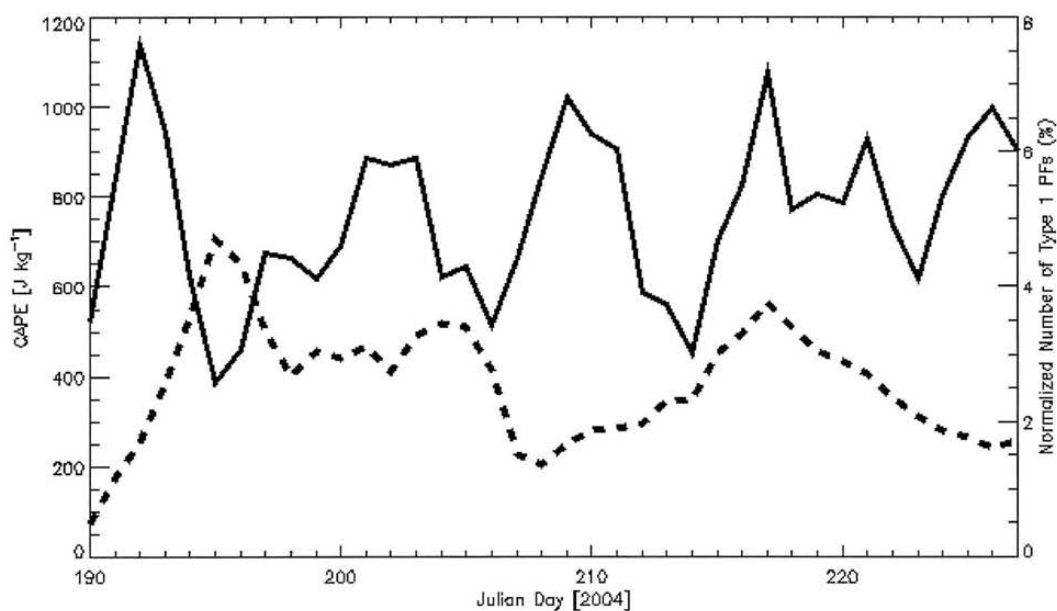


Fig. 4.2 - Three-day moving average of daily mean CAPE within the Enhanced Convection Area of NAME (solid line), and three-day moving average of the daily number of Type 1 PFs during NAME (dashed line), shown as a percentage of total number of Type 1 PFs in the entire period.

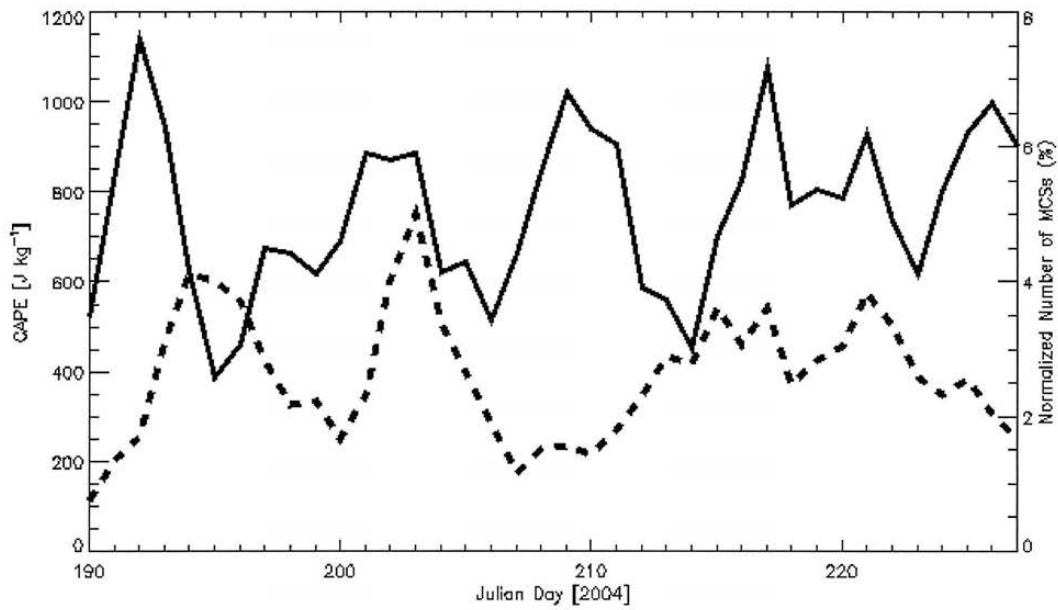


Fig 4.3 - Three-day moving average of daily mean CAPE within the Enhanced Convection Area of NAME (solid line), and three-day moving average of the daily number of MCSs during NAME (dashed line), shown as a percentage of total number of MCSs in the entire period.

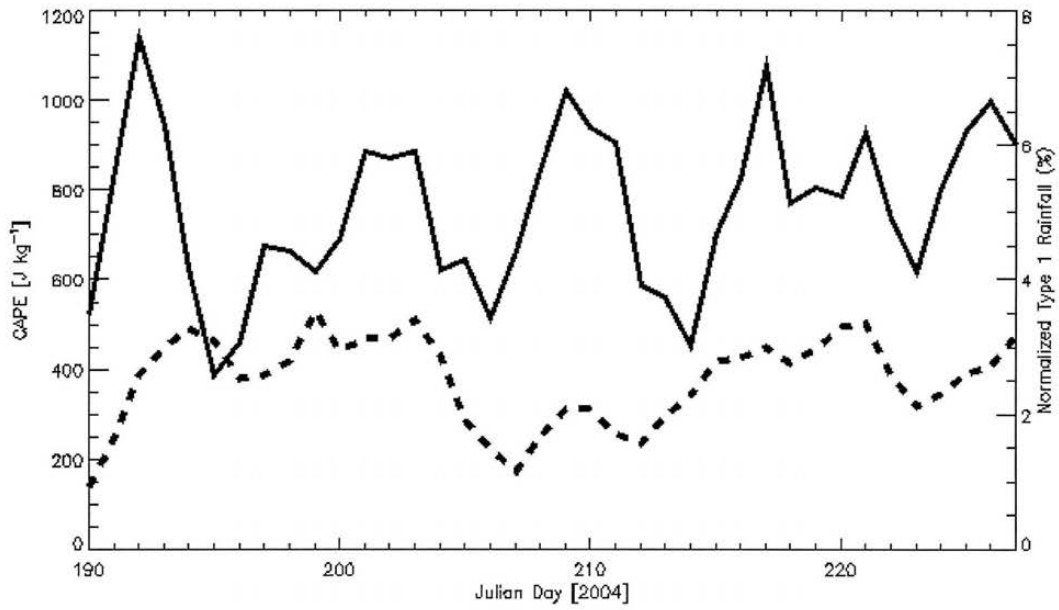


Fig 4.4 - Three-day moving average of daily mean CAPE within the Enhanced Convection Area of NAME (solid line), and three-day moving average of the daily rainfall (as a percentage of rainfall in the entire period) generated by Type 1 PFs during NAME (dashed line).

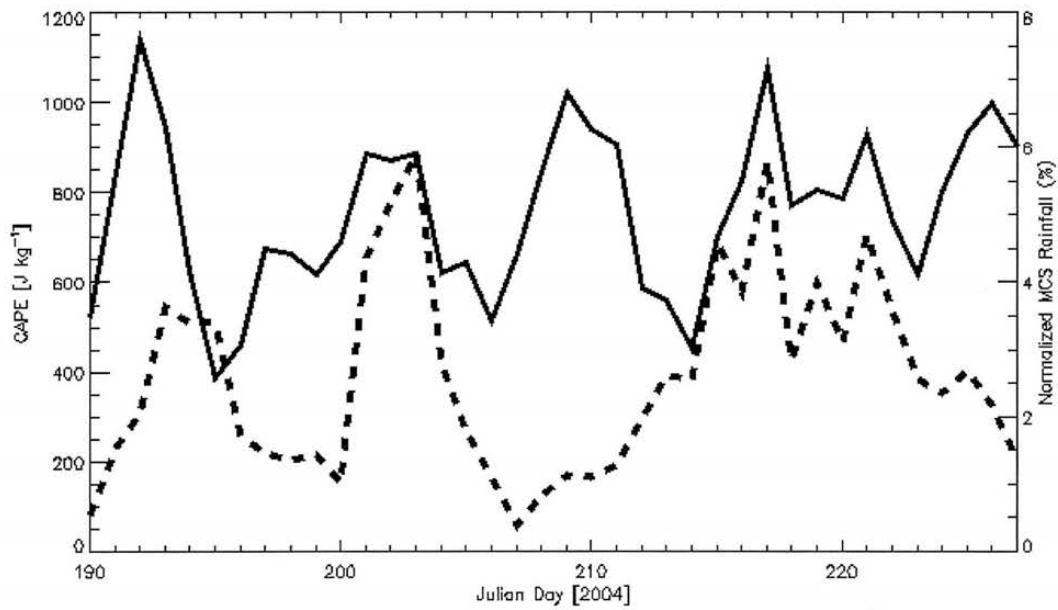


Fig 4.5 - Three-day moving average of daily mean CAPE within the Enhanced Convection Area of NAME (solid line), and three-day moving average of the daily rainfall (as a percentage of rainfall in the entire period) generated by MCSs during NAME (dashed line).

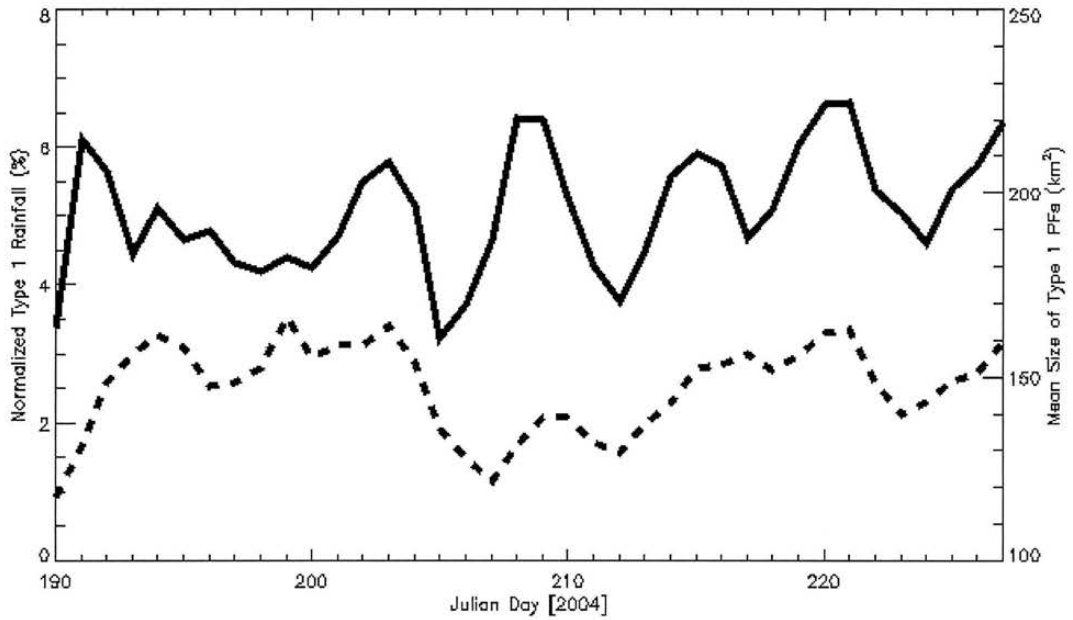


Fig 4.6 - Three-day moving average of daily mean size of Type 1 PFs within the Enhanced Convection Area of NAME (solid line), and three-day moving average of the daily rainfall (as a percentage of rainfall in the entire period) generated by Type 1 PFs during NAME (dashed line).

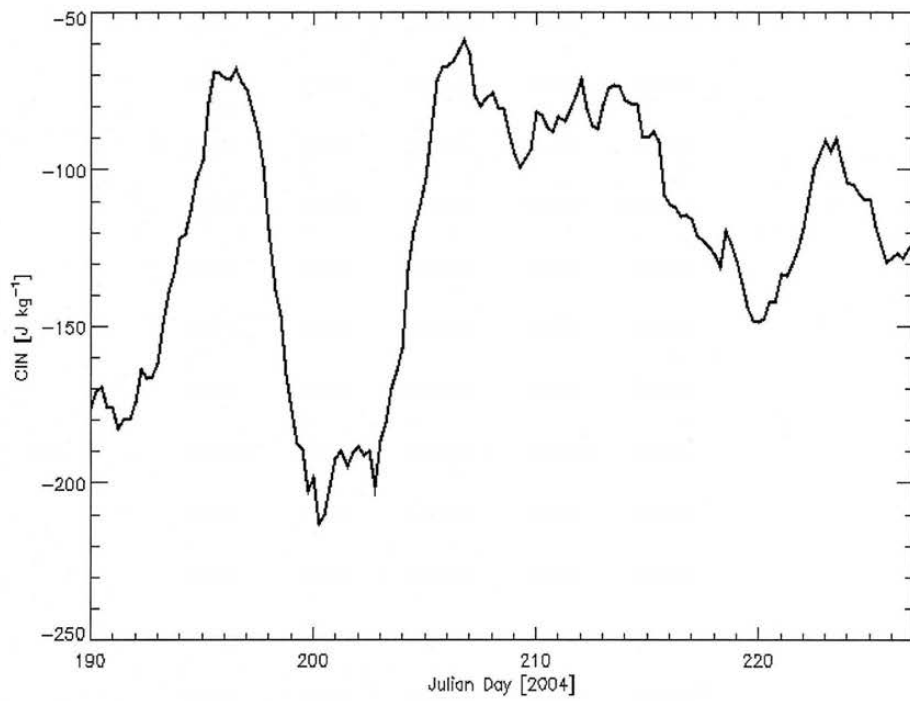


Fig 4.7 - Three-day moving average of mean Convection Inhibition (CIN) within the Enhanced Convection Area of NAME.

Table 4.1 - Thermodynamic characteristics at 12Z within the NAME Enhanced Convection Area.

Characteristic	Mean	Std. Deviation
CAPE	750 J kg ⁻¹	352 J kg ⁻¹
CIN	-122 J kg ⁻¹	66 J kg ⁻¹

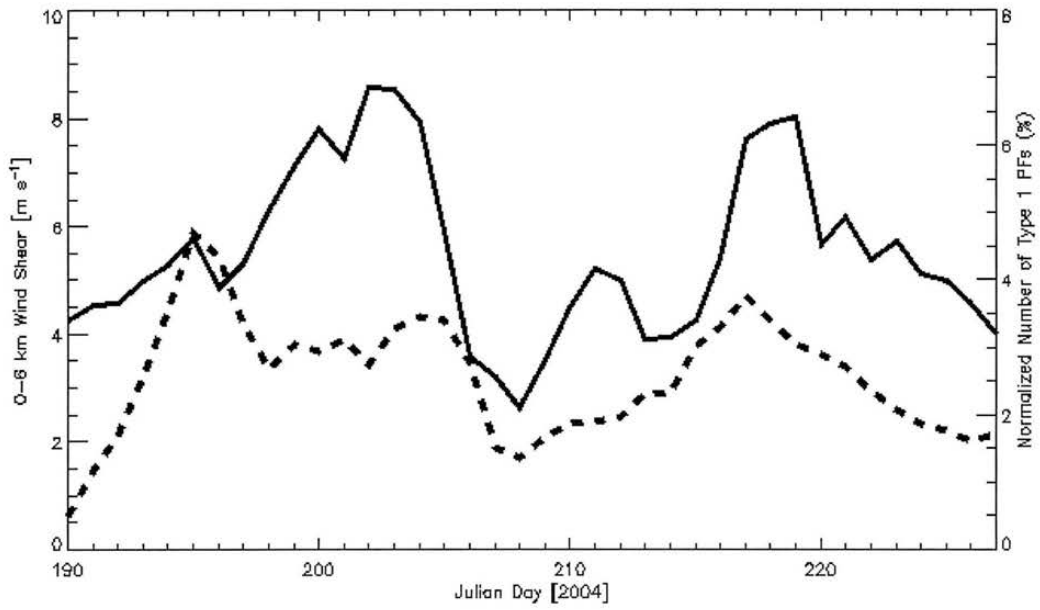


Fig. 4.8 - Three-day moving average of daily mean 0-6 km wind shear within the Enhanced Convection Area of NAME (solid line), and three-day moving average of the daily number of Type 1 PFs during NAME (dashed line), shown as a percentage of total number of Type 1 PFs in the entire period.

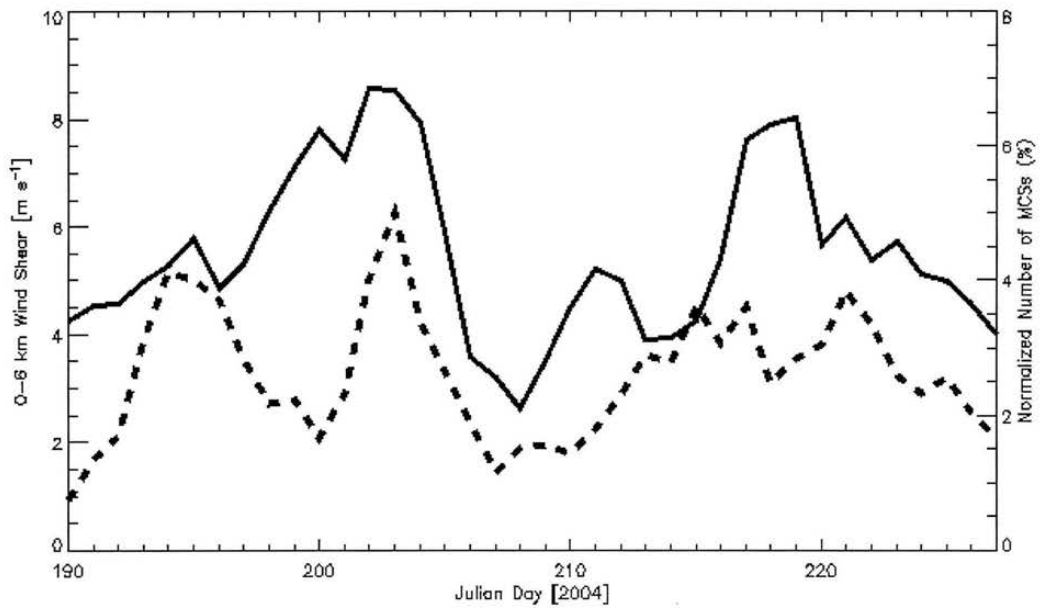


Fig. 4.9 - Three-day moving average of daily mean 0-6 km wind shear within the Enhanced Convection Area of NAME (solid line), and three-day moving average of the daily number of MCSs during NAME (dashed line), shown as a percentage of total number of MCSs in the entire period.

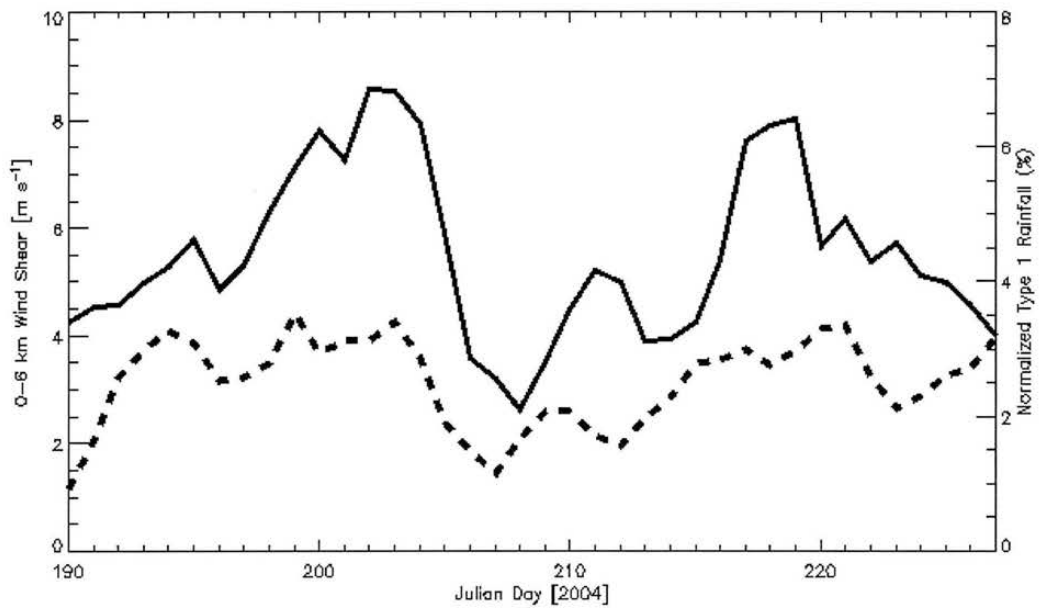


Fig. 4.10 - Three-day moving average of daily mean 0-6 km wind shear within the Enhanced Convection Area of NAME (solid line), and three-day moving average of the daily rainfall (as a percentage of rainfall in the entire period) generated by Type 1 PFs during NAME (dashed line).

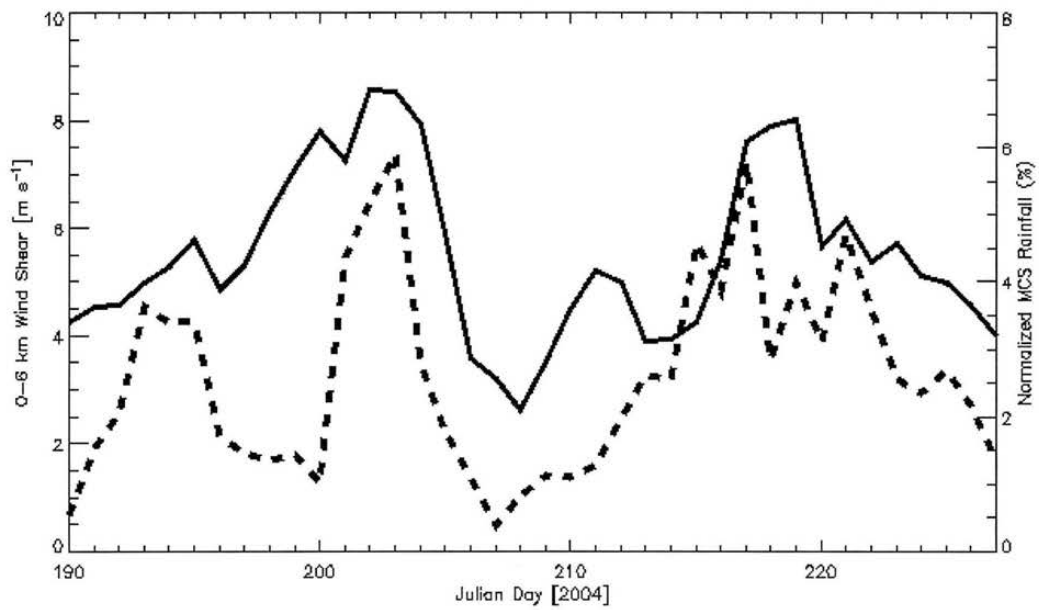


Fig 4.11 - Three-day moving average of daily mean 0-6 km wind shear within the Enhanced Convection Area of NAME (solid line), and three-day moving average of the daily rainfall (as a percentage of rainfall in the entire period) generated by MCSs during NAME (dashed line).

Table 4.2 - Mean shear conditions at 12Z within the NAME Enhanced Convection Area.

Characteristic	Mean	Std. Deviation
0-6 km Vertical Wind Shear	5.42 m s ⁻¹	2.05 m s ⁻¹

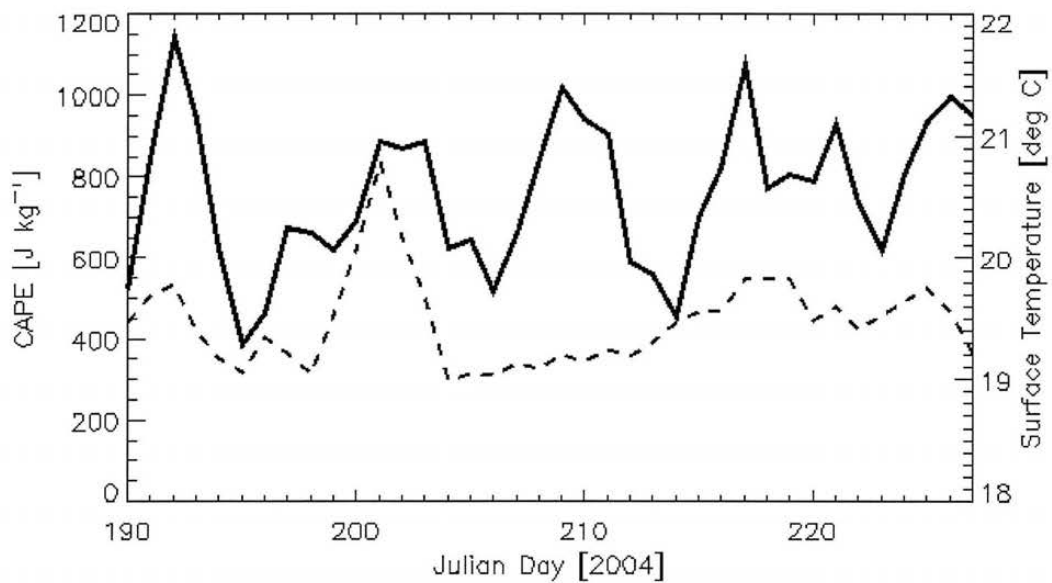


Fig 4.12 - Three-day moving average of daily mean Convective Available Potential Energy (CAPE) within the Enhanced Convection Area of NAME (solid line), and three-day moving average of 12Z surface temperature within the ECA (dashed line).

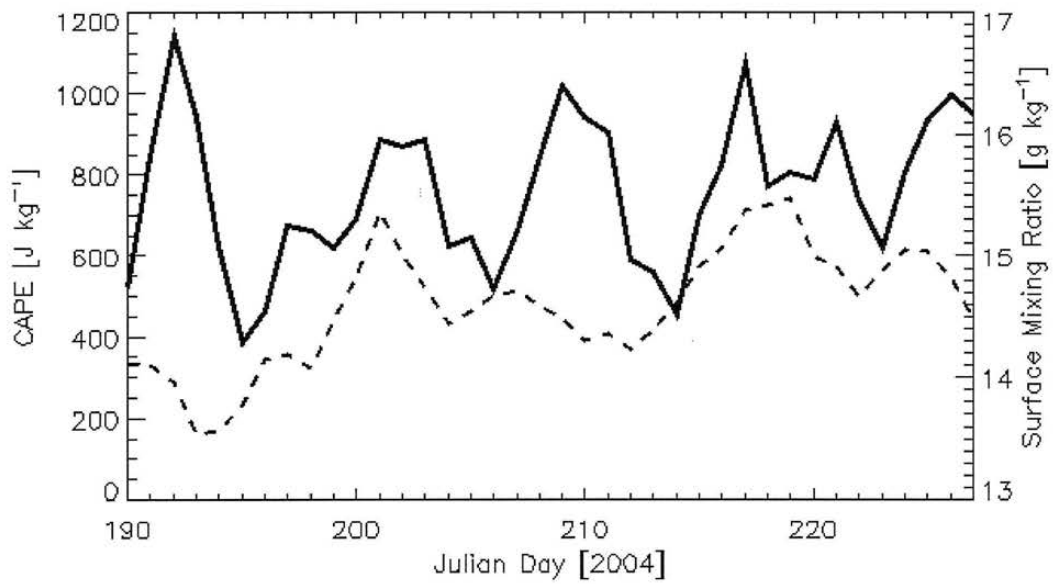
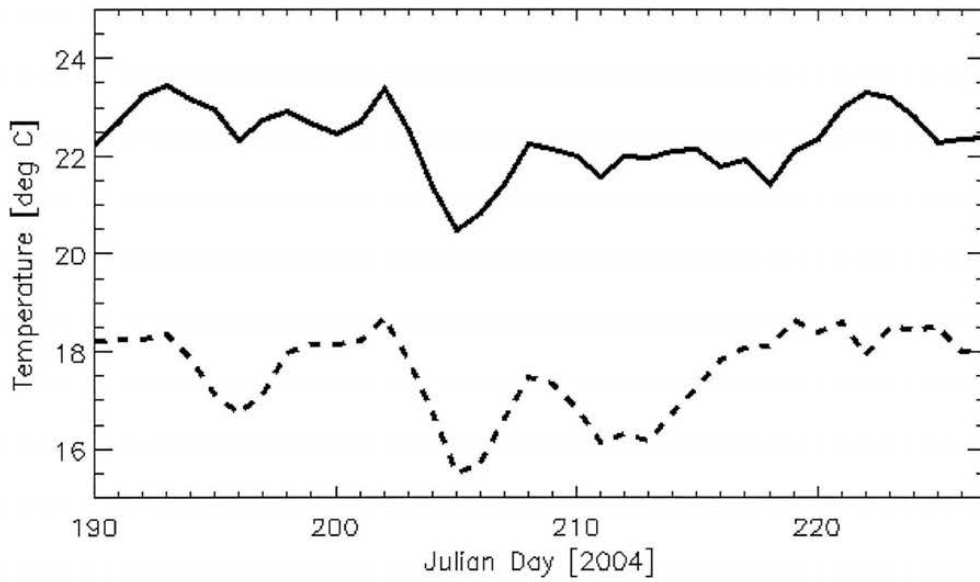


Fig 4.13 - Three-day moving average of daily mean Convective Available Potential Energy (CAPE) within the Enhanced Convection Area of NAME (solid line), and three-day moving average of surface mixing ratio within the ECA (dashed line).

a)



b)

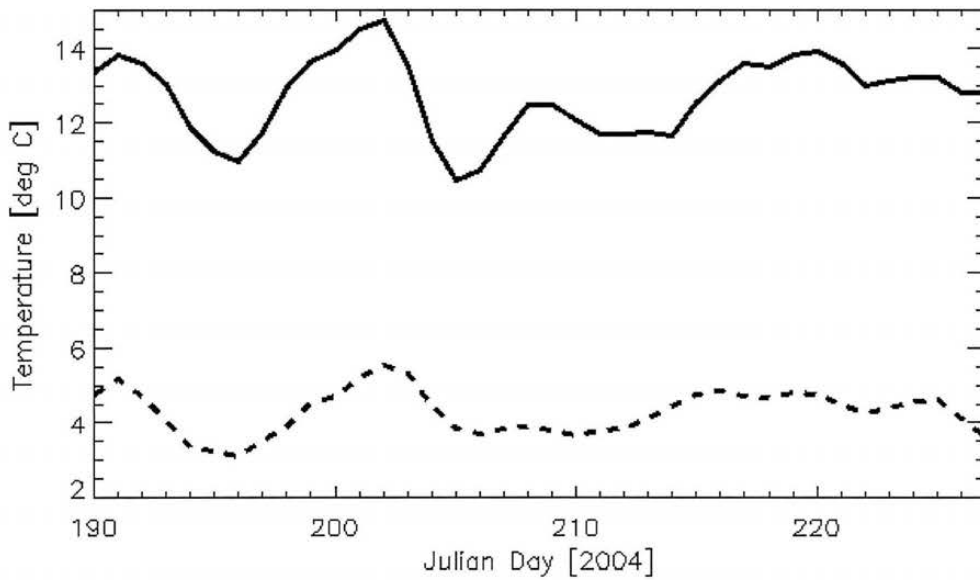


Fig. 4.14 – Three-day moving average of temperature within the Enhanced Convection Area of NAME at a) 1 km (solid line) and 2 km (dashed line) MSL; b) 3 km (solid line) and 4 km (dashed line) MSL; and c) 5 km (solid line) and 6 km (dashed line) MSL.

c)

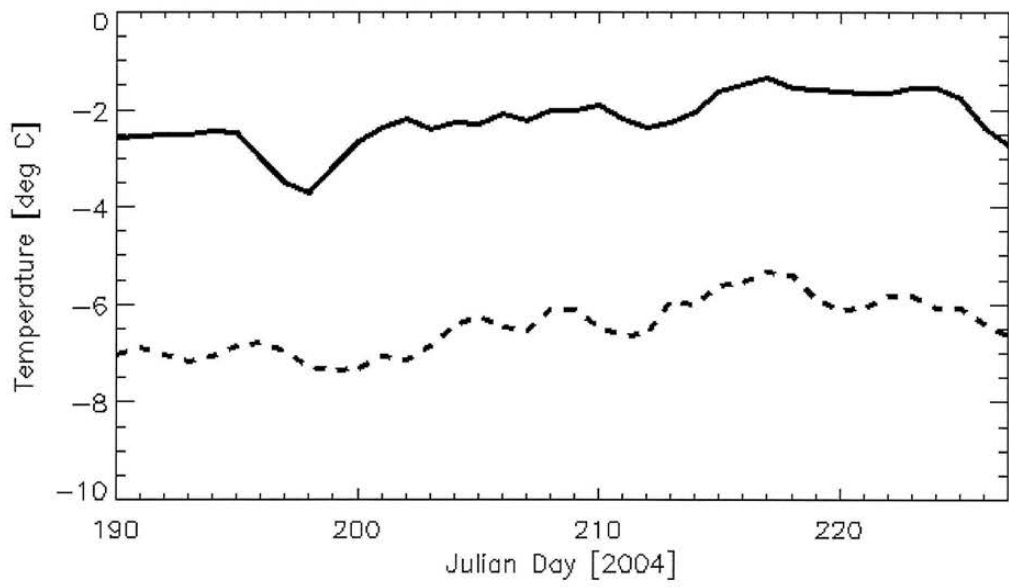


Fig. 4.14 – (cont.)

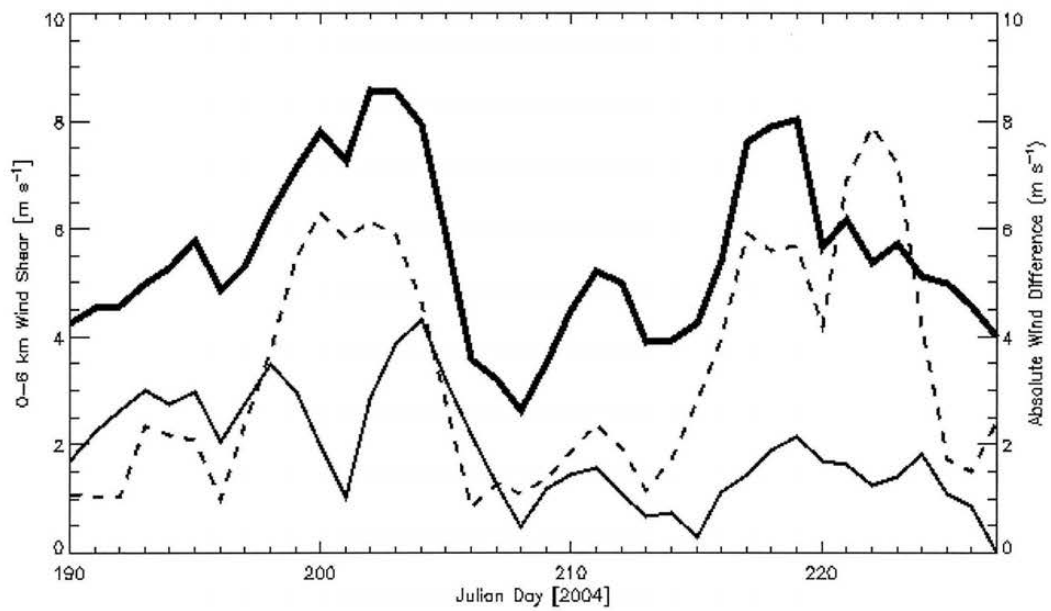


Fig. 4.15 – Three-day moving average of daily mean wind shear within the Enhanced Convection Area of NAME. The thick solid line represents the 0-6 km wind shear, while the thin solid line indicates the meridional component of the wind shear and the dashed line shows the zonal component of the wind shear.

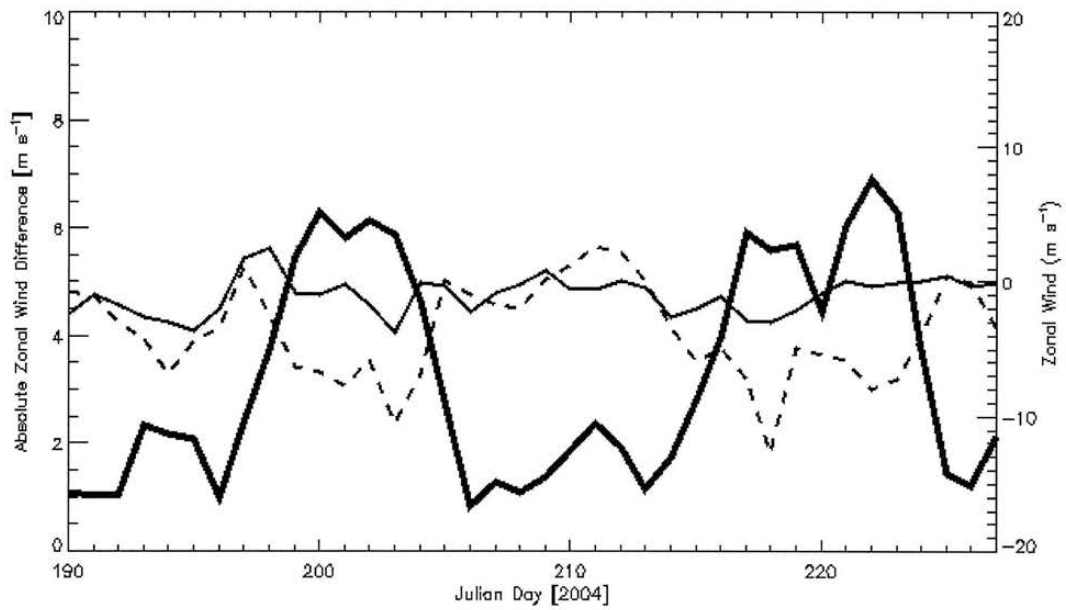


Fig. 4.16 - Three-day moving average of daily mean zonal wind shear and its components within the Enhanced Convection Area of NAME. The thick solid line represents the total zonal component of wind shear. The thin solid line indicates the average zonal wind in the lowest 500 m of the atmosphere, and the dashed line shows the zonal mean wind at 6 km AGL.

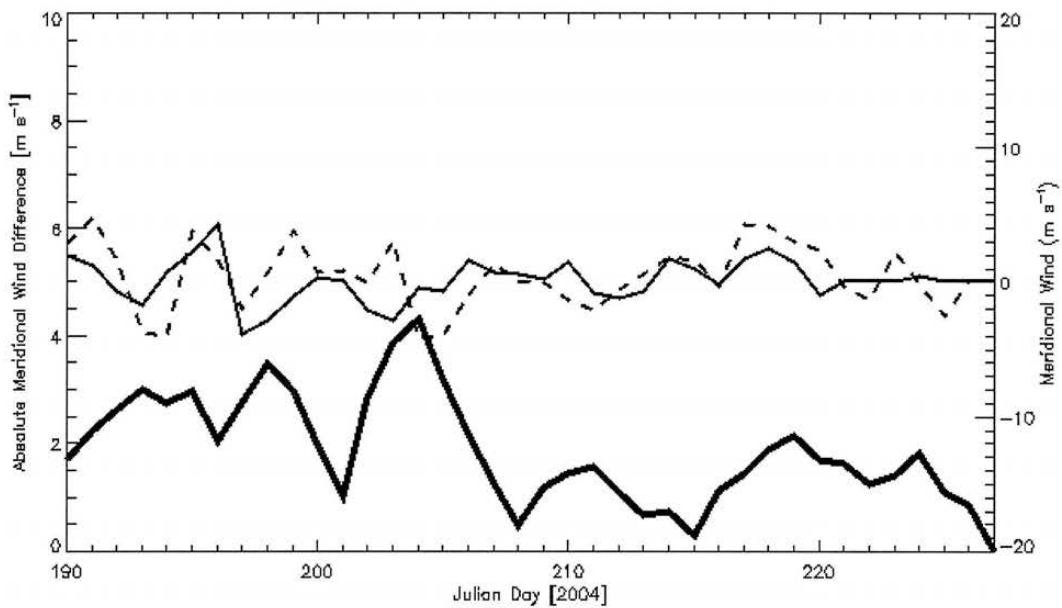


Fig. 4.17 - Three-day moving average of daily mean meridional wind shear and its components within the Enhanced Convection Area of NAME. The thick solid line represents the total meridional component of wind shear. The thin solid line indicates the average meridional wind in the lowest 500 m of the atmosphere, and the dashed line shows the mean meridional wind at 6 km AGL.

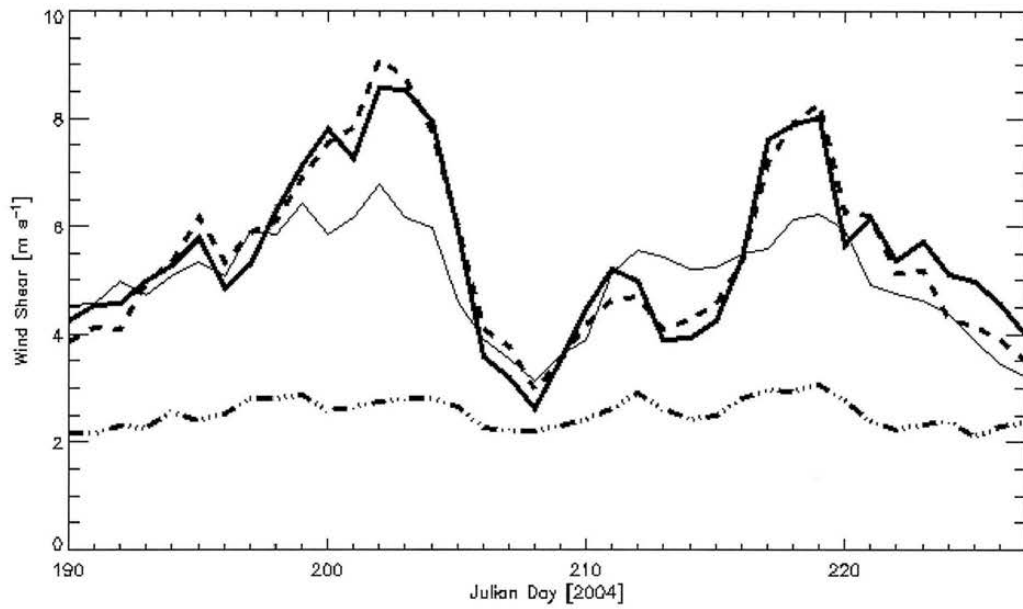


Fig. 4.18 - Three-day moving average of wind shear within the Enhanced Convection Area of NAME over different depths above ground level: 0-6 km AGL (thick solid line), 0-5 km AGL (dashed line), 0-3 km AGL (thin solid line), 0-1 km AGL (dashed-dotted line).

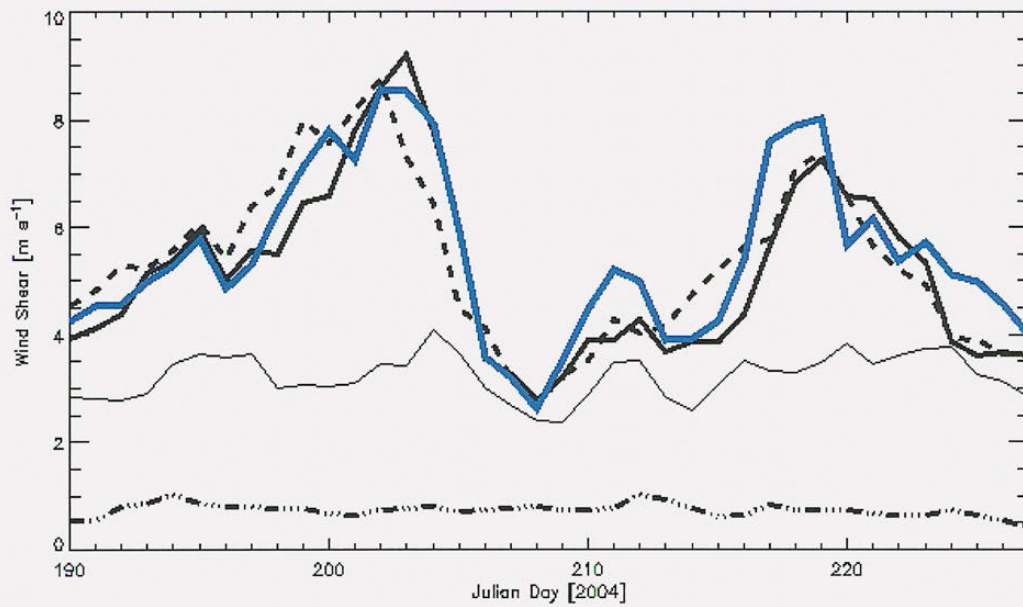


Fig. 4.19 - Three-day moving average of wind shear within the Enhanced Convection Area of NAME over different depths above mean sea level: 0-6 km MSL (thick solid line), 0-5 km MSL (dashed line), 0-3 km MSL (thin solid line), 0-1 km MSL (dashed-dotted line). The blue thick line depicts the 0-6 km AGL wind shear used in this study.

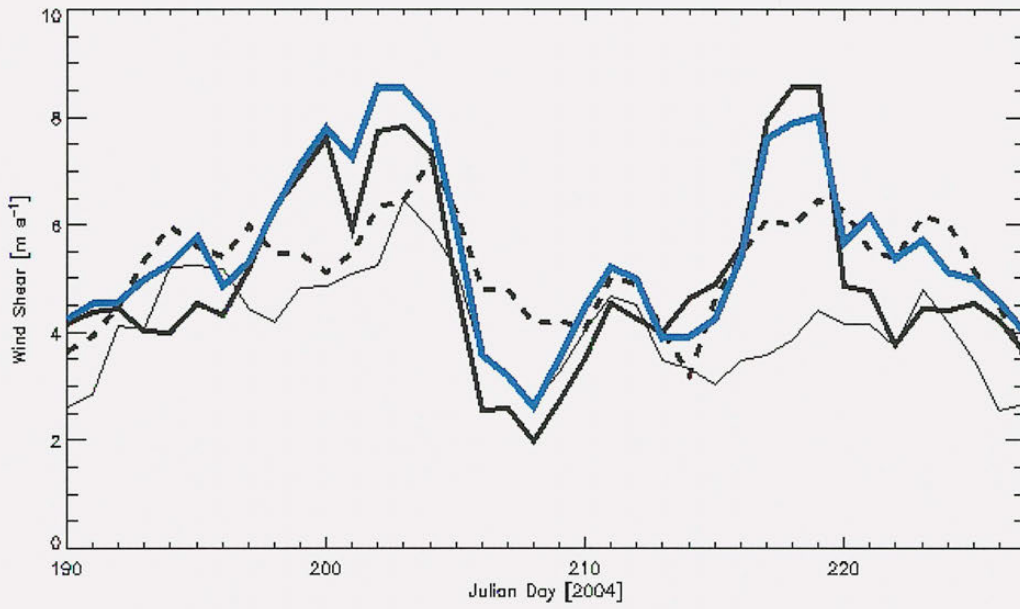


Fig. 4.20 - Three-day moving average of wind shear within the Enhanced Convection Area of NAME between different pressure levels: 800-400 hPa (thick solid line), 950-700 hPa (dashed line), 1000-800 hPa (thin solid line). The blue thick line depicts the 0-6 km AGL wind shear used in this study.

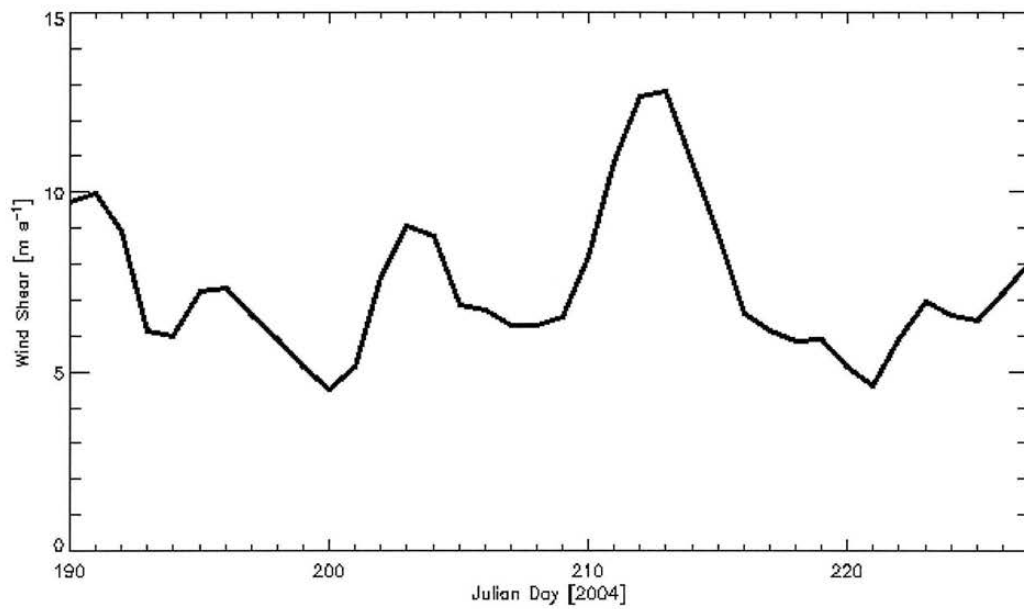


Fig. 4.21 - Three-day moving average of 5-10 AGL wind shear within the Enhanced Convection Area of NAME.

Table 4.3 – Linear correlation between total MCS rainfall within the NAME ECA and mean wind shear within the NAME ECA for different wind shear depths.

Wind Shear Depth	Correlation
0-6 km AGL	0.63
0-5 km AGL	0.63
0-3 km AGL	0.51
0-1 km AGL	0.43
0-6 km MSL	0.63
0-5 km MSL	0.62
0-3 km MSL	0.40
0-1 km MSL	0.20
800-400 mb	0.52
950-700 mb	0.39
1000-800 mb	0.40

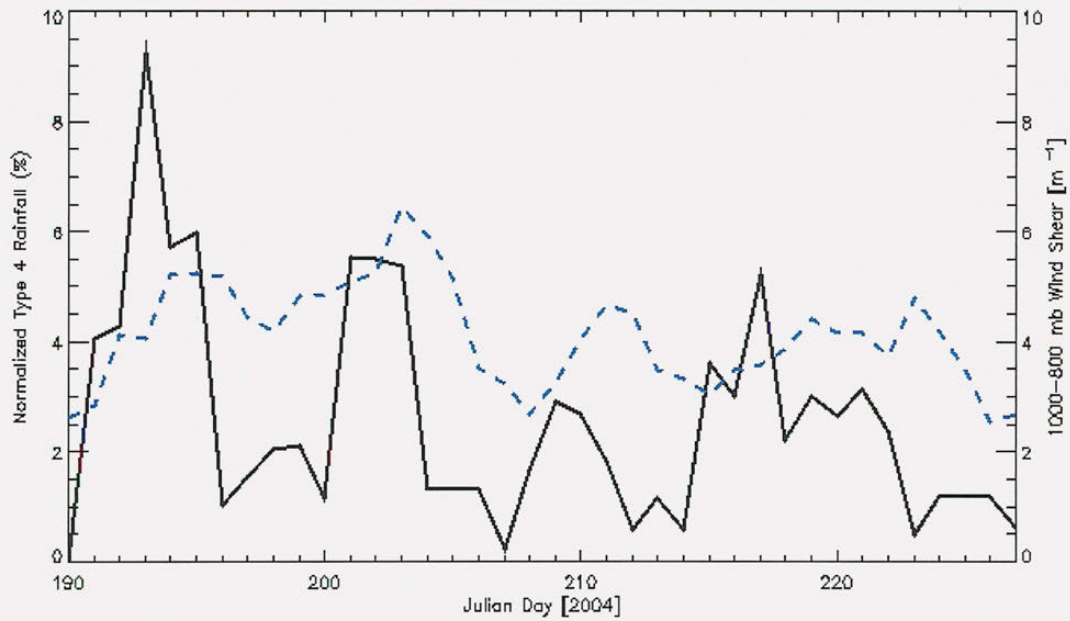


Fig. 4.22 - Three-day moving average of 1000-800 mb wind shear within the Enhanced Convection Area of NAME (blue dashed line) and three-day moving average of the daily rainfall (as a percentage of rainfall in the entire period) generated by Type 4 PFs during NAME (dashed line).

CHAPTER V

Synoptic Analysis of the Conditions Affecting the Development of Precipitating Features During NAME

5.1 Overview

This chapter examines possible couplings between thermodynamic and shear characteristics, discussed in the previous chapter, to synoptic conditions within the NAME Enhanced Convection Area (ECA). We attempt to identify how changes in the synoptic patterns relate to changes in CAPE and shear, which in turn, control or at least strongly contribute to mesoscale precipitation features. A multitude of maps and satellite images from several sources are used to examine horizontal and temporal variations in moisture, cloud cover, precipitation and winds. Given the important role of shear in the development of mesoscale-size precipitating features, which were shown in the previous chapter to produce the bulk of the precipitation in the NAME ECA region, we closely study the factors and conditions that led to the two peaks in shear observed around Julian Days 202 and 219. We also examine conditions associated with the peak in rainfall observed around JD 192. Additionally, we examine the importance of tropical easterly

waves and upper-level inverted troughs in other periods of interest.

5.2 Map Analyses

Here we focus our attention on the synoptic features affecting the southern portion of the NAME Tier 1 region. Three periods of 4 to 5 days each were chosen for in-depth analysis based on days when conditions led to increased precipitation and wind shear within the NAME ECA: 10-13 July 2004, 19-22 July 2004, and 2-6 August 2004.

5.2.1 July 10-13, 2004

This period was marked by an increase in the number and total rainfall produced by sub-mesoscale and mesoscale PFs. As discussed in Chapter 4, this period was also characterized by increased CAPE within the NAME ECA. Synoptically, the NAME region was influenced by 3 major features: the anticyclone associated with the North American monsoon ridge, an inverted trough, and the development of a tropical cyclone associated with an easterly wave. Feature maps identifying the position of these synoptic systems between 10 July and 13 July 2004 are shown in Fig. 5.1.

The upper-level anticyclone (denoted by the blue A or H in the feature maps) moved northward during this period. The position of this anticyclone is evident in the 250-mb streamline analysis shown in Fig. 5.2. The center of the anticyclone, which was located just north of Mazatlán on 10 July, moved toward the southern border on New Mexico on 11 July and then further north towards Colorado in the following two days. Fig. 5.3 shows that this movement permitted the development of an east-southeast flow

over much of Mexico. The atmospheric cross-section of winds and relative humidity along 25° N are shown in Fig. 5.4. It is evident that a fairly deep layer of moisture from the Gulf of California was brought into the NAME ECA by this east-southeast flow. This moisture advection increased the amounts of precipitable water, and favorable thermodynamics, as evidenced by CAPE of approximately 2000 J kg⁻¹ in Los Mochis (Fig. 5.5). Accordingly, large MCSs developed along the SMO on July 10-12. Unfortunately, a good portion of these MCSs were just outside the domain of the radar composite images.

The first upper-level inverted trough that affected the area of interest developed over the TX/LA/AR border on 8 July 2004 at 12Z. Its lifetime trajectory took this disturbance southward towards the Yucatan Peninsula on 10 July, which can be seen in Figs. 5.1a and 5.2a. This inverted trough (depicted in Fig 5.1 by the red C and IV#4) moved northeastward toward the central portion of Mexico by 11 July, moving only slightly eastward in the following 24 hours. The positioning of this inverted trough placed the coastal plains and adjacent foothills of the SMO within the NAME ECA under an upper-level diffluence region, as is evident in Fig. 5.2b-c. Hence, while the CAPE during the latter half of this period was less favorable than on July 10-11, dynamical uplift (as shown in Fig. 5.6) aided in the development of larger PFs on July 12. It is also important to note that southerly winds developed along the GoC in the wake of these MCSs and may have triggered a major Gulf Surge (Rogers and Johnson, 2007). On July 13 the inverted trough initiated northward move away from the NAME ECA region.

The last element to influence the region in this period was the passage of a

significant easterly wave trough (WT #20 in Fig. 5.1a-b). This trough, which had shown signs of strength just before crossing Central America, developed into Tropical Depression 3E around 12Z on 12 July 2004. The system quickly intensified and became the second named tropical cyclone of the year, Tropical Storm Blas, just six hours later. While the track of this tropical cyclone did not bring the system directly into the NAME ECA, it appears that moisture and cloudiness associated with this system moved eastward towards the southern side of the our radar domain and may have aided in the development of some PFs (Fig. 5.7). Tropical Storm Blas moved westward over colder waters and began to weaken 48 hours later.

5.2.2 July 19-22, 2004

The period of 19-22 July was also characterized by a large amount of PFs and rainfall, particularly rainfall generated by MCSs (shown in Chapter 4). This period coincided with one of the wind shear peaks within the NAME ECA (Fig. 4.11). Similarly to the period evaluated in the previous section is the period of JD 201-204, which was influenced by the monsoon anticyclone, an inverted trough, and the northward propagation of an easterly wave. Feature maps identifying the position of these synoptic systems are shown in Fig. 5.8. The upper-level anticyclone is denoted by the red A, and the TUTT cyclone and associated inverted trough are indicated, respectively by the blue C and red dashed line (IV #6).

The upper-level anticyclone was centered over New Mexico on 19 July 2004, as seen in Fig. 5.9a. Noteworthy in this figure is the presence of strong winds in the eastern

and southern sides of the anticyclone. The wind speed maximum in the southern side of the anticyclone was located right above Mazatlán. The anticyclone did not move significantly in the following 24 hours, but strengthened and its upper-level flow dominated much of the NAME Tier 1 region (Fig. 5.9b). It initiated a slow progression towards the southwest on 21 July (Figs. 5.8c and 5.9c). This was concurrent with the development of a new inverted trough (IV #6 on Fig. 5.8c) near the coast of Texas. The circulation from this upper-level cyclone interacted with that of the upper-level anticyclone described previously. This interaction appears to have drawn some of the momentum from the subtropical jet stream bringing strong wind speeds to the east of the anticyclone equatorward (Fig. 5.9b-d). This flow led to the development of a strong upper-level jet over the NAME ECA which evidently was responsible for the peak wind shear in the NAME ECA described in the previous chapter. This shear can also be seen in the cross section shown in Fig. 5.10. Additionally, this synoptic setup allowed the development of dynamical support over the NAME ECA through upper-level diffluence. The upper-level divergence, shown in Fig. 5.11, aided in the development of convection in the NAME ECA through dynamical uplift as is observed in the omega field (Fig. 5.12). The favorable dynamic conditions (including shear) and thermodynamic conditions (Fig. 5.13) allowed the development of many MCSs along the foothills of the SMO, as it can be seen in infrared satellite image shown in Fig. 5.14. These MCSs slowly migrated towards the GoC and weakened as the instability became less favorable overnight. However, the MCSs just north of the NAME ECA converged into one enormous system with Mesoscale Convective Complex (Maddox 1980) characteristics (Fig. 5.15). Intense low-level outflow from this MCC appears to have initiated a moderate influx of moisture

northward along the GoC, evident in the NOAA P-3 aircraft wind measurements at 925 hPa (Fig. 5.16) as well as the relative humidity and wind speed/direction profile time series at Empalme (Fig. 5.17), located in the central portion of the GoC coast. Lastly, it is also important to mention the development of a tropical disturbance just south of the GoC and the NAME ECA in close association with the trough axis of a tropical easterly wave (WT #24 in Fig. 5.8b-c). The line of convective features along this trough and the disturbance that formed in the northern end are visible in the infrared satellite image shown in Fig. 5.18. Some of the moisture associated with this tropical wave eventually reached the southern portion of the NAME ECA.

5.2.3 August 2-6, 2004

The period of 2-6 August 2004 (Julian Days 215-219) had alternating days of enhanced precipitation and MCSs and days where convection was closer to average conditions in the NAME ECA (i.e. many isolated convective cells with a reduced number of MCSs). Large MCSs passed through the NAME ECA on the afternoons of 3 and 5 August. This period also encompasses the second wind shear peak that took place in the southern portion of the NAME ECA. Unlike the first wind shear peak, evaluation of the wind profile across the southern portion of the GoC, shown in Fig. 5.19, indicates that the strongest winds occurred closer to mid-levels (i.e. 400-500 mb) rather than closer to the tropopause.

On 2 August the atmosphere was characterized by typical convection within the NAME ECA, with copious amounts of isolated convective cells developing over the

foothills of the SMO during the afternoon and slowly propagating towards the coast. A few mesoscale-size PFs were also evident. The synoptic setup, shown in Fig. 5.20, was dominated by the presence of an intense anticyclone at upper levels (i.e. 200-300 mb), centered over Texas. Similarly to the pattern observed on 19 July, the eastern and southern sides of the anticyclone displayed above average wind speeds with the development of a northeast-southwest oriented jet streak (Fig. 5.21). Concomitantly, an upper level inverted trough developed over the Gulf of Mexico (Figs. 5.20b and 5.22) just east of the jet streak. The other significant synoptic feature affecting the NAME region was another tropical wave trough (WT #28), shown in Fig. 5.20a-b. This tropical wave is clearly seen on satellite infrared imagery (Fig. 5.23), where convection is well developed along 105° W near the center of the wave and also in its northern tip (which is over land). The over-land convection developed into a large MCS just south of the NAME ECA and maintained a position centered right at the shoreline through the morning hours of 3 August. However, as the day progressed, the upper-level anticyclone moved southwestward towards the Texas-Mexico border and mid-level steering winds shifted from easterly to southeasterly, as shown in Fig. 5.24. As a result, the convection originally formed in association with the tropical wave instability got pushed northward into the NAME ECA on the afternoon of 3 August. Therefore, this large mesoscale PF dominated the area covered by the radar composites on this day.

Precipitation was below-average within the NAME ECA on the following day (Fig. 5.25), primarily due to a progressive decrease in moisture through the afternoon and evening hours of 4 August, and also the stabilizing effect of previous day's MCSs. This drying, evident in the water vapor satellite imagery (Fig. 5.26), was brought into the

region by the anticyclonic circulation of the upper-level high pressure centered in Texas. In Fig. 5.26, we can also easily identify the precipitation associated with two tropical waves in the region. Tropical Wave 28 had now moved westward and was found near 110° W, while Tropical Wave 29 was near 100° W. The last synoptic feature to play a role in the precipitation pattern of the NAME ECA in this period was the upper tropospheric trough (IV #8), which moved into central portion of Mexico, just southeast of the mid-level dry air. The vorticity maximum associated with this inverted trough was found to be closer to 400 mb, where the winds were strongest. The approach of the upper-level jet streak increased easterly zonal flow at mid to upper levels and, consequently, wind shear within the NAME ECA. The movement of the upper-level trough can be seen in the sequence of 400-mb vorticity analysis maps shown in Fig. 5.27. It is interesting to notice that the path of this upper-level inverted trough brought directly above the moist zone associated with the northern tip of Tropical Wave 29 (Fig. 5.20c). Fig. 5.28 shows that the upper-level inverted trough interacted with the tropical easterly wave by capturing the mid-level moisture associated with the tropical wave and wrapping around its east side. As a result, moisture was advected northward on the east side of the upper-level low and, as this disturbance moved westward, this moisture was injected right into the NAME ECA on the afternoon of 5 August 2004. Under favorable moisture and wind shear conditions, convection was rather vigorous with the development of a large MCS (Fig. 5.29) and plentiful precipitation (Fig. 5.30) over the NAME ECA that afternoon and evening. The inverted trough is clearly seen over the mouth of the GoC in WRF 500-mb wind analysis on 6 August (Fig. 5.31) as it exits the NAME ECA. The second peak in wind shear discussed in the previous chapter, which was brought about by the approach

of this inverted trough and its intense mid-level winds, is evident in the cross-section over the southern portion of the GoC shown in Fig. 5.19.

5.2.4 Other periods of interest

In the previous sections we discussed the synoptic features affecting the southern portion of NAME Tier 1 region when MCS rainfall was above average. Noteworthy was the impact that transient atmospheric disturbances, such as tropical easterly waves, and tropical upper tropospheric troughs, had in modulating moisture content and shear conditions in the NAME ECA and the overall development of periods of enhanced precipitation in the region. While previous studies have identified relationships between surges of moisture in the GoC and easterly waves (Stensrud et al. 1997, Fuller and Stensrud 2000, Higgins et al. 2004), the quantitative frequency with which moisture from tropical waves actually affects the southern portion of the North American Monsoon region remains unknown. Higgins et al. (2004) also discussed the need to elucidate the explicit role of other types of tropical disturbances, such as inverted troughs.

Synoptic maps created by the Tropical Prediction Center and from the *Servicio Meteorológico Nacional* in Mexico tracked the position of tropical easterly waves using a combination of satellite imagery (i.e. cloud clusters) and atmospheric data (i.e. maximum low-level cyclonic vorticity, minimum surface pressure, and shift in low-level meridional winds). Between 1 July 2004 and 31 August 2004, a total of 23 tropical waves traversed the East Pacific just south of the GoC (Fig. 5.32), averaging approximately 11 tropical waves per month at the height of the monsoon season. Analysis of similar maps between

16 July and 27 August 2003 showed 17 waves (Fig. 5.33), yielding an average of approximately 12 tropical waves per month. Using a similar methodology, Pasch et al. (1998) found that the periodicity of tropical waves between 1991 and 1995 was approximately once every 3 days, and that 49 to 70 tropical waves per year developed during the hurricane season between 1967 and 1995 (i.e. an average of 10-14 per month). On the other hand, Fuller and Stensrud (2000) found an average of only 3 waves per month solely using 850 hPa meridional wind data from the ECMWF Reanalysis Project between 1979 and 1993. There are two possible explanations for this significantly smaller number of tropical waves found by Fuller and Stensrud (2000). First, analyses of 700 hPa winds, the level where tropical waves are best defined (Reed et al. 1977), were not available in the dataset they used; and they acknowledge that terrain in the Caribbean and Central America, which extends above 850 hPa at some points, could disrupt the wave signal. Second, Pasch et al. (1998) found that wind shifts associated with many waves between 1991 and 1994 were not significantly marked. Hence, it is possible that only the stronger and higher amplitude tropical waves were evident in the 850 hPa analyses used by Fuller and Stensrud (2000).

Table 5.1 shows the approximate dates in which the axis of the tropical wave was found between 100° W and 110° W between 1 July and 31 August 2004. In this table, it is evident that each wave typically lingered in the region near the mouth of GoC for 2 to 3.5 days. This results in a wave speeds varying between 5 and 6.5 m s⁻¹. Reed et al. (1977) found that waves moves slightly faster in the East Atlantic Ocean, at speeds of 6 to 8 m s⁻¹. Assessment of a sequence of maps identifying the position of a tropical easterly wave indicates that, indeed, tropical waves appear to move somewhat faster over

the Atlantic Ocean than over the East Pacific. This difference in speed is seen in Fig. 5.34 as we track the same tropical wave (TW #25) as it propagates westward through the Tropics. On July 16 (Fig. 5.34a) this tropical wave was located near 40° W and 5 days later (Fig. 5.34b) it was found at 80° W, which indicates an average speed of approximately 10 m s⁻¹. Twenty four hours later it was located at 85° W (Fig. 5.34c) and on the next day at 92° W (Fig. 5.34d), yielding an average speed of roughly 4.5 m s⁻¹. It is possible that the interaction of these tropical waves, which are low-level atmospheric disturbances, with the landmass or with convection that forms over Central America slowed the propagation speed of the wave.

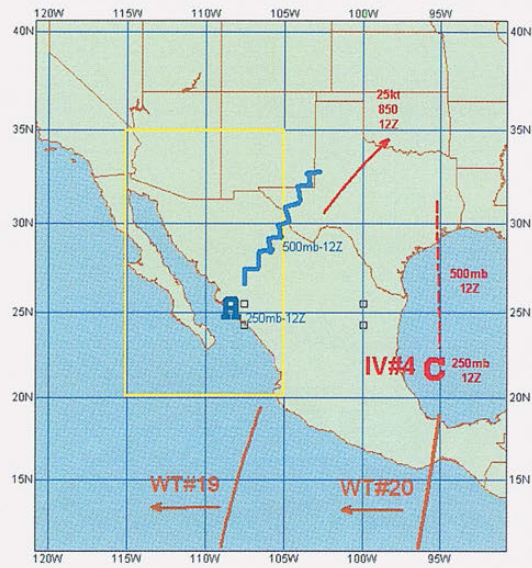
In the period evaluated in Table 5.1, there are only 3 days that did not show any tropical waves affecting the area: 29 July, 30 July, and 10 August 2004. The lull created on 10 August, was a consequence of the slower progression of Tropical Wave 31 through the Caribbean, which gave rise to Tropical Depression #2 and Tropical Storm Bonnie (also shown in Fig. 5.35b) before reaching Central America. Another interesting feature that can also be seen in the water vapor satellite image shown in Fig. 5.35b is the dry area between tropical waves 30 and 31. That dry area crossed the southern portion of NAME Tier 1 between 9 and 10 August 2004, which was one of the few periods when no tropical waves were present in the area. A sequence of daily precipitation maps over Mexico is shown in Fig. 5.36, where we find that precipitation was reduced significantly in the Mexican States south of Sinaloa on 9 August (Fig. 5.36b) when the dry interlude between tropical waves 30 and 31 was crossing the area. On the following day, when the dry area reached the GoC area, precipitation was significantly reduced along the entire Gulf of California coastal region. While deep convection, MCSs and substantial rainfall in the

NAME ECA region are a result of favorable thermodynamic, dynamic and/or kinematic conditions, the example discussed here highlights the likely importance of tropical waves as a source of instability and moisture for the development of PFs in the southern portion of the North American Monsoon region. There are other mechanisms, however, responsible for periods of reduced moisture and suppression of convection in the southern portion of the NAME ECA. Higgins et al. (2004) showed that the position of the upper-level anticyclone is also essential in the development of moisture surges in the GoC.

Finally, it is important to discuss the occurrence of one other upper tropospheric inverted trough that took place during NAME 2004. That feature developed over the Gulf of Mexico on 8 August 2004, with a closed upper-level low visible on 300 mb wind analysis by the 12 km NCAR WRF model. This upper-level inverted trough lingered over the Gulf of Mexico for a day, but the closed circulation disappeared. The inverted trough quickly moved westward, reaching the area just south of the GoC on 10 August 2004 (Fig. 5.37b). Fig. 5.38 shows this type of feature, as it occurred in the other instances described in this chapter, brought favorable dynamic conditions through upper-level divergence and stronger upper-level easterly winds (i.e. stronger shear). Nonetheless, this disturbance moved over the mouth of the GoC exactly during the period when moisture was markedly reduced in the region (as discussed previously), which rendered the favorable dynamic conditions useless to development of intense convective systems in this particular event. Nonetheless, upper level inverted troughs are only capable of generating favorable conditions to development of MCSs by interacting with the other two main synoptic features affecting the southern portion of the NAME Tier 1 region: the position of the upper-level anticyclone to the north (as on 12 and 21 July 2004) and the

passage tropical easterly waves to the south (as on 5 August 2004).

a)



b)

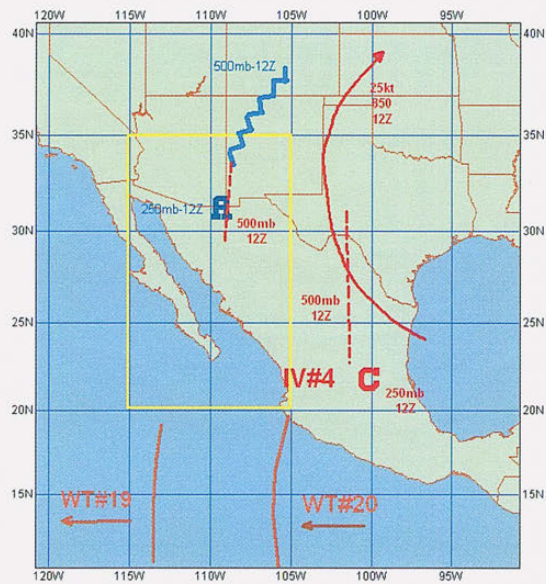
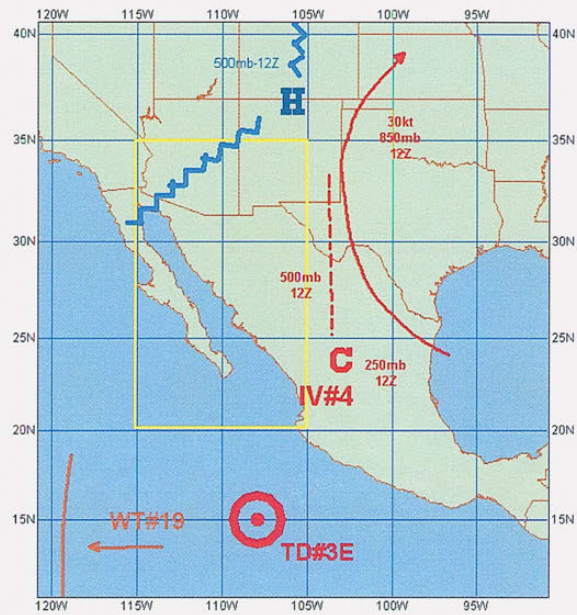


Fig. 5.1 – Map identifying synoptic features within the NAME Tier II region on a) 10 July 2004, b) 11 July 2004, c) 12 July 2004, and d) 13 July 2004.

c)



d)

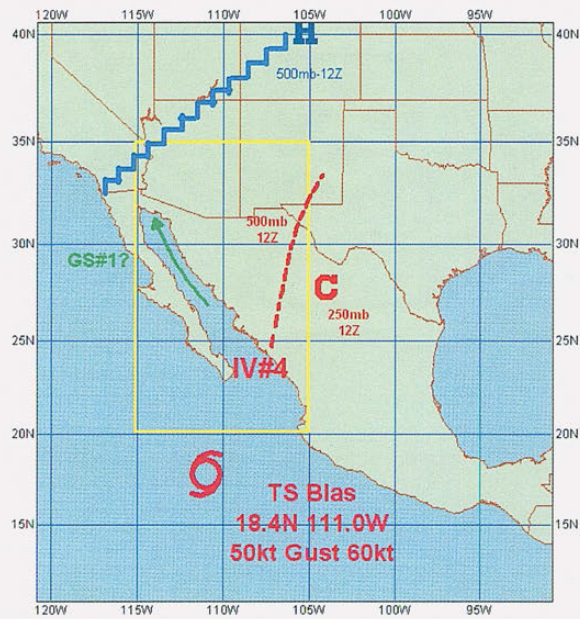
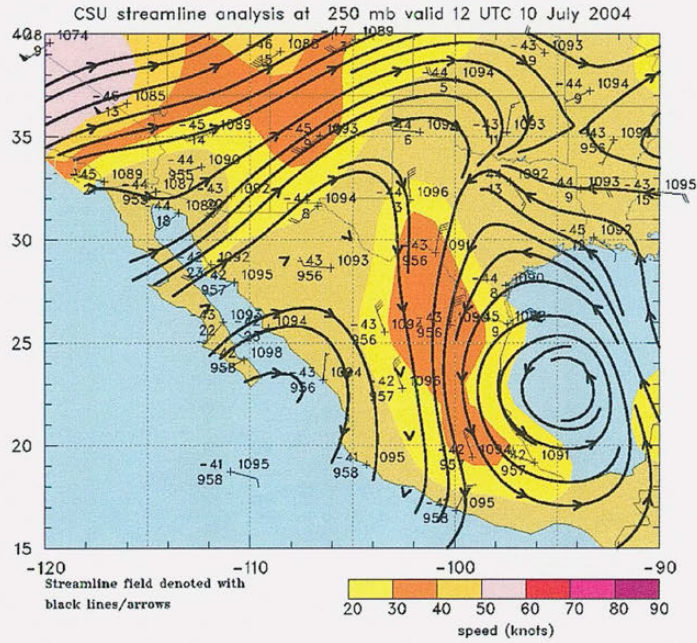


Fig. 5.1 – (cont.)

a)



b)

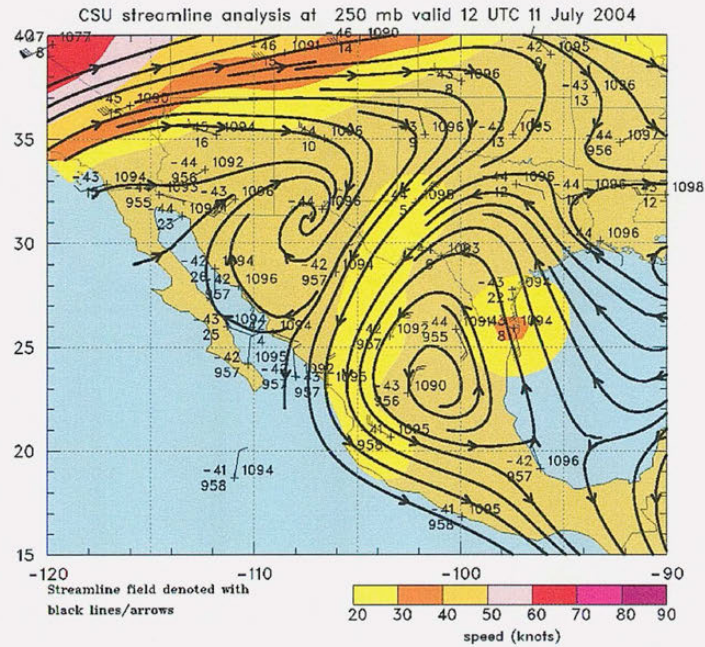
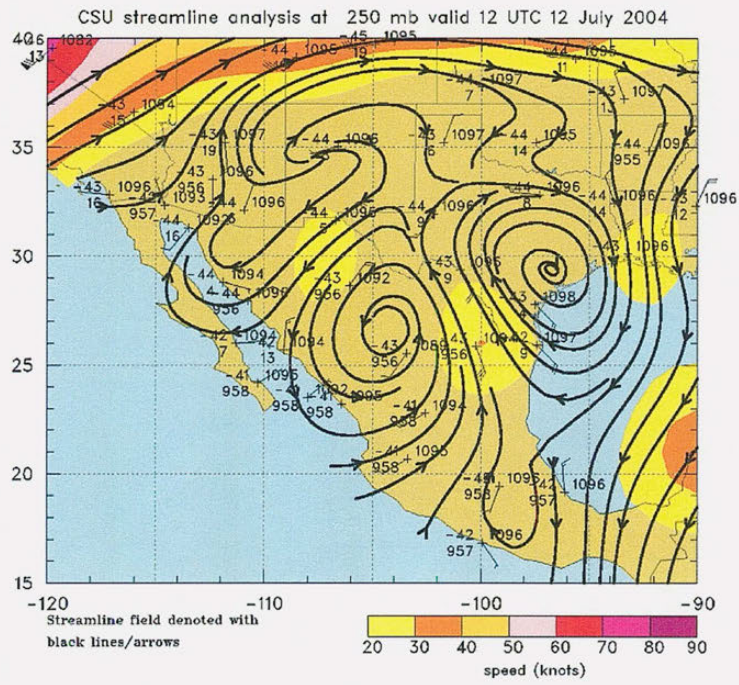
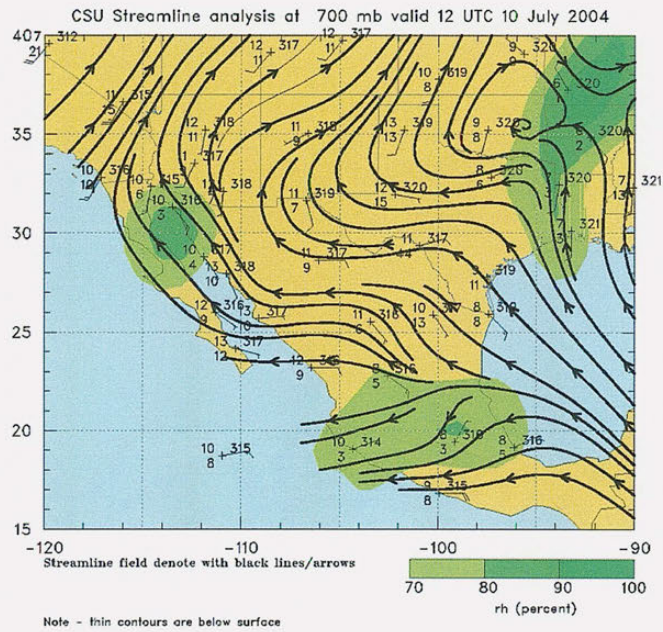


Fig. 5.2 – CSU streamline analysis map at 250 mb for a) 10 July 2004, b) 11 July 2004, c) 12 July 2004, and d) 13 July 2004.

c)



a)



b)

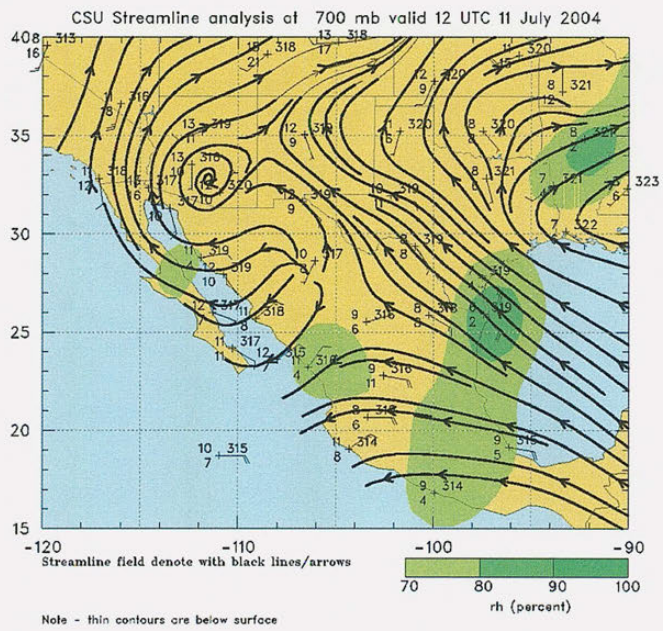
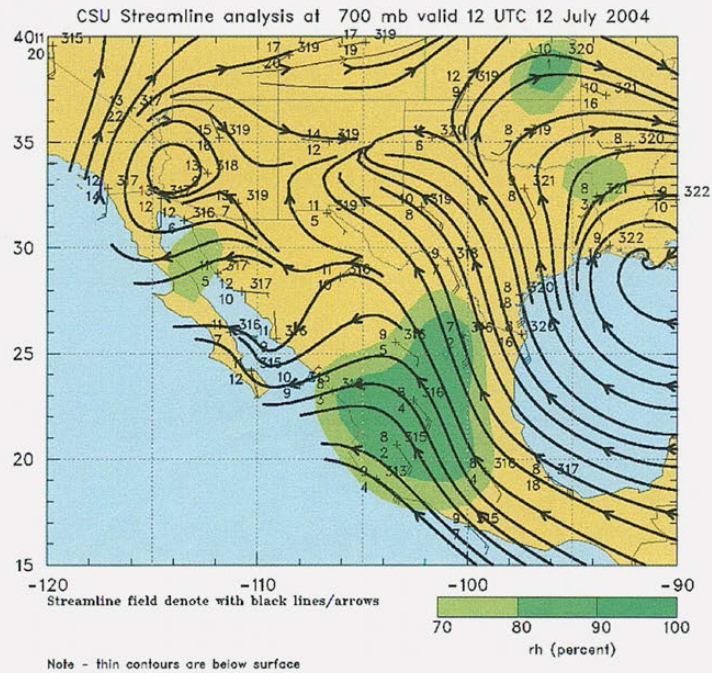


Fig. 5.3 – CSU streamline analysis map at 700 mb for a) 10 July 2004, b) 11 July 2004, c) 12 July 2004, and d) 13 July 2004.

c)



d)

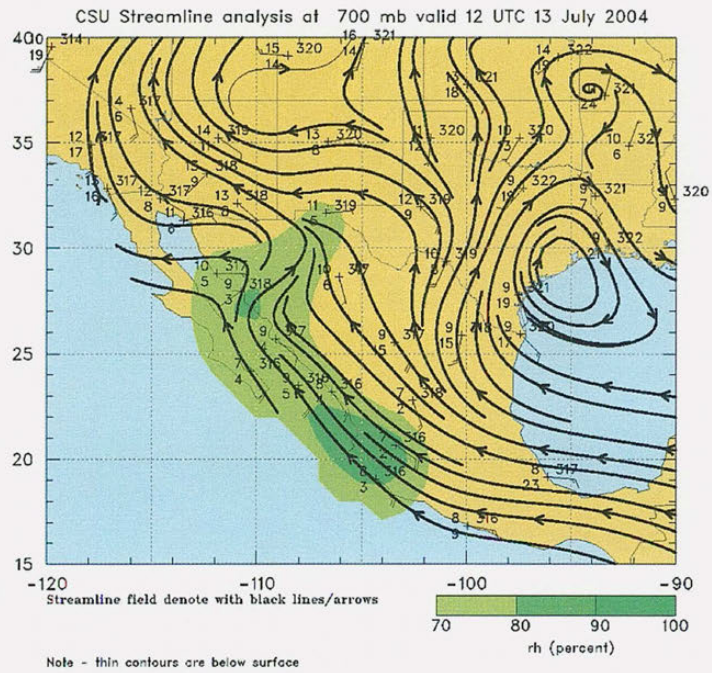
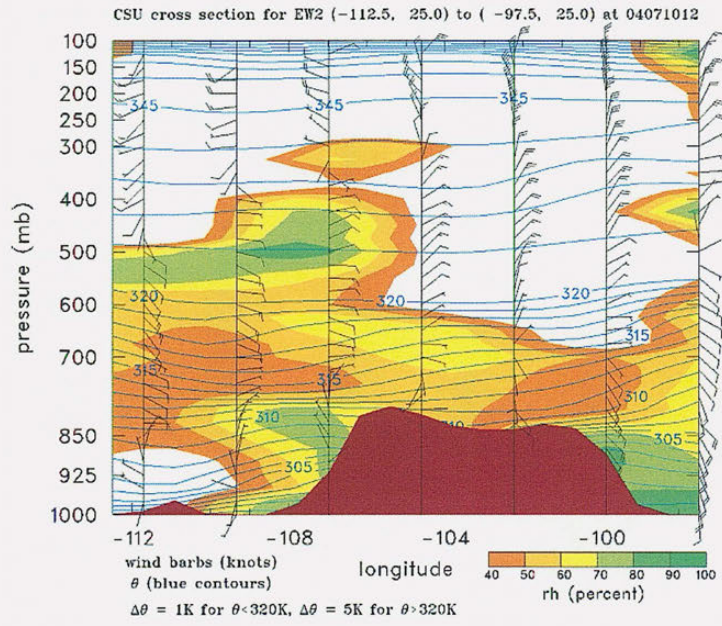


Fig. 5.3 – (cont.)

a)



b)

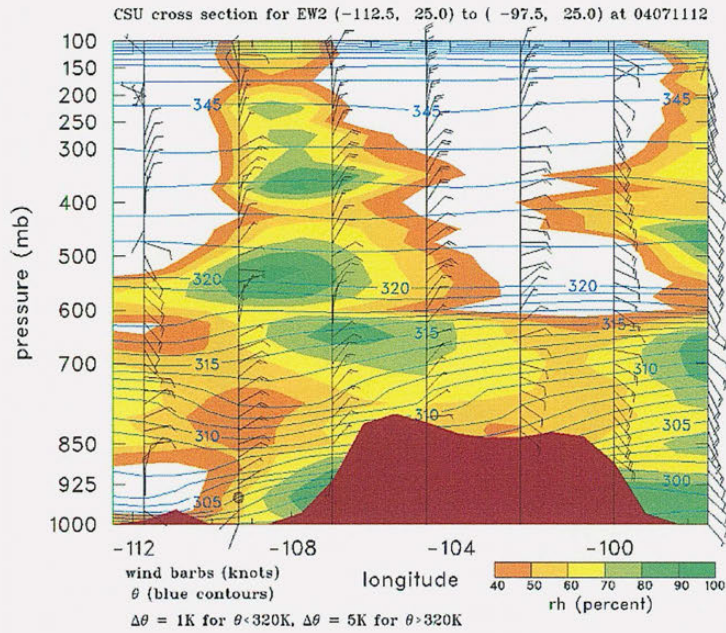
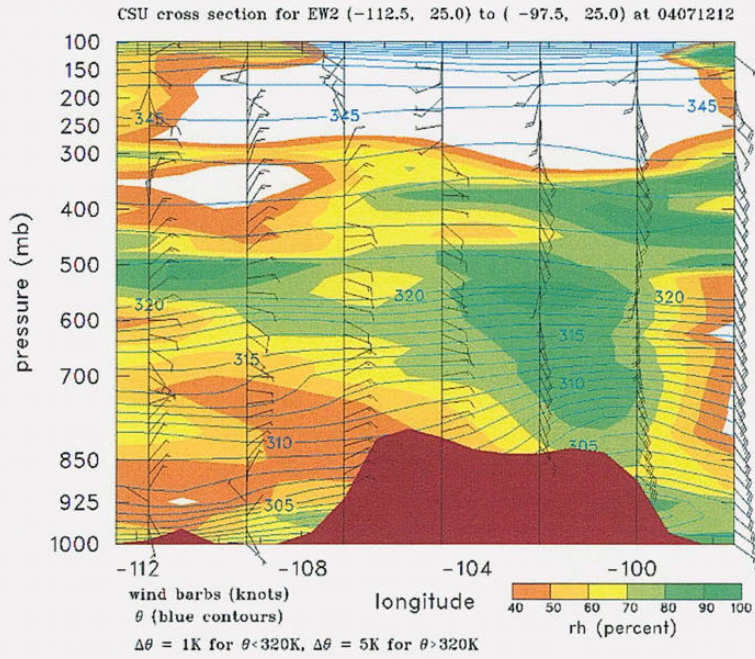


Fig. 5.4 – CSU longitudinal Cross Section at 25 °N showing the profile of relative humidity and wind barbs on a) 10 July 2004, b) 11 July 2004, c) 12 July 2004, and d) 13 July 2004.

c)



d)

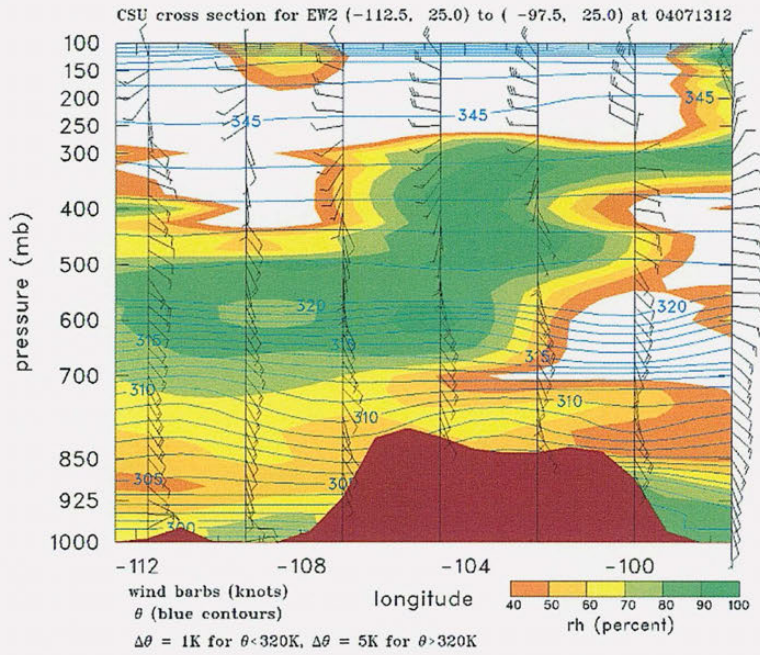


Fig. 5.4 - (cont.)

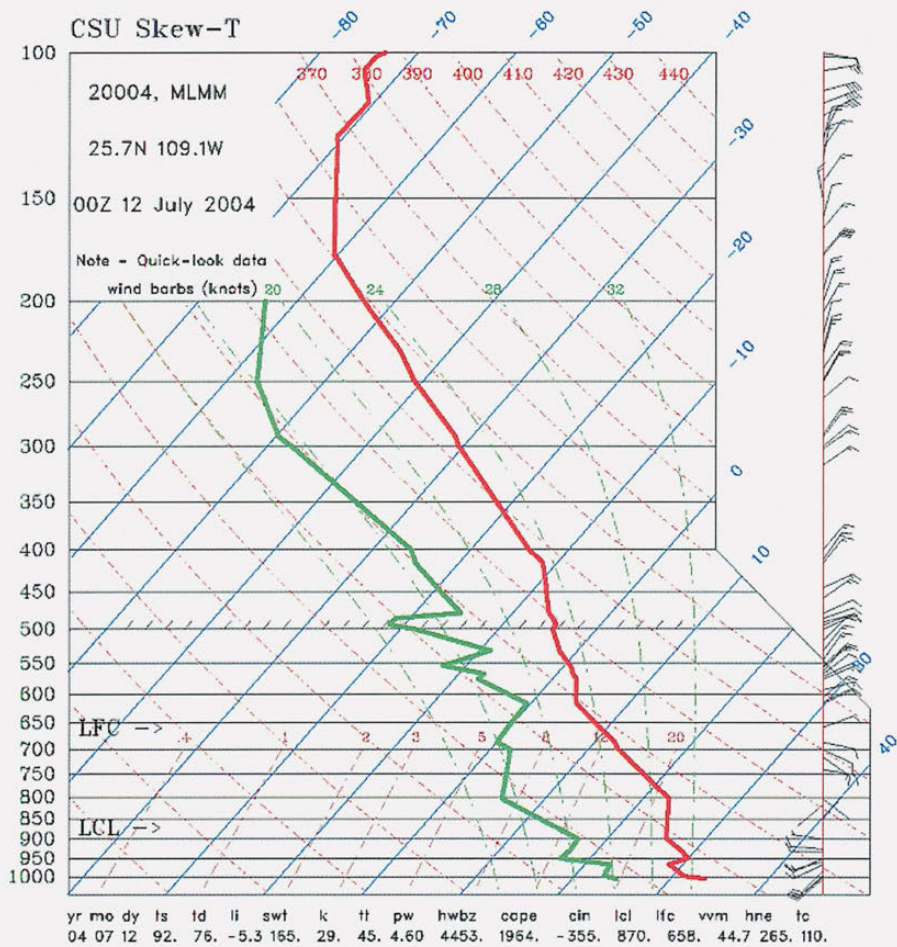


Fig. 5.5 – Skew-T plot of the sounding launched from Los Mochis, Mexico on 12 July 2004 at 00Z.

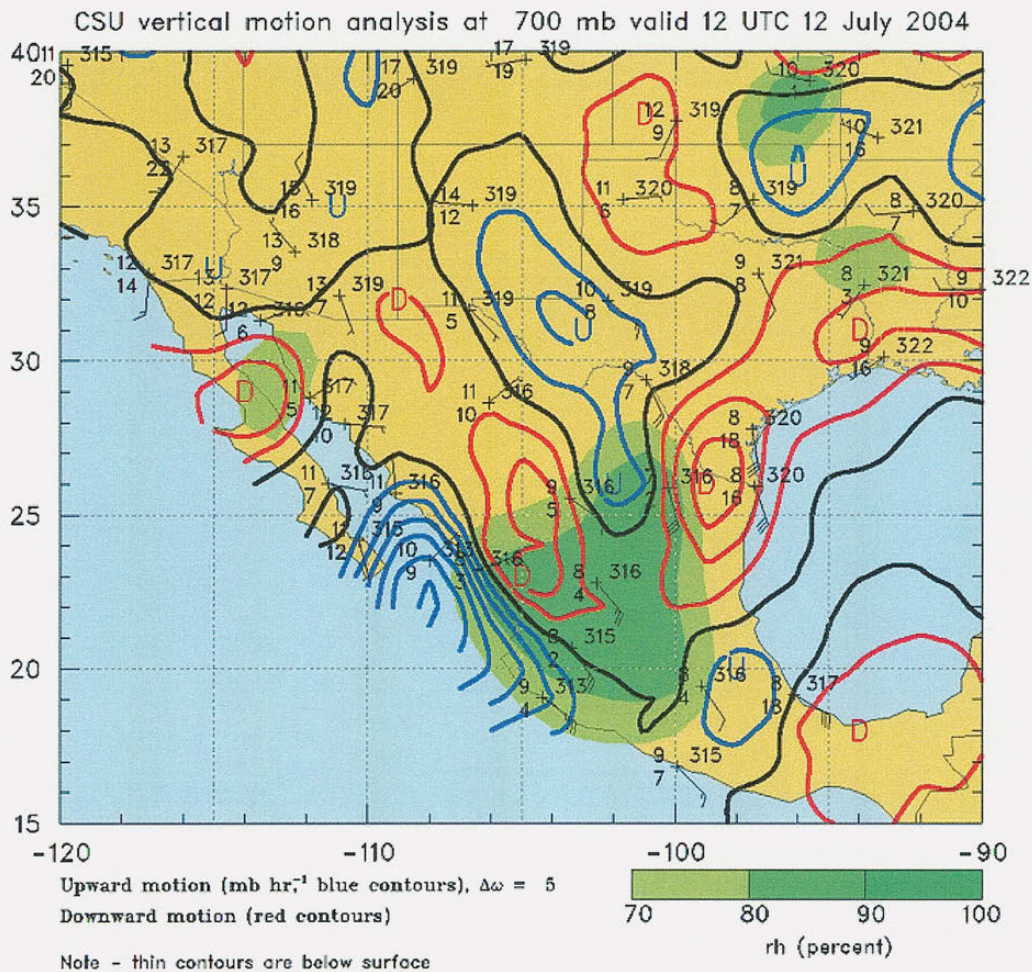


Fig. 5.6 – CSU vertical air motion analysis at 700 mb within the NAME Tier II region on 12 July 2004 at 12Z.

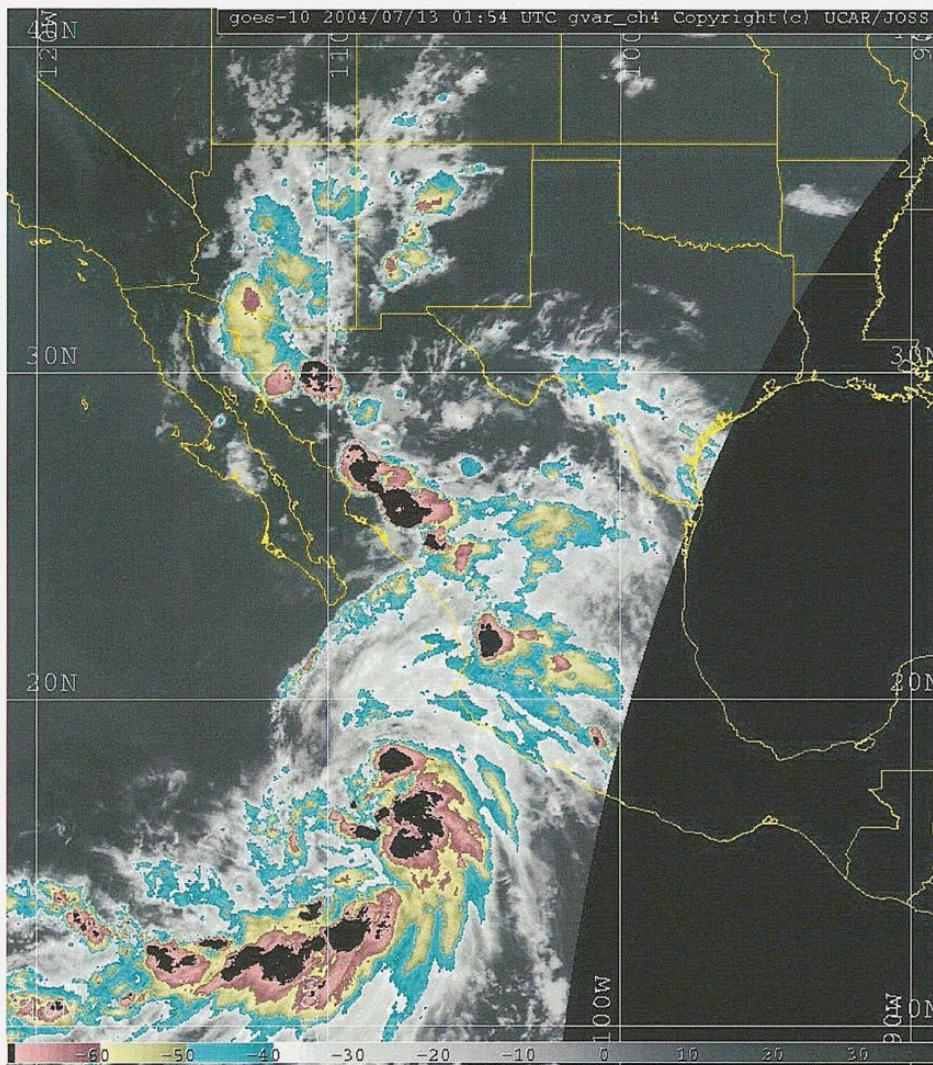
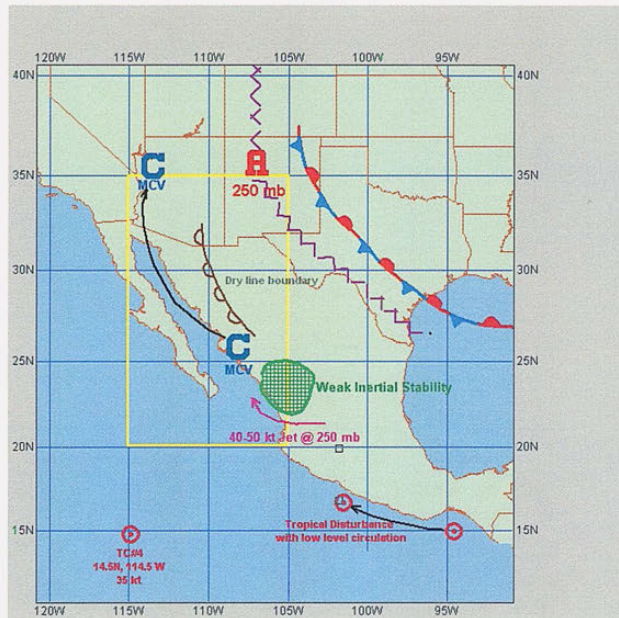


Fig. 5.7 – Infrared Satellite Image from GOES-10 on 13 July 2004 at 0154 UTC.

a)



b)

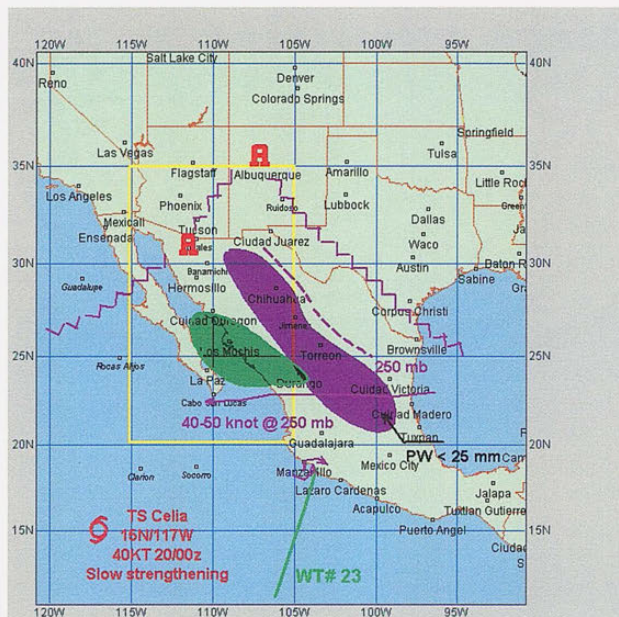
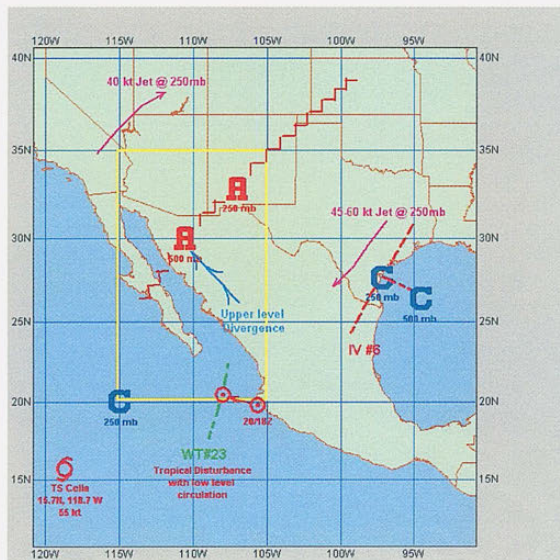


Fig. 5.8 – Map identifying synoptic features within the NAME Tier II region on a) 19 July 2004, b) 20 July 2004, c) 21 July 2004, and d) 22 July 2004.

c)



d)

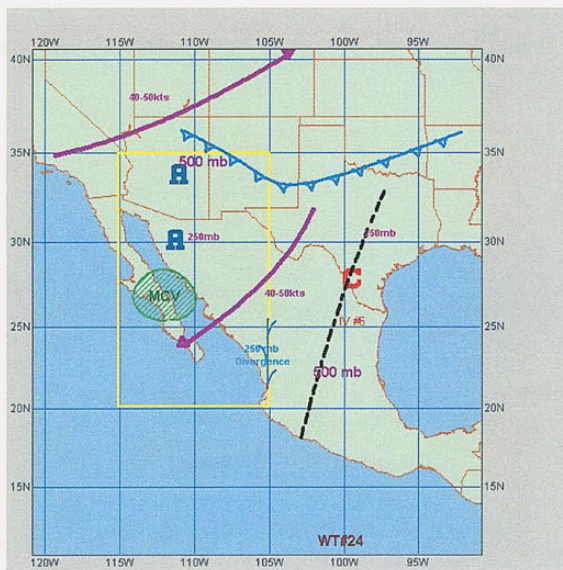
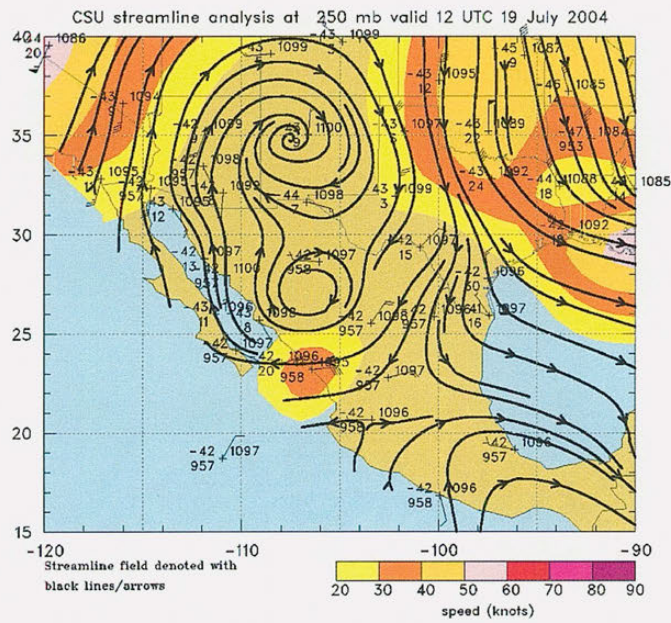


Fig. 5.8 – (cont.)

a)



b)

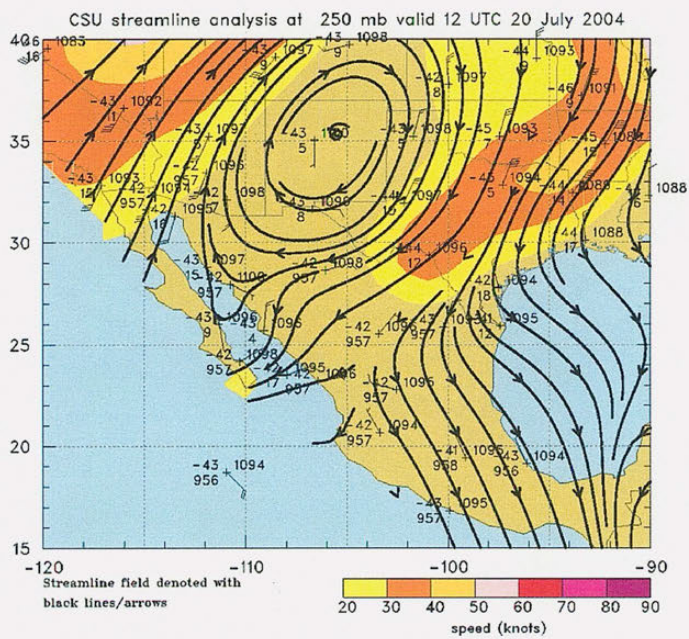
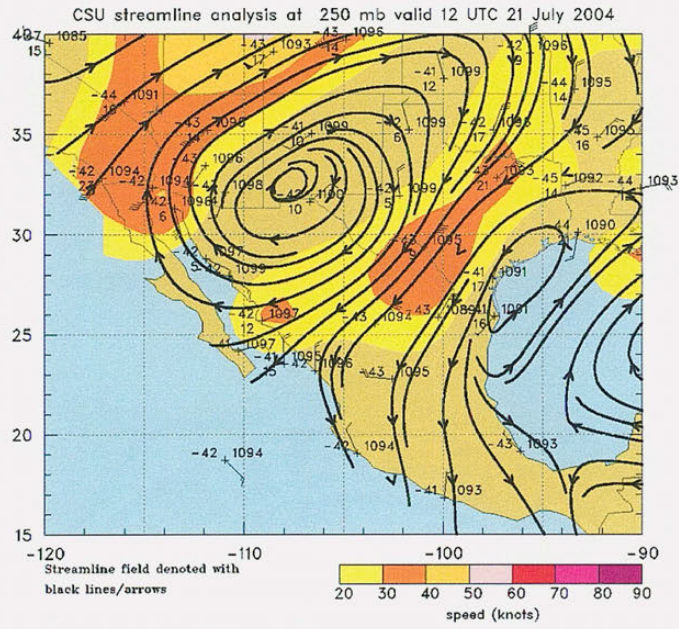


Fig. 5.9 – CSU streamline analysis map at 250 mb for a) 19 July 2004, b) 20 July 2004, c) 21 July 2004, and d) 22 July 2004.

c)



d)

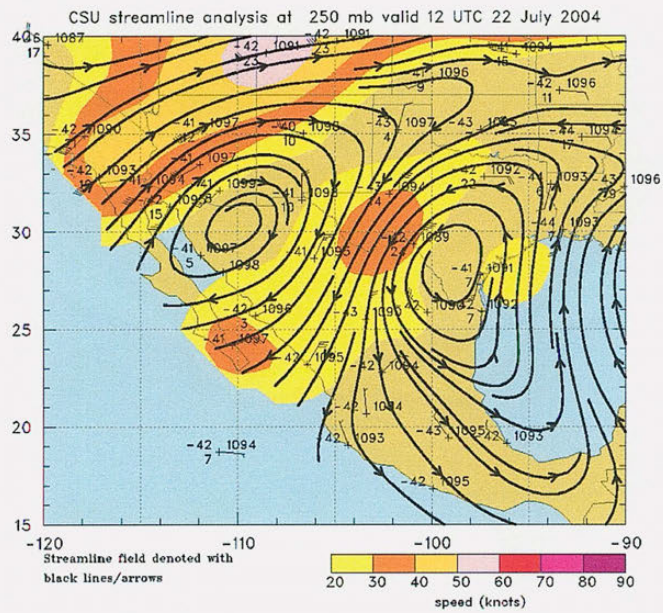


Fig. 5.9 – (cont.)

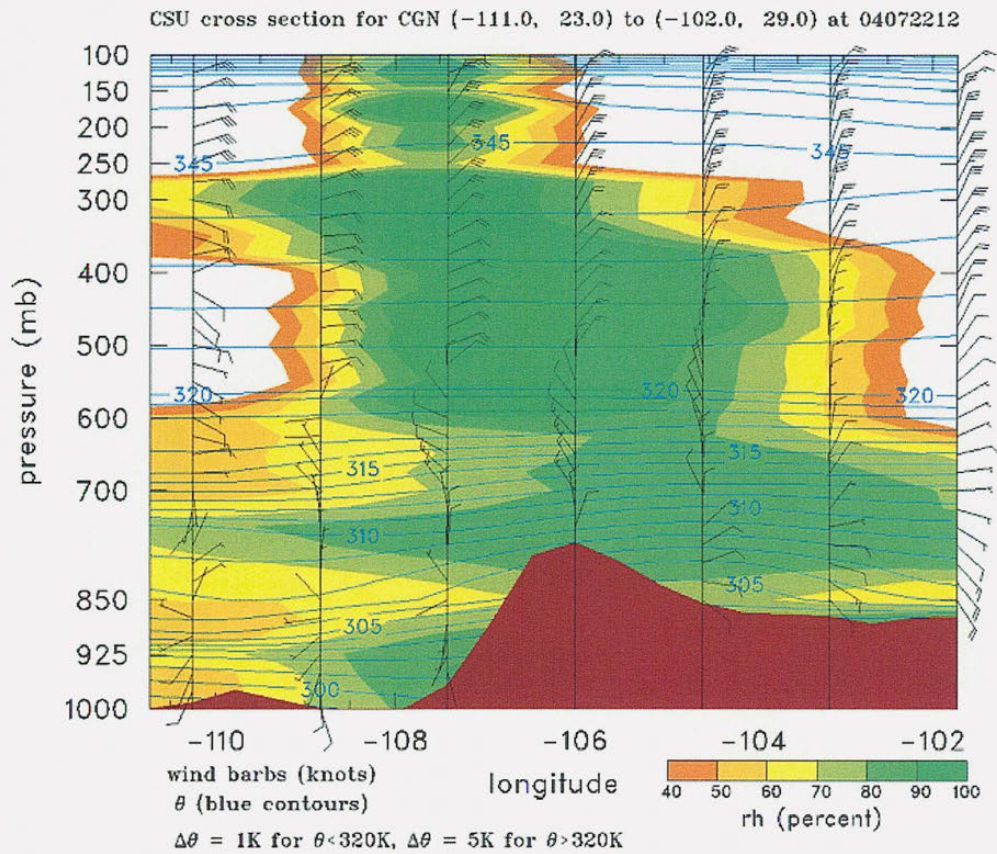


Fig. 5.10 – CSU cross section perpendicular to the southern portion of the Gulf of California from 111°N, 23°N to 102°W, 29°N showing the profile of relative humidity and wind barbs on 22 July 2004 at 12 UTC.

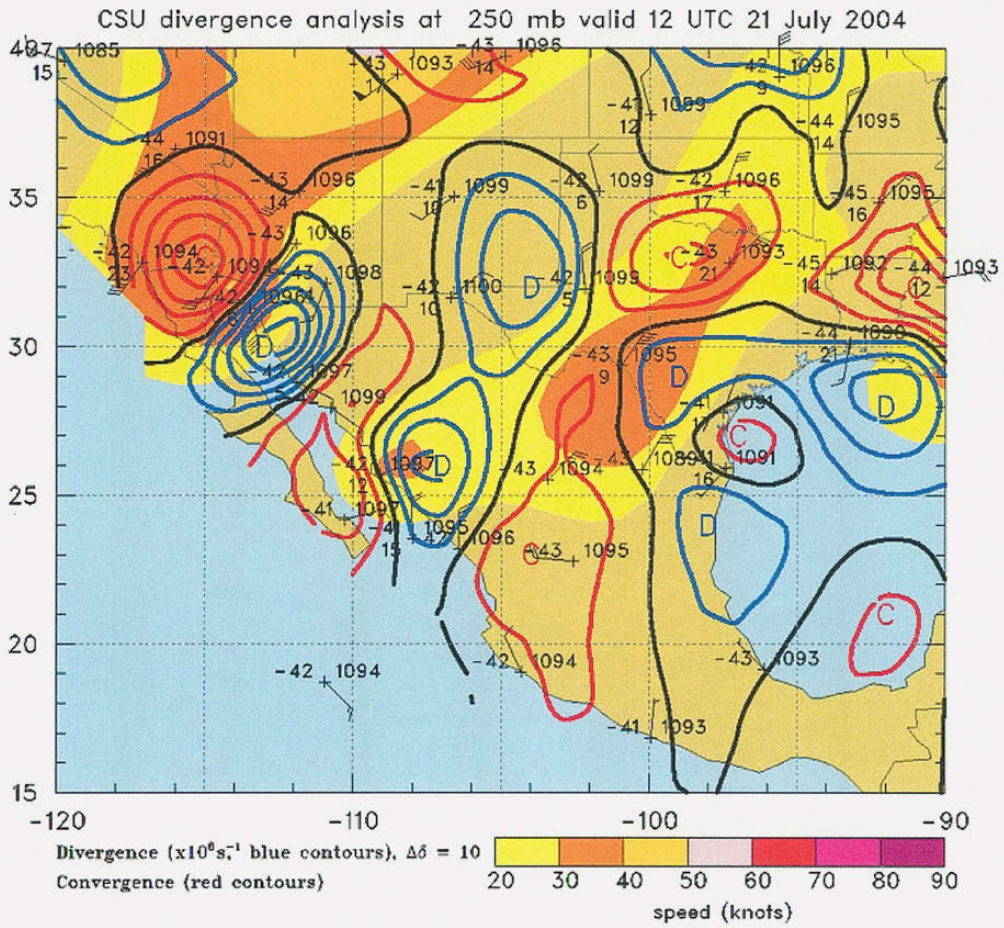


Fig. 5.11 – CSU divergence analysis at 250 mb within NAME Tier II region on 21 July 2004 at 12Z.

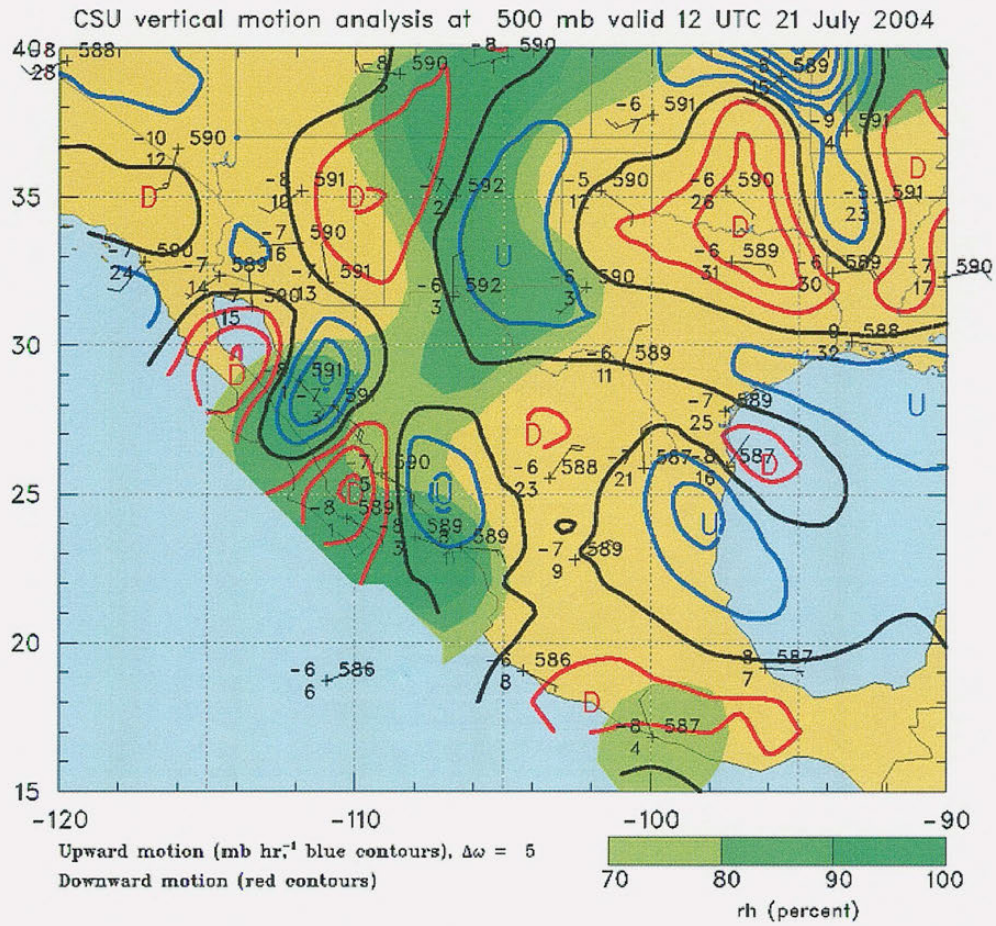


Fig. 5.12 – CSU vertical air motion analysis at 500 mb within the NAME Tier II region on 21 July 2004 at 12Z.

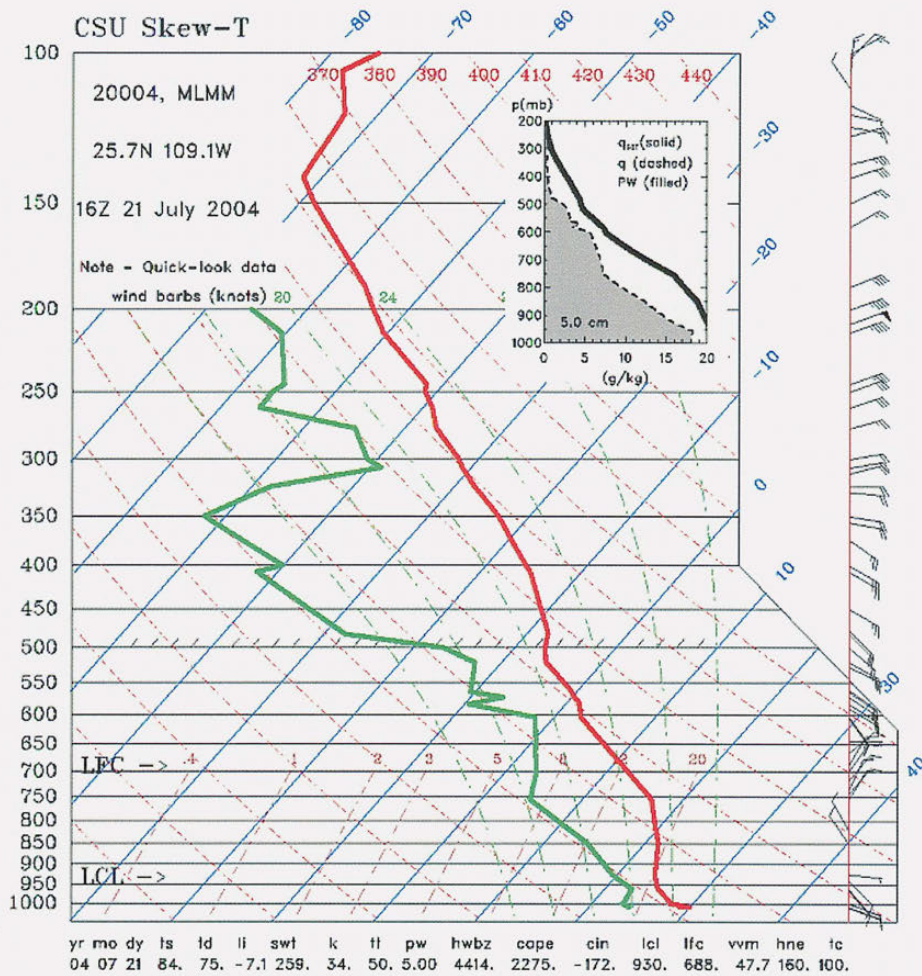


Fig. 5.13 – Skew-T plot of the sounding launched from Los Mochis, Mexico on 21 July 2004 at 16Z.

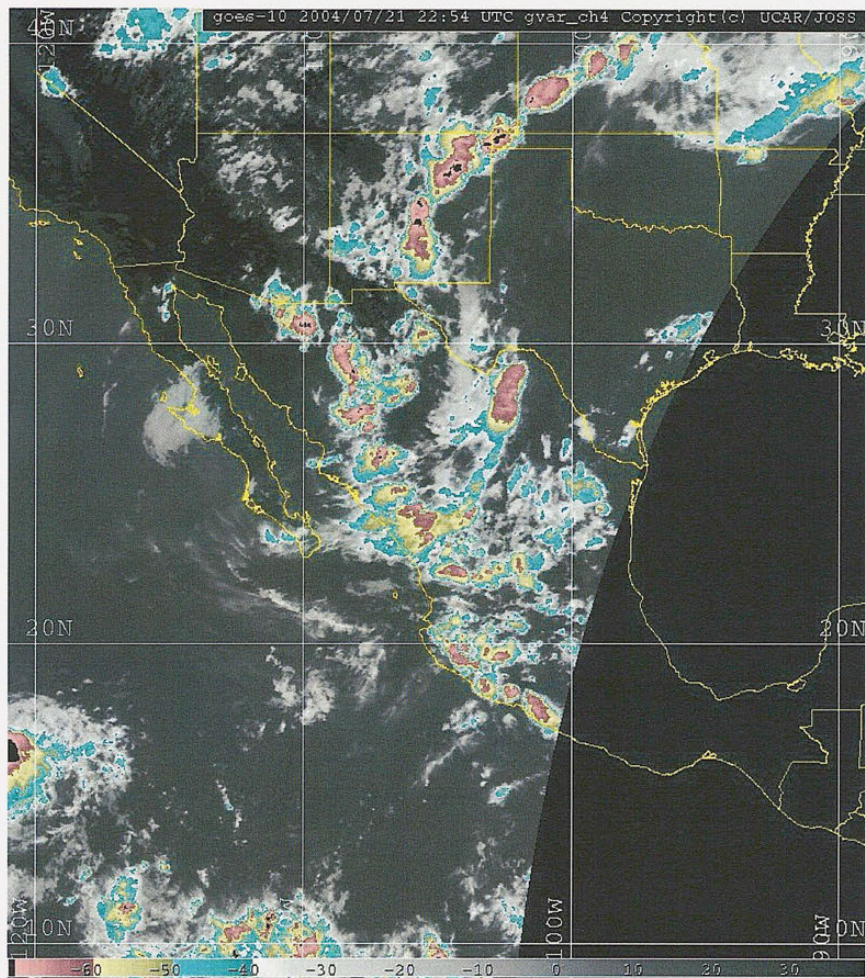


Fig. 5.14 – Infrared Satellite Image from GOES-10 on 21 July 2004 at 2254 UTC.

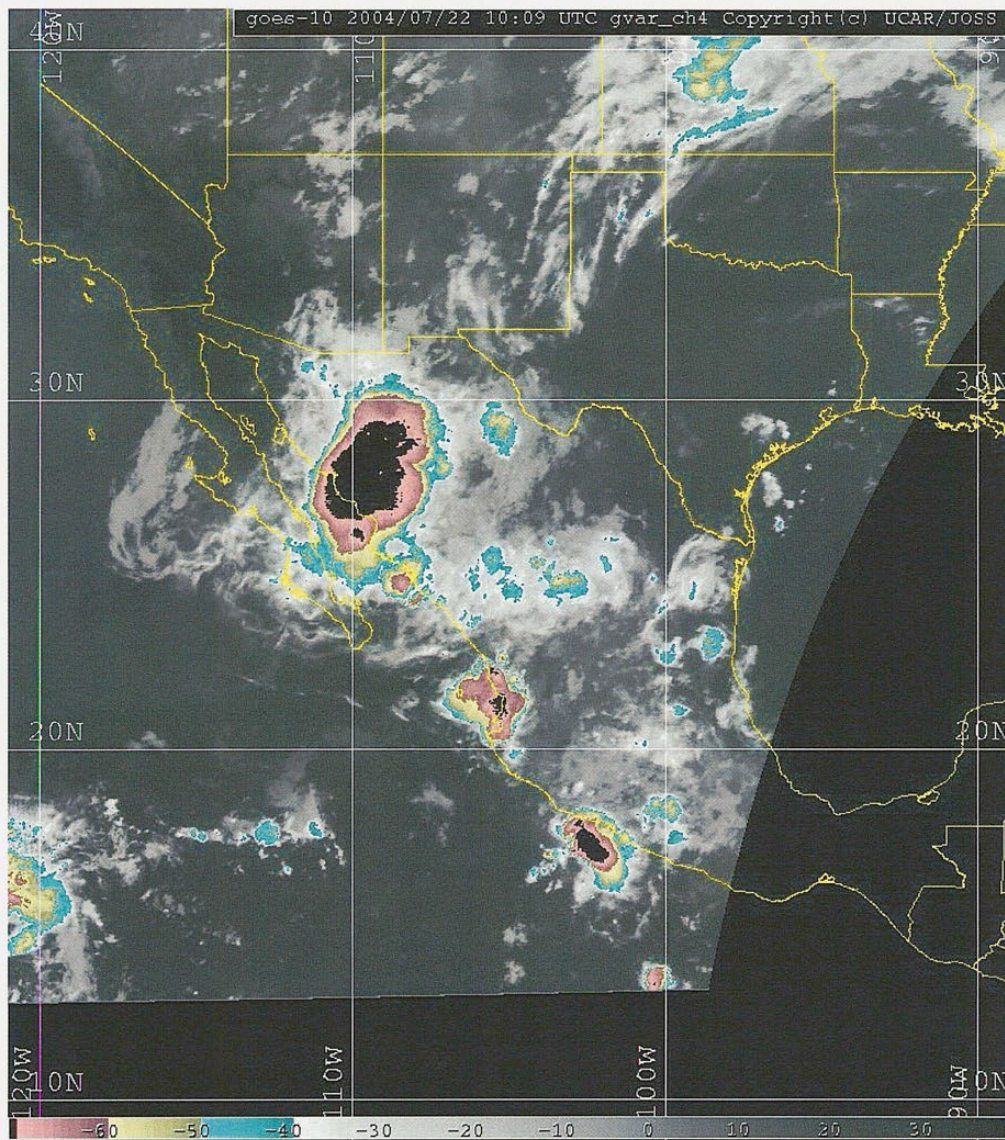


Fig. 5.15 – Infrared Satellite Image from GOES-10 on 22 July 2004 at 1009 UTC.

NAME Flight (Level= 950_mb) 2004/07/22

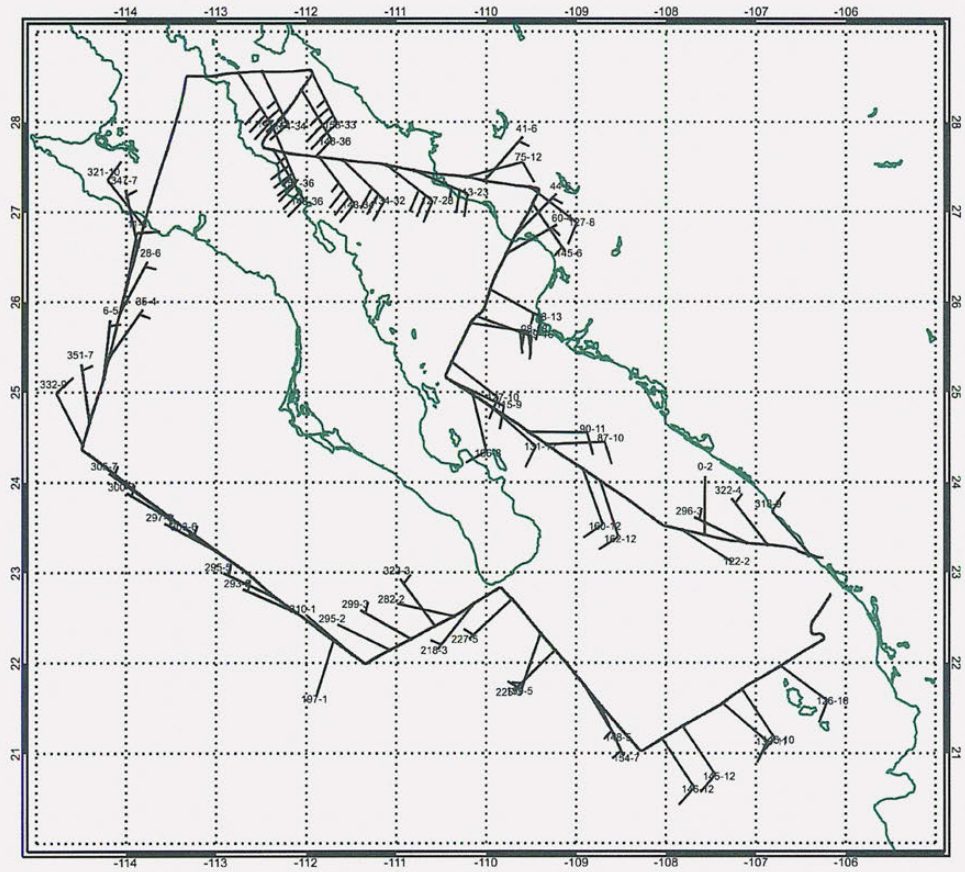


Fig. 5.16 – 950 mb wind speed and direction along the flight path of NOAA's P3 airplane on 22 July 2004 around 1300 UTC.

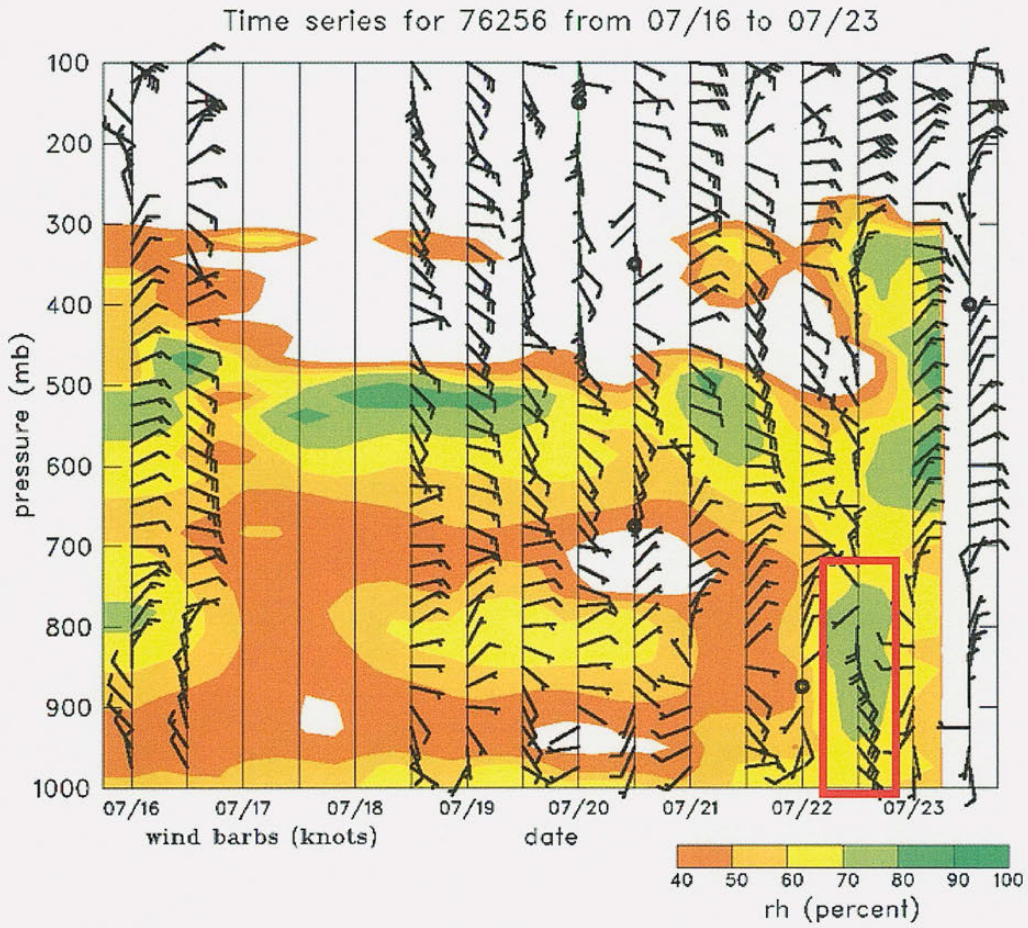


Fig. 5.17 – Wind and relative humidity profile time series at Empalme, Mexico. The red box highlights the moist southeasterly flow pushing moisture northward along the Gulf of California.

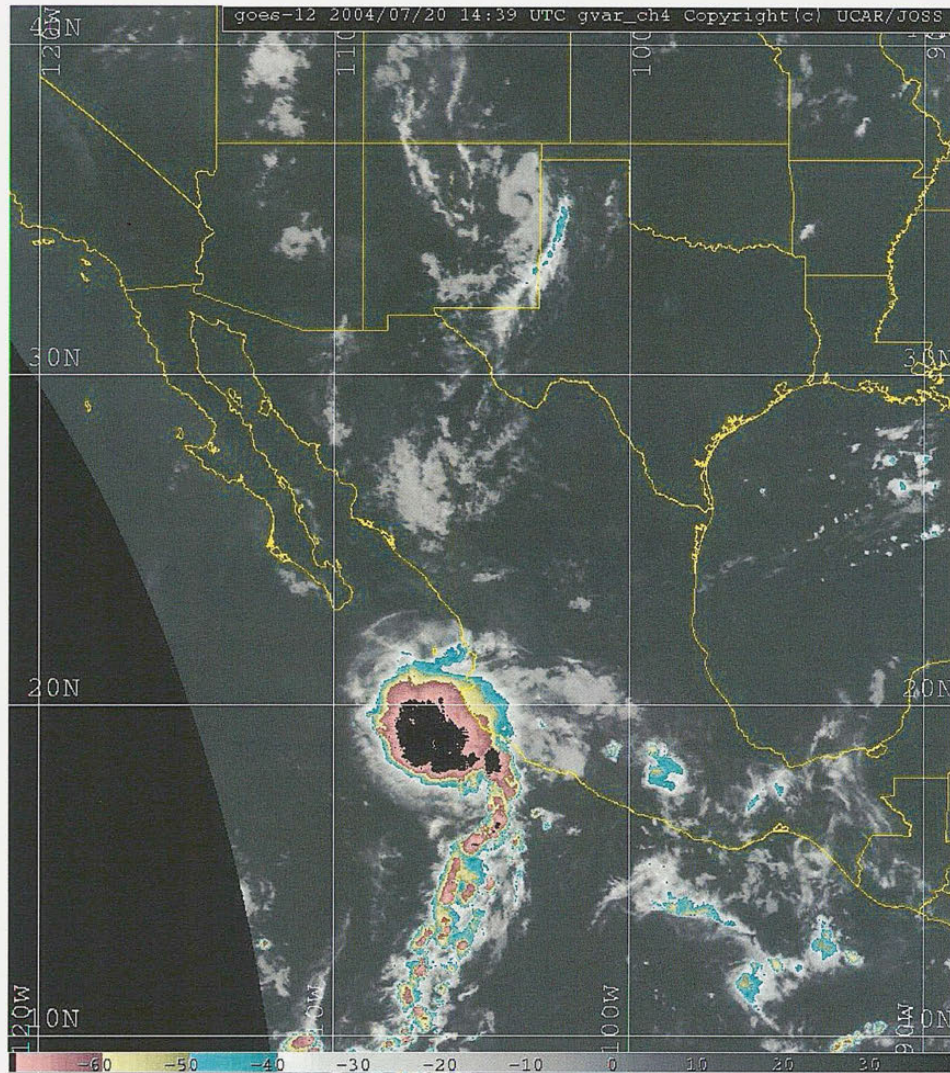
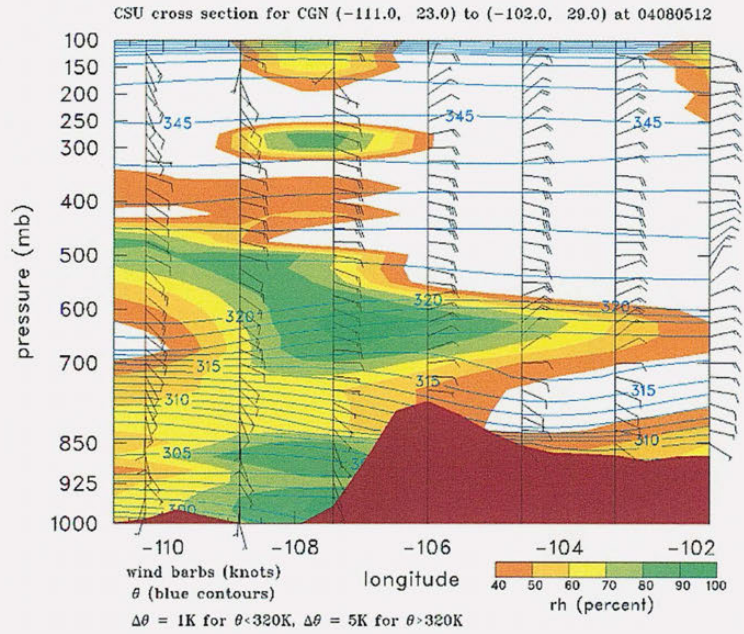


Fig. 5.18 – Infrared Satellite Image from GOES-12 on 20 July 2004 at 1439 UTC.

a)



b)

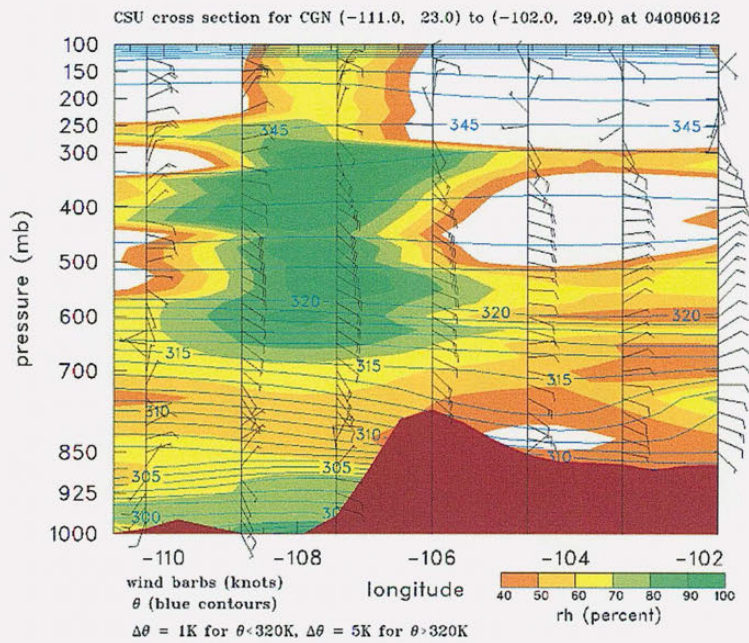
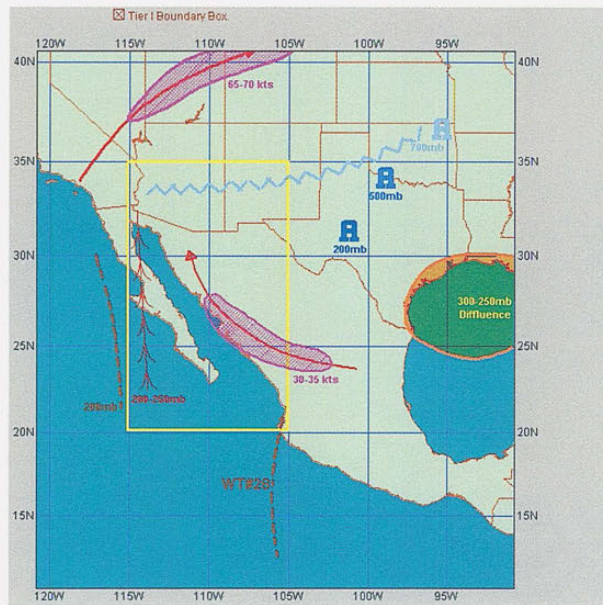


Fig. 5.19 – CSU cross section perpendicular to the southern portion of the Gulf of California from 111°N, 23°N to 102°W, 29°N showing the profile of relative humidity and wind barbs on a) 5 August 2004 at 12 UTC, and b) 6 August 2004 at 12 UTC.

a)



b)

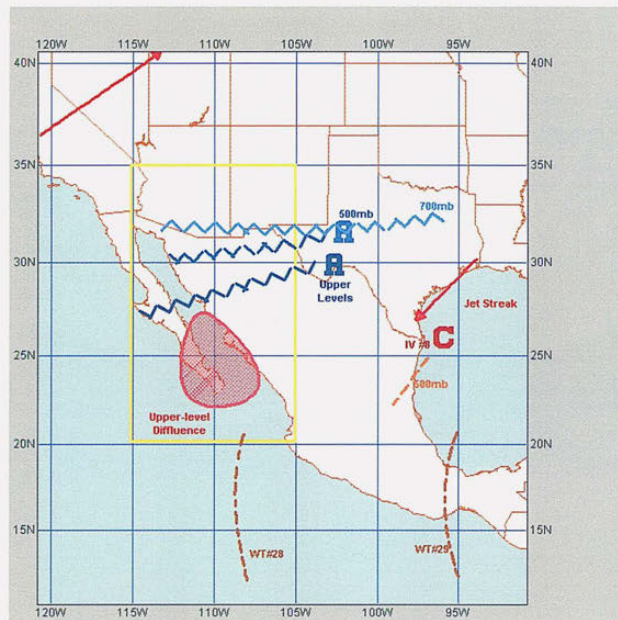
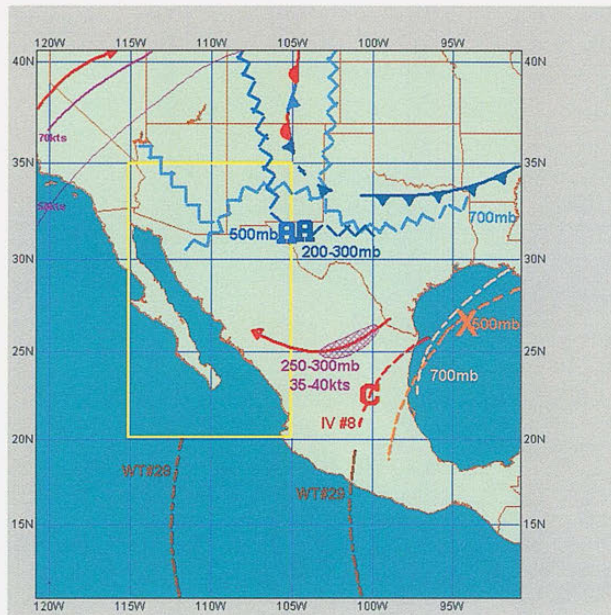


Fig. 5.20 – Map identifying synoptic features within the NAME Tier II region on a) 3 August 2004, b) 4 August 2004, c) 5 August 2004, and d) 6 August 2004.

c)



d)

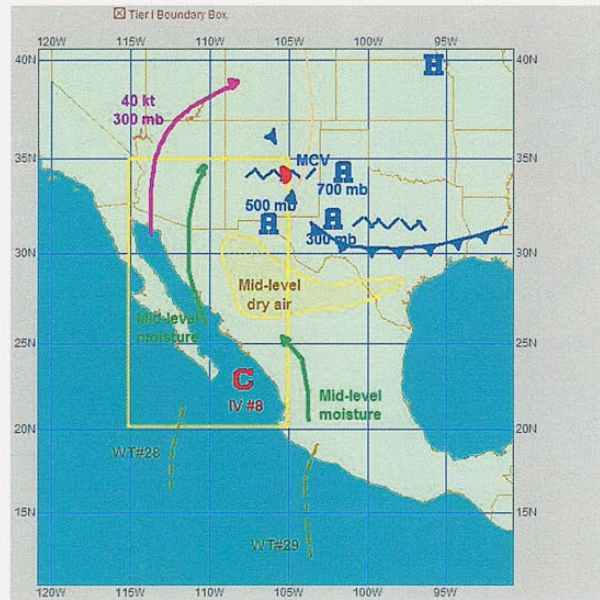
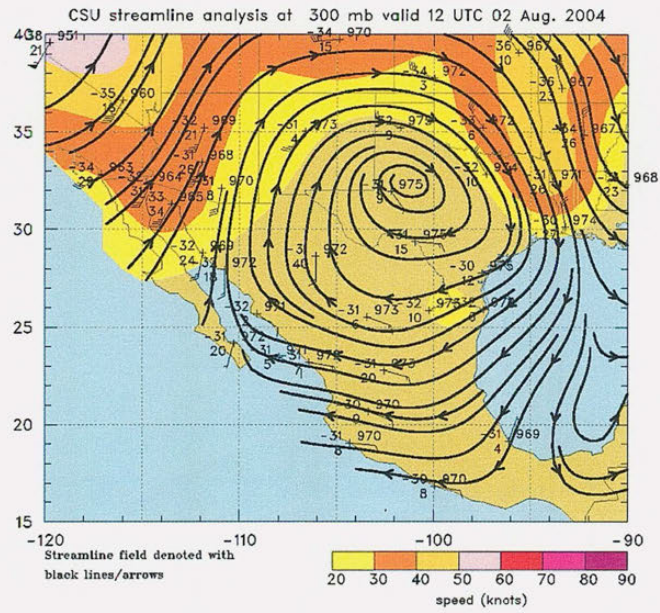


Fig. 5.20 – (cont.)

a)



b)

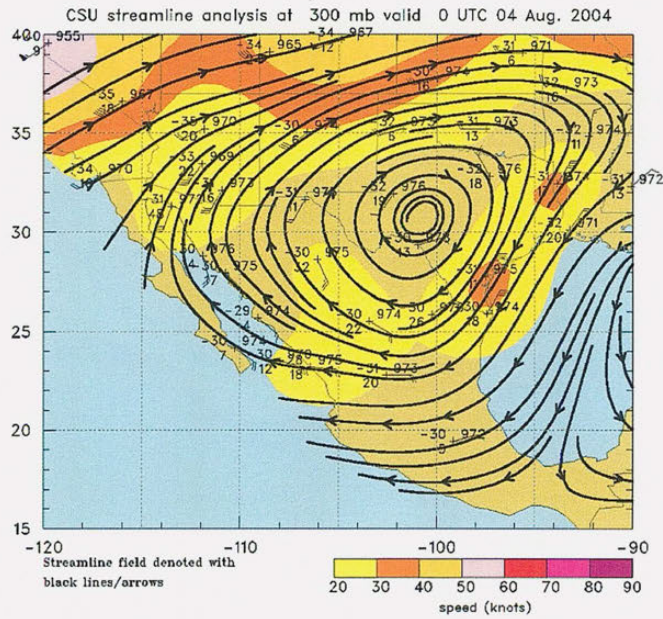


Fig. 5.21 – CSU streamline analysis map at 300 mb for a) 2 August 2004 at 12 UTC, and b) 4 August at 00Z.

250 mb rawinsonde data 12z Wed 04 Aug 2004

250 mb Heights (dm) / Isotachs (knots)

0-hour analysis valid 1200 UTC Wed 04 Aug 2004

RUC (12z 04 Aug)

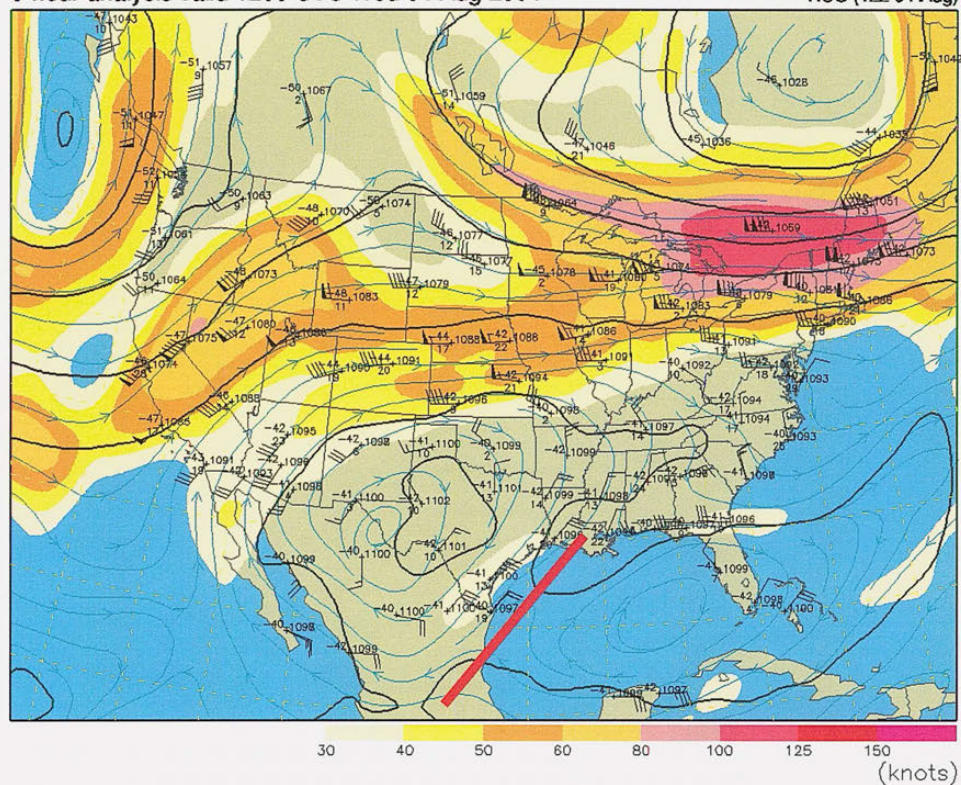
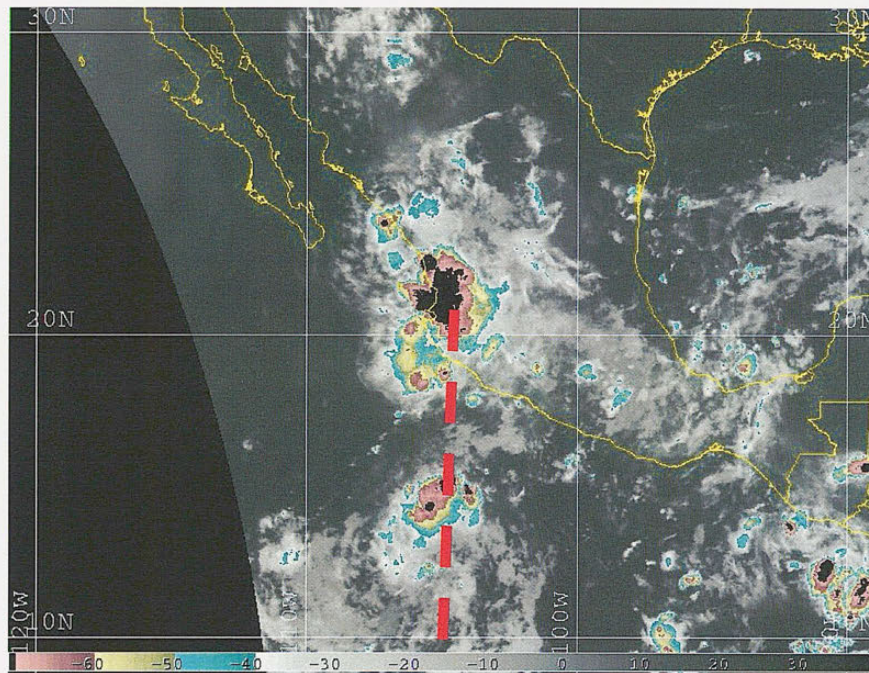


Fig. 5.22 – Rapid Update Cycle model analysis of 250 mb wind observations, with cyan streamlines for 4 August 2004 at 12 UTC. The thick red line highlights the axis of the inverted trough.

a)



b)

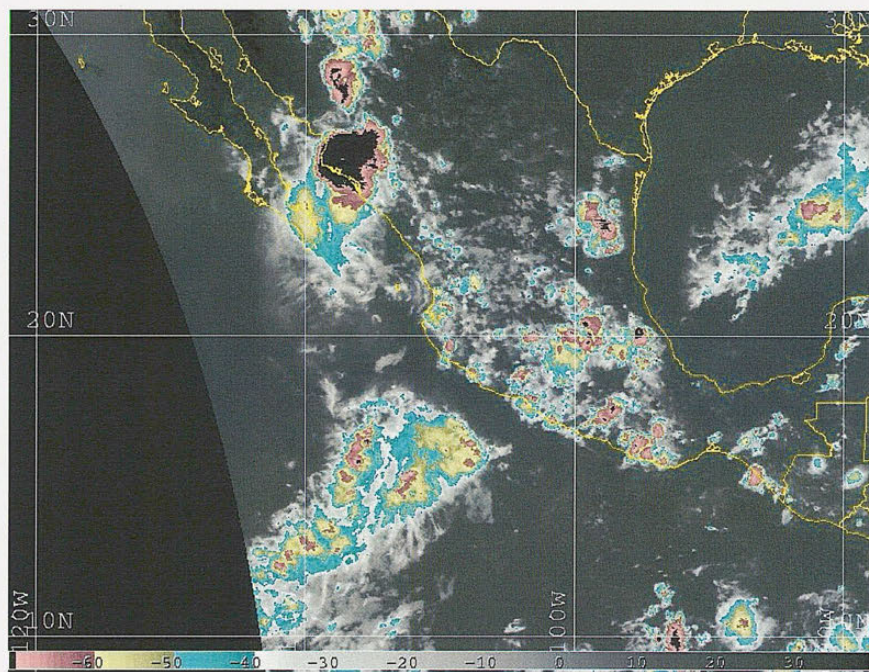
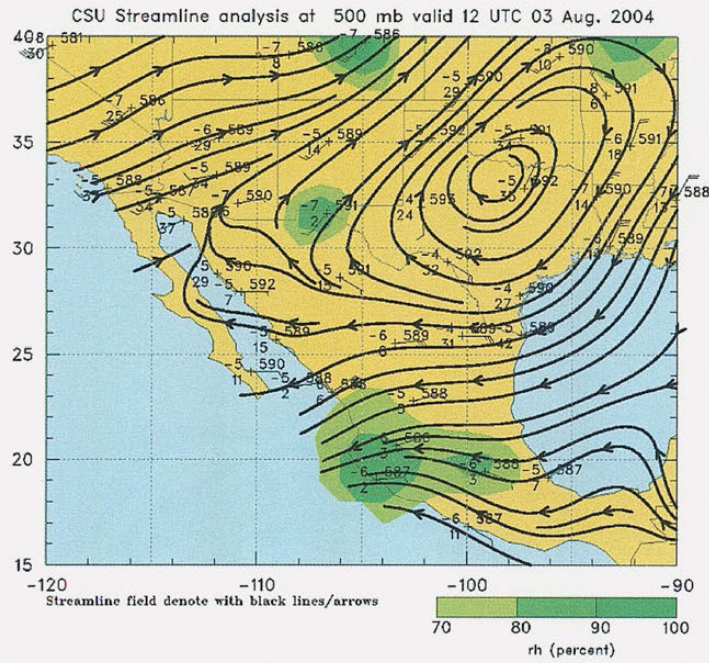


Fig. 5.23 – Infrared Satellite Image from GOES-12 on 3 August 2004 at a) 0939 UTC and b) 2238 UTC. The red dashed line indicates the position of the tropical wave.

a)



b)

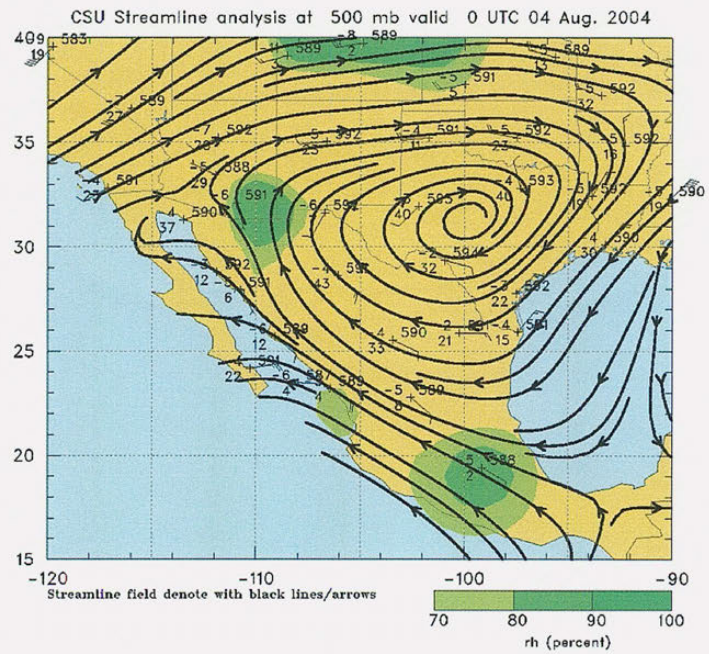


Fig. 5.24 – CSU streamline analysis map at 700 mb for a) 3 August 2004 at 12 UTC, and b) 4 August at 00Z.

24-hour Precipitation (mm) ending 12Z 20040805

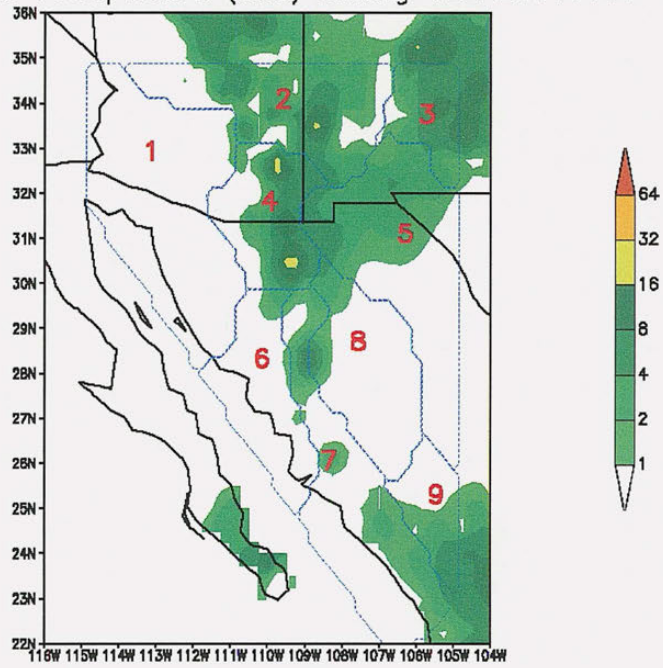


Fig. 5.25 – Climate Prediction Center/*Servicio Meteorológico Nacional* precipitation analysis within NAME Tier 1 for 4 August 2004.

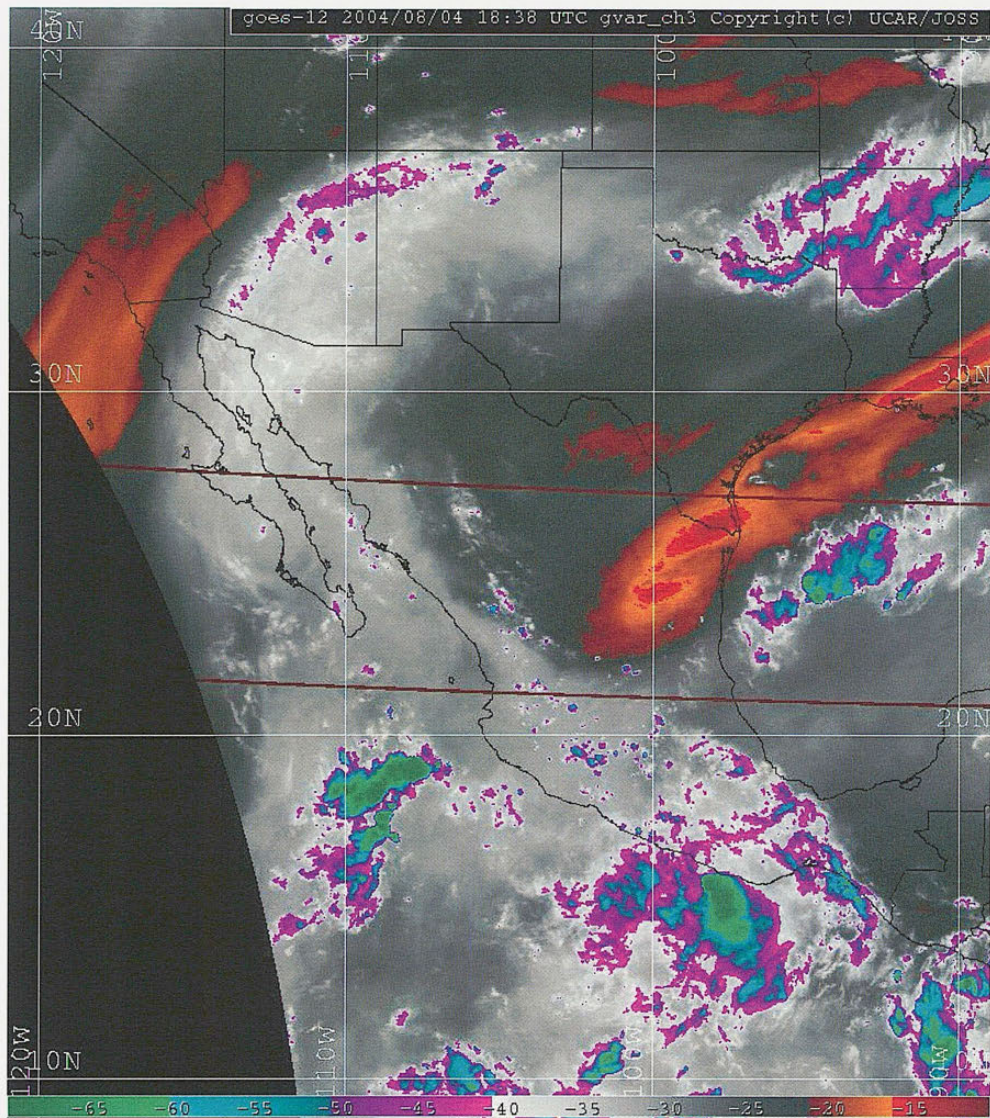
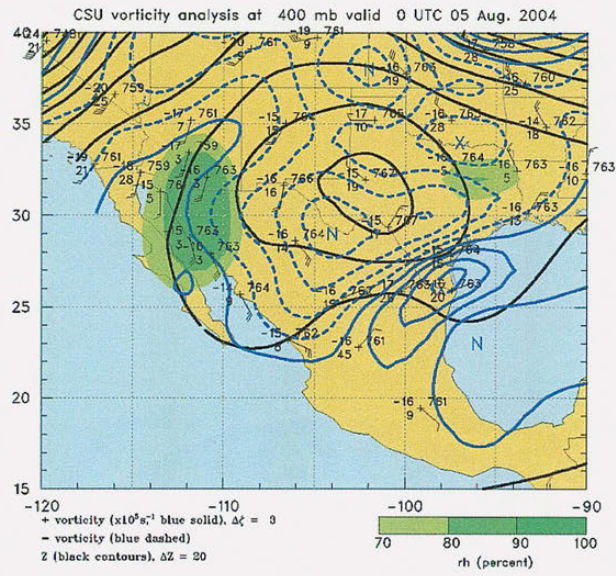


Fig. 5.26 – Water Vapor Satellite Image from GOES-12 on 4 August 2004 at 1838 UTC.

a)



b)

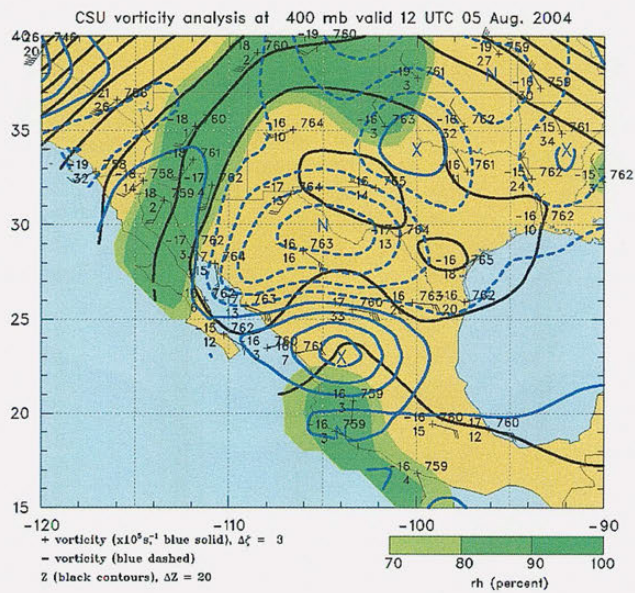
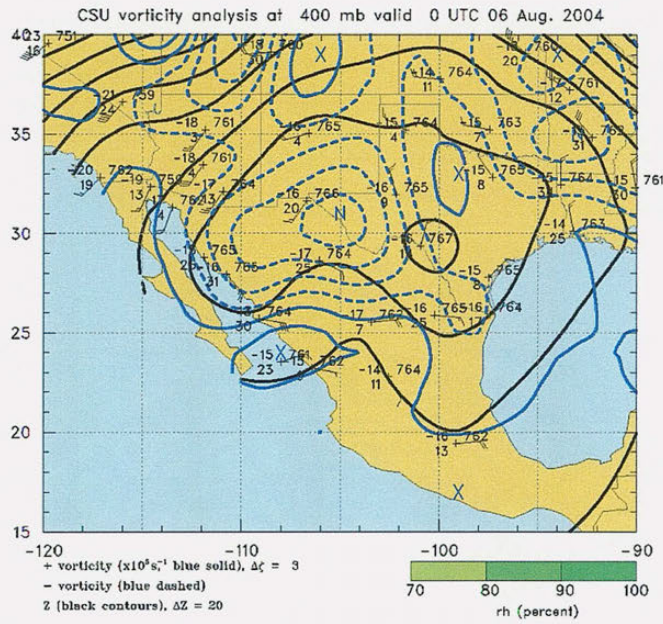


Fig. 5.27 – CSU vorticity analysis map at 400 mb for a) 5 August 2004 at 00 UTC, b) 5 August 2004 at 12 UTC, c) 6 August 2004 at 00 UTC, and d) 6 August 2004 at 12 UTC.

c)



d)

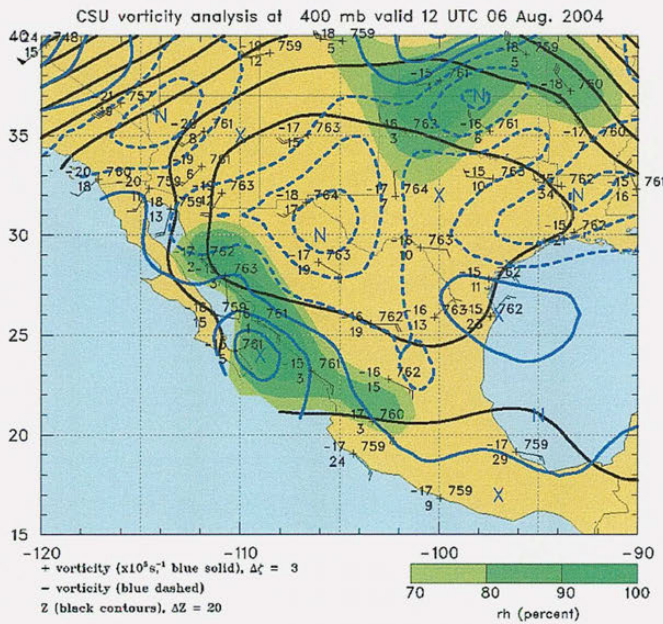


Fig. 5.27 – (cont.)

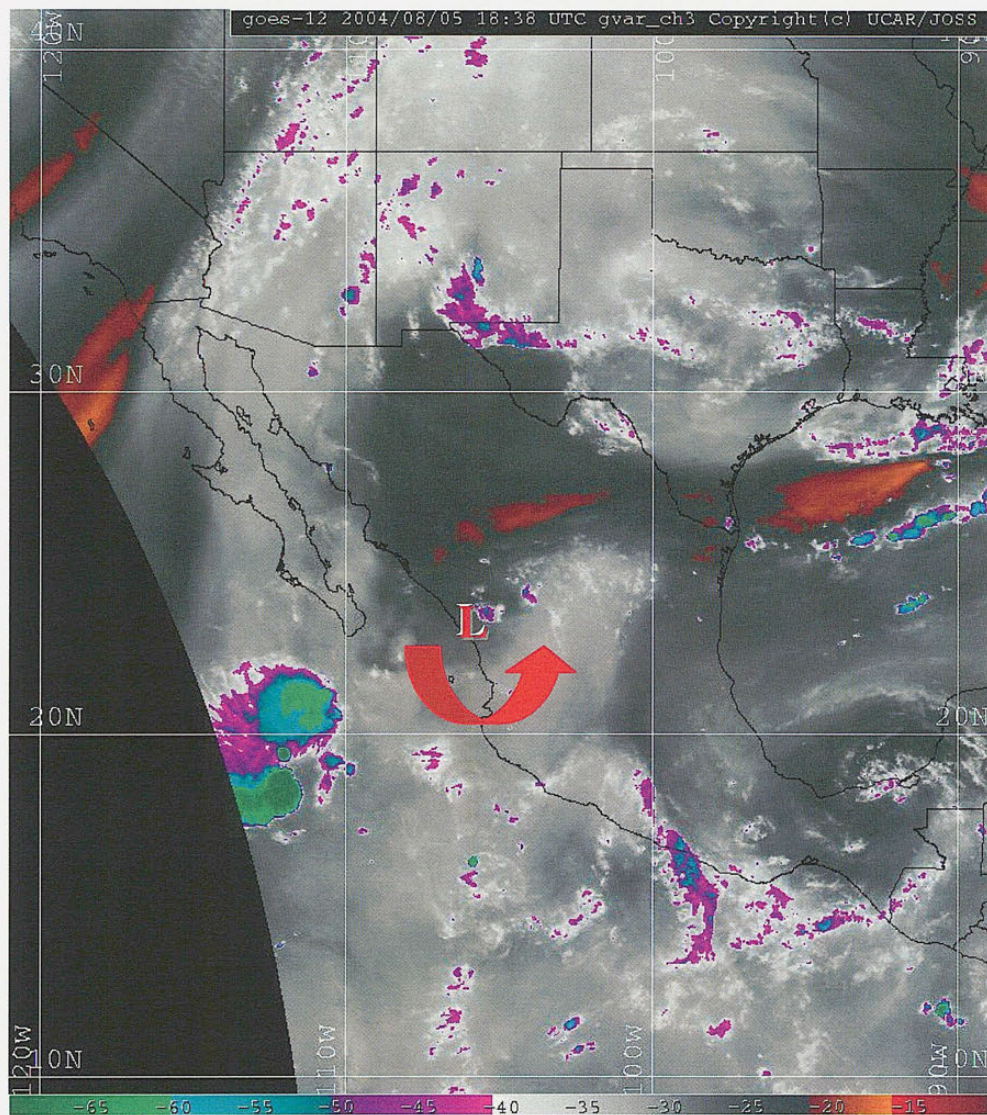


Fig. 5.28 – Water Vapor Satellite Image from GOES-12 on 5 August 2004 at 1838 UTC. The red L marks the position of the TUTT, and the arrow highlights the circulation bringing mid-level moisture into the NAME ECA region.

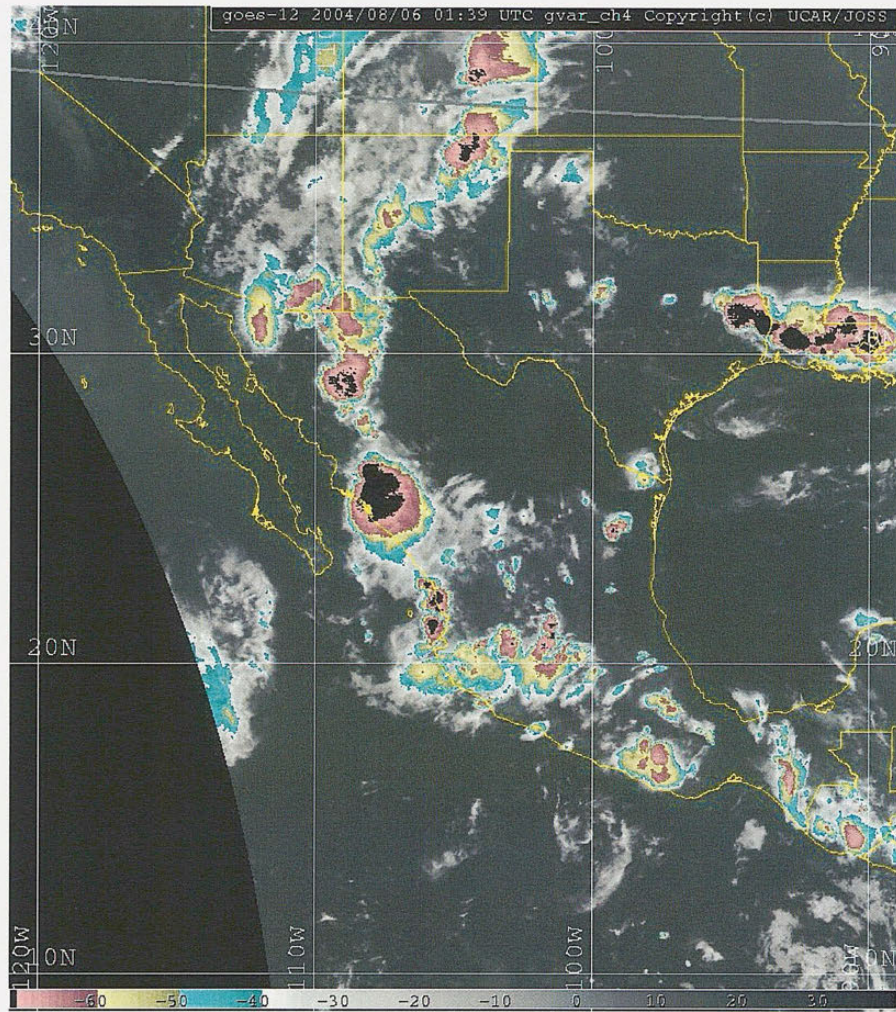


Fig. 5.29 – Infrared Satellite Image from GOES-12 on 6 August 2004 at 0139 UTC.

24-hour Precipitation (mm) ending 12Z 20040806

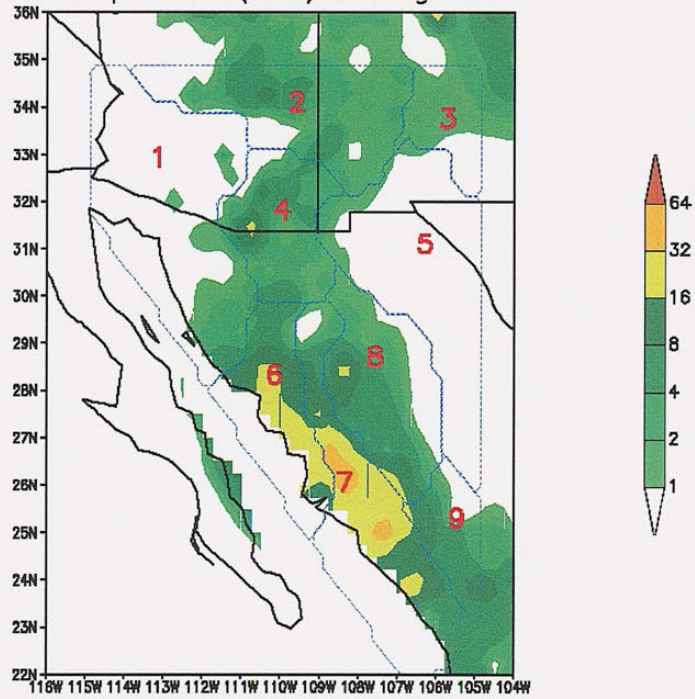


Fig. 5.30 - Climate Prediction Center/*Servicio Meteorológico Nacional* precipitation analysis within NAME Tier 1 for 5 August 2004.

500 mb Height (m, blue), T(C, red) & Winds (kts)

2004-08-06_12:00:00 = 2004-08-06_12:00:00 + 0 h

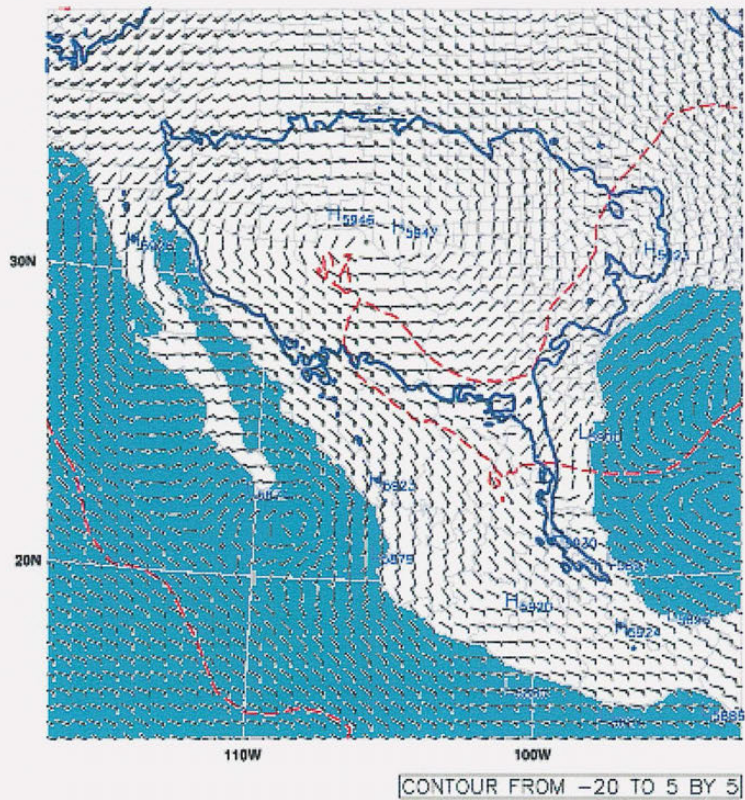
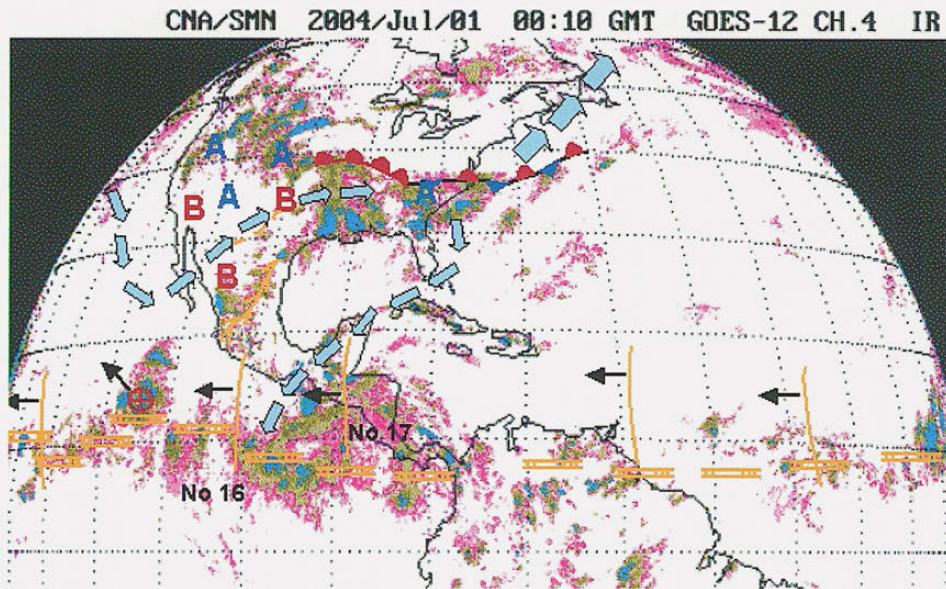


Fig. 5.31 – NCAR 12-km WRF model analysis of 500 mb winds on 6 July 2004 at 12 UTC.

a)



b)

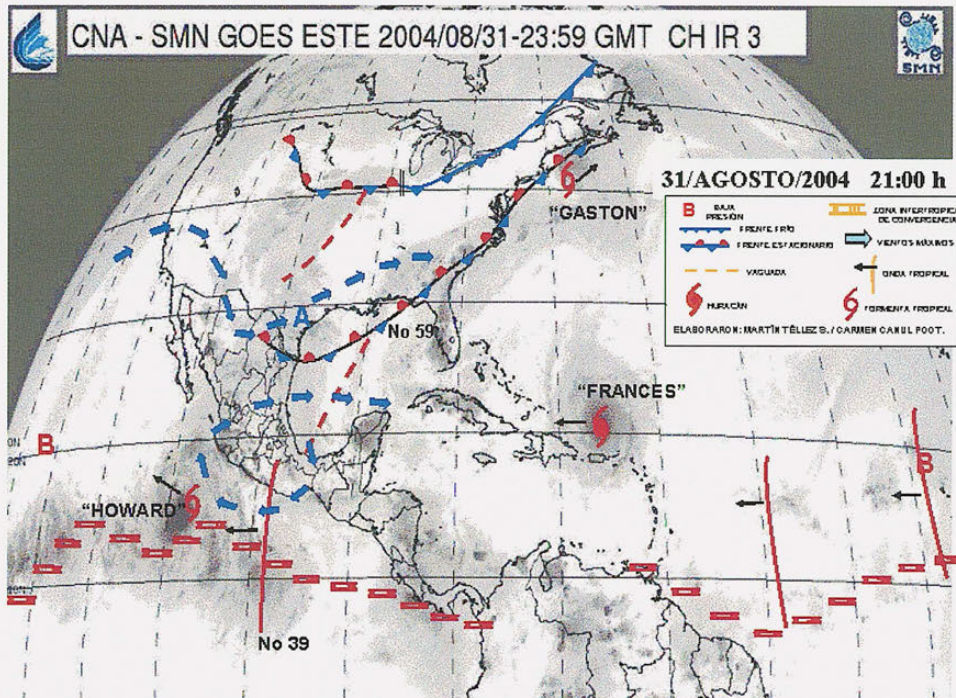
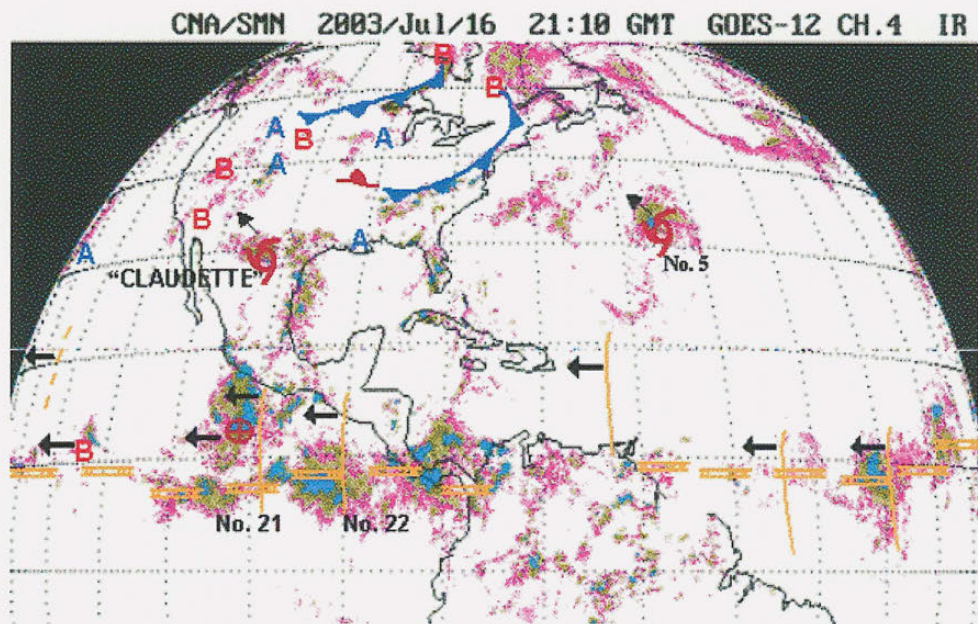


Fig. 5.32 - Servicio Meteorológico Nacional synoptic features map overlaid on satellite imagery valid on a) 1 July 2004, and b) 31 August 2004.

a)



b)

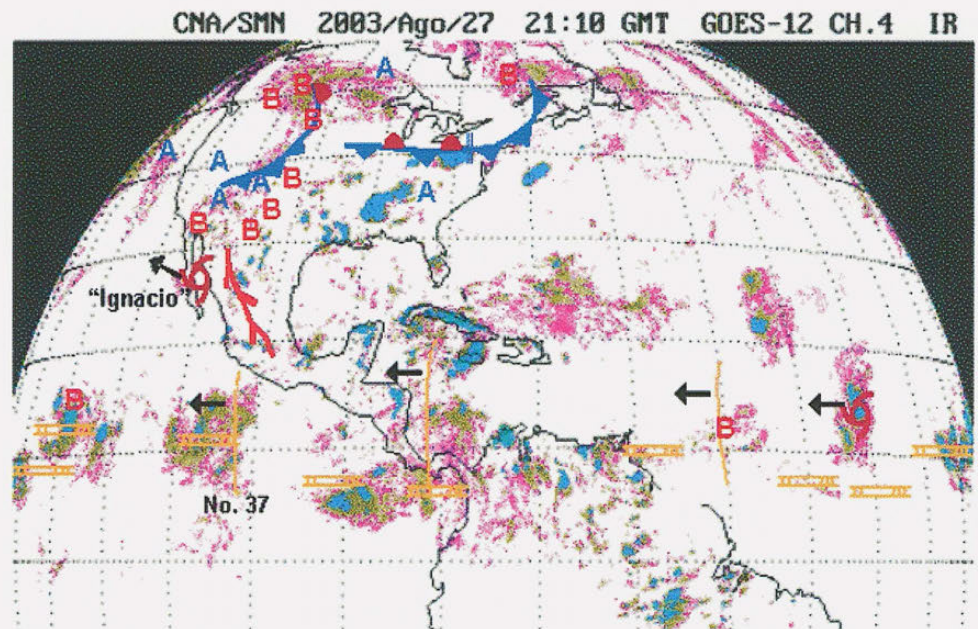
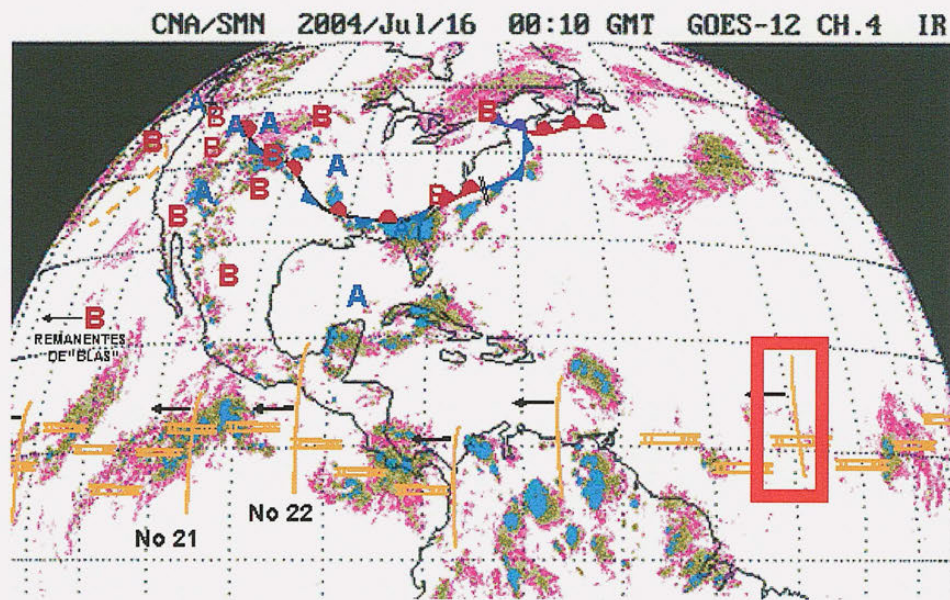


Fig. 5.33 - *Servicio Meteorológico Nacional* synoptic features map overlaid on satellite imagery valid on a) 16 July 2003, and b) 27 August 2003.

Table 5.1 – Approximate dates when tropical easterly waves were identified in synoptic maps between 100° and 110° W.

Tropical Wave	Dates	Tropical Wave	Dates
16	30 June -2 July 2004	28	1-3 August 2004
17	3-5 July 2004	29	4-7 August 2004
18	6-8 July 2004	30	7-9 August 2004
19	9-11 July 2004	31	11-12 August 2004
20	11-13 July 2004	32	13-15 August 2004
21	14-16 July 2004	33	16-17 August 2004
22	16-18 July 2004	34	18-19 August 2004
23	19-21 July 2004	35	20-22 August 2004
24	22-24 July 2004	36	23-25 August 2004
25	24-26 July 2004	37	25-26 August 2004
26	26-28 July 2004	38	28-31 August 2004
27	31 July – 1 August 2004	-	-/-

a)



b)

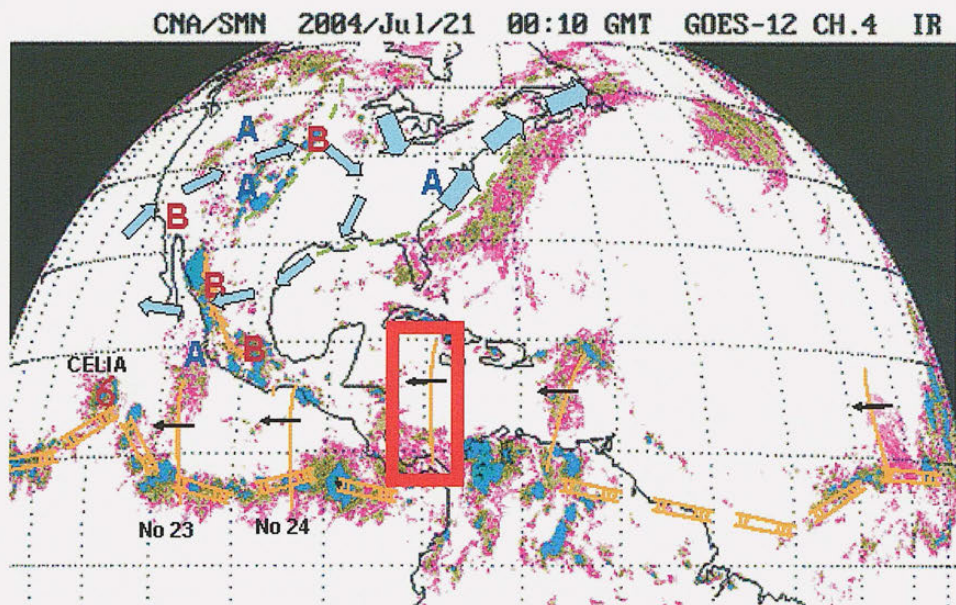
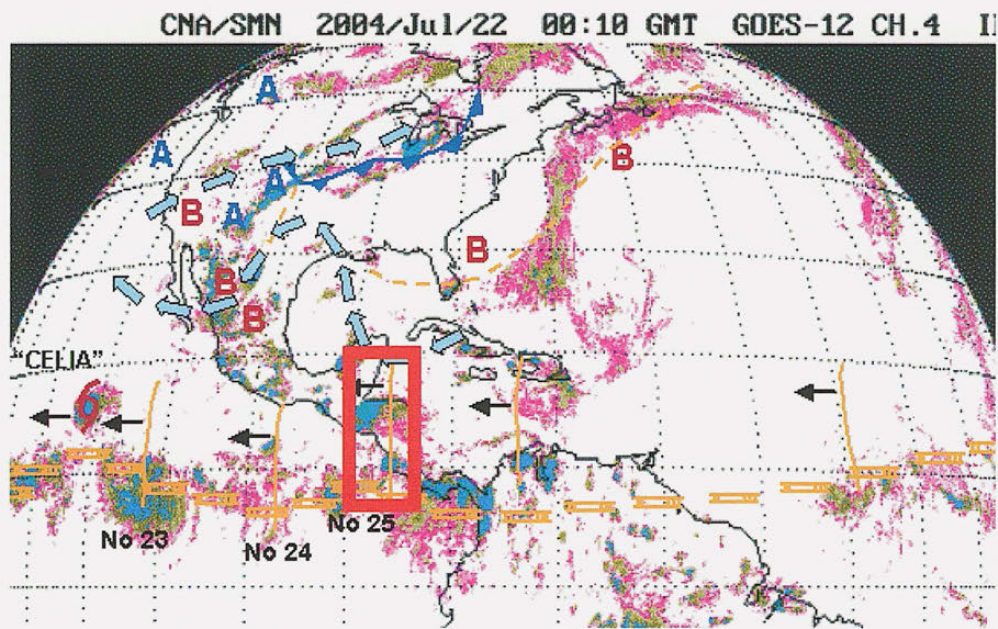


Fig. 5.34 - *Servicio Meteorológico Nacional* synoptic features map overlaid on satellite imagery valid on a) 16 July 2004, b) 21 July 2004, c) 22 July 2004, and d) 23 July 2004. The red box highlights the same tropical wave as it propagates westward.

c)



d)

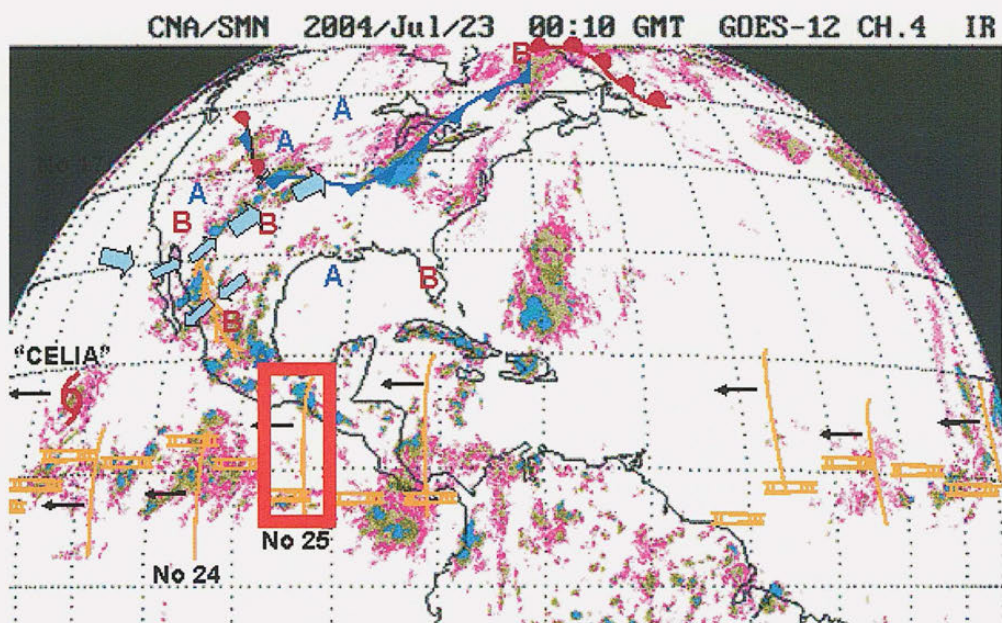
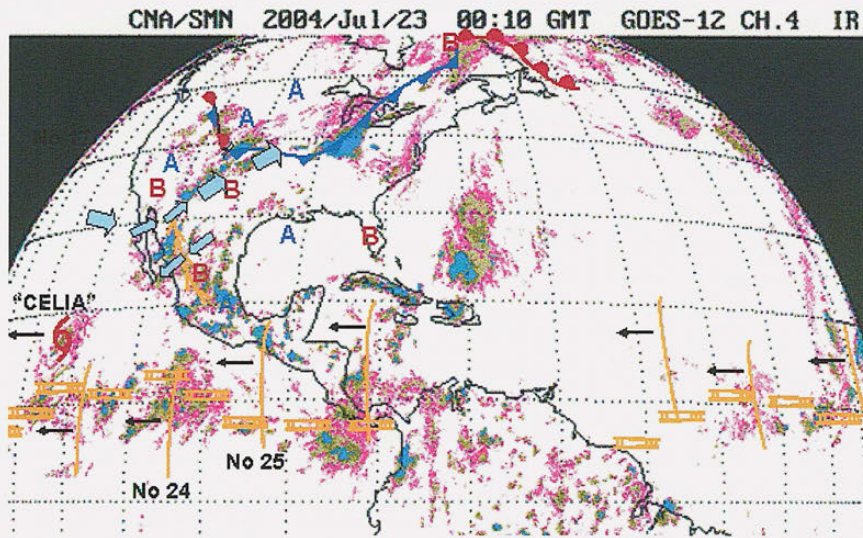


Fig. 5.34 – (cont.)

a)



b)

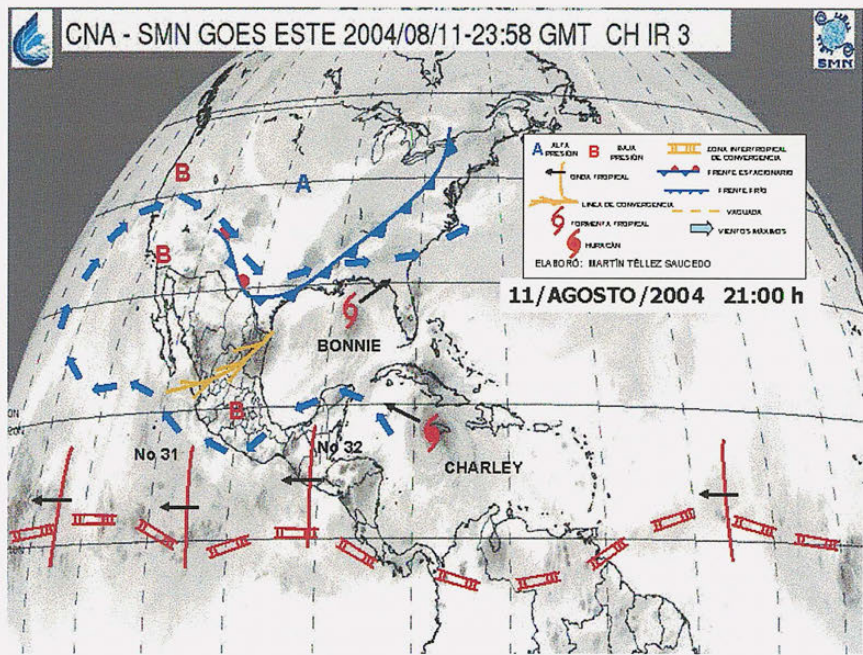
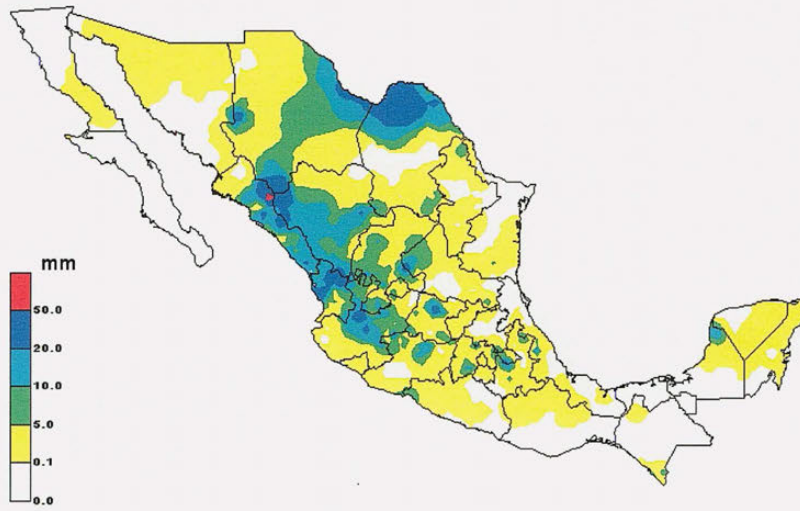


Fig. 5.35 - *Servicio Meteorológico Nacional* synoptic features map overlaid on satellite imagery valid on a) 23 July 2004, and b) 11 August 2004.

a)



b)

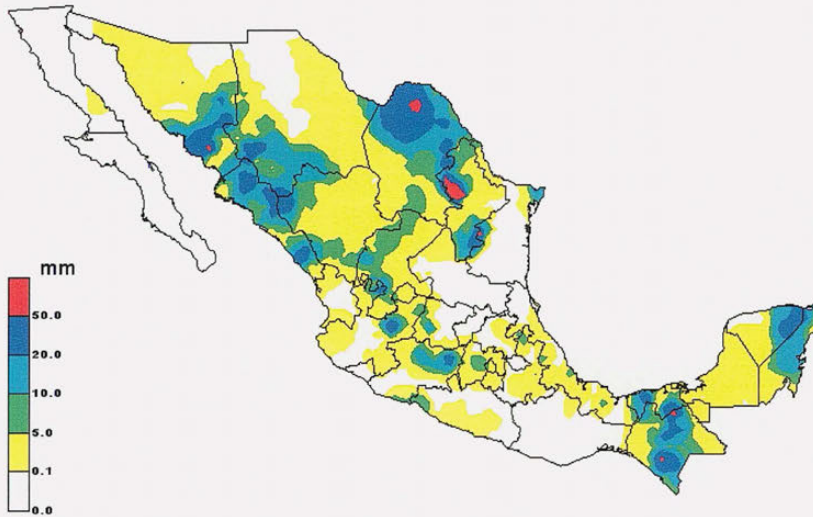
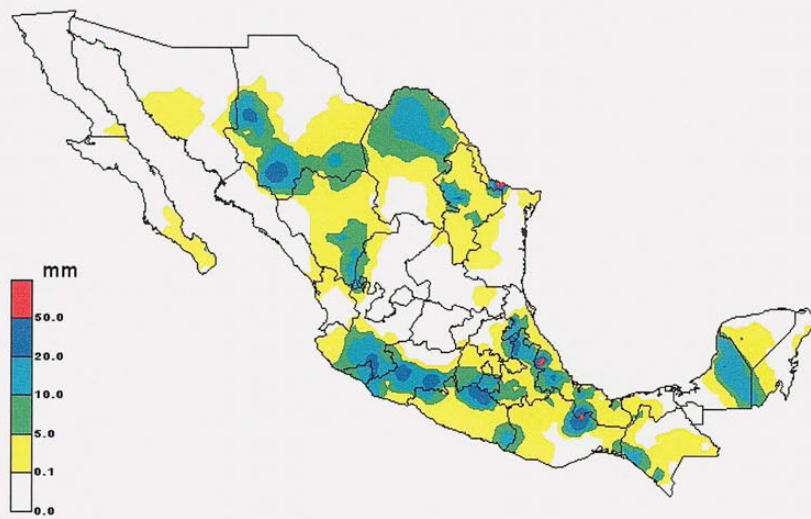


Fig. 5.36 – *Servicio Meteorológico Nacional* daily precipitation map over Mexico for a) 8 August 2004, b) 9 August 2004, c) 10 August 2004, d) 11 August 2004, and e) 12 August 2004.

c)



d)

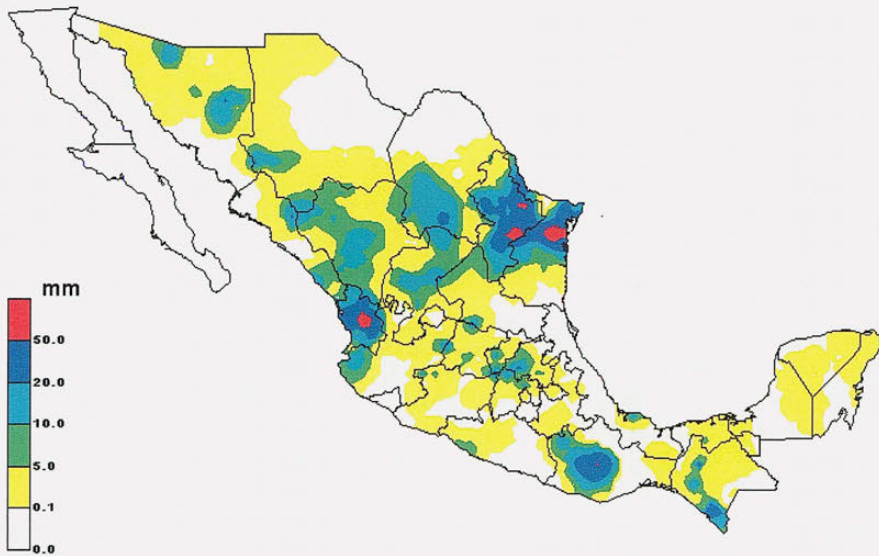


Fig. 5.36 – (cont.)

e)

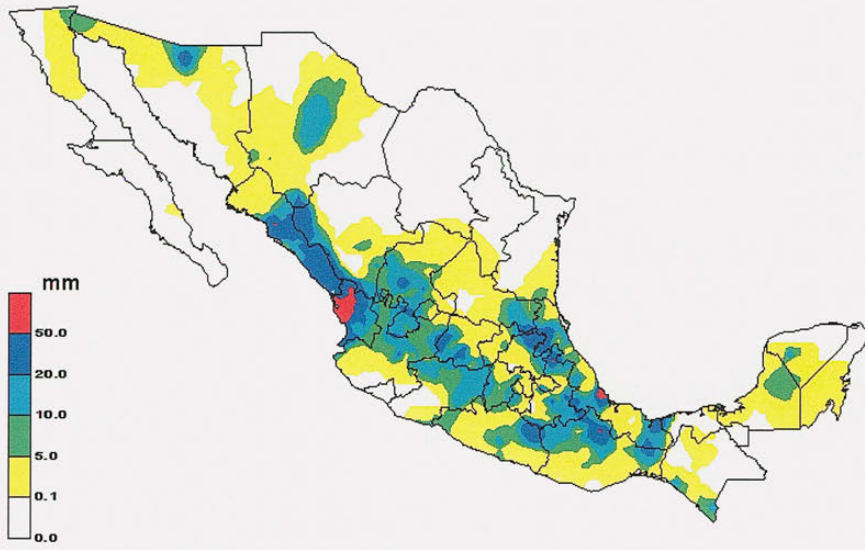
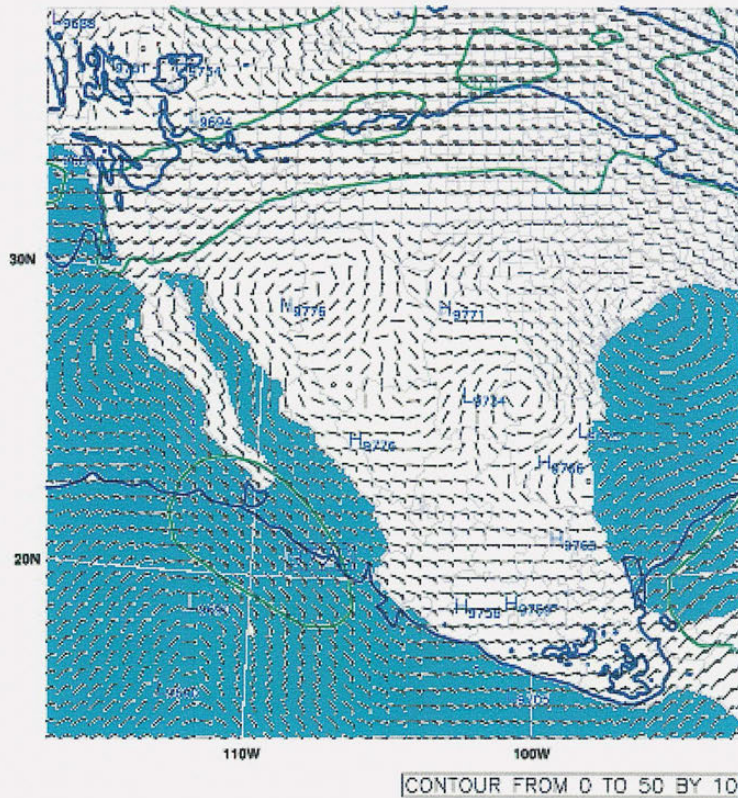


Fig. 5.36 – (cont.)

a)

300 mb Hgt (m, blue), Wind Speed (m/s, green) & Winds (kts)

2004-08-08_00:00:00 = 2004-08-08_00:00:00 + 0 h

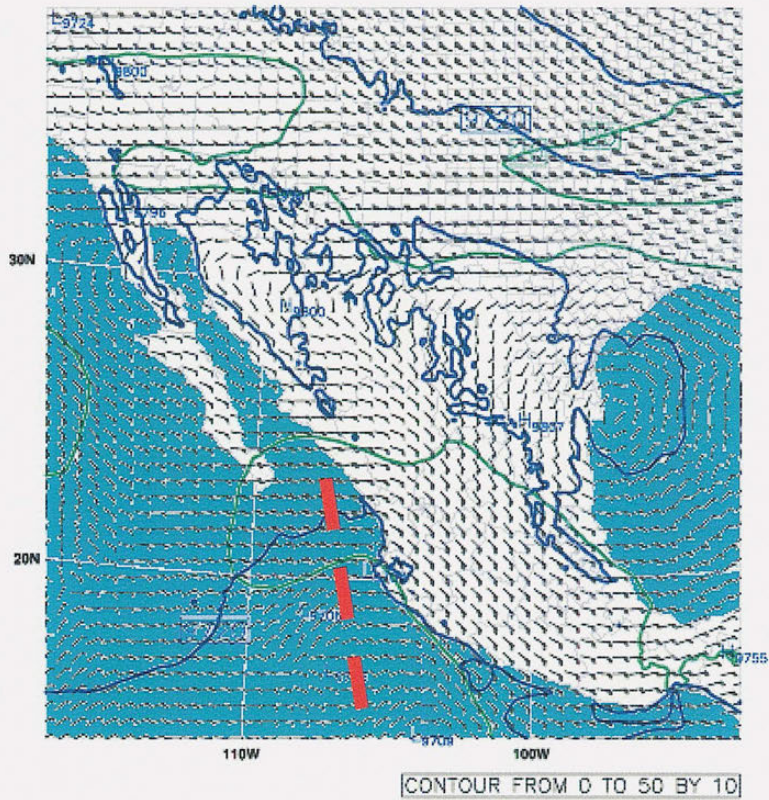


5.37 – NCAR 12-km WRF model analysis of 300 mb winds on a) 8 August 2004 at 00 UTC, and b) 10 August 2004 at 00 UTC.

b)

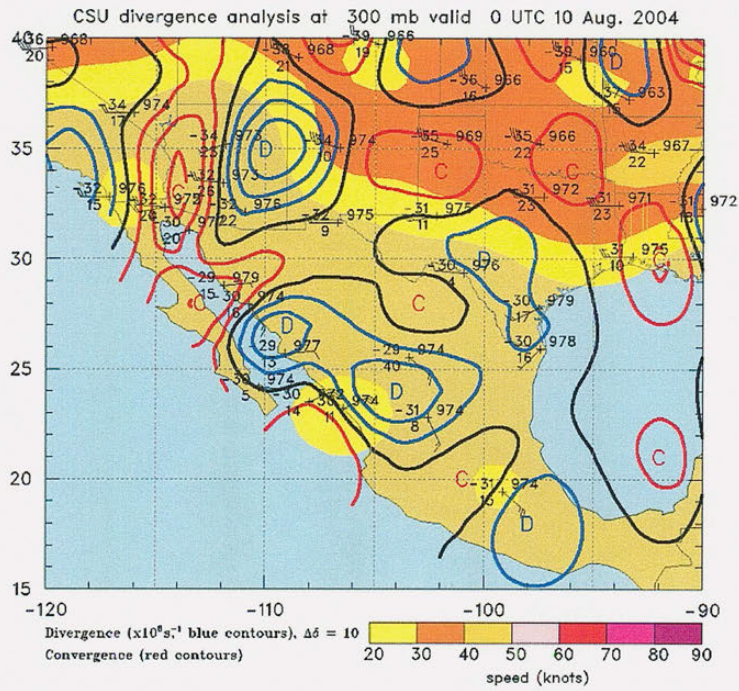
300 mb Hgt (m, blue), Wind Speed (m/s, green) & Winds (kts)

2004-08-10_00:00:00 = 2004-08-10_00:00:00 + 0 h



5.37 – (cont.)

a)



b)

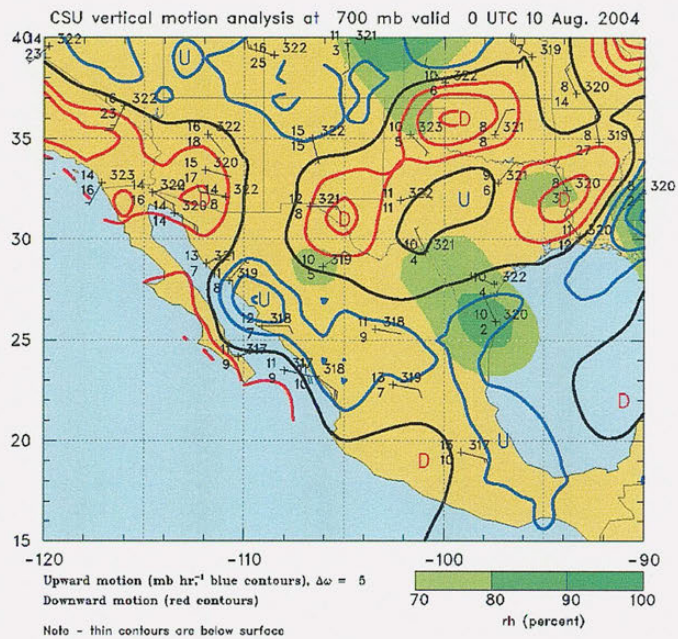


Fig. 5.38 – CSU analysis on 10 August 2004 at 00 UTC of a) 300 mb divergence, and b) 700 mb omega field.

CHAPTER VI

Conclusions

6.1 Overview

This chapter is divided into two parts: summary and conclusions, and future work. In the first part, we summarize the results presented in Chapters Three, Four and Five and present conclusions of this study. Based on the findings presented here, we offer some potential avenues for future research in the last section.

6.2 Summary & Conclusions

Characteristics of convective precipitating features during the 2004 North American Monsoon Experiment and their precursor environmental conditions are examined in an attempt to gain better insight into the predictability and variability of warm season convective processes in the southern portion of the North American Monsoon core region (Tier 1, see Fig. 2.1). Precipitating features that affect this region are very important to North American Monsoon system as they have the potential to

trigger northward propagating surges of moisture along the Gulf of California, which produce episodes of active weather and enhanced precipitation in the United States desert southwest (McCollum et al. 1995, Stensrud et al. 1995, Adams and Comrie 1997, Rogers and Johnson 2007). Two main datasets were used to achieve our objectives: a radar dataset and an environmental dataset. The former, described in Chapter Three, primarily consisted of the composite images of radar reflectivity from the three radars used in NAME. These images were used to evaluate the morphological characteristics of precipitating features, as well as their geographical distribution and rainfall intensity. The latter dataset, discussed in Chapters Four and Five, was composed of synoptic maps and satellite images used to assess the instability, wind shear and synoptic conditions that led to periods of increased or suppressed precipitation.

In Chapter Three we examined the geographical distribution of precipitating features (PFs) within the NAME radar composite region. We found that PFs, particularly Type 1 PFs, were far more common over the complex terrain of the Sierra Madre Occidental (SMO) and adjacent foothills than over the adjacent waters of the Gulf of California (GoC). Pixels over water within the NAME radar composite were affected by PFs less than 6% of the periods observed by radar (Fig. 3.1). The areas most frequently covered by PFs, dominated by Type 1, were the higher terrain of the SMO and adjacent foothills, where PFs were present as much as 18% of the time. This is consistent with the very low precipitation recorded by both cruises of the R/V Altair near the mouth of the GoC and the concentration of convective clouds and previous observations of

pronounced rainfall along the foothills of the SMO, specifically over the Mexican States of Nayarit, Sinaloa, and Sonora (Hales 1972, Douglas *et. al* 1993, Negri *et al.* 1993, Adams and Comrie, 1997, Berbery 2001, Gochis *et al.* 2007, Johnson *et al.* 2007, Lang *et al.* 2007, Rowe *et al.* 2008). The overall characteristics of PFs (regardless of organization mode) observed in the NAME radar composite region were as follows: small size (mean area of 588 km²), with low rain rates (mean rain rates of 2.4 mm h⁻¹), and clear diurnal cycle starting around midday and peaking in the middle to late afternoon. This diurnal cycle is consistent with findings of Berbery (2001), Gochis *et al.* (2003; 2004), and Rowe *et al.* (2008).

After dividing our PFs into four groups according to their size and morphology, we found that nearly 95% of the PFs were classified as type 1 (sub-mesoscale, non-linear), although this group of PFs was actually responsible for only about one quarter of all precipitation (Fig. 3.5). This rainfall contribution figure is higher than the roughly 10% found by Simpson *et al.* (1993) for Darwin, Australia and by Rickenbach and Rutledge (1998) in the West Pacific during TOGA-COARE, probably due to changes in land vs. ocean forcing and heating, and also due to small methodology differences in the calculation of Type 1 rainfall used by Rickenbach and Rutledge (1998). These isolated convective cells were small in areal coverage (mean size of 195 km²) and had a convective rainfall fraction of approximately 58%. This convective fraction is lower than in other tropical areas primarily because of the averaging of convective fractions by Type 1 PFs of widely different sizes. More than half of Type 1 PFs have convective rainfall

fractions greater than 80%, but there a few (i.e. less than 5%) of the PFs that had very low convective fractions. These, were relatively large Type 1 PFs, that did not satisfy the requirements to be classified as Type 3 or Type 4, and were primarily composed of a large stratiform region. Type 2 PFs (sub-mesoscale linear) were very rare, and constituted only 0.16% of the PF population analyzed in this study. These PFs had a more random geographical distribution, but had intense mean convective rain rates (20 mm h^{-1}). While Type 2 PFs occurred during the day, they also occurred in the early morning hours near the coast, possibly associated with the land breeze. This type of PF had the highest convective-to-total rainfall fraction: 87%. Rickenbach and Rutledge (1998) found a convective fraction of 80% for this type of PFs during TOGA-COARE.

While 95% of the PFs examined in this study were relatively small, 72% of the precipitation was generated by MCS-size precipitating features (Types 3 and 4). Type 3 PFs (mesoscale-sized non-linear) were responsible for 57% of the precipitation produced by all features analyzed here, despite making up only 4% of the overall PF population. These large PFs (mean area of $8,161 \text{ km}^2$) were more frequently observed near the foothills of the SMO at elevations around 800 m, and particularly at locations north of Mazatlán. Type 3 PFs underwent a similar diurnal cycle to that observed by Type 1 PFs, but with a slightly delayed peak at 1900 LT. The convective rainfall fraction for Type 3 PFs was the lowest, 45%, resulting from their large stratiform areas, which reduced their mean rain rate to an average value of 3.6 mm h^{-1} . Some of these characteristics were also found by Lang et al. (2007), Nesbitt et al. (2008), and Rowe et al. (2008). On the other

hand, Type 4 PFs (linear MCSs) were able to achieve mean convective rain rates of 21 mm h⁻¹, resulting in a larger convective rainfall fraction: 66%. This rainfall fraction is identical to that found by Rickenbach and Rutledge (1998) in the West Pacific. It is also fairly close to other previous studies on tropical squall lines by Houze (1977) and Houze and Rappaport (1984) who found, respectively, convective rainfall fractions of 60% and 58% in this organizational mode. Nesbitt et al. (2006) showed the importance of MCSs in overall precipitation over the Tropics using the TRMM satellite data from 1998 to 2000 and estimated the contribution by this group (linear + non-linear) to be 70% of the rainfall in the west coast of Central America and nearby East Pacific (versus 72% found here). Whilst many of our results, particularly those regarding the geographic distribution and diurnal cycle of precipitation, confirm some of the NAME findings published recently (Gochis et al. 2007, Johnson et al. 2007, Lang et al. 2007, Nesbitt *et al* 2008, Rowe et al. 2008) this work reveals the specific characteristics and overall frequency and rainfall contribution of each cloud group. Given the widely different characteristics of each group and different potential impacts in the local and regional North American Monsoon system these results should contribute to improved skill in numerical modeling and precipitation forecast, and better planning of hydrological resources in the region.

Given that MCSs play such an important role in the North American Monsoon system and in the Enhanced Convection Area (ECA), where 99% of the PFs were found in the radar composites, there are two important questions that we attempted to address in Chapters Four and Five: 1) whether the occurrence and rainfall produced by these larger

PFs in the NAME ECA somewhat uniform in time or whether they undergo periods when their occurrence was more pronounced, and 2) if their occurrence was variable, what potential factors drive this temporal variability. We found that both the number and total precipitation produced by smaller (Type 1) and larger (Types 3 and 4) PFs varied during NAME. Noteworthy was the highly variable rainfall produced by MCSs, with peaks in their total rainfall observed on 11-13 July, 20-21 July, and 3-5 August 2004 (Figs. 4.5 and 4.10). Lang et al. (2007) also noted an intraseasonal variability in rainfall over the region using Hovmöller diagrams of radar reflectivity and recognized “disturbed” periods when organized convection was more frequent.

Based on previous studies, the development of larger organized PFs has been linked to favorable thermodynamic, kinematic and dynamical conditions of the environment. Typically, one of the necessary precursors to MCS development is the presence of a thermodynamically unstable atmosphere for the development of thunderstorms, as indicated by commonly used instability parameters such as CAPE, Total Totals, SWEAT and/or the K index (Maddox 1983, Laing and Fritsch 2000, Jirak et al. 2003). Nonetheless, instability alone cannot explain the development of MCSs (Lucas and Zipser 2000), so other additional conditions must be present for MCS development. One such condition that has been theorized through modeling studies is that MCSs are favored in the presence of low-level wind shear (i.e. 0-5 km AGL) as deep lifting is generated when the ambient shear interacts with convectively-generated cold air pools (Rotunno et al. 1988, Weisman 1992, Weisman and Rotunno 2004). During TOGA-

COARE, Rickenbach and Rutledge (1998) found that MCSs were favored during periods of westerly wind bursts when the wind shear was stronger. In the middle latitudes, Coniglio et al. (2004) found that MCSs are favored to develop when upper-level wind shear was not too strong, but in the Tropics wind shear is already typically much weaker than in the midlatitudes. In addition to wind shear, the wind field may also contribute to the development of MCSs when divergent conditions are found in the upper portions of the atmosphere and dynamical uplift is generated (Maddox 1983, Cotton et al. 1989, Anderson and Arritt 1998). Lastly, Farfán and Zehnder (1994) found that MCSs with significant propagation developed over the southern portion of the Gulf of California when a stronger midlevel (700 – 500 hPa) easterly-northeasterly flow was present. Dynamical uplift was perhaps generated by an increase in cyclonic relative vorticity in the leeside of the SMO as the easterly flow and tropical waves interact with the local topography (Zehnder et al. 1999). In the northern end of the NAME Tier 1, other boundaries (such as cold and stationary fronts) have been found to play an important role in the development of MCSs (Hales 1972). We hypothesize that the episodes of enhanced MCS rainfall in the southern portion of the NAME Tier 1 region should take place when the atmosphere was relatively unstable and either wind shear was stronger, dynamical uplift was provided through upper-level divergence, or a stronger easterly component in the mid-level zonal flow was present.

The temporal variation of CAPE within the ECA shows a noticeable pattern made up of alternating periods of increasing CAPE and decreasing CAPE. A time series of the

daily mean value of 12Z CAPE within the ECA indicated peaks of approximately 1200 J kg^{-1} , with the most prominent of them occurring on JDs 192, 202, 209 and 217. The 0-6 km shear within the ECA was characterized by two main cycles, which peaked on JDs 202 and 219. While CAPE alone is not statistically well linearly correlated to rainfall (particularly MCS rainfall) the time series of these two variables (Figs. 4.4 and 4.5) did reveal a few noteworthy symmetries. First, the peaks in MCS rainfall occurred when CAPE was above the average value found in our study: 750 J kg^{-1} . However, CAPE values well above average did not necessarily imply that MCS rainfall was much higher as well. This situation is illustrated in Fig. 4.5, where we observed that CAPE was much higher on JD 192-193 than on JD 202-203, but MCS rainfall was significantly greater in the latter period. Secondly, while above average MCS rainfall occurred during periods of above average CAPE, the inverse statement is not true. In other words, not all periods of above average CAPE were matched by higher than average MCS rainfall. This is seen on JD 209, when the mean CAPE within the ECA was rather high ($\sim 1050 \text{ J kg}^{-1}$). In that period type 1 rainfall increased just slightly (Fig. 4.4), but MCS rainfall was substantially below average (Fig. 4.5). Previous findings about the role of thermodynamic instability in the development of MCSs (Lucas and Zipser 2000, Jirak and Cotton 2007) revealed it to be a necessary ingredient to the initial development of ordinary (Type 1) PFs, but insufficient to, alone, ensure that these PFs will upscale into MCSs. Interestingly, examination of the 0-6 km wind shear time series (Fig. 4.11) showed that a minimum in shear occurred around this same period when CAPE was high and MCS rainfall was low

(JD 209). Moreover, there is a relatively good linear correlation (0.63) between 0-6 km wind shear and MCS rainfall, with fairly well matched peaks as shown in Fig. 4.11. These findings supported the hypothesis that MCSs were more likely to occur when the 0-6 km wind shear was stronger in the NAME region. Furthermore, an analysis on the sources of these wind shear peaks revealed that they were associated with increases on the magnitude of the zonal wind component at the mid-levels (Figs. 4.15 and 4.16), which becomes more easterly as also previously reported by and Farfán and Zehnder (1994). Hence, it is possible that MCS development is enhanced by the interaction between low-level wind shear and convective cold pools (Weisman and Rotunno 2004) or, perhaps, the development of a cyclonic vorticity due to the interaction between the local topography and strong mid-level easterlies (Zehnder et al. 1999). Nonetheless, our results showed that the strongest peaks in MCS rainfall occurred only when both, favorable thermodynamics and wind shear conditions were present in the ECA. Moreover, the results presented here demonstrate that the link between convection organization and the environmental CAPE and shear conditions are valid not only to explain the discrete development of an organized PF, but also to explain bulk temporal variations in rainfall and organization when a large number of PFs are examined concomitantly.

The last part of this study sought to understand what particular synoptic patterns were responsible for periods of enhanced precipitation and wind shear described previously. Previous studies have documented the influence of some synoptic features into the region, such as the position of the upper-level anticyclone and tropical easterly

waves, while the impact of upper-level inverted troughs remained elusive (Fuller and Stensrud 2000, Higgins et al. 2004, Johnson et al. 2007). We examined a plethora of satellite images and environmental analysis maps to understand the role of each of these synoptic systems in the development of precipitation over the southern portion of the NAME Tier 1 region. Analysis of the synoptic conditions focused on three periods when rainfall, particularly MCS rainfall, was more pronounced: 10-13 July, 19-22 July, and 2-6 August 2004 (Fig. 4.11). In the first of these three periods we found that MCS development was aided by the existence of an upper-level diffluence area owed to the presence of an inverted trough just east of the NAME ECA. The diffluent flow was a result of the interaction between the upper-level flow around the TUTT and the flow around the North American anticyclone. Moisture was abundant with the northward transport from a vigorous tropical easterly wave, which later developed into Tropical Storm Blas just south of the Baja California Peninsula. Except for the development of a tropical cyclone, a very similar scenario was observed on the other two periods of enhanced convection. There was one other important difference: the development of a jet streak between the upper-level anticyclone and the inverted trough. On both periods, 19-22 July and 2-6 August, this northeast-southwest-oriented jet streak passed right over Mazatlán. In the former case, the jet streak was found at upper-levels (200 mb), but stronger than average winds were also found through the mid-levels, resulting in the enhanced easterly flow and wind shear in the NAME ECA observed around that period. In the latter case, the strongest winds were found at the mid-levels (400-500 mb), where a

closed low pressure center could be identified in the analysis maps. Moreover, in the latter case satellite water vapor images showed this inverted trough wrapping moisture from a nearby tropical wave to its east and advecting this moisture northward into the NAME ECA. Therefore we suggest that inverted troughs play an important role in the enhancement of precipitation in the southern portion of the NAME Tier 1 by enhancing MCS development through favorable wind shear, wind direction and/or upper-level diffluent flow. It is interesting to point out that Lucas and Zipser (2000) found that higher MCS rainfall was more likely during TOGA COARE in the presence of moderate low-level wind shear, but MCS rainfall decreased when shear became too strong. However, they noted that, during TOGA COARE, strong shear typically occurred in the presence of large-scale subsidence. On the other hand, we found that periods of peak shear during NAME occurred concomitantly with the presence of upper-level divergence and favorable large-scale dynamical lifting. Therefore, a new question that arises from this study is whether wind shear or dynamic uplift is more important to MCS development and rainfall in the NAME region. In any case, our results corroborate the suggestion by Pytlak et al. (1995) that an interaction between the upper level anticyclone and transient inverted troughs could produce areas of favored precipitation development through upper-level divergence (Fig. 5.9c-d). Our results provide evidence of this mechanism taking place, in more than one occasion, in the southern portion of the North American Monsoon system and being responsible for the largest rainfall episodes in the region during NAME. This would support the idea that a different position of the upper-level

anticyclone and the upper-level inverted trough could lead to a different orientation of this “North American Monsoon Jet Streak” (Figs. 5.2, 5.9, 5.21) and enhanced precipitation over Arizona as it was described in a hypothetical scenario by Pytlak et al. (1995). Additional studies are necessary to reveal how frequently this “North American Monsoon Jet Streak” develops in the region during the monsoon season.

Lastly, it is important to point out that an analysis of the environmental conditions on 9-10 August maps revealed the approach of an upper-level inverted trough over the region, which was a period when precipitation was rather scarce. We found that the absence of a nearby tropical wave significantly reduced the availability of moisture in the region. As a result, we determined two things from this event: 1) while inverted troughs are an important type of synoptic disturbance relative to the development of enhanced MCS rainfall in the southern portion of the NAME Tier 1 region, they may not, alone, be capable of developing such episodes if moisture is markedly reduced; and 2) tropical easterly waves are a very important source of moisture for the development of convective precipitation in the southern portion of the GoC. Since 50-80% of the annual precipitation in this region takes place during the monsoon season (Gochis et al. 2007), the adequate modeling of the upper-level anticyclone, tropical easterly waves, and tropical upper-level inverted troughs is necessary to improve the predictability of precipitation in the North American Monsoon system.

6.3 Suggestions for Future Research

One of the goals accomplished in this study was to establish a climatology of PFs during NAME 2004. This information provides a background for future research of individual case studies in the region, allowing one to assess whether a particular PF case represented a common observation or rare extreme occurrence in the region. It would be interesting to further explore differences in dynamical and microphysical characteristics of each cloud group and how they are affected by the environmental conditions. Our results have shown that strong mid-level easterly winds and strong 0-6 km wind shear occurred at the same time as peaks in MCS rainfall in the region. Additionally, these peaks occurred when upper-level divergence was present at the same time. Thus, it would be important to study which mechanism provides the greatest contribution to MCS development in the region: wind shear or dynamical uplift. It would also be interesting to examine the exact mesoscale dynamic mechanism through which shear could be contributing to longer-lasting systems in the NAME region. It would be important to reveal whether wind shear interaction with cold pools (Weisman and Rotunno 2004), the interaction between low to mid-level flow and over the local topography (Zehnder 1999), a combination of both processes, or yet another mechanism makes wind shear an important part of MCS rainfall production in the region. Finally, our work demonstrated the role of inverted troughs in the development of enhanced precipitation periods in the NAME ECA. Therefore, another possible theme for future research would be to examine the role of inverted troughs in precipitation and MCS development over other the northern portion of GoC and over the area hypothesized by Ptylak et al. (2005) to bring enhanced rainfall over Arizona. Given the typical position of the upper-level anticyclone,

one would suspect that the interaction between the anticyclone and an inverted trough further north would likely result in a different pattern for precipitation development. Additional studies on the interannual variability of the North American Monsoon Jet Streak described here would also be very helpful in understanding interannual rainfall variability within the North American Monsoon system. Finally, one question that remains open is the interannual variability of MCSs in the region, and how this variability is connected to the number of gulf surges during the North American Monsoon season.

REFERENCES

- Adams, D. K., and A. C. Comrie, 1997: The North American monsoon. *Bull. Amer. Meteor. Soc.*, **78**, 2197-2213.
- Adang, T. C., and R. Gall, 1989: Structure and dynamics of the Arizona monsoon boundary. *Mon. Wea. Rev.*, **117**, 1423-1438.
- Anderson, C. J., and R. W. Arritt, 1998: Mesoscale convective complexes and persistent elongated convective systems over the United States during 1992 and 1993. *Mon. Wea. Rev.*, **126**, 578-599.
- Badan-Dangon, A., C. E. Dorman, M. A. Merrifield, and C. D. Winant, 1991: The lower atmosphere over the Gulf of California. *J. Geophys. Res.*, **96**, 877-896.
- Barber, Dobkin, and Huhdanpaa, 1996: The quickhull algorithm for convex hulls. *ACM Trans. on Math. Software*, **22**, 469-483.
- Battan, L. J., 1973: Radar Observation of the Atmosphere. University of Chicago Press, 324 pp.
- Beals, E. A., 1922: The semipermanent Arizona low. *Mon. Wea. Rev.*, **50**, 341-347.
- Berberly, E. H., 2001: Mesoscale Moisture Analysis of the North American Monsoon. *J Climate*, **14**, 121-137.
- Biggerstaff, M. I., and S. A. Listemaa, 2000: An improved scheme for convective/stratiform echo classification using radar reflectivity. *J. Appl. Meteor.*, **39**, 2129-2150.
- Blake, D., 1923: Sonora storms. *Mon. Wea. Rev.*, **51**, 585-588.
- Bordoni, S., P. E. Ciesielski, R. H. Johnson, B. D. McNoldy, and B. Stevens, 2004: The low-level circulation of the North American Monsoon as revealed by QuikSCAT. *Geophys. Res. Letts.*, **31**, L10109, 10.1029/2004GL020009.
- Bluestein, H. B., and M. H. Jain, 1985: Formation of mesoscale lines of precipitation: Severe squall lines in Oklahoma during the Spring. *J. Atmos. Sci.*, **42**, 1711-1732.

- Brenner, I. S., 1974: A Surge of Maritime Tropical Air – Gulf of California to the Southwestern United States. *Mon. Wea. Rev.*, **102**, 375-389.
- Bringi, V. N., T. Tang, and V. Chandrasekar, 2004: Evaluation of a new polarimetrically based Z-R relation. *J. Atmos. Oceanic Technol.*, **21**, 612-623.
- Browning, K. A., 1977: The structure and mechanism of hailstorms. *Meteor. Monogr.*, **38**, Amer. Meteor. Soc., 1-39.
- Bryson, R., and W. P. Lowry, 1955: Synoptic climatology of the Arizona summer monsoon. Dept. of Meteorology, University of Wisconsin, Scientific Rep. 1., 29 pp.
- Burpee, R. W., 1972: The origin and structure of easterly waves in the lower troposphere of North Africa. *J. Atmos. Sci.*, **29**, 77-90.
- Campbell, A., 1906: Sonora storms and Sonora clouds of California. *Mon. Wea. Rev.*, **34**, 464-465.
- Carbone, R., et al., 2003: Science overview of the North American Monsoon Experiment (NAME Whitepaper), submitted to the National Science Foundation.
- Carey, L. D., R. Cifelli, W. A. Petersen, and S. A. Rutledge, 2000a: Preliminary report on TRMM-LBA rainfall estimation using the S-Pol radar. Department of Atmospheric Science. Paper 697, Colorado State University, 19 pp.
- Carey, L. D., S. A. Rutledge, D. A. Ahijevych, and T. D. Keenan, 2000b: Correcting propagation effects in C-band polarimetric radar observations of tropical convection using differential propagation phase. *J. Appl. Meteor.*, **39**, 1405-1433.
- Carleton, A. M., 1985: Synoptic and Satellite Aspects of the Southwestern U.S. "Monsoon". *J. Climatol.*, **5**, 289-402.
- Carleton, A. M., 1986: Synoptic-dynamic character of "bursts" and "breaks" in the Southwest U.S. summer Precipitation Singularity. *J. Climatol.*, **6**, 605-623.
- Carleton, A. M., D. A. Carpenter, and P. J. Weber, 1990: Mechanisms of interannual variability of the southwest United States summer rainfall maximum. *J. Climate*, **3**, 999-1015.
- Cheng, C., and R. A. Houze, 1979: The distribution of convective and mesoscale precipitation in GATE radar echo patterns. *Mon. Wea. Rev.*, **107**, 1370-1381.
- Ciesielski, P. E., and R. H. Johnson, 2006: Analysis of Heat and Moisture Budgets from NAME. Proceedings from the 27th Conference on Hurricanes and Tropical Meteorology. *Amer. Meteor. Soc.*, oral presentation.

- Ciesielski, P. E., R. H. Johnson, P. T. Haertel, and J. Wang, 2003: Corrected TOGA COARE sounding humidity data: Impact on diagnosed properties of convection and climate over the warm pool. *J. Climate*, **16**, 2370-2384.
- Cifelli, R. W.A. Petersen, L.D. Carey, and S.A. Rutledge, 2002: Radar Observations of the Kinematic, Microphysical, and Precipitation Characteristics of Two MCSs in TRMM-LBA. *J. Geophys. Res.*, **29**, 10.1029/2000JD0000264.
- Coniglio, M. C., D. J. Stensrud, and L. J. Wicker, 2004: How upper-level shear can promote organized convective systems. Preprints, 22nd Conf. on Severe Local Storms, Amer. Meteor. Soc., 4 pp.
- Cotton, W. R. and R. A. Anthes, 1989: *Storm and Cloud Dynamics*, Academic Press, 883 pp.
- Dai, A., 2001: Global precipitation and thunderstorm frequencies. Part II: Diurnal Variations. *J. Climate*, **14**, 1112-1128.
- Dai, A., F. Giorgi, and K. E. Trenberth, 1999: Observed and model simulated precipitation diurnal cycle over the contiguous United States. *J. Atmos. Sci.*, **104**, 6377-6402.
- DeMott, C. A., and S. A. Rutledge, 1998a: The vertical structure of TOGA COARE convection. Part I: Radar echo distributions. *J. Atmos. Sci.*, **55**, 2730-2747.
- DeMott, C. A., and S. A. Rutledge, 1998b: The vertical structure of TOGA COARE convection. Part II: Modulating influences and implications for diabatic heating. *J. Atmos. Sci.*, **55**, 2748-2762.
- Doswell, C.A. III, and E.N. Rasmussen, 1994: The effect of neglecting the virtual temperature correction on CAPE calculations. *Wea. Forecasting*, **9**, 625-629
- Douglas, A. V., and P. J. Englehart, 2007: A Climatological Perspective of Transient Synoptic Features During NAME 2004. *J. Climate*, **20**, 1947-1954.
- Douglas, M. W., 1995: The Summertime Low-Level Jet over the Gulf of California. *Mon. Wea. Rev.*, **123**, 2334-2347.
- Douglas, M. W., and J. C. Leal, 2003: Summertime Surges over the Gulf of California: Aspects of Their Climatology, Mean Structure, and Evolution from Radiosonde, NCEP Reanalysis, and Rainfall Data. *Wea. Forecasting*, **18**, 55-74.
- Douglas, M. W., R. Maddox, K. Howard, and S. Reyes, 1993: The Mexican monsoon. *J. Climate*, **6**, 1665-1667.

- Dunn, G. E., 1940: Cyclogenesis in the tropical Atlantic. *Bull Amer. Meteor. Soc.*, **21**, 215-229.
- Farfán, L. M., and J. A. Zehnder, 1994: Moving and stationary mesoscale convective systems over northwest Mexico during the Southwest Area Monsoon Project. *Wea. Forecasting*, **9**, 630-639.
- Nieto Ferreira, R., and W. H. Schubert, 1999: The role of Tropical Cyclones in the Formation of Tropical Upper-Tropospheric Troughs. *J. Atmos. Sci.*, **56**, 2891-2907.
- Fovell, R. G., and Y. Ogura, 1985: Effect of a Numerically Simulated Multicell Storm Structure. *J. Atmos. Sci.*, **46**, 3144-3176.
- Fuller, R. D., and D. J. Stensrud, 2000: The Relationship between Tropical Easterly Waves and Surges over the Gulf of California during the North American Monsoon. *Mon. Wea. Rev.*, **128**, 2983-2989.
- Gamache, J. F., and R. A. Houze, 1983: Water budget of a mesoscale convective system in the Tropics. *J. Atmos. Sci.*, **40**, 1835-1850.
- Giangrande, S. E., and A. V. Ryzhkov, 2005: Calibration of dual-polarization radar in the presence of partial beam blockage. *J. Atmos. Oceanic. Technol.*, **22**, 1156-1166.
- Gochis, D. J., J.-C. Leal, W. J. Shuttleworth, C. J. Watts, and J. Garatuza-Payan, 2003: Preliminary Diagnostics from a New Event-Based Precipitation Monitoring System in Support of the North American Monsoon Experiment. *J. Hydrometeor.*, **4**, 974-981.
- Gochis, D. J., A. Jimenez, C. J. Watts, J. Garatuza-Payan, and W. J. Shuttleworth, 2004: Analysis of 2002 and 2003 warm-season precipitation from the North American Monsoon Experiment event rain gauge network. *Mon Wea. Rev.*, **132**, 2938-2953.
- Gochis, D. J., C. J. Watts, J. Garatuza-Payan, and J. Cesar-Rodriguez, 2007: Spatial and Temporal Patterns of Precipitation Intensity as Observed by the NAME Event Rain Gauge Network from 2002 to 2004. *J Climate*, **20**, 1734-1750.
- Golestani, Y., V. Chandrasekar, and V. N. Bringi, 1989: Intercomparison of multiparameter radar measurements. Preprints, 24th Conference on Radar Meteorology, *Amer. Meteorol. Soc.*, 309-314.
- Green, C. R., 1963: Summer rainy days in Arizona. Technical Rep. on the Meteorology and Climatology of Arid Regions 11, The Institute of Atmospheric Physics, University of Arizona, Tucson, 61 pp.
- Green, C. R., and W. D. Sellers, 1964: Arizona Climate. University of Arizona Press, 503 pp.

- Hales, J. E., 1972: Surges of Maritime Tropical Air Northward Over the Gulf of California. *Mon. Wea. Rev.*, **100**, 298-306.
- Hales, J. E., 1974: The southwestern United States summer monsoon source - Gulf of Mexico or Pacific Ocean? *J. Appl. Meteor.*, **13**, 331-342.
- Hane, C. E., 1973: The squall line thunderstorm: Numerical experimentation. *J. Atmos. Sci.*, **30**, 1672-1690.
- Harrington, J. A., R. Cerveny, and R. Balling Jr., 1992: Impact of the Southern Oscillation on the North American Monsoon. *Phys. Geogr.*, **13**, 318-330.
- Hasimoto, R., and S. Reyes, 1988: Transporte atmosferico de vapor agua sobre la region de America tropical de Mayo a Septiembre de 1979. *Geofis. Intl.*, **27**, 199-229.
- Hastings, J. R. and R. Turner, 1965: Seasonal precipitation regimes in Baja California, *Geogr. Ann.*, **47A**, 204-223.
- Hess, S.L., 1959: *Introduction to Theoretical Meteorology*. Holt, Rhinehart, and Winston, 362 pp.
- Higgins, R. W., 2004: North American Monsoon Experiment (NAME): Science and implementation plan. [Available online at <http://www.joss.ucar.edu/name/>.]
- Higgins, R. W., D. J. Gochis, 2007: Synthesis of Results from the North American Monsoon Experiment (NAME) Process Study. *J. Climate*, **20**, 1601-1607.
- Higgins, R. W., W. Shi, and C. Hain, 2004: Relationships between Gulf of California Moisture Surges and Precipitation in the Southwestern United States. *J. Climate*, **17**, 2983-2995.
- Higgins, R. W., W. Shi, E. Yarosh, and R. Joyce, cited 2005: Improved U.S. precipitation quality control system and analysis. NCEP/Climate Prediction Center Atlas 7. [Available online at <http://www.cpc.ncep.noaa.gov/>.]
- Houghton, J. G., 1979: A model for orographic precipitation in the north-central Great basin. *Mon. Wea. Rev.*, **107**, 1462-1475.
- Houze, R. A., 1977: Structure and dynamics of a tropical squall-line system. *Mon. Wea. Rev.*, **105**, 1540-1567.
- Houze, R. A., 1982: Cloud clusters and large-scale vertical motions in the Tropics. *J. Meteor. Soc. Japan*, **60**, 396-410.

- Houze, R. A., 1993: *Cloud Dynamics*. Academic Press, 573 pp.
- Houze, R. A, and E. N. Rappaport, 1984: Air motions and precipitation structure of an early summer squall line over the eastern tropical Atlantic. *J. Atmos. Sci.*, **41**, 553-574.
- Kelley, W. E., and D. R. Mock, 1982: A diagnostic study of upper tropospheric cold lows over the western North Pacific. *Mon. Wea. Rev.*, **110**, 471-480.
- Jauregui, E., and F. Cruz, 1981: Algunos aspectos del clima de Sonora y Baja California. Equipatas y surgencias de humedad. *Bol. Inst. Geogr.*, **10**, 143-180.
- Jirak, I. L., W. R. Cotton, and R. L. McAnelly, 2003: Satellite and radar survey of mesoscale convective system development. *Mon. Wea. Rev.*, **131**, 2428-2449.
- Jirak, I. K., and W. R. Cotton, 2007: Observational Analysis of the Predictability of Mesoscale Convective Systems. *Wea. Forecasting*, **22**, 813-838.
- Johnson, R. H., P. E. Ciesielski, B. D. McNoldy, P. J. Rogers, and R. K. Taft, 2007: Multiscale Variability of the Flow during the North American Monsoon Experiment. *J. Climate.*, **20**, 1628-1648.
- Laing, A. G., and J. M. Fritsch, 1997: The large-scale environments of the global populations of mesoscale convective complexes. *Mon. Wea. Rev.*, **128**, 2756-2776.
- Landsea, C. W., 1993: A climatology of intense (or major) Atlantic hurricanes. *Mon. Wea. Rev.*, **121**, 1703-1713.
- Lang, T. J., R. E. Carbone, S. A. Rutledge, D. A. Ahijevych, and S. W. Nesbitt, 2006: NAME Regional Radar Composites, Version 2. Colorado State University, 19 pp. [Available online at http://radarmet.atmos.colostate.edu/~tlang/readme_NAME_regional_radar_composites_v2.pdf.]
- Lang, T. J, D. A. Ahijevych, S. W. Nesbitt, R. E. Carbone, S. A. Rutledge, and R. C. Cifelli, 2007: Radar-Observed Characteristics of Precipitating Systems During NAME 2004. *J. Climate*, **20**, 1713-1733.
- Leary, C. A., 1984: Precipitation structure of the cloud clusters in a tropical easterly wave. *Mon. Wea. Rev.*, **112**, 313-325.
- LeMone, M. A., 1983: Momentum transport by a lines of cumulonimbus. *J. Atmos. Sci.*, **40**, 1815-1834.
- Lucas, C, and E. J. Zipser, 2000: Environmental variability during TOGA-COARE. *J. Atmos. Sci.*, **57**, 2333-2350.

- Maddox, R. A., D. M. Rodgers, and K. M. Howard, 1982: Mesoscale Convective Complexes over the United States in 1982: Annual Summary. *Mon. Wea. Rev.*, **110**, 1501-1514.
- Maddox, R. A., 1983: Large-scale meteorological conditions associated with midlatitude mesoscale convective complexes. *Mon. Wea. Rev.*, **111**, 126-140.
- Maddox, R., D. McCollum, and K. Howard, 1995: Large-scale patterns associated with severe summertime thunderstorms over central Arizona. *Wea. Forecasting*, **10**, 763-778.
- Manvitz, J. D., 1972a: The structure and motion of severe hailstorms. Part I: Supercell Storms. *J. Appl. Meteor.*, **11**, 166-179.
- Marwitz, J. D., 1972b: The structure and motion of severe hailstorms. Part II: Multi-cell storms. *J. Appl. Meteor.*, **11**, 180-188.
- McCollum, D. M., R. A. Maddox, and K. W. Howard, 1995: Case study of a severe mesoscale convective system in central Arizona. *Wea. Forecasting*, **10**, 643-665.
- Mitchell, V. L., 1976: The regionalization of climate in the western United States. *J. Appl. Meteor.*, **15**, 920-927.
- Moncrieff, M. W., and J. S. A. Green, 1972: The propagation and transfer properties of steady convective overturning in shear. *Quart. J. Roy. Meteor. Soc.*, **98**, 336-352.
- Negri, A. J., R. F. Adler, R. A. Maddox, K. W. Howard, and P. R. Keehn, 1993: A regional rainfall climatology over Mexico and the southwest United States derived from passive microwave and geosynchronous infrared data. *J. Climate*, **6**, 2144-2161.
- Nesbitt, S. W., R. Cifelli, and S. A. Rutledge, 2006: Storm morphology and rainfall characteristics of TRMM precipitation features. *Mon. Wea. Rev.*, **134**, 2702-2721.
- Nesbitt, S. W., D. J. Gochis, and T. J. Lang, 2008: The diurnal cycle of clouds and precipitation along the Sierra Madre Occidental during the North American Monsoon Experiment: Implications for precipitation estimation in complex terrain. *J. Hydromet.*, in press.
- Nesbitt, S. W., E. J. Zipser, and D. J. Cecil, 2000: A census of precipitation features in the Tropics using TRMM: Radar, ice scattering, and lightning observations. *J. Climate*, **13**, 4087-4106.
- Newton, C. W., and H. Newton, 1959: Dynamical interactions between large convective clouds and the environment with vertical shear. *J. Meteor.*, **16**, 483-496.

- Nuss, W. A., and D. W. Titley, 1994: Use of multiquadric interpolation for meteorological objective analysis. *Mon. Wea. Rev.*, **122**, 1611-1631.
- Oki, T., and K. Musiake, 1994: Seasonal change of the diurnal cycle of precipitation over Japan and Malaysia. *J. Appl. Meteor.*, **33**, 1445-1463.
- Pasch, R. J., L. A. Avila, J-G Jiing, 1998: Atlantic Tropical Systems of 1994 and 1995: A Comparison of a Quiet Season to a Near-Record-Breaking One. *Mon. Wea. Rev.*, **126**, 1106-1123.
- Patterson, V. L., M. D. Hudlow, P. J. Pytlowany, F. P. Richards, and J. D. Hoff, 1979: GATE radar rainfall processing system. NOAA Tech. Memo. EDIS 26, NOAA, Washington, DC, 34 pp. [Available from National Technical Information Service, Sills Building, 5285 Port Royal Road, Springfield, VA 22161.].
- Pereira, L. G., and S. A. Rutledge, 2007: Diurnal Cycle of Shallow and Deep Convection for a Tropical Land and an Ocean Environment and Its Relationship to Synoptic Wind Regimes. *Mon. Wea. Rev.* **134**, 2688-2701.
- Petersen, W. A., R. Cifelli, D. J. Boccippio, S. A. Rutledge, and C. Fairall, 2003: Convection and easterly wave structure observed in the eastern Pacific warm pool during EPIC-2001. *J. Atmos. Sci.*, **60**, 1754-1773.
- Price, J. D., and G. Vaughan, 1992: Statistical studies of cut-off low systems. *Ann. Geophys.*, **10**, 96-102.
- Pytlak, E., M. Goering, and A. Bennett, 2005: Upper Tropospheric Troughs and Their Interaction with the North American Monsoon. Preprints, *19th Conf. on Hydrology*, San Diego, CA, Amer. Meteor. Soc., JP2.3.
- Rasmusson, E. M., 1967: Atmospheric water vapor transport and the water balance of North America: Part 1. Characteristics of the water vapor flux field. *Mon. Wea. Rev.*, **95**, 403-427.
- Reason, C. J. C., and D. G. Steyn, 1992: The dynamics of coastally trapped mesoscale ridges in the lower atmosphere. *J. Atmos. Sci.*, **49**, 1677-1692.
- Reed, R. J., and E. E. Recker, 1971: Structure and properties of synoptic-scale wave disturbances in the equatorial western Pacific. *J. Atmos. Sci.*, **28**, 1117-1133.
- Reed, R. J., D. C. Norquist, and E. E. Recker, 1977: The structure and properties of African wave disturbances as observed during Phase III of GATE. *Mon. Wea. Rev.*, **105**, 317-333.

- Reitan, C. H., 1957: The role of precipitable water vapor in Arizona's summer rains. Tech. Rep. on the Meteorology and Climatology of Arid Regions 2, The Institute of Atmospheric Physics, University of Arizona, Tucson, 19 pp.
- Reyes, S., and L. Cadet, 1988: The southwest brach of the North American Monsoon during 1979, *Mon. Wea. Rev.*, **116**, 1175-1187.
- Rickenbach, T. M., and S. A. Rutledge, 1998: Convection in TOGA COARE: Horizontal scale, morphology, and rainfall production. *J. Atmos. Sci.*, **55**, 2715-2729.
- Riehl, H., 1945: Waves in the easterlies and the polar front in the tropics, Misc. Rep. 17, Dept. of Meteorology, University of Chicago, 79 pp.
- Riehl, H., 1954: *Tropical Meteorology*. McGraw-Hill, 392 pp.
- Rogers, P. J., and R. H. Johnson, 2007: Analysis of the 13-14 July Gulf Surge Event during the 2004 North American Monsoon Experiment. *Mon. Wea. Rev.*, **135**, 3098-3117.
- Rotunno, R., J. B. Klemp, and M. L. Weisman, 1988: A theory for strong, long-lived squall lines. *J. Atmos. Sci.*, **45**, 463-485.
- Rowe, A. K., S. A. Rutledge, T. J. Lang, P. E. Ciesielski, and S. M. Saleeby, 2008: Elevation-dependent trends in precipitation observed during NAME. *Mon. Wea. Rev.*, in press.
- Rowson, D. R., and S. J. Colucci, 1992: Synoptic climatology of thermal low-pressure systems over southwestern North America. *Int. J. Climatol.*, **12**, 529-545.
- Sadler, J. C., 1967: The tropical upper tropospheric trough as a secondary source of typhoons and a a primary source of tradewind disturbances. Hawaii Institute of Geophysics Rep. 67-12, 103 pp. [Available from HIG, 2525 Correa Rd. Honolulu, HI 96822]
- Saleeby, S. M., and W. R. Cotton, 2004: Simulations of the North American monsoons system. Part I: Model anaylis of the 1993 monsoon season. *J. Climate*, **17**, 1997-2018.
- Scarchilli, G., E. Gorgucci, V. Chandrasekar, and A. Dobaie, 1996: Self-consistency of polarization diversity measurement of rainfall. *IEEE Trans. Geosci. Remote Sens.*, **34**, 22-26.
- Schmitz, T. J., and S. L. Mullen, 1996: Water vapor transport associated with summertime North American monsoon as depicted by ECMWF analyses. *J. Climate*, **9**, 1621-1633.

- Schumacher, C., and R. A. Houze Jr, 2003: The TRMM Precipitation Radar's View of Shallow, Isolated Rain. *J. Appl. Meteor.*, **42**, 1519-1524.
- Simpson, J. E, 1997: Gravity currents in the Environment and the Laboratory. 2nd Ed. Cambridge University Press, 244 pp.
- Simpson, J. E., T. D. Keenan, B. Ferrier, R. H. Simpson, and G. J. Holland, 1993: Cumulus mergers un the maritime continent region. *Meteor. Atmos. Phys.*, **51**, 73-99.
- Simpson, J. E., N. Frank, D. Shideler, and H. M. Johnson, 1968: The hurricane disaster potential scale. *Weatherwise*, **27**, 169 and 186.
- Steiner, M., and R. A. Houze Jr., 1993: Three-dimensional validation at TRMM ground truth sites: Some early results from Darwin, Australia. Preprints, 26th Conference on Radar Meteorology, *Amer. Meteor. Soc.*, 417-420.
- Steiner, M., R. A. Houze Jr., and S. E. Yuter, 1995: Climatological characteristics of three-dimensional storm structure from operational radar and rain gauge data. *J. Appl. Meteor.*, **34**, 1978-2007.
- Simpson, J. R., R. F. Adler, and G. R. North, 1998: A proposed Tropical Measuring Mission (TRMM) satellite. *Bull. Amer. Meteor. Soc.*, **69**, 278-295.
- Simpson, J., T. D. Keenan, B. Ferrier, R. H. Simpson, G. J. Holland, 1993: Cumulus mergers in the maritime continent region. *Meteor. Atmos. Phys.*, **51**, 73-99.
- Stensrud, D. J., R. L. Gall, S. L. Mullen, and K. W. Howard, 1995: Model climatology of the Mexican monsoon. *J. Climate*, **8**, 1775-1794.
- Stensrud, D. J., R. L. Gall, and M. K. Nordquist, 1997: Surges over the Gulf of California during the Mexican Monsoon. *Mon. Wea. Rev.*, **125**, 417-437.
- Tang, M. and E. R. Reiter, 1984: Plateau monsoons of the Northern Hemisphere: A comparison between North America and Tibet. *Mon. Wea. Rev.*, **112**, 617-637.
- Takeda, T., 1977: Numerical of a precipitating convective cloud: The formation of a "long-lasting" cloud. *J. Atmos. Sci.*, **28**, 350-376.
- Tessendorf, S. A., L. J. Miller, K. C. Wiens, and S. A. Rutledge. 2005: The 29 June 2000 supercell observed during STEPS. Part I: Kinematics and microphysics. *J. Atmos. Sci.*, **62**, 4127-4150.
- Thompson, R. M., S. W. Payne, E. E. Recker, and R. J. Reed, 1979: Structure and properties of synoptic-scale wave disturbances in the intertropical convergence zone of the eastern Atlantic. *J. Atmos. Sci.*, **36**, 53-72.

- Thorpe A. J., M. J. Miller, and M. W. Moncrieff, 1982: Two-dimensional convection in non-constant shear: A model of mid-latitude squall lines. *Quart. J. Roy. Meteor. Soc.*, **108**, 739-762.
- Wallace, J. M., 1975: Diurnal variations in precipitation and thunderstorm frequency over the conterminous United States. *Mon. Wea. Rev.*, **103**, 406-419.
- Watson, A. W., R. Holle, and R. E. Lopez, 1994: Cloud-to-ground lightning and upper-air patterns during bursts and breaks in the southwest monsoon. *Mon. Wea. Rev.*, **122**, 1726-1739.
- Weisman, M. L., 1992: The role of convectively generated rear-inflow jets in the evolution of mesoconvective systems. *J. Atmos. Sci.*, **49**, 1826-1847.
- Weisman, M. L., and J. B. Klemp, 1982: The dependence of numerically simulated convective storms on vertical wind shear and buoyancy. *Mon. Wea. Rev.*, **110**, 504-520.
- Weisman, M. L., and R. Rotunno, 2004: A theory for strong long-lived squall lines revisited. *J. Atmos. Sci.*, **61**, 361-382.
- Whitfield, M. B., and S. W. Lyons, 1992: An Upper-Tropospheric Low over Texas during Summer. *Wea. Forecastin*, **7**, 89-106.
- Wilhelmson, R. B., and Y. Ogura, 1972: The pressure perturbation and the numerical modeling of a cloud. *J. Atmos. Sci.*, **29**, 1295-1307.
- Wilks, D. E., 1994: *Statistical Methods in the Atmospheric Sciences*. Academic Press, 464 pp.
- Xu, J., X. Gao, J. Shuttleworth, S. Sorooshian, and E. Small, 2004: Model climatology of the North American monsoon onset period during 1980-2001. *J. Climate*, **17**, 3892-3906.
- Yuter, S. E., and R. A. Houze Jr., 1997: Measurements of rain drop size distributions over the Pacific warm pool and implications for Z-R relations. *J. Appl. Meteor.*, **36**, 847-867.
- Yuter, S. E., and R. A. Houze Jr., 1998: The natural variability of precipitating clouds over the western Pacific warm pool. *Quart. J. Roy. Meteor. Soc.*, **124**, 53-99.
- Zehnder, J. A., D. M. Powell, and D. L. Ropp, 1999: The Interaction of Easterly Waves, Orography, and the Intertropical Convergence Zone in the Genesis of Eastern Pacific Tropical Cyclones. *Mon Wea. Rev.*, **127**, 1566-1585.

Zipser, E. J., 1977: Mesoscale and convective-scale downdrafts as distinct components of squall-line circulation. *Mon. Wea. Rev.*, **105**, 1568-1589.